Subsonic Open Cavity Flows And Their Control Using Steady Jets

Naser Hamood Al Haddabi

Submitted in fulfilment of the requirements for the Degree of Doctor of Philosophy

School of Engineering
College of Science and Engineering
University of Glasgow

May 2018

Abstract

Cavity flow induces strong flow oscillations, which increase noise, drag, vibration, and structural fatigue. This type of flow impacts a wide range of low speed applications, such as aircraft wheel wells, ground transportations, and pipelines. The objective of the current study is to examine the reverse flow interaction inside the cavity, which has a significant impact on the cavity flow oscillations. The study also investigates the impact of steady jets with different-configurations on the time-average field and the oscillations of the cavity separated shear layer. The purpose of the steady jets is suppressing the oscillations of the cavity separated shear layer. The experiments were performed for an open cavity with $L/D = 4$ at Re_θ between 1.28×10^3 to 4.37×10^3. The steady jets were applied with different: momentum fluxes ($J = 0.11\ kg/m.s^2, 0.44\ kg/m.s^2$ and $0.96\ kg/m.s^2$), slot configurations (sharp edge and coanda), and blowing locations (blowing from the cavity leading and trailing edges). The data were acquired using qualitative (surface oil flow visualisation) and quantitative (hot-wire anemometry, laser Doppler anemometry, particle image velocimetry, and pressure measurements) flow diagnostics techniques. The study found that a low-frequency instability dominates the velocity spectra of the cavity separated shear layer. This instability decreases with increasing Re_θ and is related to the reverse flow interaction. This interaction takes place when the reverse flow influences the sensitive separation point of the cavity separated shear layer. As a result, a large amplitude flapping wave is generated and propagates downstream of the cavity separated shear. It was also revealed that increasing J for the leading and trailing edges blowing enhances the reverse flow interaction and increases the broadband level of the unsteady wall pressure spectra. Thus, these types of jet blowing are not suitable for controlling the oscillations of the cavity separated shear layer.

Contents

Abstract iii

Acknowledgments viii

Declaration ix

Nomenclature ix

1 Introduction 1

1 Aims and objectives of the study 3

2 Thesis structure 4

2 Literature Survey 7

1 The basics of the shear flows 7

1.1 Mixing layers 7

2 Time-Averaged Open Cavity Flow 11

2.1 Open cavity flow 12

2.2 Section summary 17

3 Oscillations of the cavity separated shear layer 18

3.1 Shedding of the large vortical structures 18

3.2 Flapping motion of the cavity separated shear layer 21

3.3 Dimensionless parameters for the cavity separated shear layer oscillations 22

3.4 Factors affecting the organisation of the cavity separated shear layer oscillations 23

3.5 Section summary 26

4 The feedback cycle 27

4.1 The mechanisms of feedback disturbances 29

4.2 Section summary . . . 33
5 Cavity flow control . . . 34
5.1 Geometry modification of the leading and trailing edges . . 35
5.2 Excitation of the upstream boundary layer . . . 37
5.3 Stabilising the recirculation zone . . . 38
5.4 Frequency excitation . . . 41
5.5 Phase cancellation . . . 45
5.6 Section summary . . . 46
6 Concluding remarks . . . 47

3 Experimental Set-up **49**
1 Wind tunnel . . . 49
2 Experimental model . . . 50
3 Test cases . . . 55
4 Surface oil flow visualisation . . . 57
5 Hot-wire anemometry (HWA) . . . 58
6 Laser Doppler anemometry (LDA) . . . 62
7 Particle image velocimetry (PIV) . . . 66
8 Pressure measurements . . . 71
9 Errors and uncertainty . . . 73

4 Characterisation of Free Stream, Boundary Layer, and Jets **75**
1 Free stream characteristics . . . 75
2 Flow around the model leading edge . . . 77
3 Characteristics of the referenced boundary layer . . . 77
4 Streamwise and spanwise development of the boundary layer . . . 80
5 Characteristics of the blowing jets . . . 82
5.1 Actuator outside the cavity model . . . 82
5.2 Actuator at the cavity model . . . 88
6 Concluding remarks . . . 94

5 Baseline Cavity Flow **97**
1 Time-averaged flow field . . . 97
1.1 Comparing time-averged results with the literature . . . 102
2 Oscillations of the cavity separated shear layer . . . 104
2.1 Low-frequency instabilities . . . 104

2.2 Higher-frequency instabilities 109
2.3 Influence of the Reynolds number on the oscillations of the cavity separated shear layer 112
3 Concluding remarks 115

6 Blowing from Cavity Leading Edge 117
1 Surface oil flow visualisations 117
2 Time-averaged flow field 118
2.1 Jet penetration 118
2.2 Jet impact on the cavity flow topology 120
2.3 Jet impact on the cavity separated shear layer 123
3 Oscillations of the cavity separated shear layer 126
4 Influence of the slot configuration 130
4.1 Comparison of jet penetration 131
4.2 Comparison of the time-averaged cavity flow 132
4.3 Comparison of the cavity separated shear layer oscillations 134
5 Concluding remarks 136

7 Blowing From Cavity Trailing Edge 139
1 Surface oil flow visualisations 139
2 Jet behaviour 140
3 Jet impact on the cavity flow topology 142
4 Jet impact on the cavity separated shear layer 143
5 Jet impact on the cavity separated shear layer oscillations 146
6 Comparison between blowing from the cavity leading edge and blowing from the cavity trailing edge 146
6.1 Comparison of the time-averaged cavity flow 148
6.2 Comparison of the cavity separated shear layer oscillations 150
7 Concluding remarks 152

8 Conclusions and Recommendations for Future Work 155
1 Conclusions 155
2 Recommendations for future work 159

Bibliography 161

Appendices

A Turbulent Boundary Layers **175**
1 Definition of the boundary layer 175
2 Development of the turbulent boundary layer 176
3 Characterising equations of the turbulent boundary layer 177
4 Summary 179

B Other shear flows **181**
1 Planar jet 181
1.1 Development regions of planar jets 181
1.2 Momentum flux of planar jets 182
1.3 Oscillations of planar jets 183
1.4 Section summary 184
2 Opposing planar jets 185
3 Coanda effect 186
4 Flow over backward facing step (BFS) 188

C Statistical Description of Turbulence **191**
1 Reynolds decomposition 191
2 Temporal and spatial correlations 193
3 Reynolds stresses 194

D Calculation of Stroke Number **197**

E Convergence Study for PIV **199**

F Uncertainty Calculations for the PIV Measurements **201**

G Relative Expanded Uncertainty for HWA Measurements **203**

H The proper orthogonal decomposition (POD) **205**

Acknowledgements

I am grateful for all the support and the golden advices extended to me by my supervisor Prof. Konstantinos Kontis. I would also like to thank my second supervisor Dr. Hossein Zare-Behtash for supporting, encouraging, and inspiring me throughout my study period. I would like also to thank Michea Giuni (the best trainer), John Kitching (the magic hands), John Mcculloch (the wise person), Colin Roberts (the kind man), and all the technical staff and the colleagues who supported me during my Ph.D. study. The support of EPSRC funded National Wind Tunnel Facility project (grant EP/L024888/1) is gratefully acknowledged.

Most importantly, I thank my family and close friends, especially to my wife, sons, mum and dad for their enduring support, encouragement, and motivation.

لا زالت الدار التي احتوتنا وألعاب ابني المتناثرة فيها وكل الأما كن
التي ا حتضنتنا من قسوة البرد والأيام وكل ذ كرياتنا الجميلة المخزنة فيها...
لازالت تغرد في روحي و وجداني .

نصر بن حمود بن حمد الهدابي
23 ربيع الأول 1439هـ

Declaration

I declare that, except where explicit reference is made to the contribution of others, that this dissertation is the result of my own work and has not been submitted for any other degree at the University of Glasgow or any other institution.

Naser Hamood Al Haddabi

Nomenclature

Roman Symbols

a	Hot-wire overheat ratio
b	Local half width of the jet [m]
b_0	Half width of the slot [m]
BFS	Backward facing step
C	Coanda slot
c	Speed of sound in the fluid [m/s]
CTA	Constant temperature Anemometry
C_μ	Momentum coefficient
D	Cavity depth [m]
DR	Jet decay rate
f	Frequency [Hz]
GR	Jet growth rate
H	The distance between the cavity and the top solid boundary [m]
h	Characteristic slot width [m]
h	Slot width [m]
R	Radius of the coanda surface [m]
HWA	Hot-wire anemometry

J	Jet momentum flux per unit span $[kg/m.s^2]$
K-H	Kelvin-Helmholtz instability
L	Cavity length [m]
l_y	Integral length scale
LDA	Laser Doppler anemometry
LE	Cavity leading edge
M	Mach number
N	Acoustic mode number
N	Mode of the separated shear layer oscillations
N	Number of samples
N	The ensemble size
P	Pressure [Pa]
PIV	Particle image velocimetry
POD	The proper orthogonal decomposition
R	Cylinder radius [m]
R	Velocity magnitude, where $R = \sqrt{U^2 + V^2}$ [m]
R_0	Hot-wire probe resistances at ambient temperature [Ω]
R_{mn}	Two-point spatial correlation coefficient between variables m and n
Re_d	Reynolds number based on cavity depth
Re_H	Reynolds number based on backward facing step hight
Re_h	Reynolds number based on a slot width
Re_L	Reynolds number based on cavity length
Re_m	Reynolds number based on a variable m

Re_θ	Reynolds number based on the momentum thickness of the upstream boundary layer at $x/D = -0.33$
Re_R	Reynolds number based on cylinder radius
Re_t	Reynolds number based on the model's thickness
$R(\tau)$	Auto-covariance $[m^2/s^2]$
R_w	Hot-wire probe resistances at operating temperature [Ω]
SE	Sharp edge slot
St	Non-dimensional frequency (Strouhal number)
STK	Stokes number
T	Oscillation period [s]
T	The time interval [s]
t	Penetration distance of a jet into a cylinder [m]
TBL	Turbulent boundary layer
TE	Cavity trailing edge
U	Streamwise velocity [m/s]
u'	Fluctuations of the streamwise velocity [m/s]
$\overline{u'v'}$	Reynolds shear stress $[m^2/s^2]$
y^+	Dimensionless streamwise velocity
U_0	Jet exit velocity [m/s]
U_c	Phase speed [m/s]
U_f	Free stream velocity [m/s]
U_b	Bulk velocity [m/s]
U_e	Boundary layer edge velocity [m/s]
U_m	Jet centre velocity [m/s]

U_{rms}	Root mean square magnitude of velocity fluctuations [m/s]
U_τ	Wall friction velocity [m/s]
V	Normal-to-wall velocity [m/s]
v'	Fluctuations of the normal-to-wall velocity [m/s]
W	Cavity span [m]
x	Streamwise coordinate [m]
y	Transverse coordinate [m]
y^+	Dimensionless normal-to-wall distance
z	Spanwise coordinate [m]

Greek Symbols

α	Phase lag factor between the vortex-edge interaction and generation of the upstream feedback disturbances [rad]
δ	Boundary layer thickness based on $U = 0.99U_f$ [m]
δ^*	Displacement thickness of the boundary layer [m]
δ_ω	Vorticity thickness [m]
δ_{ref}	The reference boundary layer thickness [m]
δ_ω	Vorticity thickness [m]
ΔV	The maximum particle slip velocity
κ	Ratio of the average convective speed of vortices to the free stream velocity
τ	Integral timescale [s]
μ	Dynamic viscosity [Kg/m.s]
ϕ	Phase difference between two signals [rad]
$\rho(\tau)$	Auto-correlation coefficient

σ_{est}	Relative uncertainty
σ_u	Standard deviation of velocity fluctuations [m/s]
τ	The time step or time difference [s]
τ_w	Wall shear stress $[N/m^2]$
θ	Momentum thickness of the boundary layer [m]
θ_0	Momentum thickness of the upstream boundary layer [m/s]
ϕ_{sep}	Separation angle of a wall jet at a cylindrical surface [degree]
υ	Kinematic viscosity $[m^2/s]$
ε	Relative uncertainty

Subscripts

g	The moving fluid
∞	Jet boundary
p	Seeding particles
rms	Root mean square of a variable

Superscripts

$'$	Fluctuating quantity
α	The time instance realised in the experiment
$< m >$	Time-averaged vector/scalar of quantity m
$\overline{m}$	Time-averaged vector/scalar of quantity m
$\tilde{m}$	Instantaneous vector/scalar of quantity m

List of Tables

3.1 The test cases. LE denotes cavity leading edge, while TE denotes cavity trailing edge. The subscripts SE and C denote sharp edge and coanda cases, respectively. 56
3.2 The calculated Reynolds numbers for the test cases. 56
3.3 The calculated momentum coefficients for test cases. 57
3.4 The acquisition time per each spatial point and the traverse step size for the hot-wire measurements. 63
3.5 The criteria for the filters and the post-processing tools used for PIV. 70

4.1 Time-averaged free stream velocities for empty and occupied wind tunnel. U_e: free stream velocity for the empty tunnel, U_f: free stream velocity for the tunnel with the experimental model. . . . 76
4.2 Boundary layer parameters at $x/D = -0.33$ for each free stream condition. 80

6.1 Growth rate of the cavity separated shear layer for $Re_\theta = 1.28 \times 10^3$, sharp edge at LE, different J. 125

7.1 Growth rate of the cavity separated shear layer for $Re_\theta = 1.28 \times 10^3$, sharp edge at TE, different J. 145

List of Figures

1.1 Some low speeds applications of cavity flow. 2

2.1 Formation of a mixing layer Schobeiri (2010). 8

2.2 Tne process of vortex pairing at moderate Reynolds numbers (Re_θ = 8 to 150) (Winant and Browand, 1974). 9

2.3 Sketches for: a) open cavity flow, b) transitional cavity flow, and c) close cavity flow (reproduced from Tracy et al. (1993)). 11

2.4 Typical flow topology in a shallow, open cavity. 12

2.5 Typical development of the time-averaged streamwise velocity profile in a shallow, open cavity. $L/D = 3$, $M \approx 0.1$ (Ashcroft and Zhang, 2005). 13

2.6 The dimensionless integral length scale along the cavity separated shear layer at $M \approx 0.1$ ($\bigcirc$: $L/D = 4$, $\triangleleft$: $L/D = 3$, $\diamond$: $L/D = 2$) (Ashcroft and Zhang, 2005). 15

2.7 Mean velocity streamlines showing the main recirculation vortex at M between 0.022 and 0.044 and L/D ratio of 4 (Grace et al., 2004). 16

2.8 Schematic drawing of the traverse instability wave of the main recirculation vortex (primary vortex) Neary and Stephanoff (1987). 17

2.9 Snapshots of the instantaneous velocity streamlines of a wake and self-oscillation modes. Flow was computationally simulated at Re_d= 5000 and $L/D = 4$ (Suponitsky et al., 2005). 19

2.10 Number of vortical structures spanning the cavity length at $Re_D \sim 10^5$ (Little et al., 2007). Arrows indicate large vortical structures. 19

2.11 The formation process of a vortical structure (Knisely and Rockwell, 1982). 20

2.12 Hydrogen bubble visualisation for the scenarios of the the large vortical trajectories near the cavity trailing edge. The visualisation was performed at Re_{θ_0} of 106 and L/θ_0 of 142 (Rockwell and Naudascher, 1979). 21
2.13 Dimensionless oscillation frequency as a function of the dimensionless cavity length L/δ_0. The dashed line indicates the modal jump. Data was obtained at Re_{δ_0} of $0.92 \times 10_3$ and D/θ_0 of 12.95 (Virendra Sarohia, 1975). 23
2.14 Snapshot of the instantaneous velocity field showing a sudden surge of the reverse flow. The figure was obtained at Re_{θ_0} of $1.37 \times 10_3$ and $L/D = 4$. The arrows indicate the reverse flow (Lin and Rockwell, 2001). 24
2.15 Spectral characteristics of single and double modes. The modes are indicated by arrows. The data were obtained at M between 0.3 and 0.32, and $L/D = 4$ (Yan et al., 2006). SPL: denotes sound pressure level. 25
2.16 The feedback cycle in open cavity flow. 27
2.17 Growth rates of the fundamental and the sub-harmonic frequencies with increasing downstream distance. The squares indicate the fundamental frequency, while the triangles indicate the subharmonic. The linear spatial stability theory is represented by solid and dashed lines. Data was obtained at Re_{θ_0}= 190 and L/θ_0 of 80 (Knisely and Rockwell, 1982). 28
2.18 Comparison of streamwise evolution of velocity spectra without (a) and with (b) the cavity impingement edge at corresponding locations in the cavity shear layer ($U/U_f = 0.95$) (Rockwell and Knisely, 1979). 30
2.19 The acoustic feedback mechanism hypothesised by Rossiter (1964). The sketch shows two time frames separated by a time delay Δt (reproduced from Patricia et al. (1975)). 31
2.20 Standing wave mechanism within a cavity (Patricia et al., 1975). . 33
2.21 Classification of the active devices (Cattafesta and Sheplak, 2011). 35
2.22 Types of active control systems: a) open-loop control system, b) feed-forward control system, and c) feedback control system (Gad-el Hak et al., 1998). 36

2.23 Sketch of different geometry modification approaches: (E) trailing edge offset, (F) trailing edge gradual ramp, (G) spoiler at the leading edge, (H) leading edge deflector, (J) leading edge spoiler and trailing edge ramp (Rockwell and Naudascher, 1978). 37
2.24 The experimental study of Chan et al. (2007) at $M = 0.03$ and $L/D = 1$. The black regions in subfigure (b) represent the cavity leading and trailing edges, while the light-grey strips represent the location of the plasma actuators. 38
2.25 The working principles of the sloped floor and vertical fence (Kuo and Huang, 2001). 40
2.26 Instantaneous streamlines (solid lines) and grayscale contour plots of vorticity for Yoshida et al. (2006) simulation. The simulation was carried out at Re_D of 6000 and $L/D = 2$ (Yoshida et al., 2006). 41
2.27 Simultaneous steady injection and suction. Data was simulated at Re_D of 5000 , $L/D = 4$ and C_μ of 0.8 (Suponitsky et al., 2005). . 42
2.28 Influence of increasing forcing power P_f on the velocity spectra of the cavity separated shear layer. Data was obtained at Reynolds number based on the cavity model of 24×10^3 (Gharib, 1987). . . 43
2.29 Zero-net mass, unsteady synthetic jet was used in the experimental work of Debiasi and Samimy (2004) and Little et al. (2007). . . . 44
2.30 Contours of phase-averaged normal-to-wall velocity fluctuations at $M = 0.3$ and $L/D = 4$ (Little et al., 2007). 45
2.31 Phase cancellation control loop with a vibrating surface at the cavity trailing edge (Micheau et al., 2004). 46

3.1 Sketch of De Havilland closed-return wind tunnel (top view) (Giuni, 2013). 49
3.2 Drawings and installations of the experimental model. 51
3.3 Drawings and installation of the actuator. 53
3.4 Air supply system to the actuator. Dashed lines represent flexible tubing, while solid lines represent solid piping. 55
3.5 The working principles of the CTA (Jørgensen, 2002). 58
3.6 Layout of the CTA system (Dantec Dynamics, 2013). 59
3.7 Experimental set-up of the CTA. 60
3.8 Working principles of LDA (reproduced from (Dantec Dynamics, 2016)). 64

3.9 Set-up of the LDA system. 65
3.10 The working principles of the two-dimensional PIV (Lavision, 2017a). 67
3.11 The experimental set-up for the two-dimensional PIV. 68
3.12 Convergence study at different locations in the cavity for baseline case (no-jet) at U_f of 43.7 m/s. 69
3.13 Experimental set-up for the unsteady wall pressure measurements. 72
3.14 Calibration set-up for the pressure transducers. 73

4.1 Streamwise velocity profiles at different streamwise locations. The position $y/D = 0$ denotes the model surface. 76
4.2 Formation of a separation bubble downstream of the semicircular leading edge ($Re_t \approx 190 \times 10^3$). 78
4.3 Patterns of the surface oil flow visualisations at the elliptical leading edge for different Reynolds numbers. 78
4.4 Dimensionless boundary layer velocity profiles at x/D = -0.33 for different Reynolds numbers. [circle: experimental data, solid line: $u^+ = 5.6\ log(y^+) + 4.9$]. 79
4.5 Dimensionless boundary layer velocity profiles at different streamwise stations. 81
4.6 Boundary layer velocity profiles for different spanwise stations (x/D = -0.33). 81
4.7 Cases a, b, and c: distribution of the jet time-averaged streamwise velocity along z-axis at ($x/h = 10$, $y/h = 0$). Case d: jet profiles of the time-averaged streamwise velocity at $x/h = 10$ for different locations along the z-axis. Data is acquired for actuator outside the cavity model, Coanda slot, $J = 0.96\ kg/m.s^2$. 83
4.8 Time-averaged PIV raw images for actuator outside the cavity model, different slot configurations, different J. 84
4.9 Shift of the jet centre along the x-axis for actuator outside the cavity model, different slot configurations, different J. 85
4.10 The time-averaged U and V velocity profiles at $x/h = 2.5$ for actuator outside the cavity model, different slot configurations, different J. 86
4.11 Comparison of the velocity decay $(U_0/U_m)^2$ and the dimensionless jet half width b/h for actuator outside the cavity model, different slot configurations, different J. SE: sharp edge slot, C: coanda slot. 87

4.12 The streamwise development of the U_{rms}/U_m and the dimensionless dominant frequency at $y/h = 0$ for actuator outside the cavity model, different slot configurations, different J. SE: sharp edge slot, C: coanda slot. 88
4.13 Time-averaged velocity streamlines and U/U_0 contours for actuator at the cavity model, different slot configurations, different J. 89
4.14 The time-averaged V velocity distribution along $y/D = -0.9$ for actuator at the cavity model, different slot configurations, different J. 90
4.15 Distribution of the time-averaged U/U_0 at $y/D = 0.9$ for actuator at the cavity model, different slot configurations, $J = 0.96\,kg/m.s^2$ SE: sharp edge slot, C: coanda slot. 91
4.16 Snapshot of the instantaneous R/U_0 for actuator at the cavity model, coanda slot, different J. 92
4.17 Snapshots of the instantaneous U/U_0 approximated by the first four POD modes (16.2% of the total energy) for actuator at the cavity model, coanda slot, $J = 0.11\,kg/m.s^2$. 93
4.18 Snapshots of the instantaneous R/U_0 approximated by the first four POD modes (16.7% of the total energy) for actuator at the cavity model, coanda slot, $J = 0.96\,kg/m.s^2$. 93

5.1 Time-averaged velocity fields for $Re_\theta = 1.28 \times 10^3$, different slots at LE, no jet. 98
5.2 Surface oil flow visualisation for $Re_\theta = 1.28 \times 10^3$, sharp edge at LE, no-jet. 99
5.3 Time-averaged U/U_f field and U/U_f profile at $y/D = -0.9$ for $Re_\theta = 1.28 \times 10^3$, sharp edge at LE, no-jet. 100
5.4 Time-averaged V/U_f field and vorticity thickness for $Re_\theta = 1.28 \times 10^3$, sharp edge at LE, no-jet. 100
5.5 Dimensionless Reynolds stress components and z-vorticity for $Re_\theta = 1.28 \times 10^3$, sharp edge at LE, no-jet. 102
5.6 Time-averaged streamlines for: a) current experiment ($Re_d = 49.5 \times 10^3$), and b) Grace et al. (2004) experiment ($Re_d \approx 13 \times 10^3$). . . . 103
5.7 Time-averaged $\overline{u'v'}/U_f^2$ profiles at x/L of 0.19 and 0.94 for the current experiments and Grace et al. (2004) experiments 103

5.8 Temporal evolution of U/U_f at two streamwise stations for $Re_\theta = 1.28 \times 10^3$, sharp edge at LE, no-jet. 104

5.9 Temporal evolution of U/U_f at $y/D = 0$ for $Re_\theta = 1.28 \times 10^3$, sharp edge at LE, no-jet. 105

5.10 Snapshots of the instantaneous U/U_f for $Re_\theta = 1.28 \times 10^3$, sharp edge at LE, no-jet. 105

5.11 Development of the streamwise velocity power spectra along the cavity separated shear layer ($y/D = 0$) for $Re_\theta = 1.28 \times 10^3$, no-jet. 106

5.12 Peak amplitude of the dominant frequency along the cavity separated shear layer ($y/D = 0$) for $Re_\theta = 1.28 \times 10^3$, sharp edge at LE, no-jet. 107

5.13 Development of the velocity power spectra along two flow paths for $Re_\theta = 1.28 \times 10^3$, sharp edge at LE, no-jet. 108

5.14 Energy of the spatial eigenmodes and power spectra of the first four POD temporal coefficients for $Re_\theta = 1.28 \times 10^3$, sharp edge at LE, no-jet. 108

5.15 U/U_f instantaneous fields approximated by the first POD mode for $Re_\theta = 1.28 \times 10^3$, sharp edge at LE, no-jet. 109

5.16 Snapshot of the instantiation vorticity and the fluctuating velocity streamlines with different filter sizes. The dashed arrow indicates the free stream direction. $Re_\theta = 1.28 \times 10^3$, sharp edge at LE, no-jet 110

5.17 Vortex count of the coherent vortical structures and streamwise development of the unsteady pressure power spectra and for $Re_\theta = 1.28 \times 10^3$, sharp edge at LE, no-jet. 111

5.18 Temporal evolution of U/U_f at two streamwise stations for different Re_θ, sharp edge at LE, no-jet. 113

5.19 Power spectra of the streamwise velocity at ($x/L = 0.5$,$y/D = 0$) and the unsteady pressure for different Re_θ, sharp edge at LE, no-jet. 114

5.20 Vortex count of the coherent vortical structures for different Re_θ, sharp edge at LE, no jet. 115

6.1 Surface oil flow visualisations for $Re_\theta = 1.28 \times 10^3$, sharp edge at LE, different J: a) no jet, b) $J = 0.11\ kg/m.s^2$, c) $J = 0.44\ kg/m.s^2$, and d) $J = 0.96\ kg/m.s^2$. 118

6.2 The instantaneous PIV raw images and the time-averaged V/U_f for $Re_\theta = 1.28 \times 10^3$, sharp edge at LE, different J. 119

6.3 Time-averaged U/U_f profiles at different axial stations for $Re_\theta = 1.28 \times 10^3$, sharp edge at LE, different J. C.S.S.L: denotes the cavity separated shear layer. 121

6.4 Contours of the time-averaged U/U_f for $Re_\theta = 1.28 \times 10^3$, sharp edge at LE, different J. 122

6.5 Distribution of U/U_f along the cavity floor ($y/D = -0.9$) for $Re_\theta = 1.28 \times 10^3$, sharp edge at LE, different J. 123

6.6 Contours of the time-averaged U/U_f at B_c=1% for: a) current experiments, and b) Suponitsky et al. (2005) 124

6.7 Contours of the time-averaged Reynolds shear stress for $Re_\theta = 1.28 \times 10^3$, sharp edge at LE, different J. 125

6.8 Contours of the time-averaged $\omega_z L/U_f$ at the cavity leading edge region for $Re_\theta = 1.28 \times 10^3$, sharp edge at LE, different J. 126

6.9 The time-averaged boundaries and vorticity thickness of the cavity separated shear layer along x-axis for $Re_\theta = 1.28 \times 10^3$, sharp edge at LE, different J. 126

6.10 Temporal evolution of U/U_f at x/L=0.2 and 0.8 for $Re_\theta = 1.28 \times 10^3$, sharp edge at LE, different J. 128

6.11 U Velocity spectra at $x/L = 0.9$, $y/D = 0$ and profiles of the time-averaged V/U_f along the centre of the main recirculation vortex for $Re_\theta = 1.28 \times 10^3$, sharp edge at LE, different J. 129

6.12 Snapshots of the instantaneous dimensionless z-vorticity for $Re_\theta = 1.28 \times 10^3$, sharp edge at LE, different J. 130

6.13 The unsteady wall pressure power spectra at $x/L = 0.5$ for $Re_\theta = 1.28 \times 10^3$, sharp edge at LE, different J. 131

6.14 Instantaneous raw images and contours of the time-averaged V/U_f field for $Re_\theta = 1.28 \times 10^3$, different slots at LE, $J = 0.96\ kg/m.s^2$. C: Sharp edge slot, C: coanda slot. 132

6.15 Time-averaged U/U_f profiles at different axial stations for $Re_\theta = 1.28 \times 10^3$, different slots at LE, $J = 0.96\ kg/m.s^2$. Solid line: no-jet, dotted line: blowing from the sharp edge slot, dashed line: blowing from the coanda slot. 133

6.16 Contours of the time-averaged U/U_f for $Re_\theta = 1.28\times10^3$, different slots at LE, $J = 0.96\ kg/m.s^2$. 133
6.17 Contours of the time-averaged dimensionless Reynolds shear stress for $Re_\theta = 1.28 \times 10^3$, different slots at LE, $J = 0.96\ kg/m.s^2$. . . . 134
6.18 The time-averaged boundaries of the cavity separated shear layer for $Re_\theta = 1.28 \times 10^3$, different slots at LE, $J = 0.96\ kg/m.s^2$. . . . 134
6.19 Spectra of the streamwise velocity at ($x/L = 0.9$, $y/D = 0$) for $Re_\theta = 1.28 \times 10^3$, different slots at LE, $J = 0.96\ kg/m.s^2$. SE: sharp edge slot, C: coanda slot. 135
6.20 Spectra of the unsteady wall pressure at $x/L = 0.5$ for $Re_\theta = 1.28 \times 10^3$, different slots at LE, $J = 0.96\ kg/m.s^2$. 135

7.1 Surface oil flow visualisations for $Re_\theta = 1.28 \times 10^3$, sharp edge at TE, different J: a) no-jet, b) $J = 0.11\ kg/m.s^2$, c) $J = 0.44\ kg/m.s^2$, and d) $J = 0.96\ kg/m.s^2$. 140
7.2 The time-averaged $\omega_z L/U_f$ and the instantaneous raw images for $Re_\theta = 1.28 \times 10^3$, sharp edge at TE, different J. 141
7.3 Snapshots of the instantaneous R/U_f for $Re_\theta = 1.28 \times 10^3$, sharp edge at TE, $J = 0.96\ kg/m.s^2$. 142
7.4 Contours of the time-averaged U/U_f for $Re_\theta = 1.28 \times 10^3$, sharp edge at TE, different J. C.S.S.L: denotes the cavity separated shear layer. 143
7.5 Distribution of the time-averaged U/U_f along $y/D = -0.9$ for $Re_\theta = 1.28 \times 10^3$, sharp edge at TE, different J. 144
7.6 Contours of the dimensionless Reynolds shear stress for $Re_\theta = 1.28 \times 10^3$, sharp edge at TE, different J. 144
7.7 The time-averaged boundaries and vorticity thickness of the cavity separated shear layer along the x-axis for $Re_\theta = 1.28 \times 10^3$, sharp edge at TE, different J. 145
7.8 Temporal evolution of U/U_f at $x/L = 0.2$ and 0.8 for $Re_\theta = 1.28 \times 10^3$, sharp edge at TE, different J. 147
7.9 Streamwise velocity power spectra at $y/D = 0$ for $Re_\theta = 1.28 \times 10^3$, sharp edge at TE, different J. 148
7.10 The unsteady wall pressure power spectra at $x/L = 0.5$ for $Re_\theta = 1.28 \times 10^3$, sharp edge at TE, different J. 148

7.11 Contours of the time-averaged U/U_f and profiles of the time-averaged V/U_f along the centre of the main recirculation vortex for $Re_\theta = 1.28 \times 10^3$, sharp edge at LE or TE, $J = 0.96\ kg/m.s^2$. 149
7.12 Cavity flow behaviour for leading and trailing edges blowing for $Re_\theta = 1.28 \times 10^3$, sharp edge at LE or TE, $J = 0.96\ kg/m.s^2$. . . 150
7.13 Contours of the time-averaged dimensionless Reynolds shear stress for $Re_\theta = 1.28 \times 10^3$, sharp edge at LE or TE, $J = 0.96\ kg/m.s^2$. 150
7.14 Streamwise velocity power spectra at ($x/L = 0.9$, $y/D = 0$) for $Re_\theta = 1.28 \times 10^3$, sharp edge at LE or TE, $J = 0.96\ kg/m.s^2$. . . 151
7.15 Temporal evolution of U/U_f at $x/L = 0.2$ and 0.8 for $Re_\theta = 1.28 \times 10^3$, sharp edge at LE or TE, $J = 0.96\ kg/m.s^2$. 152
7.16 Spectra of the unsteady wall pressure at $x/L = 0.5$ for $Re_\theta = 1.28 \times 10^3$, sharp edge at LE or TE, $J = 0.96\ kg/m.s^2$. 153

A.1 Boundary layer development along a flat plate (Fox, 1977). 176
A.2 Boundary layer transition process: instability amplification regime (White, 1991). 177
A.3 The dimensionless profile and the sublayers of the turbulent boundary layer (Schobeiri, 2012). 178

B.1 Definition sketch for turbulent planar jet: a) jet development regions, b) potential core, and c) jet velocity profile (Rajaratnam, 1976). 182
B.2 Shedding of counter-rotating vortices pairs in a planar jet (Browne et al., 1984). 183
B.3 Instantaneous time frames of the streamlines for deflecting oscillation regime of two opposing planar jets obtained by large eddy simulation at $Re_h = 250$ and $L/h = 10$ (Tu et al., 2014). 185
B.4 Sketches for coanda effect (D. J. Tritton, 1977) and streamwise velocity profile of a wall jet (Zhou et al., 1996). 186
B.5 Coanda effect over a convex surface (Wille and Fernholz, 1965). . 187
B.6 Main features of BFS flow (Driver et al., 1987). 188

C.1 Definition sketch for the instantaneous velocity, the averaged velocity, and the fluctuating velocity (Fredsøe, 1990). 192
C.2 Definition sketch for time and ensemble averaging of a quantity x (Yamamoto, 2004). 192

C.3 The variation of the auto-correlation coefficient with time difference (Nieuwstadt et al., 2016). 194
C.4 The orientation of the velocity fluctuations vectors (bold arrows) in spatial correlation with respect to the separation vector (Nieuwstadt et al., 2016). 194

E.1 Convergence study at different locations in the cavity for baseline case (no-jet) at U_f of 11.1 m/s. 199
E.2 Convergence study at different locations in the cavity for blowing from the cavity leading edge (wind tunnel off). The jet case is coanda ($J = 0.96\ kg/m.s^2$). 200

Chapter 1

Introduction

Flow over cavities induces strong flow oscillations, which substantially increase noise, drag, vibration, and structural fatigue. This phenomenon impacts a wide range of low speeds applications ($M \leq 0.3$), such as aircraft wheel wells, ground transportations, and pipelines, as shown in Figure 1.1. Aircraft wheel wells are a significant source of aerodynamic noise in airplanes during landing and take-off. This issue has gained more research interests since 1970's, due to the implementation of strict noise regulations of the aviation industry (Bliss and Hayden, 1976). The future noise regulations will be even more strict. A new vision (Flightpath 2050), that was released by the Advisory Council for Aeronautics Research in Europe (ACARE), aims to reduce noise emissions from aircrafts by 65% (European Union, 2011). Cavities are also widely encountered in ground transportations: gaps between coaches in high-speed trains, door gaps, and windows in cars. The noise generated from these cavities impact the comfort of the passengers. He et al. (2014) found that the cavity-like gaps between the train coaches is an important source of noise in high-speed trains. In the context of pipelines, cavities are still omnipresent: flow control devices and closed-side branches. The presence of cavities in pipelines can cause severe noise and vibration problems, which lead to the wear and failure of the fluid-handling devices (Ziada and Lafon, 2014).

Cavity flows have been investigated extensively during the past sixty years. The vast majority of these studies have focused on two aspects: investigating the cavity flow oscillations and formulating mathematical models for them, and suppressing the cavity flow oscillations by active and passive flow control methods. Between the 1960s and 1980s, the most famous theories for cavity flow oscillations were proposed. In 1964 Rossiter (1964) hypothesised that the cavity flow

(a) Wheel wells in aircraft (Parkhi, 2009)

(b) Door gaps and sunroofs in vehicles (Parkhi, 2009)

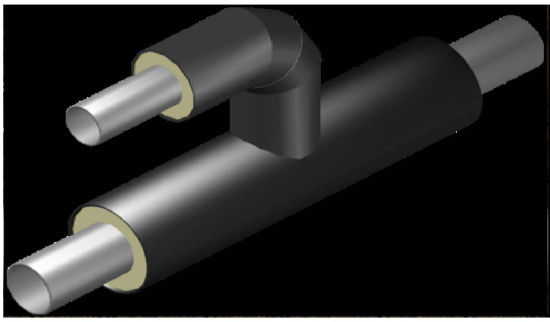

(c) Closed-side branches in pipelines (German-pipe, 2017)

(d) Inter-coach gaps in high speed trains (Skyscrapercity, 2017)

Figure 1.1: Some low speeds applications of cavity flow.

oscillations are excited by the acoustic feedback from the cavity trailing edge. Based on this theory, the author formulated a semi-empirical equation to predict the oscillation frequency at high flow speeds, which is currently referred to as the "Rossiter equation". Due to the limitations of this hypothesis, Heller et al. (1971) and Tam and Block (1978) introduced some modifications to the theory in 1971 and 1978, respectively. Another mechanism was introduced by Patricia et al. (1975) in 1975, which is the standing wave mechanism. This mechanism attributes the oscillations of the cavity flow to the stnading waves. Later, in 1979, Rockwell and Knisely (1979) experimentally proved that the cavity oscillations can be excited by the hydrodynamic feedback from the cavity trailing edge. In 2001, Lin and Rockwell (2001) observed sudden surges of reverse flow moving from the cavity trailing edge towards the cavity leading edge. These sudden surges are, at least, partially responsible for the amplitude and frequency modulations of the cavity oscillations.

During the period between the 1970s and 1990s, various passive and active control devices were implemented to suppress the cavity oscillations, such as double ramps at the cavity leading and trailing edges by Franke and Carr (1975) in 1975, steady injection from the cavity floor by Sarohia and Massier (1976) in 1977, a heating element upstream of the cavity by Gharib (1987) in 1987, a piezoelectric actuator at the cavity leading edge by Cattafesta et al. (1997) in 1997. Most of these devices effectively suppressed the cavity oscillations. To gain wider operational conditions as well as reducing the cost of electrical power consumption, various feedback control systems have been introduced to the cavity flow over the last 20 years. These systems were quite effective, however, due to the inherent limitation of these systems, they are not able to suppress the cavity oscillations completely (Rowley and Williams, 2006).

1 Aims and objectives of the study

The current study examines an open cavity flow with $L/D = 4$ at Re_θ between 1.28×10^3 and 4.37×10^3. The main objectives of this study are:

- Investigating the development and the impact of the reverse flow interaction phenomenon on the cavity flow oscillations. This investigation is motivated by the lack of information about this phenomenon in the literature.
- Quantifying the frequency of the reverse flow interaction phenomenon, and examining the Reynolds number dependency of this phenomenon, which have not been examined before in the literature.
- Investigating the impact of the leading and trailing edges blowing on the time-averaged flow field and the cavity flow oscillations. Jet blowing from cavity trailing edge is a novel cavity flow control technique, that has not been applied before for cavity flows. The purpose of the steady jets is suppressing the oscillations of the cavity separated shear layer. Steady jets will be applied in the cavity flow at $Re_\theta = 1.28 \times 10^3$ with different: momentum fluxes ($J = 0.11\ kg/m.s^2, 0.44\ kg/m.s^2$ and $0.96\ kg/m.s^2$), slot configurations (sharp edge and coanda), and blowing locations (blowing from the cavity leading and trailing edges).

Qualitative (surface oil flow visualisation) and quantitative (hot wire anemometry, laser Doppler anemometry, particle image velocimetry and pressure measurements) techniques have been utilised to reach the above objectives.

2 Thesis structure

Following this introduction the thesis is divided into the following sections:

Chapter 2 presents the state of the art research carried out on open cavity flow and cavity flow control at low speeds. This chapter also provides a background about shear flows.

Chapter 3 describes the experimental techniques and apparatus used in the current investigation.

Chapter 4 provides the main characteristics of free stream flow, upstream boundary layer and blowing jets at different Reynolds numbers.

Chapter 5 studies the time-averaged cavity flow field and the oscillations of the cavity separated shear layer for the no-jet case at $Re_\theta = 1.28 \times 10^3$. The chapter also examines the influence of increasing the Reynolds number to $Re_\theta = 4.37 \times 10^3$ on the oscillations of the cavity separated shear layer.

Chapter 6 investigates the impact of blowing from the cavity leading edge on the time-averaged cavity flow field and the oscillations of the cavity separated shear layer at $Re_\theta = 1.28 \times 10^3$. Two blowing jet cases will be examined: jets from the sharp edge slot and jets from the coanda slot.

Chapter 7 examines the impact of blowing from the cavity trailing edge on the time-averaged cavity flow field and the oscillations of the cavity separated shear layer at $Re_\theta = 1.28 \times 10^3$. This chapter also compares these results with the results of blowing from the cavity leading edge presented in Chapter 6.

Chapter 8 presents general conclusions of the current study along with recommendations for future work to be carried out.

Appendix A gives a basic description of the development of the turbulent boundary layer along with the main characterising equations for the turbulent boundary layer.

Appendix B provides the basics of shear flows which are related to the current study, such as planar jets, opposing planar jets, the conada effect, and flow over backward facing steps.

Appendix C provides information about the statical quantities used to study turbulence, for example, spatial and temporal correlations, and Reynolds shear stresses.

Appendix D presents the calculations of the Stokes number for the seeding particles used in the particle image velocimetry.

Appendix E shows additional figures for the convergence study of the particle image velocimetry measurements.

Appendix F presents the uncertainty calculations of the particle image velocimetry measurements.

Appendix G provides the calculations of the relative expanded uncertainty for the hot wire anemometry (HWA).

Chapter 2

Literature Survey

This chapter reviews and discusses the experimental and computational studies performed on rectangular, shallow open cavities at low-subsonic speeds ($M < 0.3$). It provides a review of the flow control methods applied to open cavity flows.

1 The basics of the shear flows

Before examining the cavity flow, the basics of shear flows will be summarised in this section. Shear flows possess velocity gradients across them due to the shear force between their layers. There are two types of shear flows: bounded shear flows such as boundary layers, and unbounded or free shear flows such as planar jets. This section will focus on the most basic shear flow, which is the mixing layer. Other forms of shear flows, that are relevant to the current study such as turbulent boundary layer and planar jet, are examined in the Appendices A and B.

1.1 Mixing layers

Mixing layer, as illustrated in Figure 2.1, is formed between two parallel streams moving at different velocities (U_1 and U_2) or between moving stream and stationary fluid. As soon as the two streams meet at the end of a partition (such as a splitter plate), a region of velocity discontinuity is formed between the two streams. Further downstream, the velocity changes smoothly between the two streams, due to the turbulent mixing (Dewan, 2011). According to D'Ovidio

(1998), mixing layer can be used to approximate the initial region of a jet, the near wake of a bluff body, the flow behind a backward facing step (BFS).

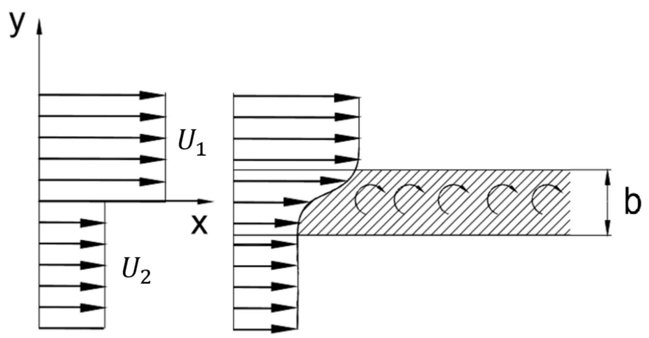

Figure 2.1: Formation of a mixing layer Schobeiri (2010).

Coherent structures in mixing layers

Generally, turbulence in mixing layers are driven by quasi-two-dimensional large eddies called "coherent structures". Fiedler (1987), defines coherent structures as "*spontaneously formed, non-stationary motional systems of correlated vorticity*". According to the author, the main characteristics of coherent structures are:

- "*Coherent structures in most cases are large scale, comparable to the lateral flow dimension, and flow specific in shape and composition*",
- "*Coherent structures are recurrent, having a characteristic life-span, typically of the average passage time of a structure*",
- "*Coherent structures exhibit a high measure of organization in structure as well as in dynamics although their appearance is at best quasi-periodic*",
- "*Coherent structures similar to the corresponding structures in the laminar-turbulent transition.*"

The formation and development of coherent structures in mixing layers

The coherent structures are formed due to Kelvin-Helmholtz instability (K-H), which occurs due to an inflection point in the velocity profile (D'Ovidio, 1998). Similar to all flow instabilities, coherent structures undergo two stages of development: (i) the stage of linear instability, and (ii) the stage of nonlinear interaction. In the former stage, the flow is subjected to a spectrum of small disturbances, and only one particular instability is amplified more than the others until it dominates the flow. When the dominant instability (the fundemnetal frequency) becomes sufficiently large, it starts to interact with other instabilities (nonlinear interaction) (Kundu and Cohen, 2010). Winant and Browand (1974) examined the linear and nonlinear interaction of the coherent structures in a turbulent mixing layer at moderate Reynolds numbers ($Re_\theta = 8$ to 150). In the linear instability region, the authors observed the generation of small waves which eventually roll into a periodic train of two-dimensional vortex structures. In the nonlinear interaction region, the vortical structures interact with each other, due to the growth of the sub-harmonic of the fundamental frequency. One example of this interaction is "vortex pairing", whereby two vortices roll around each other and eventually amalgamate into a single, larger vortex, as shown in Figure 2.2. Another example for vortex interaction is "vortex tearing", whereby the coherent structure disintegrates as it moves to the vicinity of another coherent structure or between two structures (Dimotakis and Brown, 1976).

The growth of mixing layers

As the two streams mix downstream, it entrains more fluid from the surrounding and hence the width of the mixing increases. The width of the mixing layer can be calculated using the vorticity thickness $d\delta_\omega/dx$, where the vorticity thickness is defined as

$$\delta_\omega = \frac{U_2 - U_1}{\{\frac{\partial U}{\partial y}\}_{max}} \tag{2.1}$$

where $\{\frac{\partial U}{\partial y}\}_{max}$ is the local maximum velocity gradient across the mixing layer, while U_2 and U_1 are the velocity of the two streams (D'Ovidio, 1998).

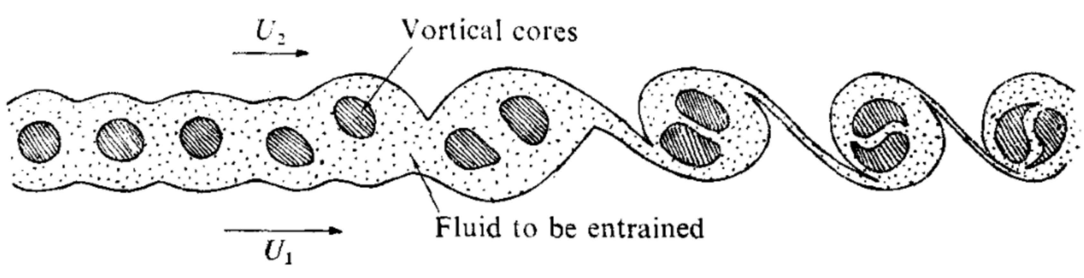

Figure 2.2: Tne process of vortex pairing at moderate Reynolds numbers ($Re_\theta = 8$ to 150) (Winant and Browand, 1974).

The growth rate or the entrainment of the mixing layer is greatly affected by the "mixing transition" of the coherent vortical structures. The mixing transition, which takes place beyond a critical Reynolds number ($Re_c \approx 2 \times 10^4$), is associated with a noticeable increase in the growth rate of the mixing layer due to the formation of three-dimensional, small-scale structures superimposed on the large coherent structures (Konrad, 1977). D'Ovidio and Coats (2013) performed an experimental investigation on pre- and post-mixing transition at Reynolds number in the order of magnitude of 10^4. According to the study, in the stage of pre-mixing transition, the mixing layer grows by vortex pairing, while the growth in the post-mixing stage is driven by the constant growth rate of the coherent vortical structures.

The growth rate of the mixing layer is also affected by the intermittency of the coherent vortical structures. At Reynolds number in the order of magnitude of 10^4, D'Ovidio and Coats (2013) discoverd that there are periods of no coherent structures within the mixing layer (unstructured mixing layer). During these periods, entrainment and steady growth of the mixing layer significantly reduced. The same behavior was observed by D'Ovidio (1998) at a Reynolds number in the order of magnitude of 10^4 to 10^5. According to the author, the intermittency of the coherent structures is a possible cause for the inconsistency in the published data for the mixing layer growth rates.

Section summary

The mixing layer is an example of shear flows. The mixing layer is formed due to the mixing between two parallel streams moving at different velocities. The velocity difference causes Kelvin-Helmholtz instability (K-H), which generates small instability waves which eventually roll into coherent vortical structures. The formed coherent structures interact with each other to form a larger vortex (vortex pairing) or destroy each other (vortex tearing). Due to the mixing between the two streams, the thickness of the mixing layer increases. The growth rate of the mixing layer is greatly affected by the mixing transition and the intermittency of the coherent vortical structures.

2 Time-Averaged Open Cavity Flow

Flow over cavities is more complicated than mixing layers, as it involves flow reattachment at the cavity trailing edge. Depending on the reattachment location, cavities are categorised into three types: (i) open cavity, (ii) transitional cavity, and (iii) closed cavity, as illustrated in Figure 2.3. The cavity is called "open" when the cavity separated shear layer completely bridges the cavity and reattaches downstream of the cavity trailing edge. The open cavity is further classified into deep cavity $L/D < 1$, and shallow cavity $L/D > 1$, where L and D are the cavity length and depth, respectively. As the ratio of cavity length to depth ratio L/D increases, the cavity flow gradually moves to the "transitional cavity" flow regime. In this regime, the cavity separated shear layer reattaches between the cavity floor and the cavity trailing edge. When the L/D is large enough, the cavity becomes "closed". In a closed cavity, the separated shear layer reattaches on the cavity floor and separates again upstream of the cavity trailing edge due to the adverse pressure.

To determine the L/D ratios for the three regimes, Ng (2012) performed an experimental study at at $M \approx 0.03$. The cavity was found: (i) open at $L/D < 6.5$, (ii) transitional at $6.5 < L/D < 15$, and (iii) closed at $L/D > 15$.

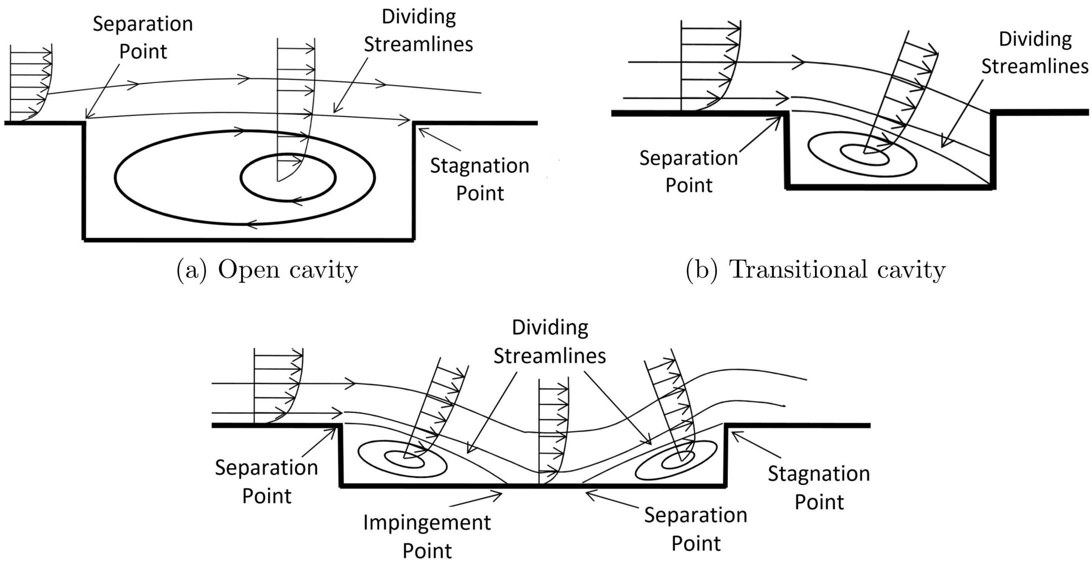

(a) Open cavity

(b) Transitional cavity

(c) Close cavity

Figure 2.3: Sketches for: a) open cavity flow, b) transitional cavity flow, and c) close cavity flow (reproduced from Tracy et al. (1993)).

However, according to the author, these ratios may vary with Reynolds number and Mach number. The following sections will only investigate flows over shallow open cavities, as they are relevant to the current study.

2.1 Open cavity flow

A typical flow topology in a shallow open cavity is illustrated in Figure 2.4. Due to momentum transfer, the cavity separated shear layer expands as it develop downstream (Ashcroft and Zhang, 2005). Eventually, it impinges on the cavity trailing edge. As a result, a portion of the separated shear layer flow deflects back towards the cavity leading edge, forming a large recirculation vortex inside the cavity (main recirculation vortex). Driven by the main recirculation vortex, a weaker recirculation vortex (secondary vortex) is usually formed near the cavity leading edge (Ukeiley and Murray, 2005).

Cavity separated shear layer

The flow in the cavity separated shear layer is predominantly streamwise. The streamwise velocity profile of the separated layer undergoes a substantial change at the cavity leading edge region. In this region, the shape of the profile changes from a boundary layer-like profile to a hyperbolic profile (Gharib and Roshko, 1987). As the separated shear layer develops downstream, it expands and the gradient of the velocity profile smears out, as illustrated in Figure 2.5.

The growth rate of the cavity separated shear layer, which is usually calculated using the vorticity thickness or the momentum thickness, is a measure of the fluid entrained by the cavity separated shear layer (Virendra Sarohia, 1975). According

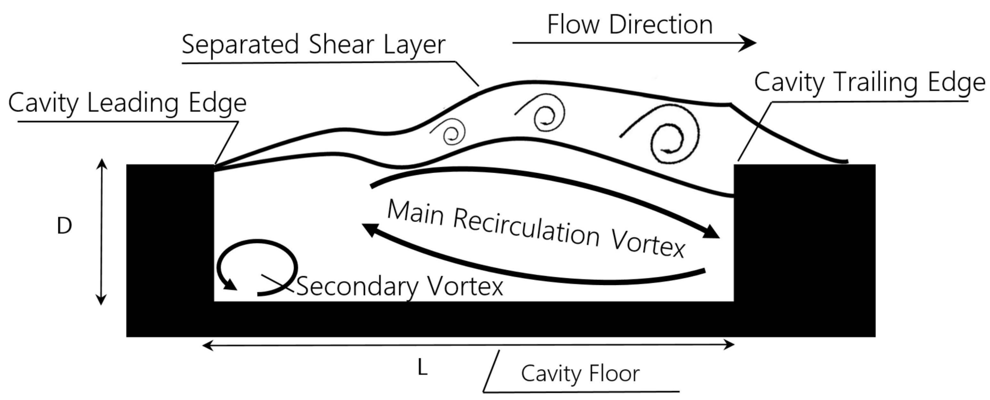

Figure 2.4: Typical flow topology in a shallow, open cavity.

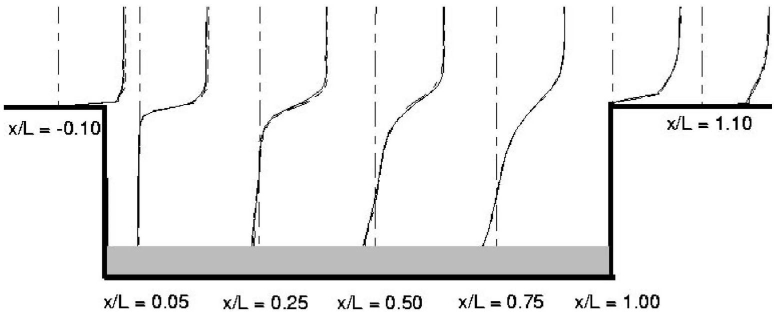

Figure 2.5: Typical development of the time-averaged streamwise velocity profile in a shallow, open cavity. $L/D = 3$, $M \approx 0.1$ (Ashcroft and Zhang, 2005).

to Virendra Sarohia (1975), the entrainment of the cavity separated shear layer is mainly due to the oscillations of this layer, which will be examined later in this chapter. In their computational simulation at $M = 0.25$ and $L/D = 2$, Kourta and Vitale (2008) reported four regions of growth rates along the cavity separated shear layer: (i) the region of exponential growth near the cavity leading edge at $x/L \lessapprox 0.15$, (ii) the region of linear growth at $0.15 \lessapprox x/L \lessapprox 0.5$, (iii) the region of saturated growth at $0.5 \lessapprox x/L \lessapprox 0.95$, and (iv) the region of a sudden growth reduction at $x/L \gtrapprox 0.95$.

The reported growth rate in the linear-growth region varies significantly between studies. Chatellier et al. (2004) reported a vorticity thickness growth rate $d\delta_\omega \setminus dx$ of approximately 0.128 at $M = 0.09$ and $L/D = 1$. At $M \approx 0.1$ and L/D between 2 and 4, Ashcroft and Zhang (2005) reported a vorticity thickness growth rate of approximately 0.143. On the other hand, at $M \approx 0.2$ and $L/D = 5.16$, Ukeiley and Murray (2005) found that the vorticity thickness growth rate is 0.118. The discrepancy between these rates is also reported by Rodi (1975) for a mixing layer. The author attributed this discrepancy to the following possible reasons: (i) the dependency on free stream turbulence, (ii) the dependency on initial conditions, and (iii) the sensitivity to outer flow field.

The turbulence quantities in the cavity separated shear layer have also been examined by different studies. The fundamentals of turbulence quantities, such as velocity fluctuation level, Reynolds stresses, temporal and spatial correlations, are summarised in Appendix C. As the separated shear layer develops in the streamwise direction, the level of velocity fluctuation increases substantially until it reaches the peak value upstream of the cavity trailing edge (Al Haddabi et al., 2016). According to the experimental studies of Al Haddabi et al. (2016) and Ukeiley and Murray (2005), the peak location is close to $x/L = 0.8$. In the proximity of this location, Grace et al. (2004) and Ukeiley and Murray (2005) found the peak of the Reynolds shear stress $\overline{u'v'}$. In the experiment of Ukeiley and Murray (2005) ($M \approx 0.2$ and $L/D = 5.16$), the peak values of the streamwise and normal-to-wall velocity fluctuation levels were 25% and 15% of the free stream velocity, respectively. On the other hand, the Reynolds shear stress was approximately 1.5% of the square of the free stream velocity.

The spatial structures of the cavity separated shear layer turbulences have been examined using two-point spatial correlation R_{ij}. By performing R_{uu}, R_{vv}, and R_{uv} correlations at different locations along the cavity separated shear layer, Ukeiley and Murray (2005) observed an evolution of a spatial scale across the separated layer at $M \approx 0.2$ and $L/D = 5.16$. These evolving spatial scales, according to Ashcroft and Zhang (2005), indicate the size of the coherent vortical structures which are the dominant turbulent structures in the cavity separated shear layer. Consequently, an integral length scale $l_y = \int_0^\infty R_{uu} dy$ was proposed by the authors to examine the growth rate of the coherent vortical structures, as shown in Figure 2.6. The investigation showed that at $M \approx 0.1$ and L/D between 2 and 4, the structures' size increases steadily and rapidly at the central portion of the cavity. However, almost zero-growth rate was observed near the cavity leading and trailing edge regions. The zero-growth rate at the leading edge region was attributed to the insufficient resolution of the measurement technique, while the zero-growth at the cavity trailing edge was linked to the structure-trailing edge impingement that impedes any further growth.

The recirculation vortices

The centre, the size, and the strength of the recirculation vortices strongly depend on the L/D ratio. At $M = 0.2$ Ukeiley and Murray (2005) investigated the recirculation zone for: (i) a shallow cavity with L/D of 5.16 and (ii) a deep cavity with $L/D = 1.49$. The study found that the deep cavity is dominated by a single recirculation vortex centred at the front third of the cavity. The shallow cavity, on the other hand, contains two counter-rotating recirculation vortices: a large, strong vortex centred near the cavity trailing edge (main recirculation vortex) and a smaller, weaker vortex located at the bottom corner of the cavity leading edge (secondary vortex). Ukeiley and Murray (2005) found in their experimental study that the maximum speed of the main recirculation vortex in the deep cavity was 25% of the free stream velocity, while this speed reached 30% of the free stream

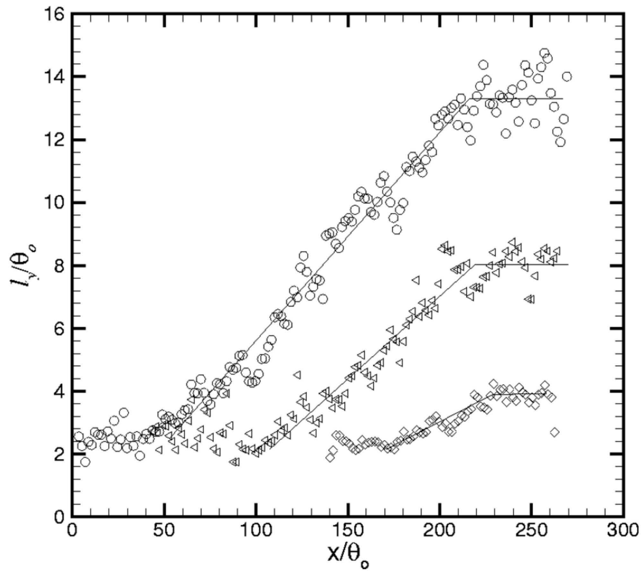

Figure 2.6: The dimensionless integral length scale along the cavity separated shear layer at $M \approx 0.1$ ($\bigcirc$: $L/D = 4$, $\triangleleft$: $L/D = 3$, $\diamond$: $L/D = 2$) (Ashcroft and Zhang, 2005).

velocity in the shallow cavity. The size of the secondary vortex, in contrast, increases with increasing L/D ratio (Ashcroft and Zhang, 2005).

The upstream boundary layer also affects the recirculation vortices. At $M = 0.022$ to 0.044 and L/D ratio of 4, Grace et al. (2004) investigated the recirculation vortices under the following upstream boundary layer conditions: (i) laminar boundary layer, and (ii) turbulent boundary layer. The switching from the laminar to the turbulent condition was made by tripping the upstream boundary layer. The investigation revealed that the main recirculation vortex in the laminar case was concentrated and strong, whilst the main recirculation vortex in the turbulent case was weaker and diffused, as evident from Figure 2.7. The reason behind this, according to the authors, is the higher entrainment rate in the upstream half of the separated shear layer in the turbulent case compared to the laminar case. As a result, the higher entrainment rate forces the main recirculation vortex in the turbulent case to extend towards the cavity leading edge region, leading to a diffused and weaker vortex.

Three-dimensional effect

The three-dimensionality of the cavity flow is caused by: (i) the side wall effect, and (ii) a traverse instability wave. The side wall effect was reported by Neary

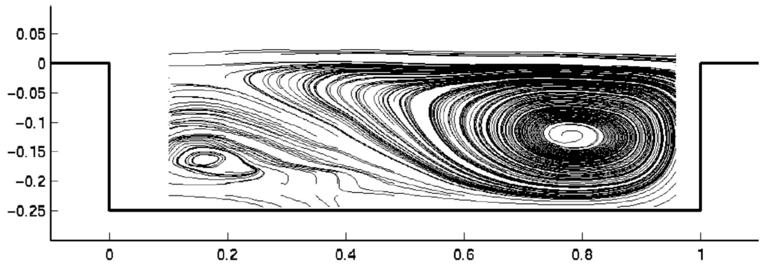

(a) Open cavity flow with laminar upstream boundary layer

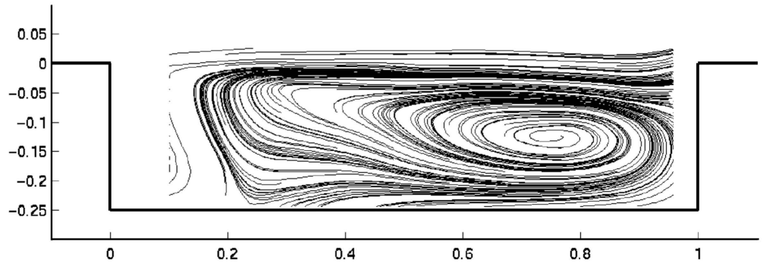

(b) Open cavity flow with turbulent upstream boundary layer

Figure 2.7: Mean velocity streamlines showing the main recirculation vortex at M between 0.022 and 0.044 and L/D ratio of 4 (Grace et al., 2004).

and Stephanoff (1987) at $31900 \leq Re_L \leq 33500$, where Re_L is the Reynolds number based on the distance between the model leading edge and the cavity leading edge. The authors observed a significant spanwise curvature in the core of the vortical structures due to the side wall effect. This curvature, according to the authors, was also observed in cavities with large aspect ratios W/L.

A transverse instability wave, according to Neary and Stephanoff (1987), travels along the cavity span and forces the main recirculation vortex (primary vortex) to compress and expand, as illustrated in Figure 2.8. The transverse instability wave is probably generated due to the interaction between the spanwise and the streamwise vorticity of the cavity separated shear layer (Knisely and Rockwell, 1980). The impact of this instability wave is evident from the wavy pattern (cellular pattern) of the separation line between the main recirculation vortex and the secondary vortex (Neary and Stephanoff, 1987). This cellular pattern was also observed by East (1963) at $M \approx 0.18$.

The spectral signiture of the transverse instability wave was obsrved by Neary and Stephanoff (1987) at $31900 \leq Re_L \leq 33500$, where Re_L is the Reynolds number based on the distance between the model leading edge and the cavity leading edge. The authors found a broad spectral peak due to the amplitude modulation of the wall pressure signal. The Reynolds number-independence of

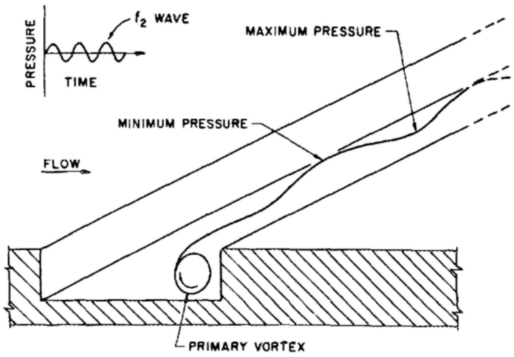

Figure 2.8: Schematic drawing of the traverse instability wave of the main recirculation vortex (primary vortex) Neary and Stephanoff (1987).

this peak, according to the authors, suggests that the peak is not related to the oscillations of the cavity separated shear layer, but to the transverse instability wave.

2.2 Section summary

At the leading edge of the shallow open cavity, the flow separates forming a separated shear layer. As the cavity separated shear layer develops downstream, it expands and grows. The growth rate of the cavity separated shear layer undergoes four sequential stages: exponential, linear, saturated and eventually declined growth. The experimental studies have shown a noticeable discrepancy in the growth rate, which is probably attributed to the variation in the flow conditions.

The reviewed studies have also revealed some information about turbulent characteristics of the cavity separated shear layer. It was found that the velocity fluctuations of the cavity separated shear layer increase in the streamwise direction until it peaks upstream of the cavity trailing edge. Additionally, the two points spatial correlation showed that the turbulence length scale increases steadily along the cavity separated shear layer until it levels out near the cavity trailing edge. Some researchers, such as Ashcroft and Zhang (2005), associated this length scale to the size of the large coherent vortical structures formed within the cavity separated shear layer.

As the cavity separated shear layer impinges on the cavity trailing edge, it deflects back towards the cavity leading edge forming the main recirculation vortex, which derives a smaller recirculation vortex (secondary vortex). The size, the strength, and the centre of these vortices depend on the L/D ratio and the upstream boundary layer condition.

The three-dimensional effect in the cavity flow is attributed to: (i) the side wall effect, and (ii) a transverse instability wave. The side wall effect causes a significant spanwise curvature in the core of the vortical structures. On the other hand, the three-dimensional effect of the transverse wave instability is evident from the cellular pattern of the separation line between the main recirculation vortex and the secondary vortex. According to one research, this instability, which is Reynolds number-independent, modulates the amplitude of the wall pressure signal.

3 Oscillations of the cavity separated shear layer

This section examines the oscillations of the cavity separated shear layer. It focuses on the characteristics of these oscillations and the factors influences them.

There are three modes of oscillations in open cavity flows at low speeds: (i) no-oscillation mode, (ii) the wake mode, and (iii) the self-oscillation mode (Gharib and Roshko, 1987). The no-oscillation mode occurs in cavities with small L/θ_0, where θ_0 is the momentum thickness of the boundary layer upstream of the cavity. In this mode, the separated shear layer smoothly bridges over the cavity with no noticeable oscillations. The wake mode, on the other hand, is associated with temporary reattachment of the separated shear layer on the cavity floor and shedding of very large vortical structures inside the cavity similar to that found behind bluff bodies, as shown in Figure 2.9 (a). This mode is usually found in cavities behind bluff bodies (Gharib and Roshko (1987)) and flows past closed branches of a pipe (Sapienza and Eudossiana, 1995). In the self-oscillations mode, the separated shear layer oscillates vertically in an organised manner (Suponitsky et al., 2005), as shown in Figure 2.9 (b). The following sections will focus on the self-oscillation mode, as it is relevant to the current study.

3.1 Shedding of the large vortical structures

The self-oscillation mode of the cavity separated shear layer is associated with: (i) shedding of large, coherent vortical structures, and (ii) flapping motion of the cavity separated shear layer. The shedding of the large vortical structures is considered by many studies, such as Gharib and Roshko (1987), as the dominant instability in the cavity separated shear layer.

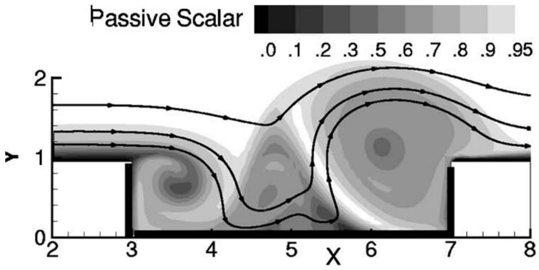

(a) Wake mode

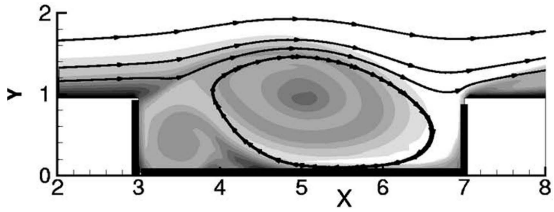

(b) Self oscillations mode

Figure 2.9: Snapshots of the instantaneous velocity streamlines of a wake and self-oscillation modes. Flow was computationally simulated at Re_d= 5000 and L/D = 4 (Suponitsky et al., 2005).

Different approaches have been applied to reveal and identify the coherent vortical structures within the cavity separated shear layer, such as smoke visualisation, vorticity maps, and manipulation of the instantaneous velocity field. Little et al. (2007) successfully visualised the vortical structures using smoke visualisation at $Re_d \sim 10^5$, as shown in Figure 2.10. Lin and Rockwell (2001), on the other hand, used the instantaneous vorticity field to reveal these structure at $Re_d \sim 27 \times 10^3$. The main disadvantage of this method is that the vorticity contours do not distinguish between the shear effect of the separated shear layer and the rotational motion of the vortical structures (Garrido, 2014). A more successful vortex identification approach is probably the manipulation of the instantaneous velocity field. Ashcroft and Zhang (2005) revealed large vortical structures spanning a cavity by manipulating the velocity field using the Galilean decomposition technique at $Re_d \sim 10^5$. This technique works by subtracting the averaged propagation speed of the vortical structures from the instantaneous

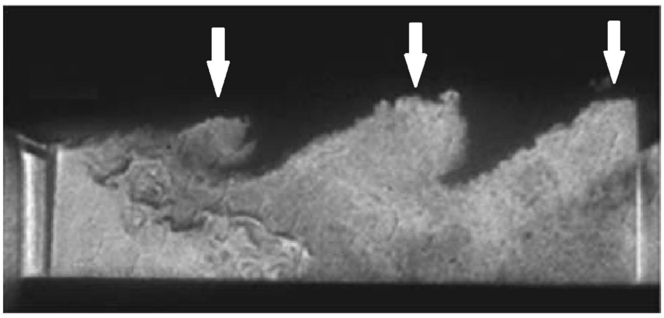

Figure 2.10: Number of vortical structures spanning the cavity length at $Re_D \sim 10^5$ (Little et al., 2007). Arrows indicate large vortical structures.

velocity field.

The formation process of the coherent vortical structures has been investigated by different studies. For an axi-symmetrical cavity at a Reynolds number based on the model diameter between 2×10^4 and 10^5, Virendra Sarohia (1975) reported that the vortical structures are formed due to the interaction between the oscillating separated shear layer and the cavity trailing edge. The flow visualisation images showed that the cavity separated shear layer starts oscillating vertically near the cavity leading edge. As the separated layer approaches the cavity trailing edge, the oscillations increase significantly. Consequently, as the separated shear layer deflects downwards at the trailing edge region, the separated layer rolls into a vortex, which sheds as the separated shear layer deflects upwards.

The formation mechanism of the coherent vortical structures in two-dimensional rectangular cavities is different. The formation mechanism in these cavities is due to the instability of the cavity separated shear layer, as illustrated in Figure 2.11. When the cavity separated shear layer moves over the initially-stagnant cavity flow, the shearing action generates instability waves due to the Kelvin-Helmholtz instability. The instability waves, then, grow along the streamwise direction and eventually roll into discrete vortical structures (Chan et al., 2007). The estimated scale of a typical vortex, according to experimental study of Rockwell and Knisely (1979), is approximately $6\theta_0$, where θ_0 is the momentum thickness of the upstream boundary layer.

As the vortical structures propagate downstream, the size of these structures increases and may interact with each other. At Re_{θ_0} of 1.37×10^3, Lin and

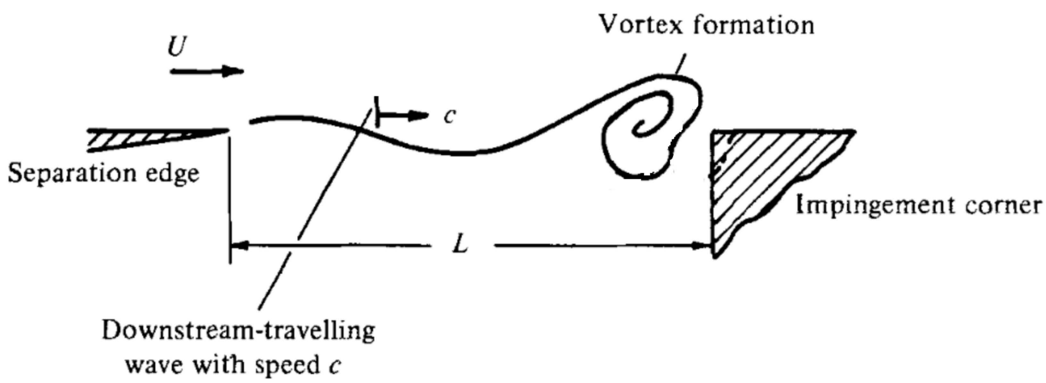

Figure 2.11: The formation process of a vortical structure (Knisely and Rockwell, 1982).

Rockwell (2001) claimed that the small vortical structures merge to form larger vortical structures. However, the authors did not provide any evidence for this interaction. In contrast, no vortex merging was reported by Little et al. (2007) At $Re_D \sim 10^5$. Rockwell and Knisely (1979) and Knisely and Rockwell (1980) also did not observe this interaction within the cavity separated shear layer at Re_{θ_0} between 106 and 324.

The generated vortical structures propagate downstream at a constant speed. This speed can reach more than 50% of the free stream velocity (Rockwell and Knisely, 1979). However, it decreases as it approaches the cavity trailing edge. According to Rockwell and Knisely (1979), the speed reduction starts at a distance of approximately $4\theta_0$ from the cavity trailing edge.

Near the cavity trailing edge, the trajectory of the large vortical structures, according to Rockwell and Naudascher (1979), takes one of three scenarios, as shown in Figure 2.12: (i) complete impingement at the cavity trailing edge, whereby the vortex is swept down into the cavity; (ii) partial impingement, which involves vortex severing; or (iii) complete escape, whereby the vortex is convected above the cavity trailing edge. Knisely and Rockwell (1982) attributed this trajectory variation of the vortical structures to the flapping motion of the cavity separated shear layer.

3.2 Flapping motion of the cavity separated shear layer

The flapping motion is a cyclic vertical displacement of the cavity separated shear layer. This motion tends to modulate the pressure signal at the cavity trailing edge (Knisely and Rockwell, 1982). The lack of quantitative information in the literature about the flapping motion is probably due to the random nature of this

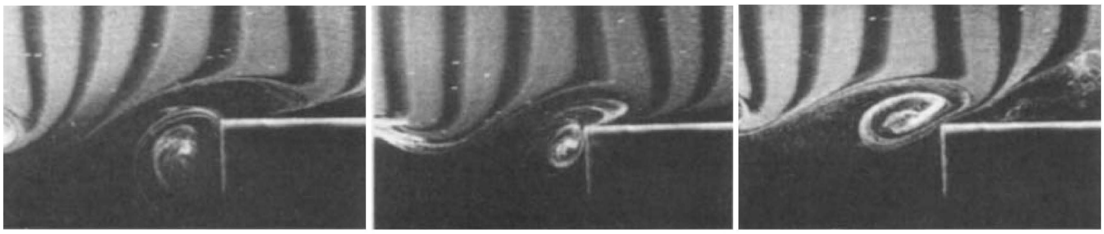

(a) Complete impingement (b) Partial impingement (c) Complete escape

Figure 2.12: Hydrogen bubble visualisation for the scenarios of the the large vortical trajectories near the cavity trailing edge. The visualisation was performed at Re_{θ_0} of 106 and L/θ_0 of 142 (Rockwell and Naudascher, 1979).

motion.

Virendra Sarohia (1975) attributed the flapping motion to the change in the pressure across the cavity separated shear layer. As the cavity separated shear layer deflects upwards, the pressure inside the cavity decreases. Under the influence of the pressure difference, the separated shear layer deflects downwards towards the cavity. As a result, the pressure inside the cavity increases and bushes the separated layer upwards again. Knisely and Rockwell (1982) investigated the flapping motion of the cavity separated shear layer at $Re_{\theta_0} \sim 10^2$ and L/θ_0 between 50 abd 160. The study revealed that the flapping motion travels downstream as a wave with a particular propagation speed. This speed, according to the study, is similar to the propagation speed of the large vortical structures.

3.3 Dimensionless parameters for the cavity separated shear layer oscillations

The main dimensionless parameters for the oscillations of the cavity separated shear layer are: (i) the dimensionless propagation speed U_c/U_f, (ii) the dimensionless oscillation frequency St, and (iii) the oscillation mode m. The dimensionless propagation speed is the ratio between the propagation speed of the oscillation and the free stream velocity. This ratio can reach as high as 0.57 (Rossiter, 1964). The dimensionless oscillation frequency, loosely termed as the dimensionless resonance frequency, non-dimensionalises the oscillation frequency by the free stream velocity and the cavity length $St = fL/U_f$.

The oscillation mode m is the integer number of the large vortical structures spanning the cavity length simultaneously. As the cavity length and/or the free stream velocity increases gradually, the oscillation mode does not change until a certain point is reached, at which the mode "jumps" suddenly from a lower mode to a higher one, as illustrated in Figure 2.13. This jump is associated with a sharp increase in the dimensionless oscillation frequency. As the cavity length and/or the free stream velocity continues to increase, the oscillation continues to jump to higher modes until the oscillations become irregular (Virendra Sarohia, 1975).

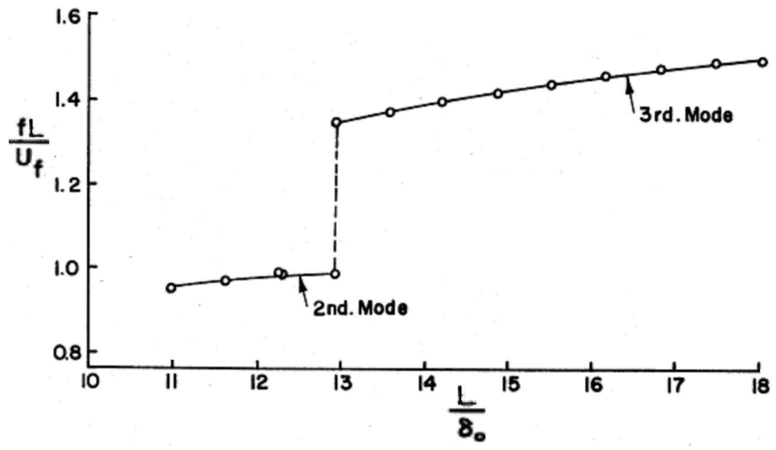

Figure 2.13: Dimensionless oscillation frequency as a function of the dimensionless cavity length L/δ_0. The dashed line indicates the modal jump. Data was obtained at Re_{δ_0} of $0.92 \times 10_3$ and D/θ_0 of 12.95 (Virendra Sarohia, 1975).

3.4 Factors affecting the organisation of the cavity separated shear layer oscillations

The organisation or the regularity of the cavity separated shear layer oscillations is recognised from the oscillations spectra. Highly organised regular oscillations exhibit a well defined spectral peak or peaks, while low organised random oscillations are associated with a broadband spectra. The oscillations organisation is affected by different factors: (i) The feedback cycle, (ii) the reverse flow interaction, (iii) the double oscillation mode, (iv) the intermittency of the vortex shedding phenomena, (v) the small-scale disturbances, and (vi) the interaction with the streamwise vorticity. The feedback cycle, which will be discussed in the next section, highly organises and enhances the cavity separated shear layer oscillations. On the other hand, the reverse flow interaction modulates these oscillations. The remaining factors reduce the oscillations' organisation.

Within the recirculation zone, sudden surges of reverse flow were observed by Lin and Rockwell (2001) at Re_{θ_0} of $1.37 \times 10_3$ and $L/D = 4$. These occasional flow surges occur due to the downward deflection of the separated shear layer at the cavity trailing edge. As a result, the flow is deflected at the cavity trailing edge and returned back towards the cavity leading edge, as demonstrated in Figure 2.14. The reverse flow interaction with cavity leading edge influences the initial development of the cavity separated shear layer. The evidence presented

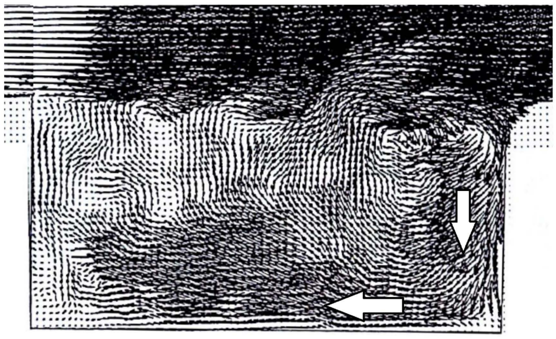

Figure 2.14: Snapshot of the instantaneous velocity field showing a sudden surge of the reverse flow. The figure was obtained at Re_{θ_0} of $1.37 \times 10_3$ and $L/D = 4$. The arrows indicate the reverse flow (Lin and Rockwell, 2001).

in the study suggest that the reverse flow interaction is, at least, partially responsible for the amplitude and frequency modulations of the cavity separated shear layer oscillations. Although this phenomenon has a significant impact on the oscillations of the cavity separated shear layer, rare studies have investigated it.

The cavity separated shear layer usually oscillates at a particular oscillation mode (single mode). However, within the modal jump region, the oscilations randomly switch between the lower and the higher oscillation modes (Virendra Sarohia, 1975). This is called the double oscillation mode. This behaviour was investigated by Yan et al. (2006) at M between 0.3 and 0.32 and $L/D = 4$. The investigation revealed that the oscillation frequency for the single mode does not vary with time, and hence, the frequency spectrum is dominated by a relatively large amplitude peak as shown in Figures 2.15(a) and 2.15(c). On the other hand, the oscillations in the double mode switch rapidly between two modes, and hence the single spectral peak is split into two smaller peaks as illustrated in Figures 2.15(b) and 2.15(d)(Yan et al., 2006). The intermittency of the vortex shedding phenomenon also affects the organisation of the cavity separated shear layer oscillations. As the shedding of the large vortical structures becomes intermittent, the spectrum of the cavity separated shear layer becomes broadband with no distinct peaks (Ashcroft and Zhang, 2005).

The impact of the small-scale disturbances on the organisation of the cavity separated shear layer oscillations was investigated by Ashcroft and Zhang (2005) at $M \approx 0.1$ and L/D between 2 and 4. These small-scale disturbances, according to the authors, are less organised and have a shorter lifespan than the large

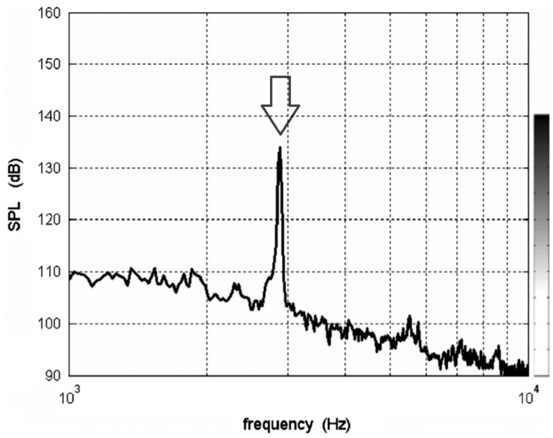

(a) spectral of SPL (single mode)

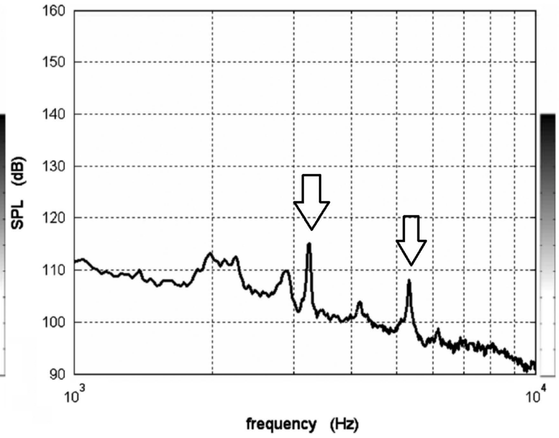

(b) spectral of SPL (double mode)

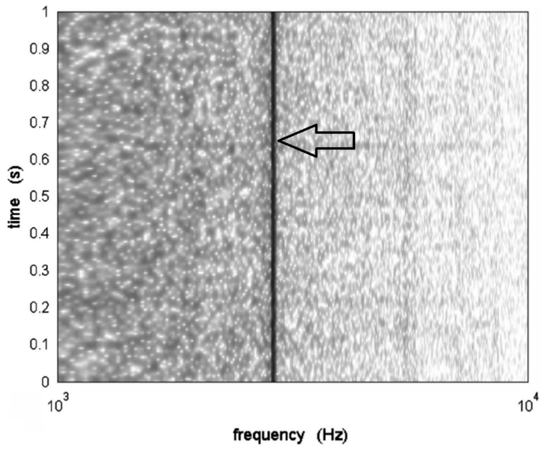

(c) spectrogram (single mode)

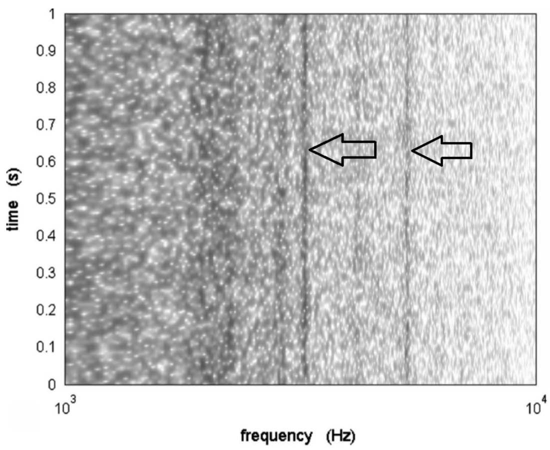

(d) spectrogram (double mode)

Figure 2.15: Spectral characteristics of single and double modes. The modes are indicated by arrows. The data were obtained at M between 0.3 and 0.32, and $L/D = 4$ (Yan et al., 2006). SPL: denotes sound pressure level.

vortical structures. The authors claim that these small disturbances affect the location and the geometry of the large vortical structures, which leads to an increase in the spatial intermittency of the large vortical structures. As a result, the spectra of the wall pressure signal becomes broadband. This claim is consistent with the findings of Roos and Kegelman (1986) on a separated shear layer over a backward facing step. According to the study, tripping the laminar boundary layer generates more disturbances in the separated shear layer and causes more irregularity in the trajectory of the large vortical structures. Another influencing factor is the interaction between the spanwise coherent vortical structures and the streamwise vorticity generated in the cavity separated shear layer. This interaction destroys the coherence of the spanwise vortical structures (Rockwell and Naudascher, 1979).

3.5 Section summary

The main instabilities in the cavity separated shear layer are: (i) the shedding of large coherent vortical structures, and (ii) the flapping motion of the cavity separated shear layer. Different approaches have been applied to reveal the coherent vortical structures within the cavity separated shear layer, such as smoke visualisation, vorticity maps and manipulation of the instantaneous velocity field. The coherent vortical structures in the rectangular cavities are formed due to the Kelvin-Helmholtz instability. After generation, these structures convect at a constant speed of more than 50% of the free stream velocity. Near the cavity trailing edge, the coherent structures slow down and take one of these three scenarios: (i) complete impingement at the cavity trailing edge, (ii) partial impingement, or (iii) complete escape from the cavity trailing edge. This variation in the trajectories of the coherent structures is attributed to the flapping motion, which is a cyclic vertical displacement of the cavity separated shear layer. The flapping motion is caused by the change in the pressure across the cavity separated shear layer. The lack of quantitative information in the literature about the flapping motion is probably due to the random nature of this motion.

The main dimensionless parameters for the oscillations of the cavity separated shear layer are: (i) the dimensionless propagation speed U_c/U_f, (ii) the dimensionless oscillation frequency $St = fL/U_f$, and (iii) the oscillation mode m. As the cavity length and or the free stream velocity increases, the oscillation mode "jumps" suddenly from a lower mode to a higher one. This jump is associated with a sharp increase in the dimensionless oscillation frequency. The oscillation mode continue to jump to higher modes until the oscillations become irregular.

The organisation or the regularity of the cavity separated shear layer oscillations is affected by different factors: (i) the double oscillation mode, (ii) the intermittency of the vortex shedding phenomena, (iii) the small-scale disturbances, (iv) the interaction with the streamwise vorticity, (v) the reverse flow interaction, and (vi) The feedback cycle. The first four factors reduce the oscillations' organisation. The reverse flow interaction phenomenon has a significant modulating impact on the oscillations of the cavity separated shear layer. However, rare studies have investigated this phenomenon. The last factor is the feedback cycle, which highly organises and enhances the cavity separated shear layer oscillations. This cycle will be discussed in the next section.

4 The feedback cycle

This section describes the mechanisms of the feedback cycle and the associated predicting equations for the dimensionless oscillation frequency.

In feedback cycle, the disturbances are generated in the cavity and then feedback towards the cavity separated shear layer to organise and enhance the oscillations of this layer. As illustrated in Figure 2.16, the cycle consists of three stages: (i) the amplification/interaction of the instabilities along the cavity separated shear layer, (ii) the generation of the feedback disturbances, and (iii) the feedback of these disturbances towards the cavity separated shear layer.

The amplification/interaction of the instabilities along the cavity separated shear layer

Similar to the mixing layers, the instabilities of the cavity separated shear layer undergo two stages of development: (i) linear growth, and (ii) nonlinear interaction. The concept of each stage is provided in Section 1.1. These stages were investigated by Knisely and Rockwell (1982) at $Re_{\theta_0} \sim 10^2$ and L/θ_0 between 50 and 160. The study was carried out using hot-film measurments on the separation point of the cavity separated shear layer. Within the region of the linear growth, two frequencies were found most amplified, which are the oscillation frequency (or

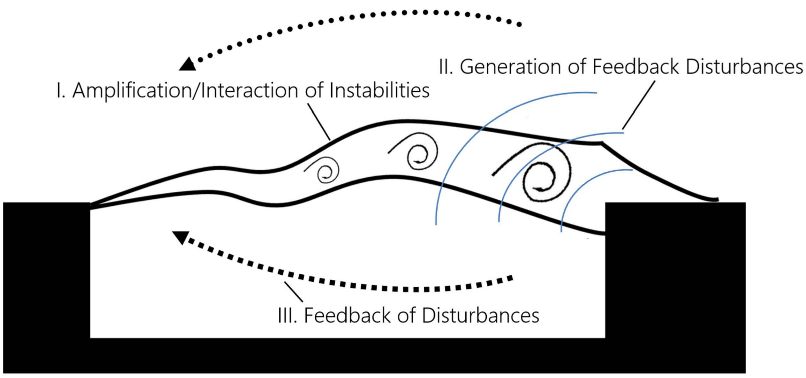

Figure 2.16: The feedback cycle in open cavity flow.

the fundamental frequency) and the sub-harmonic of the fundamental frequency. The fundamental and the sub-harmonic are attributed to the shedding of the large vortical structures and the flapping motion, respectively. The instability growth rate in this region, according to the study, is constant, rapid, and follows the linear spatial-stability theory for inviscid shear layer proposed by Betts and Umiastowski (1976), as illustrated in Figure 2.17.

The study of Knisely and Rockwell (1982) found that beyond approximately $L/\theta_0 = 20$ the nonlinear interaction between the fundamental and the sub-harmonics takes place. This interaction either reinforces the sub-harmonics or generates additional weaker sub-harmonics. It was also found that the fundamental frequency interacts with itself to form new harmonics, and then the new harmonics interact with the fundamental frequency to generate higher harmonics. The harmonic and the sub-harmonics of the fundamental frequency was also reported in the velocity spectra of Rockwell and Knisely (1979) experiment at Re_{θ_0} of 106 and 324, and $L/\theta_0 \sim 10^2$. In contrast, Little et al. (2007) did not find any harmonics nor sub-harmonics in the wall pressure spectra at $M = 0.3$ and $L/D = 4$. This discrepancy is probably because of the spectral analysis in the experiments of Rockwell and Knisely (1979) and Knisely and Rockwell (1982)

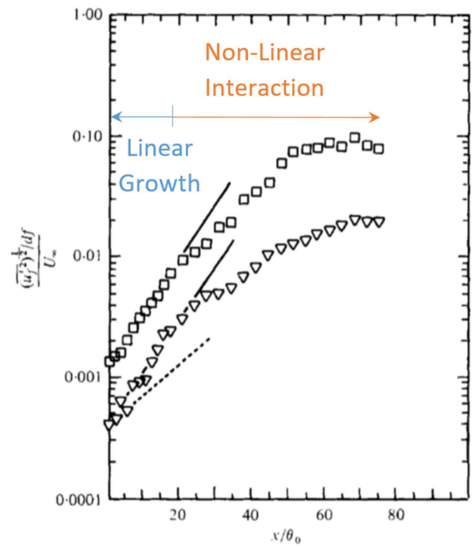

Figure 2.17: Growth rates of the fundamental and the sub-harmonic frequencies with increasing downstream distance. The squares indicate the fundamental frequency, while the triangles indicate the sub-harmonic. The linear spatial stability theory is represented by solid and dashed lines. Data was obtained at Re_{θ_0}= 190 and L/θ_0 of 80 (Knisely and Rockwell, 1982).

were performed using the velocity fluctuations of the cavity separated shear layer, while the spectral analysis in the Little et al. (2007) experiments were performed using the wall pressure fluctuations of the cavity floor.

4.1 The mechanisms of feedback disturbances

Different feedback mechanisms have been found in open cavity flows. These mechanisms include: (i) the hydrodynamic feedback, (ii) the acoustic feedback, (iii) the standing wave, and (iv) the fluid-elastic interaction. The fourth mechanism (the fluid-elastic interaction) will not be examined in this section since it is not relevant to the current study. This type of interaction is associated with the displacement of the cavity solid boundaries, such as a cavity with a vibrating component. In the present study, the cavity model is sufficiently stiff, and hence the fluid-elastic interaction has been prevented.

The Hydrodynamic Feedback

The hydrodynamic feedback is also referred by Rockwell and Naudascher (1978) as the "fluid-dynamic" interaction. As the separated shear layer impinges on the cavity trailing edge, velocity and pressure changes in this region. These disturbances are then convected upstream to impact the separated shear layer, particularly the sensitive separation region at the cavity leading edge (Knisely and Rockwell, 1982). The harmony between the fluctuations in the cavity leading and trailing edges organises the oscillations of the cavity separated shear layer. This influence was uncovered by Rockwell and Knisely (1979) at Re_{θ_0} between 106 and 324. The study found that placing an impingement edge downstream of a backward facing step increases the organisation and the amplitude of the oscillations of the cavity separated shear layer. This is evident from the narrow-band peak in the velocity spectra of the cavity separated, as shown in Figure 2.18. According to the authors, this organising effect includes the fundamental, the harmonic, and the sub-harmonic frequencies of oscillation. The authors attributed this organising effect to the hydrodynamic feedback from the impingement edge. Further investigations, carried out by Gharib and Roshko (1987) on an axisymmetric cavity at a Reynold number based on the model diameter of 2.4×10^4, revealed that the harmony between the leading and trailing edges fluctuations are satisfied by the "phase criterion". According to this criterion, the phase difference between

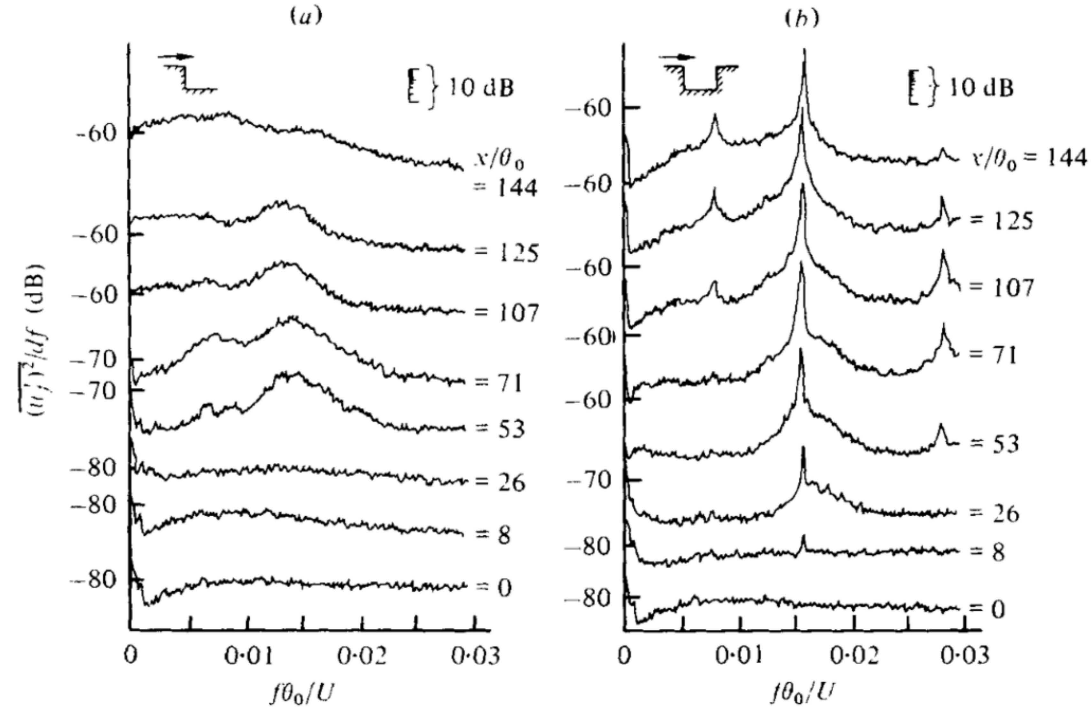

Figure 2.18: Comparison of streamwise evolution of velocity spectra without (a) and with (b) the cavity impingement edge at corresponding locations in the cavity shear layer ($U/U_f = 0.95$) (Rockwell and Knisely, 1979).

the fluctuations in the cavity leading and trailing edges is an integer multiple of 2π. The author expressed this mathematically as follows

$$\frac{\phi}{2\pi} = \frac{L}{\lambda} = \frac{fL}{U_c} = m \tag{2.2}$$

where ϕ is the overall phase difference of the fluctuations between the two cavity corners, λ is the oscillation wavelength, f is the oscillation frequency, U_c is the propagation speed of the disturbances, and m is the order of the oscillation mode which is an integer number. However, as the cavity length increased beyond $L/\theta_0 = 155$, the phase criterion lost its validity, and the oscillations of the cavity separated shear layer become random. Similar phase criterion was reported by Knisely and Rockwell (1982) for a rectangular cavity at $Re_{\theta_0} \sim 10^2$. Another version of the phase criterion was proposed by Virendra Sarohia (1975) for an axisymmetric cavity at a Reynolds number based on the model diameter between 2×10^4 and 10^5. According to this study, the phase criterion satisfies $\phi/2\pi = L/\lambda = m + 0.5$. This formula was satisfied until the oscillations in the study became random at approximately $L/\delta_0 \geq 18$.

The Acoustic Feedback

Acoustic waves can enhance the oscillations of the cavity separated shear layer. Rossiter (1964) performed a number of experiments on the open cavity flow at transonic and subsonic speeds. The study yields the Rossiter hypothesis on acoustic feedback, which states that the cavity acoustic noise is generated due to the passage of the vortical structures over the cavity trailing edge, and that the generated acoustic waves propagate upstream to excite the vortical structures at the cavity leading edge, as shown in Figure 2.19. Based on this hypothesis, the author derived the following semi-empirical equation to predict the cavity oscillations frequency, which is referred to as the "Rossiter equation":

$$St = fL/U_f = \frac{m - \alpha}{M + \frac{1}{\kappa}} \tag{2.3}$$

where m is the oscillation mode (also known as Rossiter mode), M is Mach number, κ is the ratio of the propagation speed of the vortical structures to the free stream velocity, and α is the phase lag factor between the vortex-edge interaction and the generation of the upstream feedback disturbances. The empirical constants, α and κ, in the experiment of Ahuja and Mendoza (1995) at M= 0.065 to $M = 1$ were 0.25 and 0.65, respectively.

The Rossiter equation is less successful at $M < 0.4$ (Tam and Block, 1978). Thus, various researchers, such as Tam and Block (1978), modified this equation. Tam and Block (1978) modified the Rossiter model by including the effect of the reflections of the acoustic feedback on the cavity walls. The authors found a

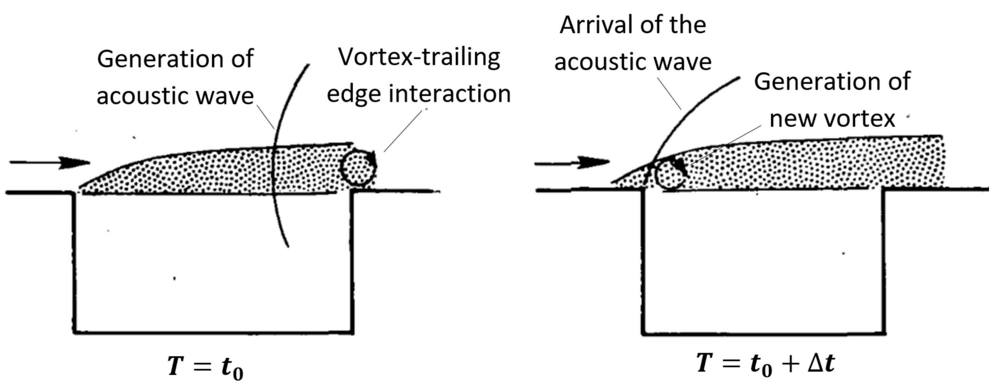

Figure 2.19: The acoustic feedback mechanism hypothesised by Rossiter (1964). The sketch shows two time frames separated by a time delay Δt (reproduced from Patricia et al. (1975)).

good agreement between the proposed model and the experimental data within $0.2 < M < 1.2$, but the model was less accurate at lower Mach numbers $M < 0.2$.

Although the Rossiter equation was originally proposed for high speed cavity flows, some low speed studies $M \leq 0.3$ have claimed good agreement between the measured oscillations frequency and the frequency predicted by the Rossiter equation. At $M = 0.2$ and $L/D = 1.49$, Ukeiley and Murray (2005) reported two sharp spectral peaks. One of them, according to the authors, agrees with the Rossiter equation. Daoud et al. (2006) also claimed good agreement with the Rossiter equation at $M = 0.086$ and $L/D = 8$. However, mode number m, α, and κ in both studies were selected based on the best fit and the experiments of Rossiter (1964) at high speeds. No measurements were provided for these parameters. The agreement between these experiments and the Rossiter equation maybe be attributed to the flexibility of the equation, not to the actual existence of the acoustic feedback mechanism. Moreover, there has not been any study in the literature which proves the validity of the Rossiter equation at low speeds.

The Standing Wave

The oscillations in the standing wave mechanisim are excited by acoustic standing waves. According to Patricia et al. (1975), when the broadband noise generated in the cavity separated shear layer coincides with one of the cavity acoustic natural modes, the oscillations of the cavity separated shear layer receive great enhancement, as illustrated in Figure 2.20. These acoustic natural modes are geometry-dependant. They are generated due to the noise interaction with: (i) the cavity length (length mode), or (ii) cavity depth (depth mode), or (iii) cavity span (width mode). According to Patricia et al. (1975), the length modes f_L and the width modes f_W are calculated as follows,

$$f_L = \frac{Nc}{2L} \tag{2.4}$$

$$f_W = \frac{Nc}{2W} \tag{2.5}$$

where N is the acoustic mode number (N = 1,2.... etc.) and c is the sound speed in the fluid.

The acoustic standing wave can also be generated between the cavity and any

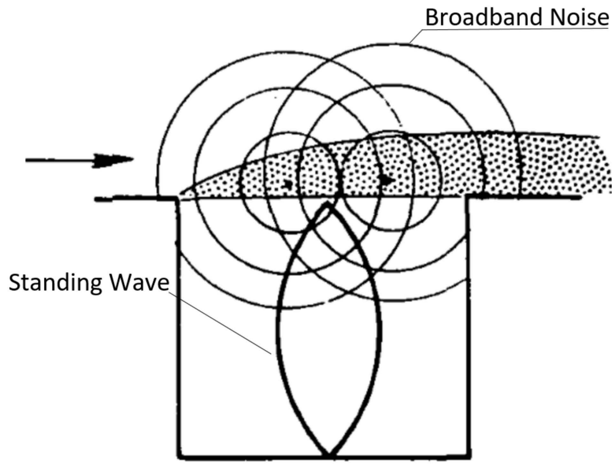

Figure 2.20: Standing wave mechanism within a cavity (Patricia et al., 1975).

solid boundary above it, such as the standing wave between a cavity and the top roof of a wind tunnel or a duct. Ziada et al. (2003) proposed the following equation to predict this acoustic transversal mode,

$$f_T = \frac{Nc}{2H} \tag{2.6}$$

where N = 1,2.... etc, and H is the distance between the cavity and the top solid boundary.

The standing wave mechanism has been reported in various low speed cavity experiments, such as Ziada et al. (2003) experiment for a confined shallow cavity at M between 0.1 and 0.3 and Samimy et al. (2007) experiment at M between 0.2 and 0.7.

4.2 Section summary

The feedback cycle greatly organises and enhances the oscillations of the cavity separated shear layer. The cycle consists of three stages: (i) the amplification/interaction of the instabilities along the cavity separated shear layer, (ii) the generation of the feedback disturbances, and (iii) the feedback of these disturbances towards the cavity separated shear layer.

In the first stage, some instabilities get amplified. The amplified instabilities then interact with each other to reinforce particular instabilities or generate new instabilities. In the second stage, the amplified instabilities generate feedback disturbances via: the fluid-elastic interaction, hydrodynamic feedback, standing wave or acoustic feedback. The fluid-elastic interaction is not relevant to the current study. The hydrodynamic feedback and the standing wave mechanisms have been reported in low speeds cavity experiments, and they are linked to the equations of the phase criterion and the cavity acoustic modes, respectively. The acoustic feedback is predicted using the Rossiter equation. Although some low speed studies have claimed good agreement with the Rossiter equation, these studies have not provided any measurements for the equation parameters (m, α, and κ). Moreover, there has not been any study in the literature yet proves the applicability of the Rossiter equation at low speeds.

5 Cavity flow control

The term "flow control" in aerodynamics refers to any mechanism or process used to favourably alter a particular characteristic of the flow field (Gad-el Hak et al., 1998). According to Gad-el Hak et al. (1998), is "*whether the task for flow control is to delay/advance transition, to suppress/enhance turbulence or to prevent/provoke separation, useful end results include drag reduction, lift enhancement, mixing augmentation and flow-induced noise suppression*".

Based on the power requirements, flow control methods are classified into passive and active control methods. Passive control methods do not require input power, for instance, vortex generators and riblets. On the other hand, the active control methods consume power. As illustrated in Figure 2.21, the active devices (actuators) can be: (i) fluidic, such as steady and unsteady jets, (ii) Moving object/surface, for example a rotating surface, (iii) Plasma actuator, or (iv) others such as electromagnetic devices (Cattafesta and Sheplak, 2011). These devices are usually incorporated in open-loop, feed-forward or feedback control systems, as shown in Figure 2.22 (Gad-el Hak et al., 1998). The open-loop control systems do not contain any sensing element, and hence the actuator action is predetermined. In contrast, the actuator action in the feed-forward control systems is determined by the signal received from the sensing element. While the feed-forward control systems do not monitor the controlled variable itself, the controlled variable in the feedback control systems is monitored, fed back and compared with a reference input.

Controlling the open cavity flow at low Mach numbers $M < 0.3$ has been

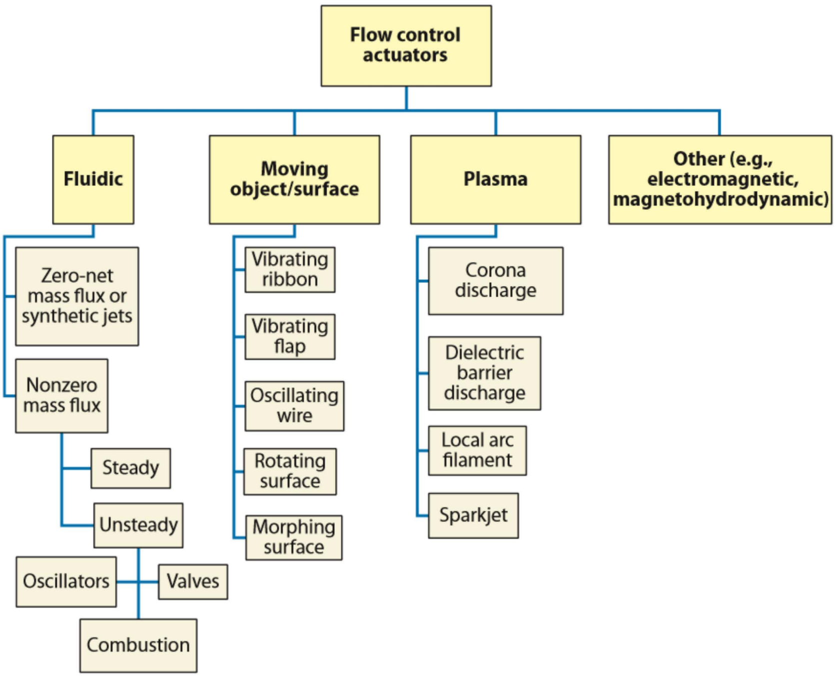

Figure 2.21: Classification of the active devices (Cattafesta and Sheplak, 2011).

investigated thoroughly in the past 60 years. The main objectives of these investigations have been to: (i) suppress the narrow-band peaks of the cavity separated shear layer oscillations, and (ii) attenuate the narrow-band acoustic tones and the overall sound pressure level (OSPL) of the cavity-induced noise. Generally, stabilising the cavity separated shear layer (first objective) implies a reduction in the noise level (second objective) (Sarohia and Massier, 1976).

In the current study, the cavity flow control methods will be classified based on the working principles into five categorises, which are: (i) geometry modification of cavity leading and trailing edges, (ii) excitation of the upstream boundary layer, (iii) stabilising the recirculation zone, (iv) frequency excitation, and (v) phase cancellation.

5.1 Geometry modification of the leading and trailing edges

Geometry modification of the cavity leading and trailing edges (Figure 2.23) has been widely used for cavity flow control at high speeds $M \geqslant 0.3$. This method aims to minimise the interaction between the separated shear layer and the cavity trailing edge. Franke and Carr (1975) suppressed the cavity oscillations using double ramps at the cavity leading and trailing edges. Ethembabaoglu (1973)

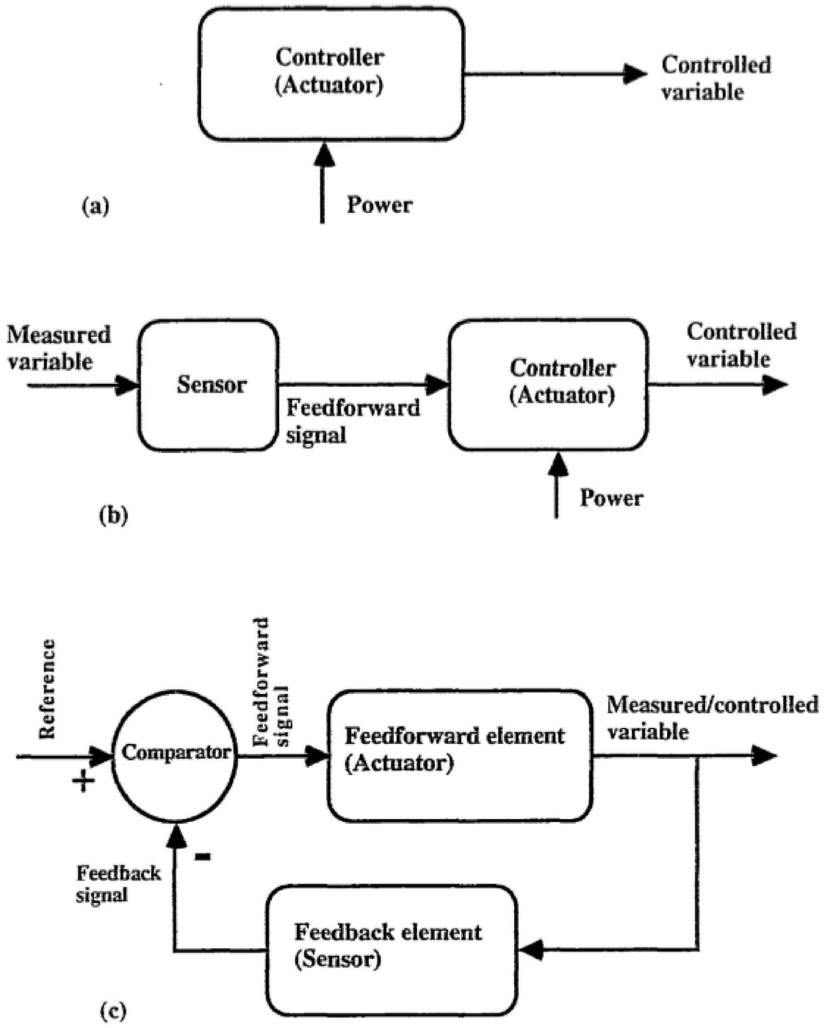

Figure 2.22: Types of active control systems: a) open-loop control system, b) feed-forward control system, and c) feedback control system (Gad-el Hak et al., 1998).

achieved a significant oscillations reduction by ramping, rounding, and offsetting the cavity trailing edge. A similar effect can be achived by installing a spoiler at the cavity leading edge. The spoiler, according to Cattafesta et al. (2003), shifts the reattachment location of the separated shear layer downstream of the cavity trailing edge, and hence the feedback disturbances are minimised. Overall, the geometry modification approach has been highly successful in suppressing the cavity oscillations.

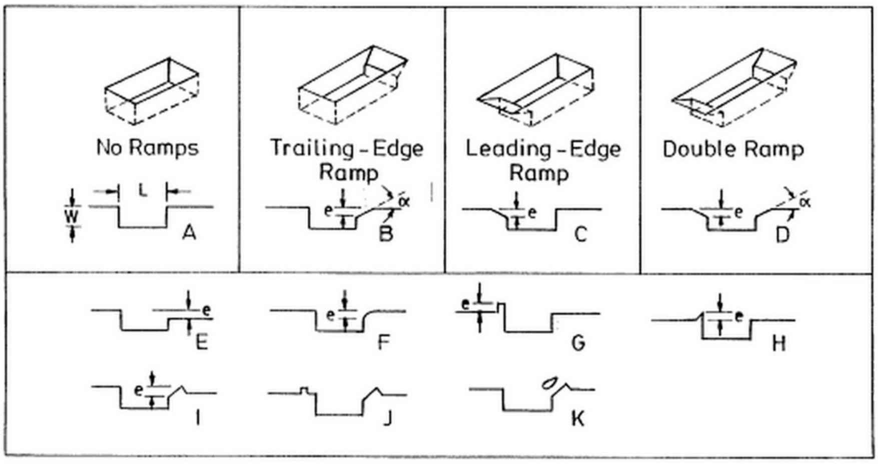

Figure 2.23: Sketch of different geometry modification approaches: (E) trailing edge offset, (F) trailing edge gradual ramp, (G) spoiler at the leading edge, (H) leading edge deflector, (J) leading edge spoiler and trailing edge ramp (Rockwell and Naudascher, 1978).

5.2 Excitation of the upstream boundary layer

Another method of supressing the cavity separated shear layer oscillations is by exciting the boundary layer upstream of the cavity. A typical example of this approach is the experiments of Patricia et al. (1975). The authors installed fences and roughness elements upstream of the cavity at M between 0.12 and 0.24, and L/D between 1 and 4. According to this study, the tripping devices generated broadband turbulences that dis-organised the cavity oscillations. The hydrodynamic and the acousitc pressure spectra showed that the roughness elements suppressed some acoustic modes without any net reduction in the overall noise. However, the tripping devices were found less effective at higher free stream velocities, possibly due to the reduction of the boundary layer thickness. Similar effects were observed with increasing the cavity length. On the other hand, Chan et al. (2007) used an active device to excite the upstream boundary layer at M between 0.03 and 0.06, and $L/D = 1$. A streamwise array of plasma actuators was installed upstream of the cavity in order to induce streamwise vortical structures, as shown in Figure 2.24 (a). The particle image velocimetry results suggest that the streamwise structures are convected downstream along the separated shear layer, as evident from Figure 2.24 (b). According to the study, the induced structures impede the development of the spanwise vortical structures in the cavity separated shear layer. Consequently, the shedding phenomena became more intermittent. The plasma excitation completely suppressed the dominant

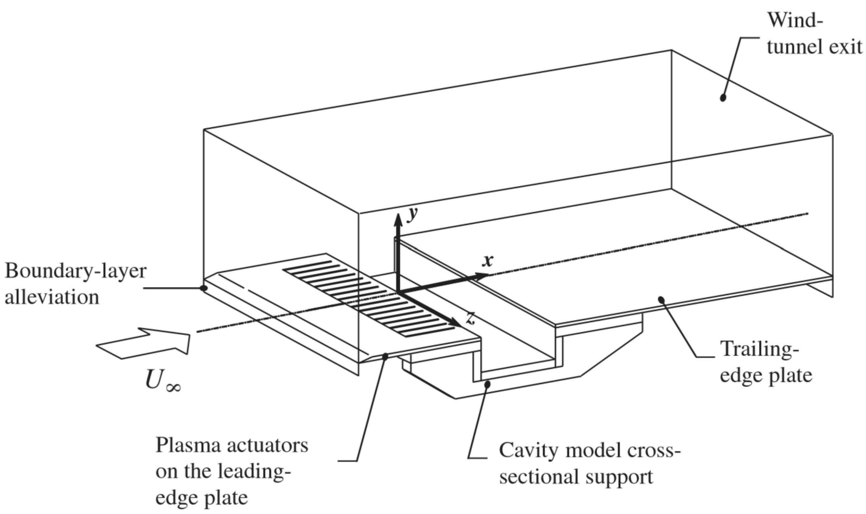

(a) Schematic of the control arrangement

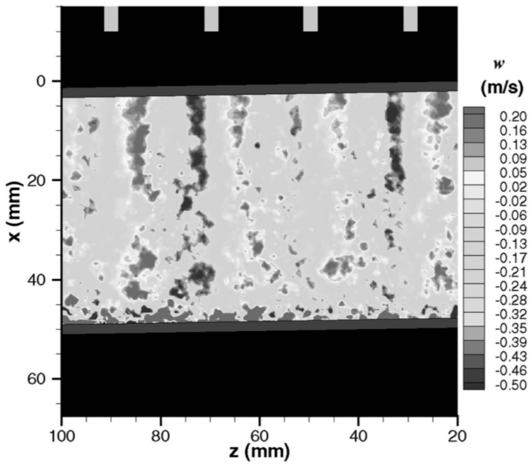

(b) Contours of the spanwise velocity (top view)

Figure 2.24: The experimental study of Chan et al. (2007) at $M = 0.03$ and $L/D = 1$. The black regions in subfigure (b) represent the cavity leading and trailing edges, while the light-grey strips represent the location of the plasma actuators.

acoustic tone along with its harmonics. Although the plasma actuators generate narrow-band spectral peaks, the overall sound pressure level (OSPL) reduced by approximately 22%.

5.3 Stabilising the recirculation zone

The continuous mass exchange within the recirculation zone (the inflow and outflow at the cavity leading and trailing edges) enhances the oscillations of the cavity separated shear layer Sarohia and Massier (1976). Therefore, stabilising the recirculation zone is an effective way of suppressing the cavity oscillations. Sarohia and Massier (1976) forced a steady jet of fluid from the cavity floor at M between 0.18 and 0.35, and L/D from 0.5 to 1.5. The fluid was injected along the cavity floor. The velocity spectra of the cavity separated shear layer showed that the injection suppressed the dominant spectral peak, but it increased the amplitude of the lower-frequency peak. According to the authors, the injection of the steady flow along the cavity floor eliminates any mass imbalance between the inflow and outflow to the cavity. Furthermore, the jet pushed the cavity separated shear layer upwards and away from the cavity trailing edge. As a result, the feedback of disturbances towards the cavity separated shear layer is minimised. Consequently, the cavity induced noise is significantly reduced.

At $Re_\theta = 194$, Kuo and Huang (2001) minimised the cavity separated shear layer oscillations by reducing the interaction between the main recirculation vortex and the cavity separated shear layer. In this experimental study, the authors examined various passive control devices: (i) positively and negatively sloped cavity floor, and (ii) a vertical fence installed at different streamwise locations on the cavity floor as shown in Figure 2.25. The velocity spectra and the velocity auto-correlation revealed that as the positive or negative slope increases, the oscillations of the cavity separated shear layer decrease until they are completely suppressed. As illustrated in Figure 2.25 (a), the negative slope generates an adverse pressure gradient on the recirculation flow. This pressure gradient slows the recirculation vortex and reduces its interaction with the cavity separated shear layer. The positive slope, on the other hand, reduces the oscillations of the cavity separated shear layer due to two reasons. Firstly, it reduces the effective area of the cavity trailing edge, and hence the feedback of the cavity separated shear layer disturbances is significantly suppressed. Secondly, the positive slope reduces the size of the main recirculation vortex. Consequently, the main recirculation vortex affects a smaller portion of the cavity separated shear layer, as demonstrated in Figure 2.25 (b). The authors also found that installing the vertical fence at $x/L = 0.3$, 0.5, and 0.8 significantly suppresses the cavity oscillations. The fence, according to the authors, forces the recirculation vortex to impinge and bifurcate at a certain point on the cavity separated shear layer, as shown in Figure 2.25 (c). As a result, the oscillations are suppressed due to the out-of-phase relationship between the impinging recirculating flow and the oscillations of the cavity separated shear layer.

Yoshida et al. (2006) performed a computational simulation of the cavity flow with a moving cavity floor. The simulation was carried out at a Re_D of 6000 and $L/D = 2$. The simulation discovered that moving the cavity floor with sufficient speed rearranges the recirculation vortices in a way that enhances the stability of the cavity separated shear layer. Moving the cavity floor in the anti-streamwise direction at a speed of more than 10% of the free stream velocity (U_f) generates a large clockwise recirculation vortex (Figure 2.26 (b)), while moving the cavity floor in the streamwise direction at a speed of more than 19.5% of U_f produces two parallel and horizontally-oriented recirculation vortices (Figure 2.26 (c)). In both cases, the stability of the cavity separated shear layer is enhanced and the oscillations are almost suppressed. Another computational study was carried out by Suponitsky et al. (2005) at Re_D of 5000 and $L/D = 4$. In this study, steady flow is simultaneously injected and sucked at the cavity leading and trailing edges, respectively, as demonstrated in Figure 2.27 (a). According to the

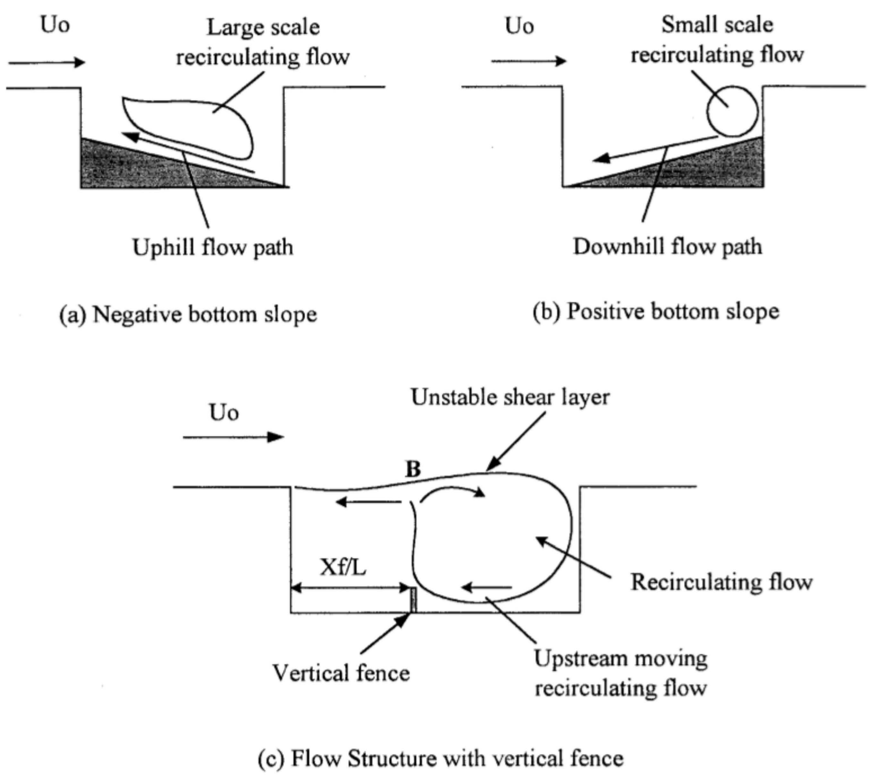

Figure 2.25: The working principles of the sloped floor and vertical fence (Kuo and Huang, 2001).

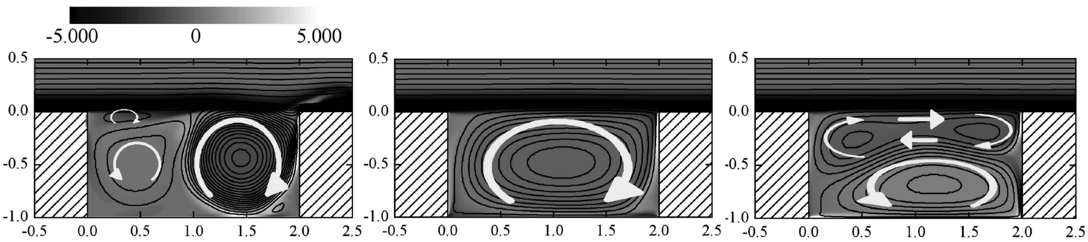

(a) $U_{floor} = 0$ (b) $U_{floor} = -0.1U_f$ (c) $U_{floor} = +0.195U_f$

Figure 2.26: Instantaneous streamlines (solid lines) and grayscale contour plots of vorticity for Yoshida et al. (2006) simulation. The simulation was carried out at Re_D of 6000 and $L/D = 2$ (Yoshida et al., 2006).

study, increasing the injection rate beyond a threshold value causes the cavity separated shear layer to be isolated from the recirculation zone. As a result, the main recirculation vortex becomes weaker and the momentum of the reverse flow decreases, as evident from Figure 2.27 (b). Consequently, the cavity separated shear layer becomes more stable and the oscillations are effectively suppressed. The threshold value for the injection rate was found to be $C_\mu \approx 0.11\%$, where C_μ is the momentum coefficient, that is expressed as,

$$C_\mu = \frac{\rho_j U_j^2 A_j}{0.5 \rho_f U_f^2 A_{cavity}} \tag{2.7}$$

where j and f denote the injected flow and the free stream, respectively. A_j and A_{cavity} are the slot area and the cavity floor area, respectively. A similar effect was achieved with injection alone. Therefore, the suction from the cavity trailing edge, according to the authors, does not seem to have any significant impact on the oscillations apart from keeping the net forced mass flux zero.

5.4 Frequency excitation

Although the aforementioned control techniques are relatively simple and easy to implement, the effectiveness of some of them is limited to a narrow range of flow conditions. Recently, more research has been adopting the frequency excitation and the phase cancellation approaches. These approaches rely on easy-controlled actuators, such as zero-net mass unsteady synthetic jets (Debiasi and Samimy (2004) and Little et al. (2007)), and vibrating elements (Cattafesta et al. (1997)). Furthermore, these approaches can be easily incorporated within a feedback control system to gain wider operational conditions as well as reducing the cost of

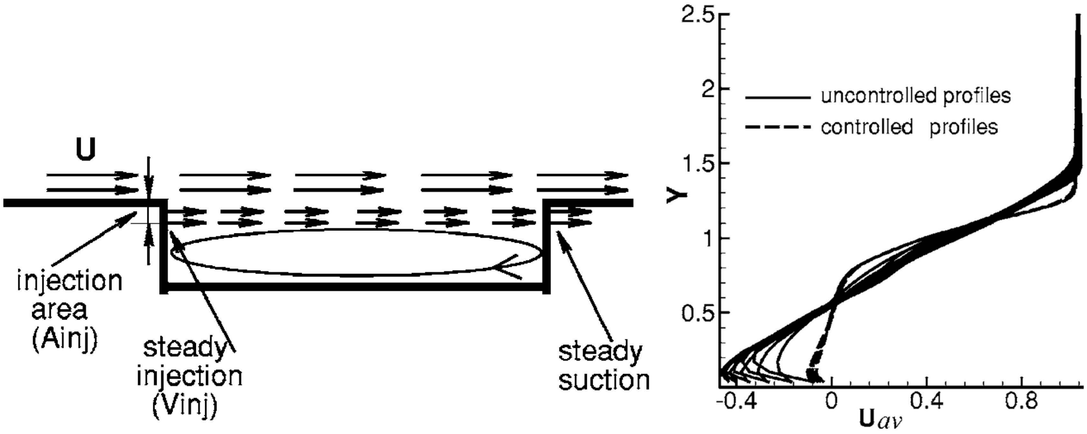

(a) sketch of the control approach

(b) Dimensionless time-averaged streamwise velocity profiles at $0.75 \leqslant x/L \leqslant 1$

Figure 2.27: Simultaneous steady injection and suction. Data was simulated at Re_D of 5000 , $L/D = 4$ and C_μ of 0.8 (Suponitsky et al., 2005).

electrical power consumption.

Frequency excitation works by forcing a new frequency into the cavity separated shear layer to disorganise the oscillations of the cavity separated shear layer. Frequency excitation can be classified into three categories: (i) near-instability excitation, whereby the forcing frequency is slightly different from the oscillation frequency, (ii) mode excitation which involves exciting an additional oscillation mode, and (iii) high-frequency excitation, whereby the forcing frequency is substantially higher than the oscillation frequency.

Near-instability excitation

The working principles of the near-instability excitation are revealed by the experimental work of Gharib (1987) at a Reynolds number based on the cavity model of 24×10^3. In this study, a heated strip was installed upstream of the cavity to excite Tollmien-Schlichting waves at a particular forcing frequency F_f. As shown in Figure 2.28, increasing the forcing power P_f gradually suppresses the natural oscillation frequency F(cases (a) to (d)). The forcing and natural frequencies then equalise in case (d). Increasing the forcing power further causes the forcing frequency to dominate the cavity separated shear layer, as evident from cases (e) to (g). According to the author, the total amplitude of the coexisting peaks (cases (b) to (f)) is less than the amplitude of a single peak (cases (a) and (g)). This behaviour, which explains the effectiveness of the near-instability excitation, is attributed to the destructive interaction between the forcing and natural oscillation frequencies (Grundmann and Tropea, 2009). Another study on near-instability excitation was performed by Cattafesta et al. (1997) at $M \approx 0.11$. In this experimental study, the frequency was excited using segmented piezoelectric actuators installed at the cavity leading edge. According to the authors, the forcing frequency suppressed the oscillation frequency, as well as the broadband level of the oscillations.

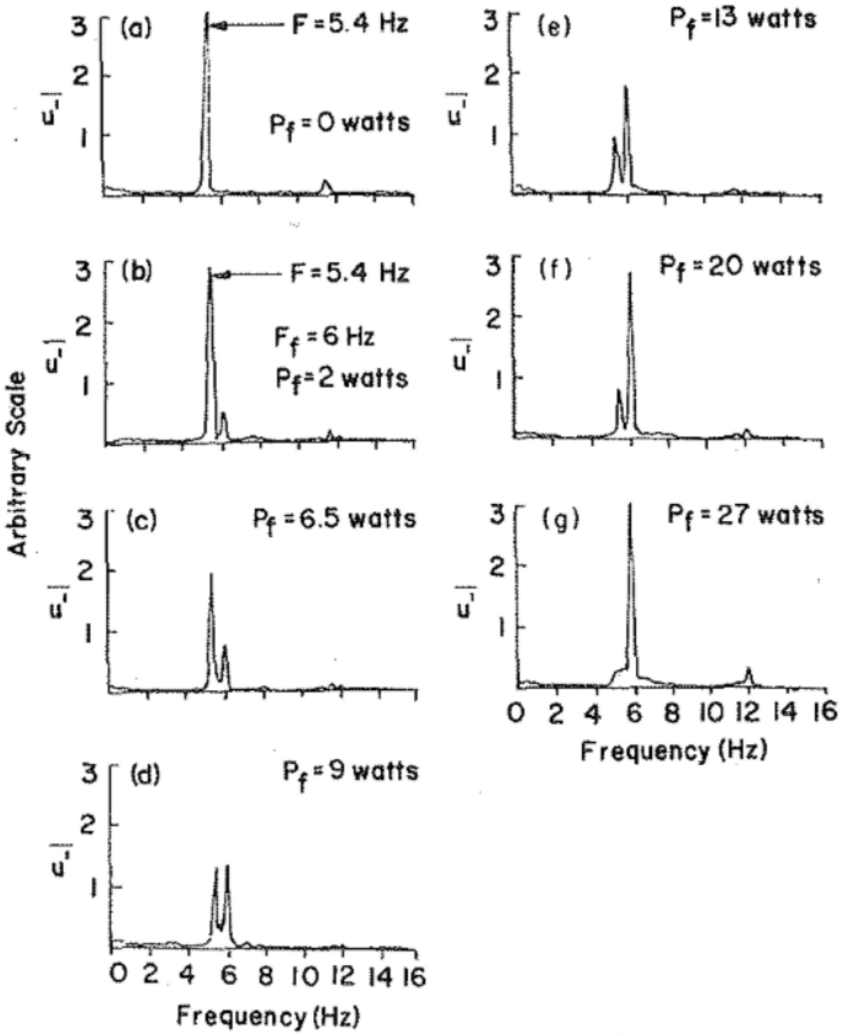

Figure 2.28: Influence of increasing forcing power P_f on the velocity spectra of the cavity separated shear layer. Data was obtained at Reynolds number based on the cavity model of 24×10^3 (Gharib, 1987).

Mode excitation

The principles of mode excitation are similar to the double mode oscillations. It involves switching between two frequencies, and hence the single spectral peak is split into two smaller peaks. Over a wide range of free stream velocities ($0.25 < M < 0.5$) Debiasi and Samimy (2004) applied a zero-net mass, unsteady synthetic jet from the cavity leading edge, as illustrated in Figure 2.29. The jet was controlled by a logic-based controller, that monitors the flow condition inside the cavity and then searches for the optimum forcing frequency in order to achieve maximum spectral peak reduction. The study found that the optimum control of the single mode oscillation is achieved by exciting an additional oscillation mode. At $M = 0.3$ and $L/D = 4$, Little et al. (2007) attempted to suppress a single mode oscillation by exciting: (i) a higher-order mode, or (ii) a lower-order mode. It was found that forcing the lower-order mode shifts the oscillation frequency without any peak reduction. On the other hand, forcing at the higher-order mode significantly suppresses the natural oscillation mode. The authors attributed the effectiveness of the higher-order mode excitation to the merging/pairing of the large vortical structures at the downstream portion of the separated shear layer. The events of the merging/pairing, according to the authors, destroy the coherence of the vortical structures. This is evident from the lack of coherent structures in the downstream portion, as illustrated in Figure 2.30 (b). Furthermore, the merging/pairing events generate a sub-harmonic that randomly switches with the oscillation frequency. Due to all of these factors, the dominant oscillation frequency is effectively suppressed.

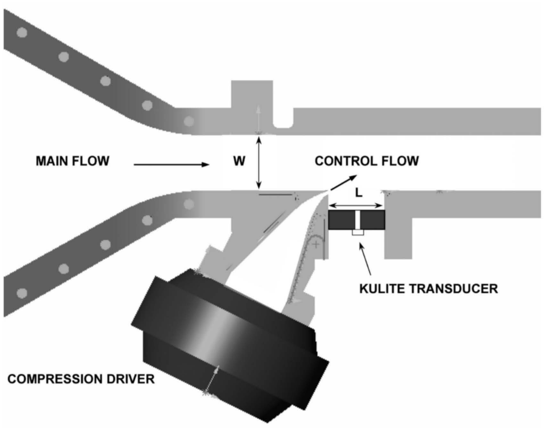

Figure 2.29: Zero-net mass, unsteady synthetic jet was used in the experimental work of Debiasi and Samimy (2004) and Little et al. (2007).

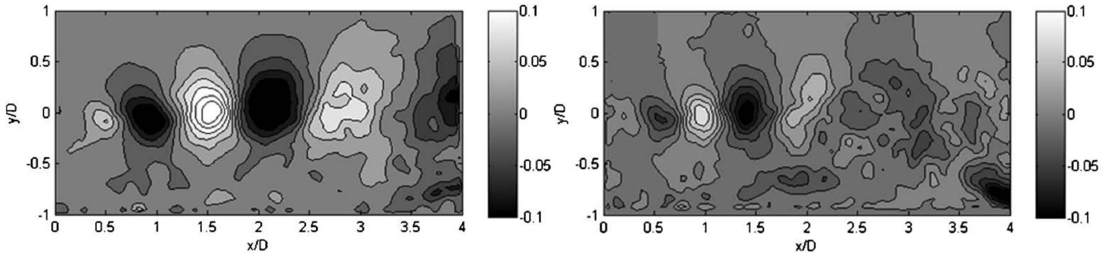

(a) Baseline flow (no jet) (b) With higher-order mode excitation

Figure 2.30: Contours of phase-averaged normal-to-wall velocity fluctuations at $M = 0.3$ and $L/D = 4$ (Little et al., 2007).

High-frequency excitation

The third category of the frequency excitation is the high-frequency excitation (HF), which has been applied at high speeds. HF devices, such as resonance tubes and rods, are usually installed upstream of the cavity. These devices generate disturbances at frequencies much higher than the oscillations frequency. According to Stanek et al. (2000), HF devices work by accelerating the energy cascade, so that all coherent structures within the cavity separated shear layer are replaced by a large population of small disturbances.

5.5 Phase cancellation

The phase cancellation approach works by forcing the cavity separated shear layer to oscillates at a phase angle different from the phase angle of the feedback disturbances. As a result, a destructive interaction takes place between the feedback disturbances and the oscillations of the cavity separated shear layer, and hence the cavity oscillations are suppressed (Little et al., 2007). This approach was introduced to the cavity flow by Gharib (1987). The author attenuated the cavity oscillations by manually adjusting the phase of the excited disturbances upstream of the cavity. However, due to a small phase drift in the cavity oscillations, the author could not maintain the attenuation for a long period of time. Recently, the phase-cancellation approach has been incorporated in a feedback control system, whereby the cavity oscillation signal is monitored and time-delayed before it is fed back to the actuator, as illustrated in Figure 2.31. This control system, which has been implemented by several researchers (Williams et al., 2000, Ziada et al., 2003, Little et al., 2007, Micheau et al., 2004), effectively suppresses the oscillations of the cavity separated shear layer. At $M = 0.3$ and $L/D = 4$, Little et al. (2007) compared the phase cancellation control method against the mode excitation approach. The comparison revealed that the phase-cancellation control method is slightly more effective in suppressing the dominant spectral peak than the mode excitation approach. The flow visualisation results showed that the former approach reduces the coherence of the vortical structures more effectively than the latter approach.

Rowley and Williams (2006) claimed that complete attenuation of the dominant oscillation frequency with a feedback control systems is theoretically impossible. According to the authors, this limitation is due to the "peak splitting" phenomena. At a certain point of increasing the control gain of the actuator, the dominant oscillation peak is split into two peaks. Peak splitting, according to the authors, is a fundamental limitation in the feedback control systems, particularly with narrow-band width actuators and large time-delay controllers. The authors attributed this phenomenon to the area rule which states that any decrease in the sensitivity over one frequency range must be balanced by an increase for some other frequencies. To minimise the impact of this issue, the authors suggested using a wide broadband actuator.

5.6 Section summary

The main objectives of open cavity flow control are to :(i) suppress the narrow-band peaks of the cavity separated shear layer oscillations, and (ii) attenuate the narrow-band acoustic tones and the overall sound pressure level (OSPL) of

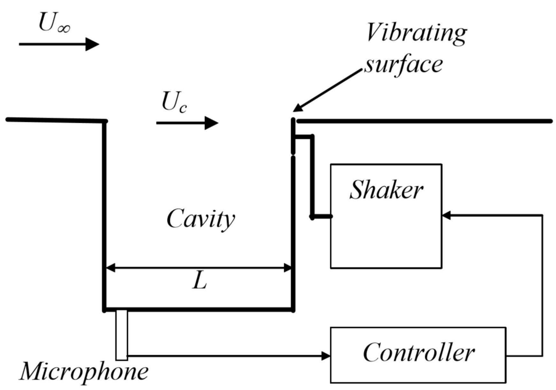

Figure 2.31: Phase cancellation control loop with a vibrating surface at the cavity trailing edge (Micheau et al., 2004).

the cavity-induced noise. The current study classifies the open cavity flow control methods at low-subsonic speeds into five categorises: (i) geometry modification of cavity leading and trailing edges, (ii) excitation of the upstream boundary layer, (iii) stabilising the recirculation zone, (iv) frequency excitation, and (v) phase cancellation. Although the first three control techniques are relatively simple and easy to implement, the effectiveness of some of them is limited to a narrow range of flow conditions. On the other hand, frequency excitation and the phase cancellation approaches: (i) rely on easy-controlled actuators, and (ii) can be easily incorporated within a feedback control system to gain wider operational conditions as well as reducing the cost of electrical power consumption. However, complete attenuation of the dominant oscillation frequency with a feedback control systems is theoretically impossible due to the "peak splitting" phenomena.

6 Concluding remarks

Numerous studies have been conducted to examine the time-averaged characteristics of the cavity flow and the oscillations of the cavity separated shear layer. However, most of these studies focus on the large vortical structures of the cavity separated shear layer. Rare studies have investigated the phenomenon of the reverse flow interaction, which has a significant effect on the oscillations of the cavity separated shear layer. This leaves a wide gap in this field of research. Studying the development and the impact of this phenomenon on the stability of the cavity separated shear layer and quantifying its frequency over a wide range of Reynolds numbers would be highly interesting from an academic point of view.

As it was seen, various cavity flow control methods have been implemented to suppress the cavity-induced noise and the oscillations of the cavity separated shear layer. The current study introduces a novel flow control strategy to the cavity flow. In this study, steady jets will be applied to the cavity flow with different: momentum fluxes, slot configurations, and blowing locations. The jets impact on the time-averaged flow field and the cavity separated shear layer oscillations will be investigated. The purpose of the steady jets is suppressing the oscillations of the cavity separated shear layer.

Chapter 3

Experimental Set-up

This chapter provides the details of the wind tunnel facility, the experimental model, the test cases, and the utilised flow diagnostic techniques. The chapter also discusses the experimental procedure and the limitations of the flow diagnostic techniques used. Uncertainty estimations are provided at the end of the chapter.

1 Wind tunnel

The experiments were carried out in the De Havilland tunnel, which is a closed-return wind tunnel, as shown in Figure 3.1. The wind speed at the test section can reach up to approximately 76 m/s. The air is circulated in the tunnel via

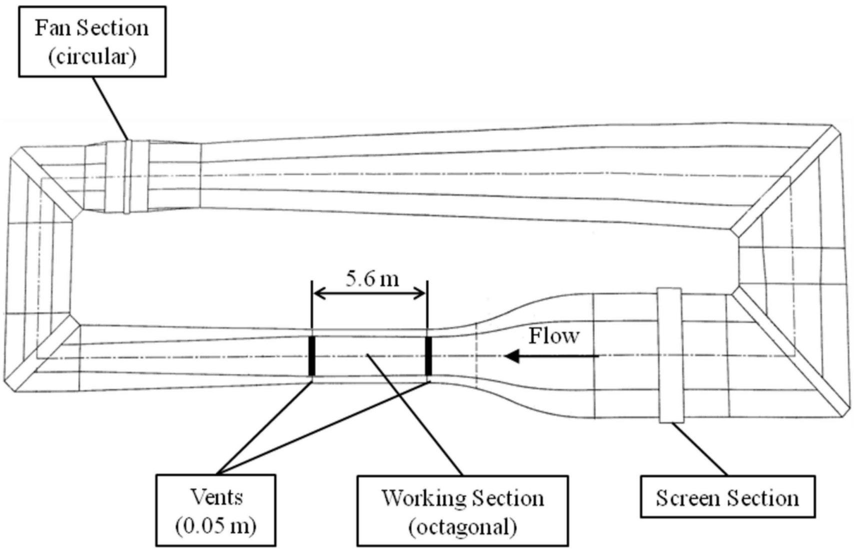

Figure 3.1: Sketch of De Havilland closed-return wind tunnel (top view) (Giuni, 2013).

a 3 m-diameter fan. The octagonal test section of the tunnel is 2.04 m high, 2.65 m wide, and 5.60 m long. Gaps of 5 cm are provided upstream and downstream of the test section in order to keep the test section static pressure equal to approximately the atmospheric pressure. The test section is equipped with a pitot tube and thermocouple to monitor the velocity and temperature of the free stream upstream of the model. The test section is also equipped with several windows allowing a wide optical access from the sides and from the top. The test section has a rotating floor to align the model with respect to the centerline of the test section. The tunnel is equipped with honeycombs and fine meshes upstream of the test section in order to reduce the turbulence intensity of the free stream. The averaged turbulence intensities of the free stream, evaluated by laser Doppler anemometry at different locations within the test section, are 1.82%, 1.95%, and 2.29% for free stream velocities of 11.1, 22.1, and 43.7 m/s, respectively.

2 Experimental model

Figure 3.2 shows the experimental model. The main body of the model is made of wooden panels and painted black to minimise laser reflections for laser-based flow diagnostic methods. The model was aligned with the centreline of the test section and fastened to the floor by four airfoil-shaped carbon fibre legs. Two inter-changeable 2.9 m×0.57 m side plates were bolted to the sides of the model. One of the side plates is made of perspex to allow optical access for flow diagnostic techniques, while the other was made of wood. To add rigidity to the perspex plate, two thin carbon fibre airfoils were bolted between the two side plates, thus the perspex plate was structurally supported by the wooden plate. Both airfoils have a symmetrical profile with a maximum thickness of 25 mm and a cord length of 162.5 mm. The supporting airfoils were positioned 300 mm above the model surface to avoid interaction with the cavity flow. With a model span of 800 mm along the z-coordinate, the estimated model's blockage ratio is approximately 5.9%.

The model was positioned 0.98 m above the tunnel floor. The leading edge of the model has a smooth elliptic shape with a length of 400 mm and a width of 100 mm, which yields an axis ratio of 4. The same ellipsoid ratio was used by number of researchers in the past (Ashcroft and Zhang (2005) and Lin and Rockwell (2001)) and separation at the model leading edge was not reported. To

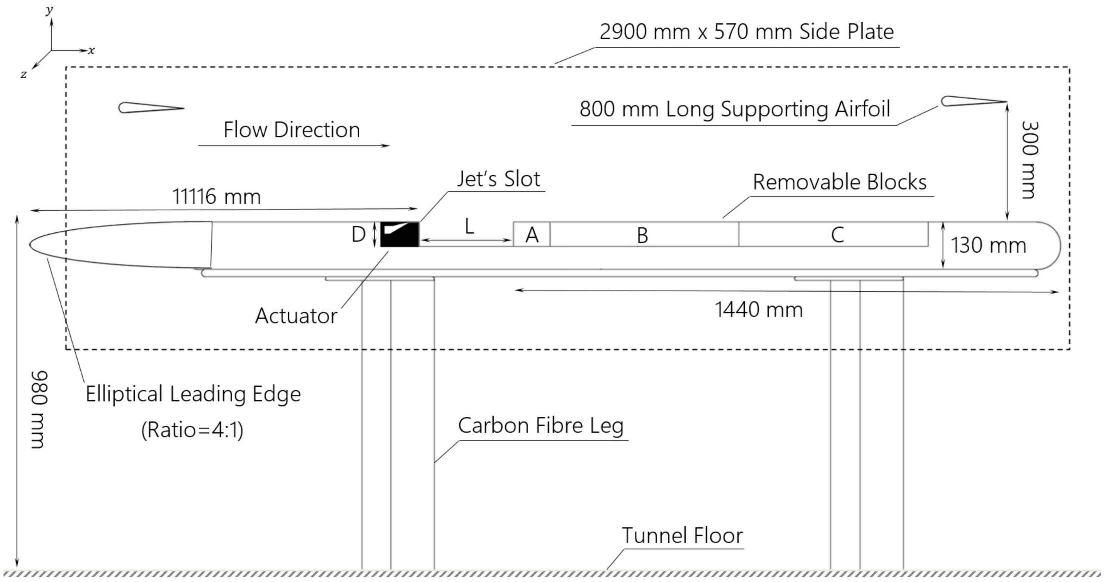

(a) Side view sketch (actuator at the cavity leading edge)

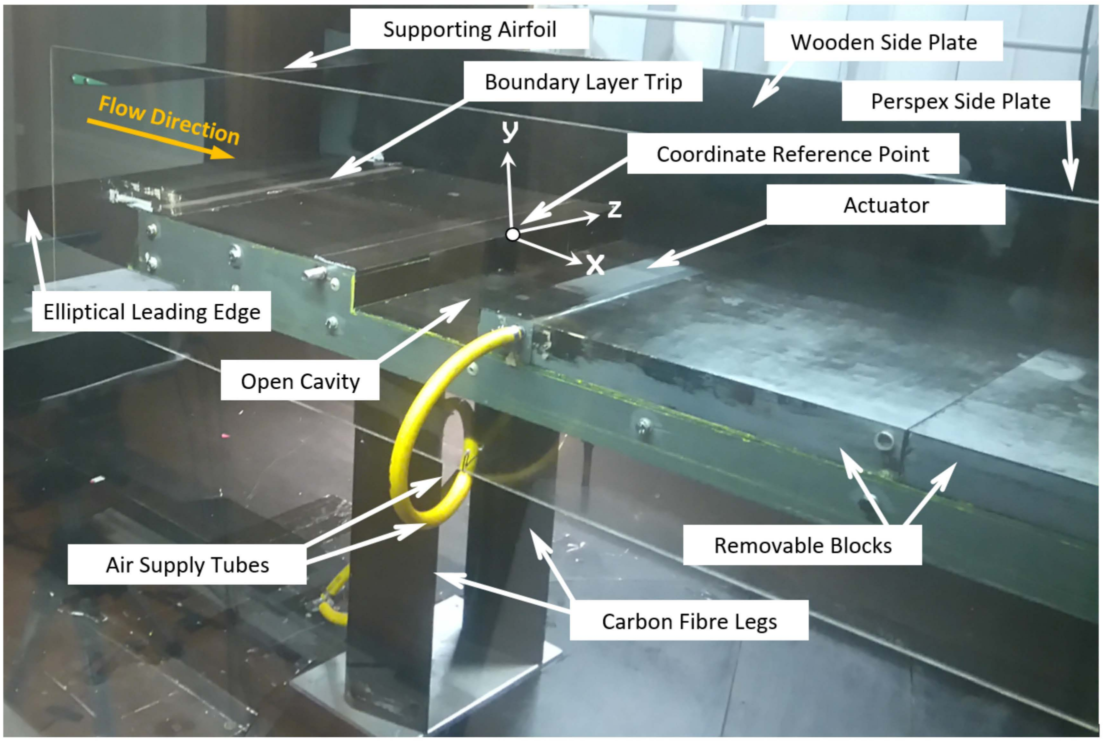

(b) Inside the test section (actuator at the cavity trailing edge)

Figure 3.2: Drawings and installations of the experimental model.

allow full development to a turbulent boundary layer, the cavity is located 1116 mm downstream of the model leading edge. Additionally, a trip, made of a sand-paper strip, was glued to the model's surface 600 mm upstream of the cavity leading edge. The experiments were performed on an open cavity with length L, depth D, and span W of 260 mm, 65 mm, and 800 mm, respectively. This yields a L/D ratio of 4 and a length to span ratio L/W of 0.325. The model has the capability to increase L/D ratio up to 20 by removing the removable blocks "A","B", and "C". However, the L/D ratio in the current study was fixed at 4 for all experimental cases. The reference point for the coordinate system is located at the cavity leading edge, as illustrated in Figure 3.2 (b). The x-axis corresponds to the streamwise direction, while the y-axis is in the vertical direction. The z-axis is along the span of the model.

Two actuator locations were examined in this study: (i) actuator positioned at the cavity leading edge, and (ii) actuator located at the cavity trailing edge. At the former location, the jet is parallel to the free stream, while at the latter location the jet direction is opposite to the direction of the free stream. After installing the actuator on the model, the actuator was masked by an adhesive tape to eliminate any gap between the actuator and the model. By swapping between the actuator and the removable block "A" (As shown in Figure 3.2 (a)), the actuator can be placed at the cavity leading or trailing edges. Both the actuator and the removable blocks were fastened to the model by bolts screwed from underneath the model.

To reduce the manufacturing cost and air supply requirements, the actuator covers only the central portion of the cavity span. As illustrated in Figures 3.3 (a) and (b), the actuator consists of an actuator housing, removable plastic insert, perforated tube, top plate, air chamber, a mesh, nozzle, knife edge, and jet outlet. The air-tight actuator housing, which was made of aluminium, is 65 mm high, 100 mm wide, and 420 mm long. The plastic inserts were made from plastic using a 3D printer, then surface-smoothed with sandpaper. As shown in figure 3.3 (d), two plastic insert configurations were used in this study: one with a flat jet outlet (sharp edge), and the other with a rounded jet outlet (coanda surface). The purpose of the sharp edge slot is to generate a tangential jet, while the purpose of the coanda slot is to produce a curved jet that adheres to the coanda surface and then bends towards the cavity floor. Swapping between the two configurations was done by removing the top plate and unscrewing two bolts from underneath the actuator. The top plate was mainly made of aluminium, but the 0.7 mm-thick knife edge was made of carbon fibre.

Three design elements were added to the actuator to ensure a uniform jet along the span of the slot, as illustrated in Figures 3.3 (b) and 3.3 (c): (i) perforated tube to provide a uniform air supply, (ii) a chamber where the air mixes, and (iii) a mesh downstream of the air chamber to increase the pressure in the chamber, which enhances the mixing. The mesh was made of brass wires and has an

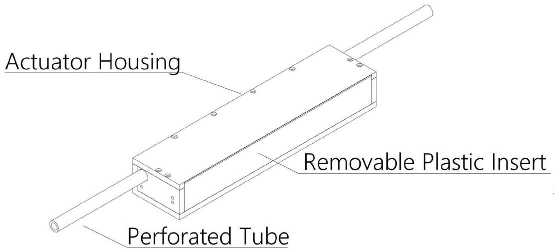

(a) Isometric projection

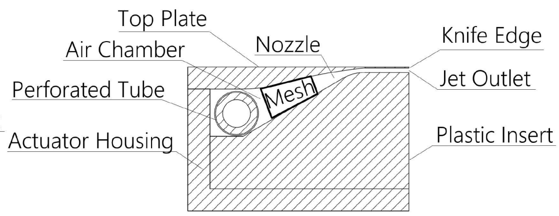

(b) Actuator components (side view)

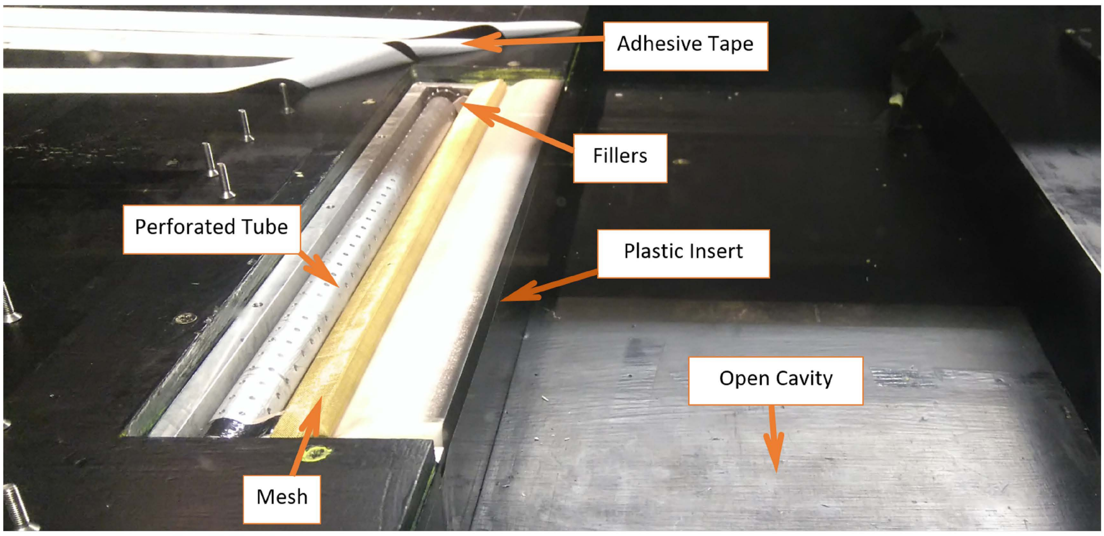

(c) Actuator at the cavity leading edge

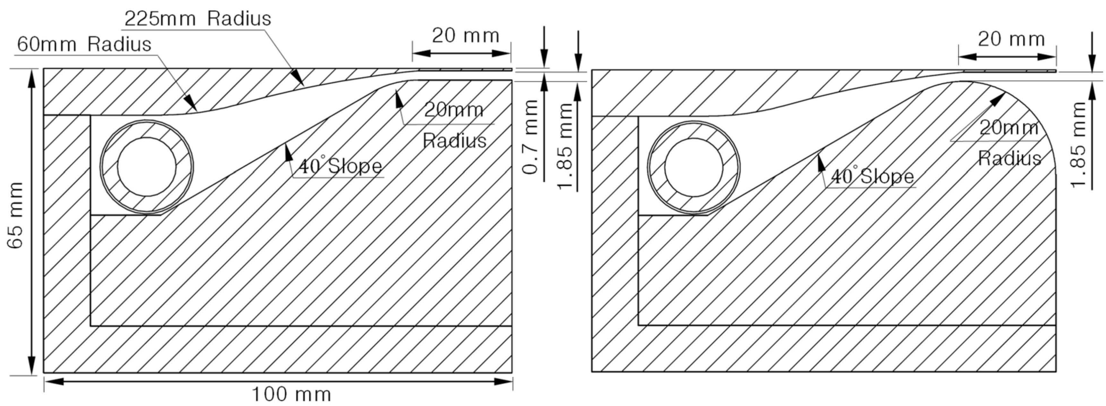

(d) Actuator dimensions for the sharp-edge and coanda slots (side view)

Figure 3.3: Drawings and installation of the actuator.

aperture of 0.263 mm, a wire diameter of 0.16 mm, and an open area of 39%. The mesh was folded into a wedge-shaped cage in order to fix its position with the help of the top plate, the plastic insert, and some fillers, as shown in Figures 3.3 (b) and (c). To avoid flow separation and reduce instability growth, the lower surface of the nozzle is sloped by 40°, while the upper surface has a large radius of 225 mm.

Figure 3.3 (d) shows the dimensions of the actuator with the two jet outlet configurations. In both configurations, the characteristic slot height h is approximately 1.85 mm. As shown in the figure, the characteristic slot height for the sharp edge case is the height of the slot, while the characteristic slot height for the coanda case is the height of the nozzle's throat. The radius of the coanda surface R is 20 mm, which yields a height to radius ratio h/R of 0.09. In his experiment on airfoil circulation control, Englar (1975) reported that within $0.01 < h/R < 0.05$, the jet was strongly attached to the coanda surface. The h/R ratio could be reduced further from 0.09 to 0.05 by either doubling the coanda radius or halving the slot height. However, these options were not implemented, due to the limitation of the model size for the first option and the limitation of the maximum flow rate in the second option. Moreover, the knife edge location in the current study differs from its usual location. In most of the coanda effect experiments, such as Englar (1975), the knife edge ends upstream of the coanda radius. In the present study, the knife edge is extended above the coanda radius, as evident from Figure 3.3 (d). This extension of the knife edge aims to avoid any gap at the cavity leading edge, that will perturb the cavity flow. More information about the coanda effect is provided in Appendix B.

The air supply system to the actuator is shown in Figure 3.4. A rotary-screw compressor (KAESER-SM 15) was used to pressurise the air into an air receiver. The air flow to the actuator was adjusted via a pressure regulator and monitored using a pressure transducer (Kulite XT-190M). The averaged pipe static pressure was used to ensure a repeatable air flow rate before each experimental case. The averaged pipe static pressure was calculated by averaging 1800 samples acquired at a sampling rate of 10 Hz. An air chamber was added to the connections to damp any oscillations in the air supply. Before reaching the actuator, the incoming air flow was split by a tube splitter into two equal parts. Each part was delivered to one side of the perforated tube via a flexible piping. The tubes were fastened tightly to the model's legs and the side plates to avoid tube vibration

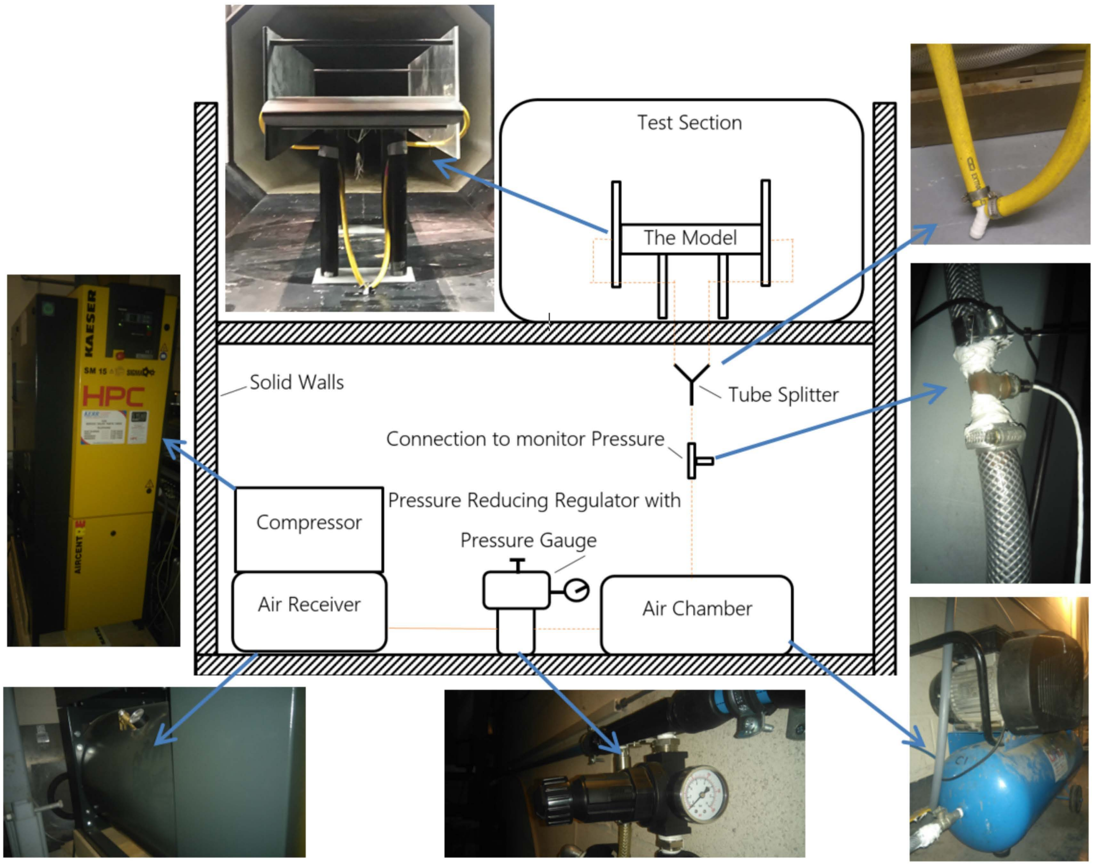

Figure 3.4: Air supply system to the actuator. Dashed lines represent flexible tubing, while solid lines represent solid piping.

during the wind-on conditions.

3 Test cases

Table 3.1 shows the test cases of the current study. The table contains three columns. The first left-hand side column shows the three actuator configurations. The second column shows the free stream velocities. The third column shows the momentum fluxes per unit width J and the Reynolds numbers Re_{bulk} of the jet. It is important to note that the sharp edge cases will be compared with the coanda cases at identical J values but at different Re_{bulk} values, as evident from the Table. This is because, according to Rajaratnam (1976), the behaviour of the planar jets can be determined from the jet momentum flux. The jet momentum flux per unit width J is:

Table 3.1: The test cases. LE denotes cavity leading edge, while TE denotes cavity trailing edge. The subscripts SE and C denote sharp edge and coanda cases, respectively.

Jet Cases	U_f $(m/s)/Re_\theta$	J $(kg/m.s^2)/Re_{bulk}$
Sharp Edge at LE	Wind tunnel Off	No-jet
Coanda at LE	11.1 ($Re_\theta = 1.28 \times 10^3$)	0.11 ($Re_{SE} \approx 290, Re_C \approx 525$)
Sharp Edge at TE	22.1 ($Re_\theta = 2.02 \times 10^3$)	0.44 ($Re_{SE} \approx 465, Re_C \approx 1095$)
	43.7 ($Re_\theta = 4.37 \times 10^3$)	0.96 ($Re_{SE} \approx 965, Re_C \approx 1410$)

Table 3.2: The calculated Reynolds numbers for the test cases.

U_f (m/s)	Re_θ	Re_d	Re_L
11.1	1.28×10^3	49.5×10^3	198×10^3
22.1	2.02×10^3	101×10^3	404×10^3
43.7	4.37×10^3	201×10^3	804×10^3

$$J = \int_b^{-b} \rho_j U_j^2 \, \mathrm{d}y \tag{3.1}$$

where b, ρ_j, and U_j denote the half jet width, jet density and jet streamwise velocity, respectively. The jet Reynolds number Re_{bulk} is based on the jet full width $2b$ and the jet bulk velocity at $x/h = 2.5$. The jet bulk velocity U_b is:

$$U_b = \frac{\int_b^{-b} \rho_j U_j \, \mathrm{d}y}{\int_b^{-b} \rho_j \, \mathrm{d}y} \tag{3.2}$$

For the test cases, Table 3.2 shows the Reynolds numbers based on the momentum thickness of the boundary layer at $x/D = -0.33$ (Re_θ), cavity depth (Re_d), and cavity length (Re_L). The table 3.3 shows the calculated momentum coefficient C_μ of each test case. The momentum coefficients for the sharp edge cases are identical to these for the coanda cases. The momentum coefficient is calculated by

$$C_\mu = \frac{J \times W}{0.5 \times \rho_f \times U_f^2 \times W \times L} \tag{3.3}$$

where J, W, L, ρ_f, and U_f denote the jet momentum flux per unit width, cavity span, cavity length, free stream density, and free stream velocity, respectively.

Table 3.3: The calculated momentum coefficients for test cases.

$U_f(m/s)$	$J\ (kg/m.s^2)$	C_μ (%)
11.1	0.11	0.57
11.1	0.44	2.31
11.1	0.96	5.04
22.1	0.11	0.14
22.1	0.44	0.58
22.1	0.96	1.26
43.7	0.11	0.036
43.7	0.44	0.14
43.7	0.96	0.32

4 Surface oil flow visualisation

Surface oil flow visualisation is a simple and effective flow diagnostic technique that is used to show the surface flow patterns. In this technique, a low-viscosity oil is mixed with finely powdered pigments. The mixture is then applied to the surface of interest as a thin layer. When the moving air passes over the layer, it displaces the oil and leaves the streaky pigments, which indicates the direction of the flow at the surface. The formed pigments patterns are then used to examine the surface flow behaviour (Merzkirch, 1987). The flow representation of this technique, according to Merzkirch (1987), depends on the wall shear stress and the pressure gradient along the direction of the oil displacement. If the wall shear stress is much larger than the pressure gradient, the oil flow will be a correct representation of the surface flow. On the other hand, if the pressure gradient is larger than the wall shear stress, the oil film will accumulate in a particular region, as a result, the surface flow will decelerate rapidly, imposing an early flow separation.

In the current experiments, the surface oil flow visualisation was used to examine the surface flow at the model leading edge and cavity floor. Paraffin oil was mixed with fluorescent pigments with a mixture ratio (Paraffin oil volume to fluorescent pigments volume) of 4 to 1. The mixture was then applied to the locations of interest as a thin layer by a paint roller. After predetermined running time at the targeted speed, the shape of the formed patterns became time-independent. The running time was 20 minutes for U_f of 11.1 and 22.1 m/s, and 10 minutes for U_f of 43.7 m/s. While the wind tunnel is running, the mixture is illuminated with a UV-LED light source and real-time images for the formed patterns were captured from the top of the test section by a Canon EOS 600D camera.

5 Hot-wire anemometry (HWA)

The Hot-wire anemometry (HWA) is based on the convective heat transfer between a heated sensing element (such as a wire or a film) and the surrounding moving fluid. The convected heat is then converted into a velocity signal with the help of a calibration curve. The HWA has different approaches. One of them works by fixing the temperature of the sensing element. This approach is called constant temperature anemometry (CTA)(Jørgensen, 2002). Due to the high-spatial resolution and the fast frequency response of this approach, the CTA was implemented in the current experiments to characterise the jet outside the cavity model. No attempt was made to characterise the jet inside the cavity model using CTA, as this requires a complicated linking arm between the sensing element and the traverse system inside the test section. Moreover, this linking arm will be highly intrusive to the cavity flow.

The CTA uses a well-designed electrical circuit to overcome the high thermal inertia of the sensing element and substantially increase frequency response. This electrical circuit consists of an electrical bridge (known as Wheatstone bridge) and feedback loop, as shown in Figure 3.5. The Wheatstone bridge contains four

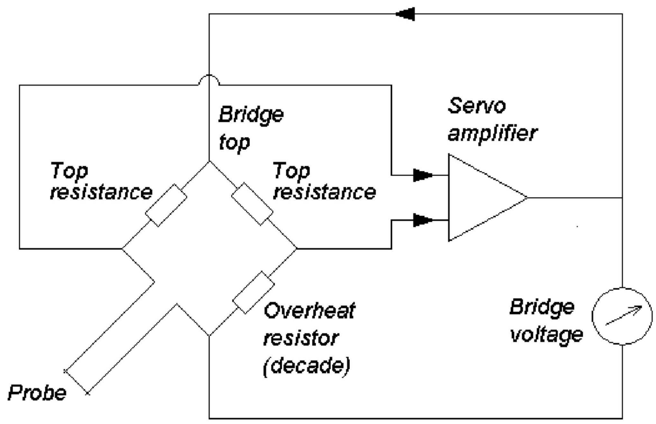

Figure 3.5: The working principles of the CTA (Jørgensen, 2002).

resistances, which are: (i) the resistance of the sensing element (the probe), (ii) the precision decade resistor, and (iii) two additional resistances. This electrical bridge is initially balanced (i.e. no voltage difference across it). However, as the moving fluid convects heat from the sensing element, the probe resistance changes. As a result, the electrical bridge becomes electrically imbalanced, and hence a voltage difference is generated across the bridge. This imbalanced bridge is corrected via the feedback loop, and the bridge is rebalanced. In this way, the probe resistance is always kept constant, and hence the voltage difference across the Wheatstone bridge becomes purely dependent on the cooling velocity of the surrounding fluid. The voltage output is then filtered, amplified, digitised, and converted into velocity signal (Jørgensen, 2002).

For the CTA measurements, a StreamLine-Pro system from Dantec Dynamics

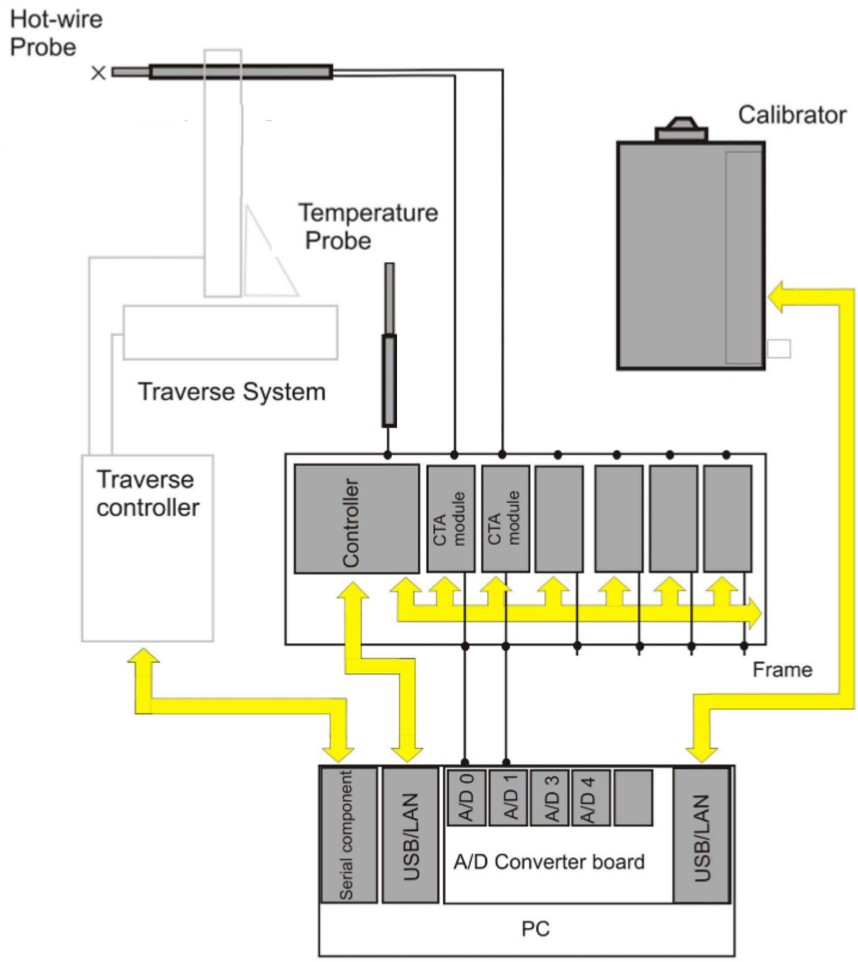

Figure 3.6: Layout of the CTA system (Dantec Dynamics, 2013).

was used. The system, as illustrated in Figure 3.6, consists of the hot-wire probe, the CTA frame, the analogue to digital converter (A/D), and a PC. The auxiliary components of the system include an automatic calibrator to calibrate the system, and a traverse unit with its own controller to traverse the hot-wire probe. An x-wire miniature probe (55P61) was aligned parallel to the jet flow with each probe wire forming an angle of 45° with respect to the jet direction in order to measure the cross components of velocity, as shown in Figures 3.7 (a) and 3.7 (c). Each probe wire was made of tungsten and has a diameter and a length of $5\mu m$ and 1.2 mm, respectively. The probe was inserted into a straight probe support, which connects each probe wire to an individual module in the CTA frame via

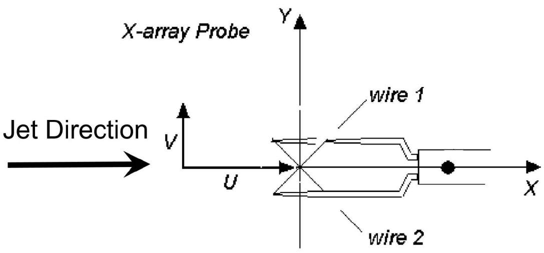

(a) Probe orientation during experiments

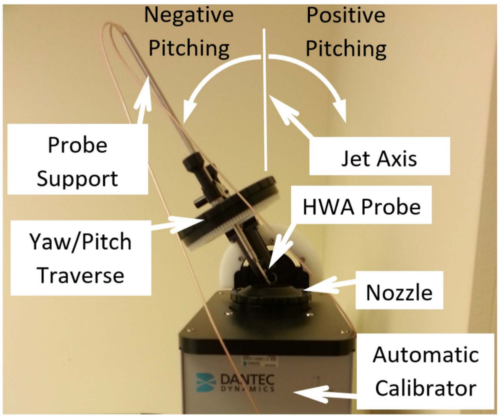

(b) Directional calibration

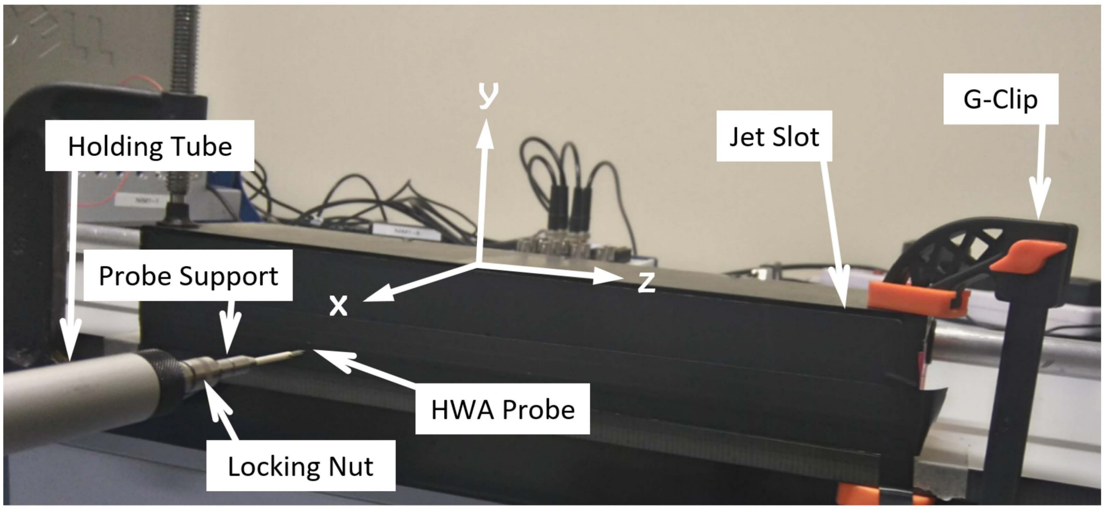

(c) Experimental set-up

Figure 3.7: Experimental set-up of the CTA.

a short-length BNC cable. The bandwidth of the CTA module is typically 100-250 kHz. Each module consists of 1:20 general-purpose Wheatstone bridge and a feedback loop to convert the convected heat into voltage. The module also contains a signal conditioner, which filters the voltage signal and then amplifies it to the desired level. The signal is then sent to a 16 bit A/D converter board through a connection box. The A/D converter board (National Instrument PCI-6143) has 8 individual channels with a simultaneous sampling rate of 250 KS/s per channel and an analogue input resolution of 16 bit. This yields an analogue input resolution of 0.067 mV for input voltages between 0 to 5 volts. The A/D converter digitises the voltage signal and saves it onto the PC, where it is converted into a velocity signal using the calibration curve.

The system was calibrated using a Streamline-Pro automatic calibrator. The automatic calibrator is equipped with a precision pressure regulator, a high resolution control valve, and a series of Laval nozzles to maintain a stable mass flow through the calibrator. The calibrator is also equipped with a heat exchanger, silencer, settling chamber, and an elliptical nozzle to ensure a flat-profile low-turbulence jet. The calibrator jet velocity is measured using a differential pressure transducer, an absolute pressure transducer, and two temperature transducers. To measure velocities less than 5 m/s, the calibrator is also equipped with a low-speed transducer, that consists of a reference nozzle and a differential pressure transducer (Dantec Dynamics, 2013).

Velocity calibration and directional calibration were performed for the system. The former calibration correlates the output voltage to the cross components of velocity, while the latter calibration is used to decompose the cross components of velocity into the U and V velocities. Velocity calibration was carried out between 0.5-40 m/s using the automatic calibrator. Fourth-order polynomial curve fitting was used to establish the voltage-velocity relationship. On the other hand, the directional calibration was carried out by pitching the probe at discrete points from +40 to -40 degrees around the axis of the calibrator's jet with the help of a pitch/yaw manipulator, as illustrated in Figure 3.7 (b). The individual directional sensitivity coefficients components determined from this process were used to decompose the calibrated velocities into the U and V velocities.

During the data acquisition, the influence of the ambient temperature variation on the velocity calibration was greatly minimised by automatically adjusting the overheat ratio. The overheat ratio is a function of the probe resistance at the operating temperature and the ambient temperature. The automatic overheat adjustment involves the following steps: (i) the velocity calibration is performed at a particular overheat ratio, (ii) before each data acquisition the probe resistance, which varies with the ambient temperature, is measured, (iii) the decade resistance is adjusted to maintain a constant overheat ratio. Keeping this ratio constant, greatly minimises the influence of the ambient temperature variation. Following this procedure yielded a highly repeatable CTA measurements during the experimental campaign.

The hot-wire probe was traversed using a two-axis traverse system, Figure 3.7 (c). The traverse system has a step resolution of less than 0.125 mm and traverses along the y- and z-coordinates. The probe was manually moved to the streamwise stations x/h of 2.5, 5, 10, 20, 40, and 80, where h is the characteristic slot height. The probe was aligned with respect to the actuator using a digital inclinometer for the pitch angle, L-square for the yaw angle, and a height gage for the roll angle.

During the experimental campaign, the overheat ratio of the Wheatstone bridge was fixed at 0.8, which is recommended by the manufacturer for air measurements. The data was acquired at a sampling rate of 75 kHz. According to Nyquist (2002), the minimum sampling frequency required to avoid the signal aliasing must be at least two times higher than the maximum signal frequency. The 75 kHz is sufficient to prevent any signal aliasing issue, which occurs when the sampling frequency is not sufficient to resolve the time variation of the signal. The data was acquired with a 30 kHz Butterworth-low pass filter in order to remove the electronic noise and to avoid the aliasing problem at high frequencies. For the time-averaged measurements, the acquisition time at each spatial point was determined by a convergence study at each streamwise station. Different traverse step sizes were used to resolve the jet streamwise velocity profile. The acquisition time for each spatial point and the traverse step size are shown in Table 3.4. For the velocity spectral analysis, 3 million samples were acquired.

6 Laser Doppler anemometry (LDA)

Laser Doppler anemometry (LDA) is a non-intrusive, high-spatial resolution flow diagnostic technique. For these reasons, LDA was used in the current study for the characterisations of the upstream boundary layer and the wind tunnel. As

Table 3.4: The acquisition time per each spatial point and the traverse step size for the hot-wire measurements.

x/h	Acquisition time (s)	traverse step size (mm)
2.5	2	0.125
5	2	0.125
10	2	0.25
20	2	0.5
40	8	1
80	32	4

illustrated in Figure 3.8, the technique works by seeding the flow with reflective particles and intersecting two coherent laser beams at the point of measurement. At the intersection point, bright and dark stripes (referred to as optical fringes) are formed. Consequently, when a seeding particle crosses the optical fringes, a burst of a scattered light is omitted. Each burst consists of a number of pulses that correspond to the number of the optical fringes. The scattered light is then received by a photo-detector and sent for signal processing. The magnitude of the flow velocity is calculated by dividing the known distance between the optical fringes (d) by the particle travel time between these fringes (t), which is obtained from the processed signal (Dantec Dynamics, 2016). The direction of the flow is determined by shifting the frequency of one of the emitted laser beams. This shift generates dynamic fringes, which move with respect to each other at the shifting frequency. The effective frequency of the processed signal becomes the sum of the particle frequency and the shifting frequency. When the particle travels opposite to the direction of the moving fringes, the effective frequency is higher than the shifting frequency, and vice versa for the particle traveling in the direction of the moving fringes (Dantec Dynamics, 2016).

A two-dimensional LDA system from Dantec Dynamics was used in the experiments. The layout of the LDA system is shown in Figure 3.9 (a). Two Argon-ion laser heads with a maximum laser power output of 1 Watt were used to emit 514.4 nm green-laser and 488 nm blue-laser beams. Each laser beam is split by a beam splitter into two beams. One of the beams is shifted by 40 MHz using a Bragg cell. All laser beams are sent through a multimode fiber to a 112 mm transmitting probe, where the four laser beams are emitted. In order to intersect the omitted laser beams at a single point (measurement volume), a beam expander with a focal length of 2000 mm and expansion ratio of 1.5 is fitted to the probe. The beam expander also reduces the measurement volumes and increases the power density. Two coincident measurement volumes (for blue and green lasers) were generated at the point of measurement. The size of each measurement volume was approximately 0.21 mm $\times$ 0.21 mm $\times$ 7.2 mm. The transmitting probe is equipped with backscattering-receiving optics, which receive the scattered light and send it to the colour separator, where the scattered light is separated into green and blue light. Next, the scattered light is filtered through the interface filter and sent to the photo-multipliers, where the scattered light is converted into an amplified electrical signal. Eventually, the signal reaches the processing unit (BSA 60) for further signal processing (Dantec Dynamics, 2016). BSA Flow software was used for real-time data monitoring, data processing, and post-processing.

For traversing the transmitting probe, a three-axis traverse system with a traversing step resolution of 0.1 mm was used, as shown in Figure 3.9 (b). The alignment of the LDA system with respect to x, y, and z axes was checked by moving the control volume along these axes. Olive oil particles were injected into the flow during the experiments to seed the flow.

The signal bursts were validated using a level validation ratio of more than 4, and a coincidence time window of 1×10^{-5} seconds. The former criterion looks for the ratio between the two highest peaks in the burst spectrum, while the coincidence-window criterion requires that both bursts from the blue and the green lasers are detected within a pre-determined time window. However,

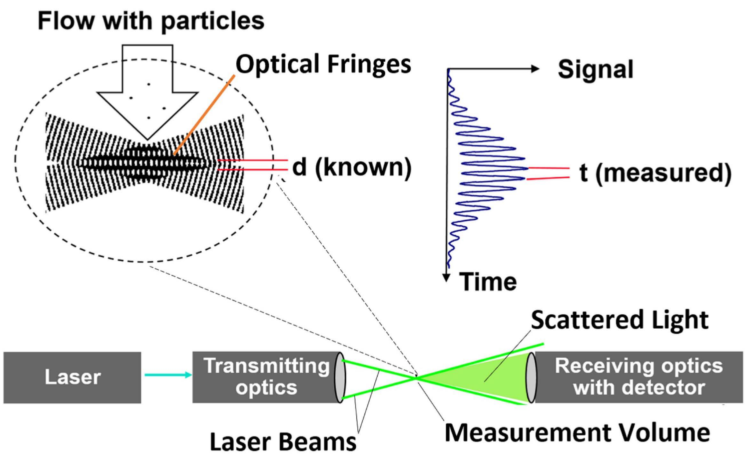

Figure 3.8: Working principles of LDA (reproduced from (Dantec Dynamics, 2016)).

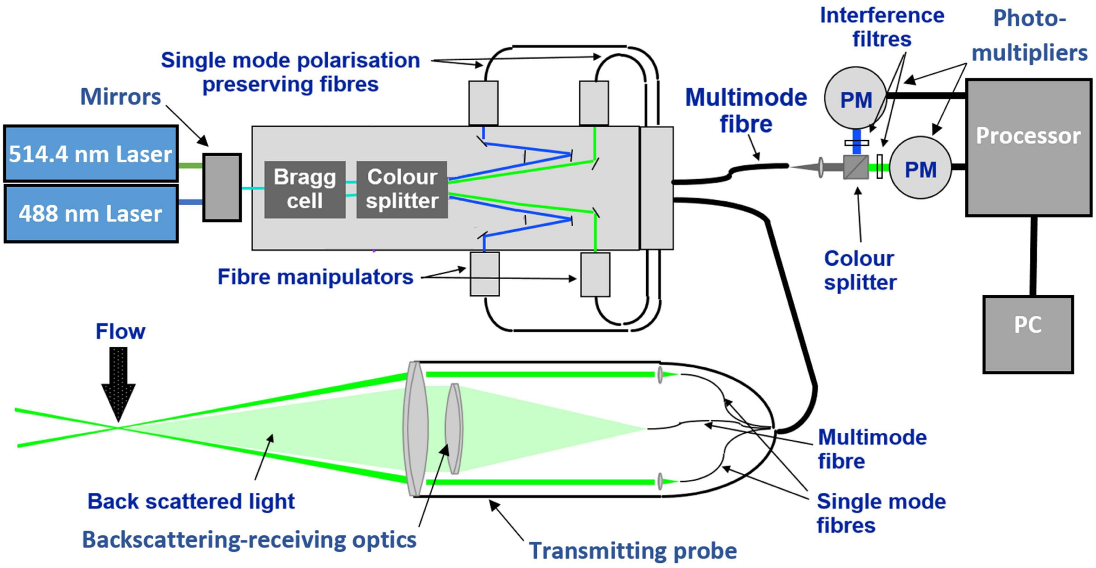

(a) Configuration of the LDA system (Dantec Dynamics (2016))

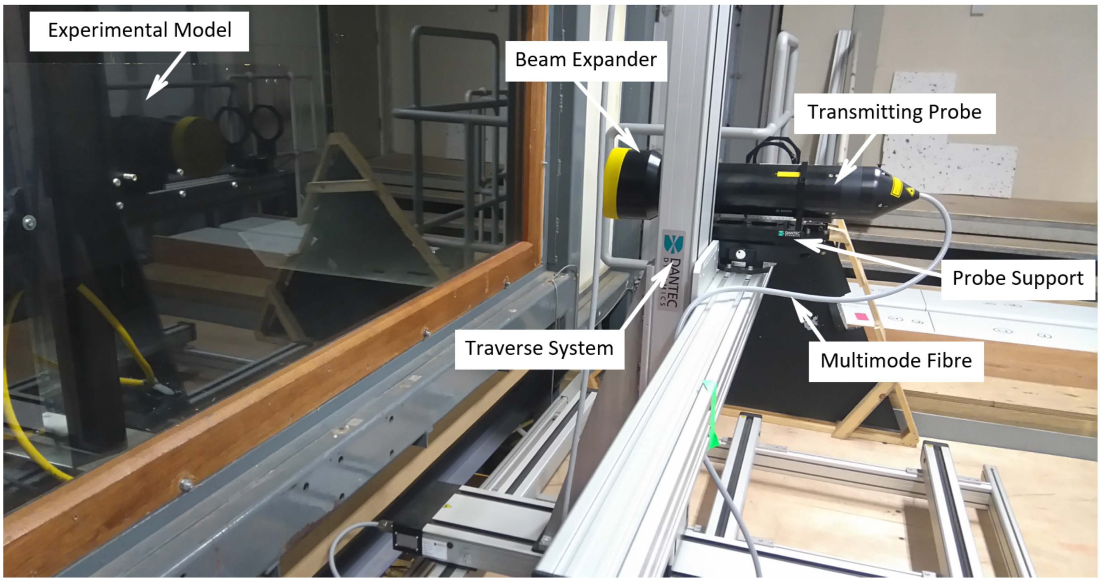

(b) Transmitting probe and traverse system

Figure 3.9: Set-up of the LDA system.

achieving the latter criterion in axially-dominated flow using a two-perpendicular measurement volumes is rather difficult. Therefore, it was decided to rotate the transmitting probe by 45°. This arrangement allowed the system to measure the cross components of the velocity which are then transformed into the normal components of velocity using the following equations,

$$U = 0.707U_1 + 0.707U_2 \tag{3.4}$$

$$V = 0.707U_1 - 0.707U_2 \tag{3.5}$$

where U_1 and U_2 are the cross components of the velocity. The transmitting probe was also tilted by 2.5° to prevent the model blocking the laser beams. This tilting angle has a negligible impact on Equations 3.4 and 3.5. The acquisition time for boundary layer characterisation was 40 seconds per each spatial point, which was sufficient to ensure converged velocity profiles. A traversing step resolution of 0.1 mm to 0.5 mm was used to resolve the profiles of the boundary layer. The step was then increased to 50 mm in the free stream region. For the wind tunnel characterisation, a volume of 1000 mm × 600 mm × 600 mm at the centre of the test section was scanned with traversing step resolutions of 200 mm × 300 mm × 300 mm for x, y, and z coordinates, respectively. 10,000 samples per each spatial point were acquired during the wind tunnel characterisation tests at a sampling rate of at least 1 kHz.

7 Particle image velocimetry (PIV)

The particle image velocimetry (PIV) technique has enabled the experimentalists all around the world to acquire velocity measurements over relatively large areas without interfering with the flow. Figure 3.10 (a) shows the basic working principles of the two-dimensional PIV. As shown in the figure, the air flow is seeded with reflective particles, while a pulsating laser sheet illuminates the measurement area. The pulsating laser sheet is formed by two laser pulses separated by a microsecond time delay (dt) and repeated at a specific repetition rate. These pulses are synchronised with the image frames of a high-spatial resolution camera that captures the raw images of the illuminated particles. The raw images are then stored in a computer where they are processed. Each double frame (at t and $t + dt$) is used to generate a single velocity field. This process relies on the high light contrast between the bright seeding particles and the dark image background, which allows the tracking of the particle displacements between the two frames. In order to spatially resolve the velocity distribution over the entire the measurement area, each frame is subdivided into smaller regions, called an interrogation area, as illustrated in Figure 3.10 (b). A correlation algorithm (such as cross-correlation) is applied at each interrogation area to determine the local displacement vector of the moving particles. The correlation peak is then

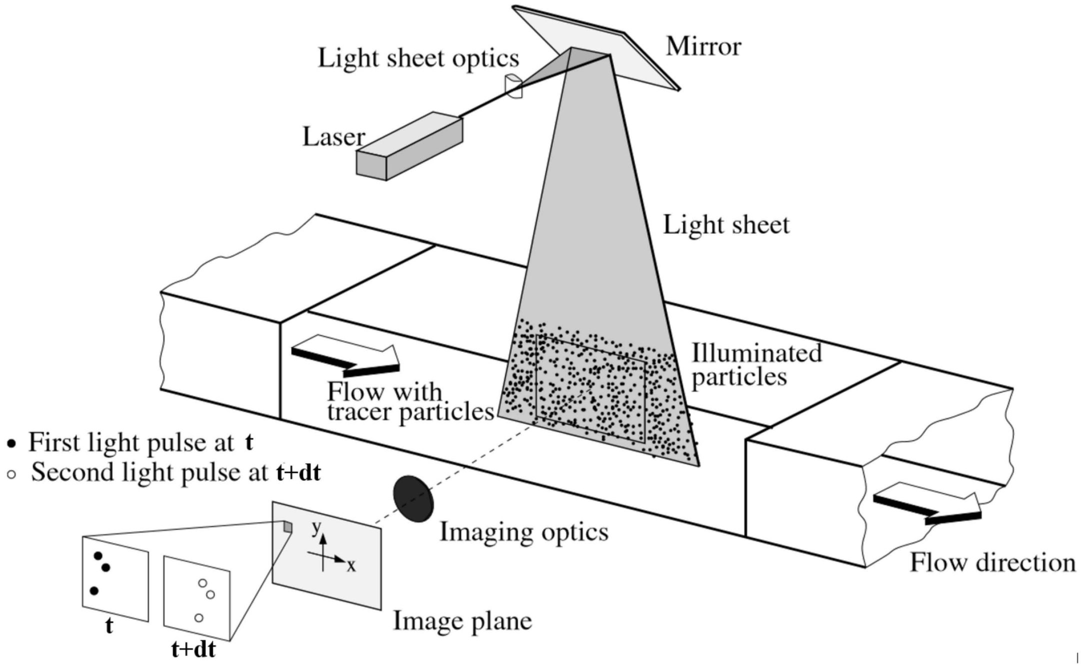

(a) Acquiring images

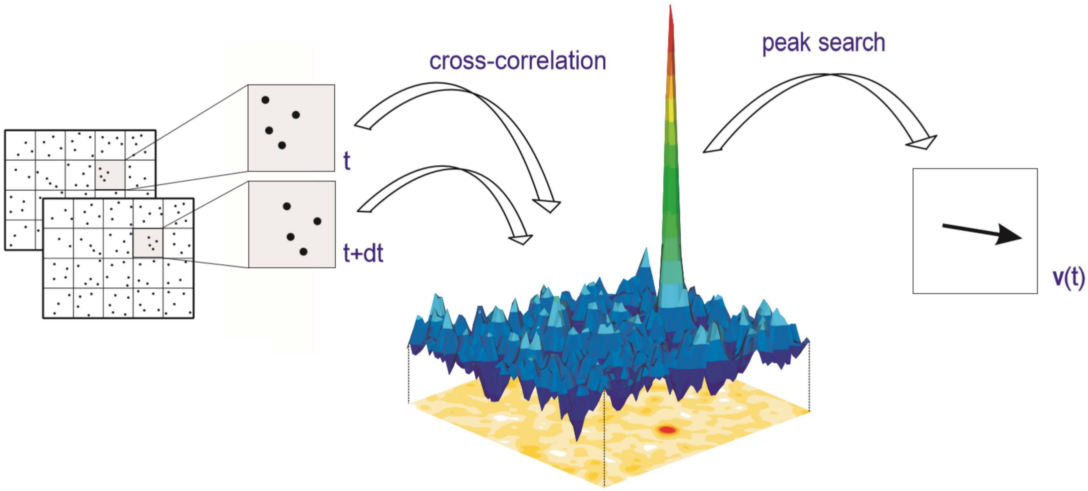

(b) Image processing

Figure 3.10: The working principles of the two-dimensional PIV (Lavision, 2017a).

detected and the displacement vector is calculated. This displacement vector is then converted into a velocity vector by taking into account the time delay between the two frames (dt) and the image-magnification factor obtained from a pre-calibration (Raffel et al., 2012).

A two-dimensional PIV system, which is shown in Figure 3.11, was used to study the cavity velocity field. The laser beam is emitted from Two-pulsed Litron

Nd:YAG laser head, that has a maximum repetition rate of 200 Hz and wavelength of 532 nm. The laser head consists of two laser resonators, each emitting a laser beam. The laser beam is guided via a number of fixed mirrors into the laser sheet optics at the top of the test section, where the beam is expanded by a cylindrical lens into a thin laser sheet. The laser sheet optics are mounted on a rail so that the optics can be moved along the streamwise direction. The raw images were captured using a Phantom V341 digital high-speed video camera, which was perpendicular to the laser sheet. The camera is fitted with 105 mm Sigma lens and equipped with CMOS sensor, which has a full resolution of 2560 x 1600 pixel at a frame rate of 10 to 800 frame/second. The camera also has a built-in memory to temperately store the acquired images, which are then transferred to a computer through an Ethernet cable. The camera was triggered and synchronised with the laser pulses by a high-speed controller (art. 1108075)

The image magnification factor was calculated daily using the scaling method. The scaling method was performed by positioning a calibration plate at the location of the laser sheet. Then, the plate dimension was scaled to the associated number of pixels in the image, which yields the image magnification factor.

Olive oil particles were generated from an Aerosol Generator PivPart160 atomiser and injected into the wind tunnel before acquiring the images. Olive oil particles are widely used in low-speed wind tunnels (Little et al., 2010, Kourta and Leclerc, 2013, Mathis et al., 2009). Additionally, the Stokes number of the

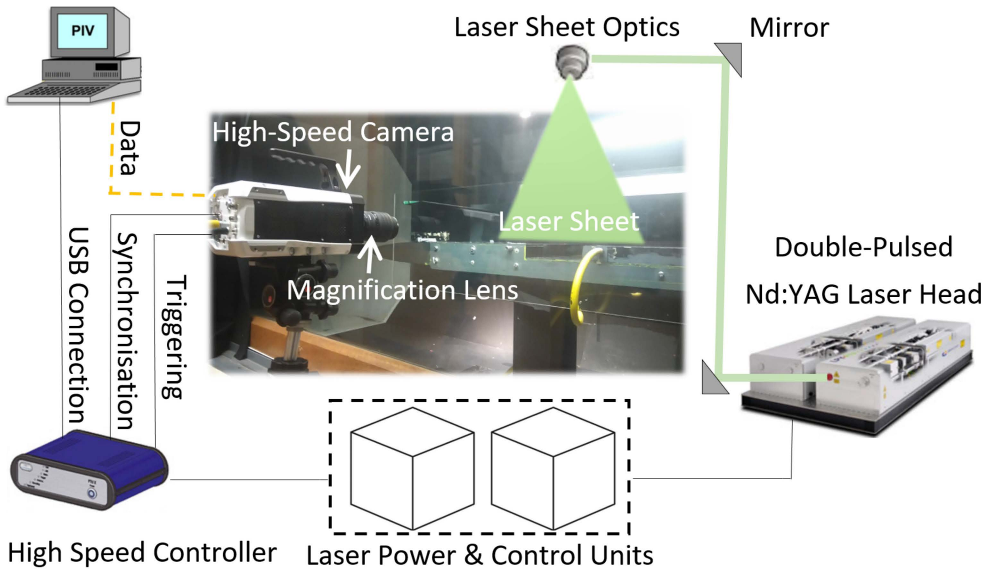

Figure 3.11: The experimental set-up for the two-dimensional PIV.

particles is much smaller than 0.1, hence the tracking error of the particles is negligible in the current study. The theory and calculation of the Stokes number is provided in Appendix D. Each interrogation area contained a considerable number of seeding particles $N \ggg 1$, which enhances the signal-to-noise ratio (Raffel et al., 2012). Before acquiring the images, sufficient time was allowed for the particles to distribute homogeneously in the wind tunnel.

The time step dt was calculated based on the one-quarter rule. According to this rule, the optimum detection probability of a valid correlation peak is achieved when the particle displacement is 25% of the interrogation window size (Keane

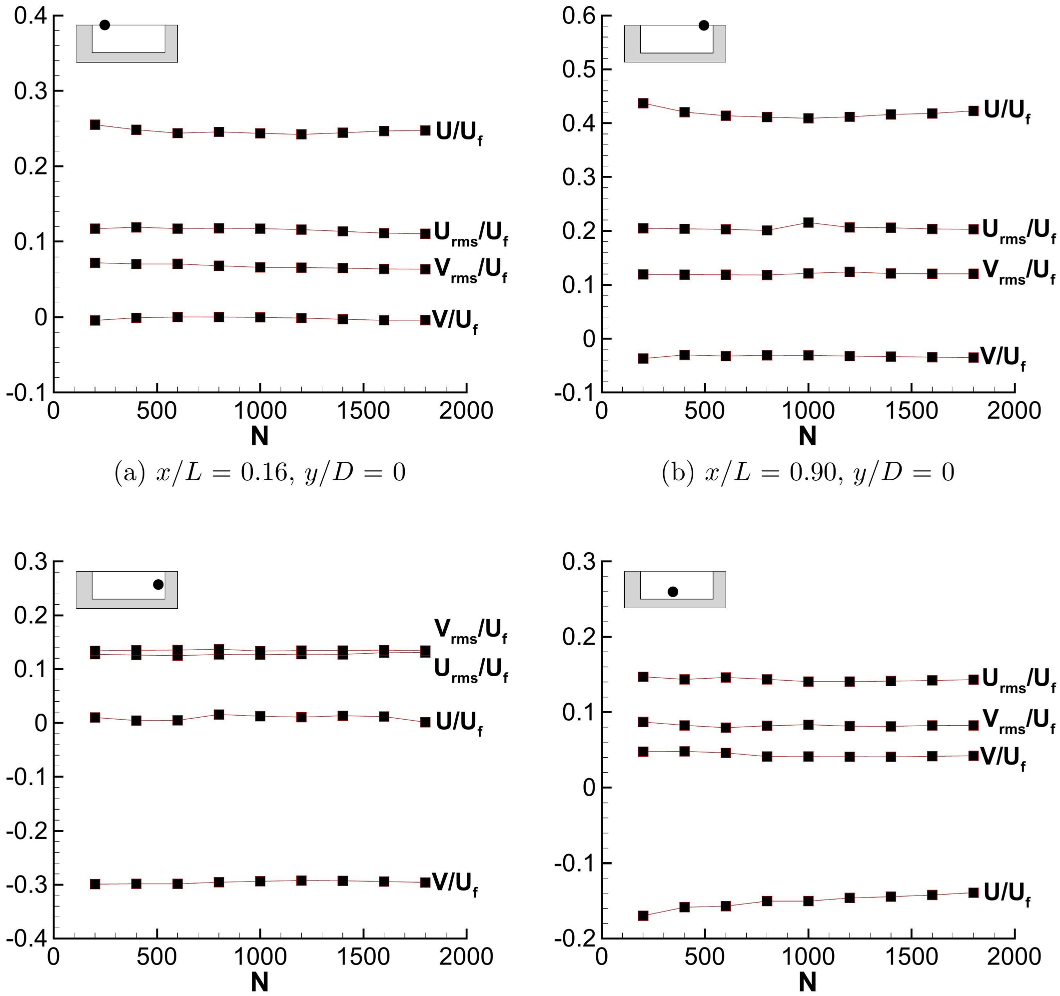

(a) x/L = 0.16, y/D = 0 (b) x/L = 0.90, y/D = 0

(c) x/L = 0.94, y/D = -0.46 (d) x/L = 0.43, y/D = -0.79

Figure 3.12: Convergence study at different locations in the cavity for baseline case (no-jet) at U_f of 43.7 m/s.

and Adrian, 1990). The raw images were acquired at a frequency of 200 Hz, which is the maximum repetition rate of the laser system. A convergence study for the PIV measurements is shown in Figure 3.12 and Appendix E. The convergence study includes the maximum and the minimum free stream velocity cases and examines the most unstable flow locations. It is concluded from the convergence study that 1800 images are sufficient to ensure a converged time-averaged flow field, and hence it was decided to acquire 1800 images for each test case.

Davis 8 software from Lavision was used to process and post-process the raw images. The images were processed using multi-pass cross-correlation with decreasing interrogation windows from 32×32 pixels (2 passes) to 16×16 pixels (3 passes). The size of the interrogation windows could not be reduced further due to the limited number of particles. However, the interrogation windows were overlapped by 50%, which increased the spatial resolution to approximately 1 mm×1 mm. Basic filters and post-processing tools, including correlation value limit, median filter, peak ratio, and smoothing filter were applied to the processed images. The criteria for these filters and post-processing tools are shown in Table 3.5. Correlation value limit determines the minimum value of a valid correlation peak. Median filter compares the centre vector with its 8 neighbouring vectors using the difference to average ratio (Df/Avg) and the standard deviation of the neighbouring vectors (σ_{neigh}). Peak ratio is the ratio between the highest correlation peak and the second highest correlation peak. The smoothing filter is averaging-based filter, that is used to suppress noise and tiny details (Lavision, 2017b).

Table 3.5: The criteria for the filters and the post-processing tools used for PIV.

Post-processing tool	Criteria	Iterations
Correlation value limit	Minimum is 0.2	1
Median filter	Remove if $Df/Avg > 2\sigma_{neigh}$ Reinsert if $Df/Avg < 5\sigma_{neigh}$	2
Peak ratio	Minimum is 1.3	1
Smoothing filter	3×3 pixels smoothing filter	3

8 Pressure measurements

The pressure measurements were utilised in the current study to carry out the spectral analysis of the wall pressure fluctuations. The set-up for the unsteady wall pressure measurements is shown in Figure 3.13. 16 pressure taps were drilled along the cavity floor. Only one tap at a time was used for measurements. The tap was connected to a differential pressure transducer via a hypodermic and a 1 mm diameter flexible tube of a total length of approximately 85 mm. The second port of the transducer is connected to the atmospheric pressure (outside the wind tunnel), which is the reference pressure. A 5-core cable connected the transducer to a DC voltage supply module (NI 9246), a data acquisition module (NI 9205) and a grounding connection. The two modules were inserted into a grounded compact chassis (NI cDAQ-9178), which is connected via a USB connection to a computer with LabVIEW program.

The differential pressure transducer (First Sensor-LBA series) is a bi-directional transducer with an operating pressure of 0 to 5 mbar and a full-scale output voltage of 0.5 to 4.5 volts. The total accuracy of the transducer is ± 1.5% of the sum of the pressure reading and the full-scale span. The pressure transducer has a maximum frequency response of 1 kHz, which is sufficient to resolve the frequencies up to the fifth oscillation mode (≈ 450 Hz) predicted by the Rossiter Equation. The fifth mode is the highest oscillation mode found in the literature for the cavity separated shear layer.

The DC voltage supply module (NI 9246) from National Instrument consists of single-ended channels. The channels have gain and offset errors of less than 1% and noise of 500 μV_{rms}. On the other hand, the absolute accuracy, random noise, and sensitivity of the data acquisition channels (NI 9205) are 0.174 mV, 0.01 mV_{rms}, and 0.004 mV, respectively for a nominal voltage range of ± 200 mV.

The unsteady pressure measurements were performed at x/L of 0.5 and 0.75. A total of 4.4 million samples were acquired for these measurements at a sampling rate of 20 kHz. Matlab software was used for data processing. In order to produce clear spectral maps, the pressure-time series was multiplied by a window function before executing Fast Fourier transform (FFT) algorithm (Schmid, 2012). 10,000 points FFT with Hanning window was used to compute the power specta.

Additionally, an absolute pressure transducer (Kulite XT-190M) was used to calculate the average static pressure of the air supply (see Figure 3.4). The transducer has an operating pressure of 0 to 0.7 bar (absolute) and a full-scale output voltage of 100 mV. The combined non-linearity, hysteresis, and repeatability of this transducer contributes to 0.1% of the full-scale output. 1800 samples were used to calculate the averaged pipe static pressure at a sampling rate of 10 Hz. Both pressure transducers (the differential and the absolute pressure transducers) were calibrated using Druck DPI 610 portable pneumatic calibrator, which has an accuracy of 0.025% (full span) and an operating range of -1 to 2 bar (gauge). The calibrator is equipped with a built-in vacuum pump, hand-pump, and a fine pressure adjuster and a release valve. The calibration set-up is shown in Figure 3.14. The electrical connections of the transducer were identical to Figure 3.13. Each transducer was calibrated across its operating pressure range. Twenty

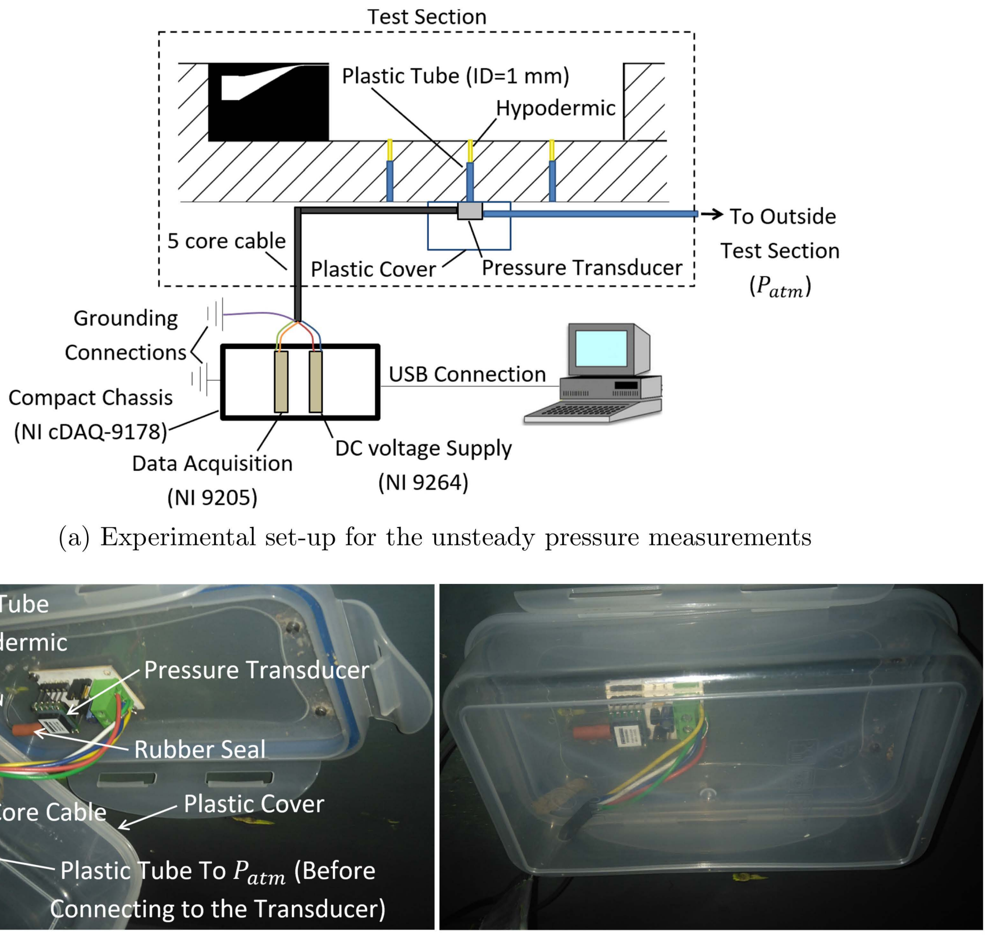

(a) Experimental set-up for the unsteady pressure measurements

(b) During installation

(c) After installation

Figure 3.13: Experimental set-up for the unsteady wall pressure measurements.

calibration points were used to generate the linear fit.

9 Errors and uncertainty

The measurements uncertainties of the flow diagnostic techniques must be estimated. The combined uncertainty for the time-averaged PIV measurements is 3.45%. The calculations of the combined uncertainty for PIV is shown in Appendix F. For HWA, the sources of errors include drift, calibration equipment, curve-fitting of the calibration curve, analogue to digital converter board resolution, probe positioning, temperature variations, ambient pressure variations and gas composition. The relative expanded uncertainty for HWA velocity sample at normal experimental conditions is approximately 2.47%. The majority of this error is attributed to the calibration equipment and the curve fitting errors. The calculation of the HWA relative expanded uncertainty is shown in Appendix G.

For the LDA measurements, the relative sampling uncertainty ε for the time-averaged velocity U_{mean} is below 1%. The uncertainty σ_{est} and the relative uncertainty ε were estimated by

$$\sigma_{est} = \frac{U_{rms}}{\sqrt{N}} \tag{3.6}$$

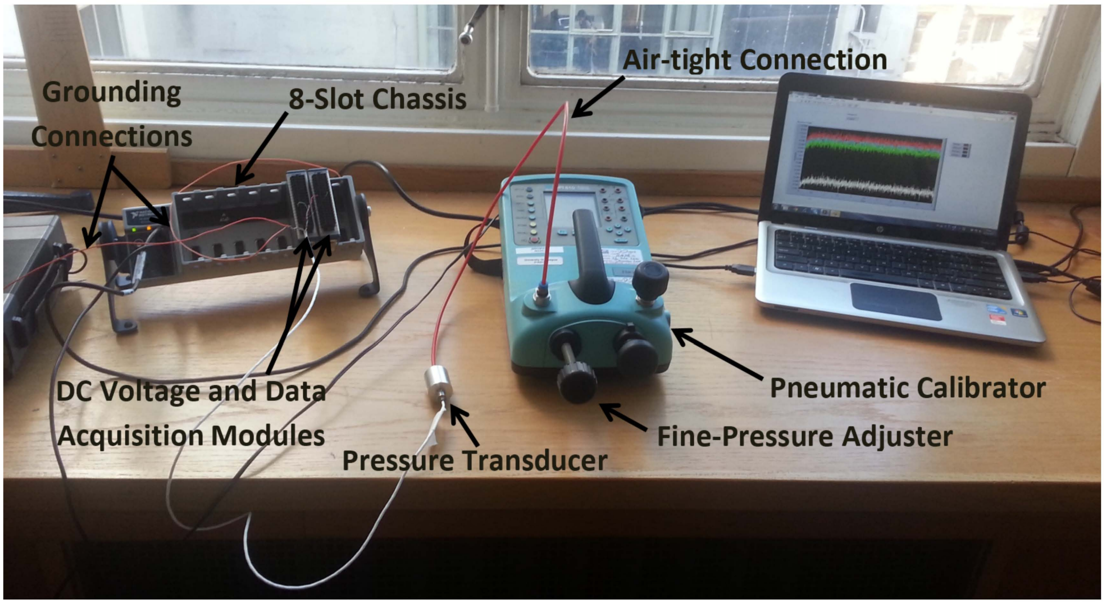

Figure 3.14: Calibration set-up for the pressure transducers.

$$\varepsilon = \frac{\sigma_{est}}{U_{mean}} = \frac{U_{rms}}{U_{mean}\sqrt{N}} \tag{3.7}$$

where U_{rms} and N are the root mean square velocity and number of acquired samples (Dantec Dynamics, 2016).

Chapter 4

Characterisation of Free Stream, Boundary Layer, and Jets

This chapter examines the characteristics of the free stream flow, upstream boundary layer, and blowing jets at different Reynolds numbers. The outcome of this chapter will be used to non-dimensionalise important parameters in the following chapters.

1 Free stream characteristics

Before conducting any experimental test in wind tunnels, it is essential to quantify the free stream velocity and the turbulence intensity of the free stream. The free stream velocity is characterised by laser Doppler anemometry and averaged over different spatial points within the free stream region. Table 4.1 compares the free stream velocities for the empty tunnel (without the experimental model) and the tunnel with the experimental model. As shown in the table, the free stream velocities for the tunnel with the experimental model U_f is higher than those for the empty tunnel case U_e by 3.65% to 3.8%. This increase is because the model blocks approximately 5.9% of the flow area of the test section. In this study, the free stream velocities of the tunnel with the experimental model will be used to non-dimensionalise velocity, vorticity, and turbulence quantities. The turbulence intensity of the free stream is also evaluated using laser Doppler anemometry and averaged over different spatial points. The time-averaged turbulence intensities $u^{'}/U$ are 1.82%, 1.95%, and 2.29% for free stream velocities of 11.1, 22.1, and 43.7 m/s, respectively.

Table 4.1: Time-averaged free stream velocities for empty and occupied wind tunnel. U_e: free stream velocity for the empty tunnel, U_f: free stream velocity for the tunnel with the experimental model.

U_e (m/s)	U_f (m/s)	$\{U_f - U_e\}/U_e$
10.69	11.1	3.8%
21.32	22.1	3.65%
-	43.7	-

Figure 4.1 shows the distribution of the dimensionless time-averaged streamwise velocity above the model's surface ($y/D = 0$) for $U_f = 11.1$ m/s and 43.7 m/s. As evident from the figure, the streamwise velocity within the free stream region is uniform for both cases, except the velocity defect region ($y/D = 4$) at $U_f = 11.1$ m/s. This defect is due to the wake of the supporting airfoil. This wake region is far from the separated shear layer of the open cavity, and hence does not affect it. As the free stream velocity increases to $U_f = 43.5$ m/s, the velocity defect diminishes, due to a rapid mixing between the wake and the free stream.

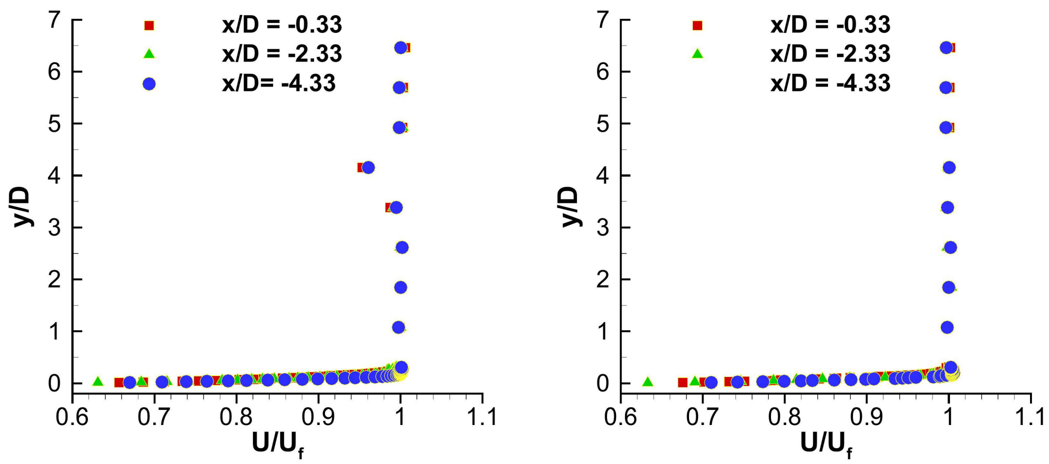

(a) $U_f = 11.1$ m/s (b) $U_f = 43.7$ m/s

Figure 4.1: Streamwise velocity profiles at different streamwise locations. The position $y/D = 0$ denotes the model surface.

2 Flow around the model leading edge

The formation of a separation bubble at the leading edge of the model table can significantly influence the measurements at the open cavity. Thus, it is essential to ensure that the model leading edge is free from separation. At the beginning of the experimental campaign, the model leading edge was semicircular with a radius of 65 mm. However, the surface oil flow visualisations showed a formation of separation bubble downstream of the leading edge, as evident from Figure 4.2. The flow separates because of the abrupt turning angle at the leading edge. Due to the backflow of the separation bubble, a portion of the oil is displaced upstream and accumulates at the model leading edge.

The semicircular leading edge was then replaced with an elliptical leading edge (length to thickness ratio = 4). The reasons behind this selection were explained in Chapter 3. Figure 4.3 shows the surface oil flow patterns for the elliptical leading edge at different Reynolds numbers based on the thickness of the model leading edge. The oil at $Re_t \approx 96 \times 10^3$ accumulates at certain locations on the elliptical leading edge (Figure 4.3 (a)). The oil accumulation at this Reynolds number is not due to separation, but because the wall shear stress imposed by the airflow is too weak to displace the oil layer. As the Reynolds number increases further (Figures 4.3 (a) and 4.3 (b)), no flow separation is noticed. However, regions of side interaction are observed, due to the interaction between the incoming airflow and the side plates. These interaction regions are far from the model's mid-span, where measurement is taken. Therefore, this interaction is not affecting the current results.

3 Characteristics of the referenced boundary layer

The Reynolds number of the cavity separated shear layer in the current study is calculated based on the referenced boundary layer. The position of the referenced boundary layer is at x/D = -0.33, which is slightly upstream of the separation point of the cavity separated shear layer. The boundary layer was not characterised at the separation point, as the characterising equations of the turbulent boundary layer are not applicable there (Schetz, 1984). More information about the main characterising equations of the turbulent boundary layer is found in Appendix A. To determine the state of the referenced boundary layer,

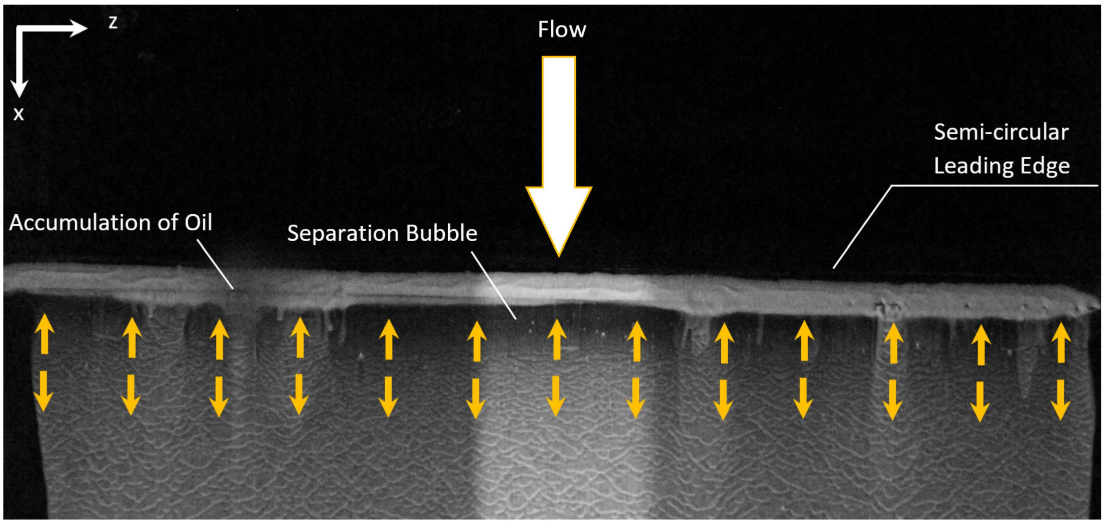

Figure 4.2: Formation of a separation bubble downstream of the semicircular leading edge ($Re_t \approx 190 \times 10^3$).

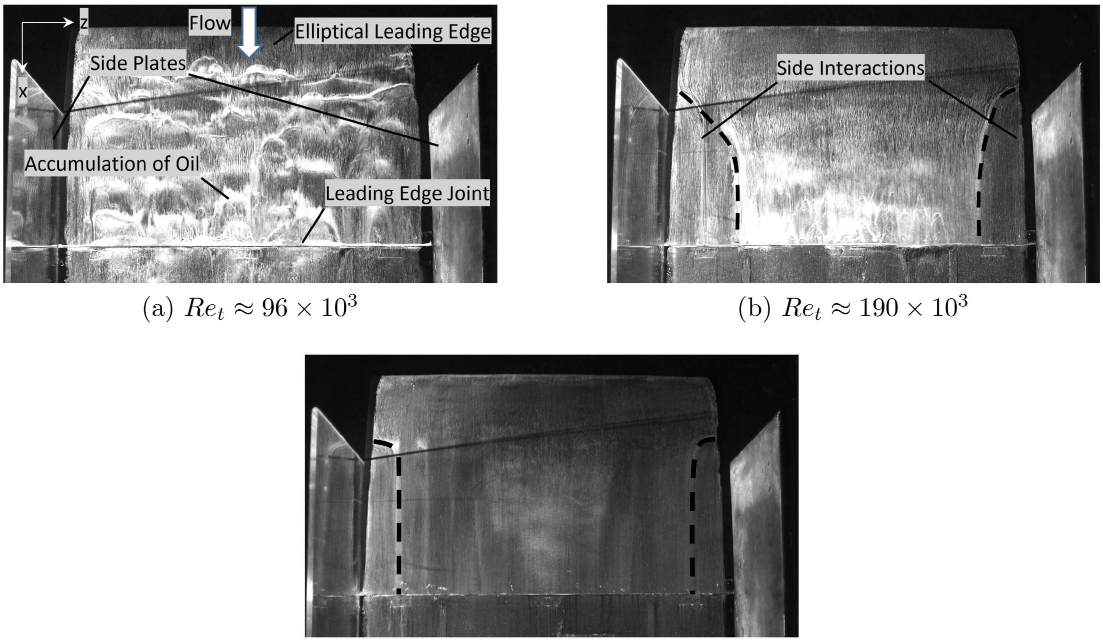

(a) $Re_t \approx 96 \times 10^3$

(b) $Re_t \approx 190 \times 10^3$

(c) $Re_t \approx 377 \times 10^3$

Figure 4.3: Patterns of the surface oil flow visualisations at the elliptical leading edge for different Reynolds numbers.

the boundary layer profile is compared with the universal law of the wall. This law is applicable for all streamwise pressure gradients, and hence it is widely used to characterise the turbulent boundary layers (Schetz, 1984). Figure 4.4 compares between the experimental data and the universal law of the wall at

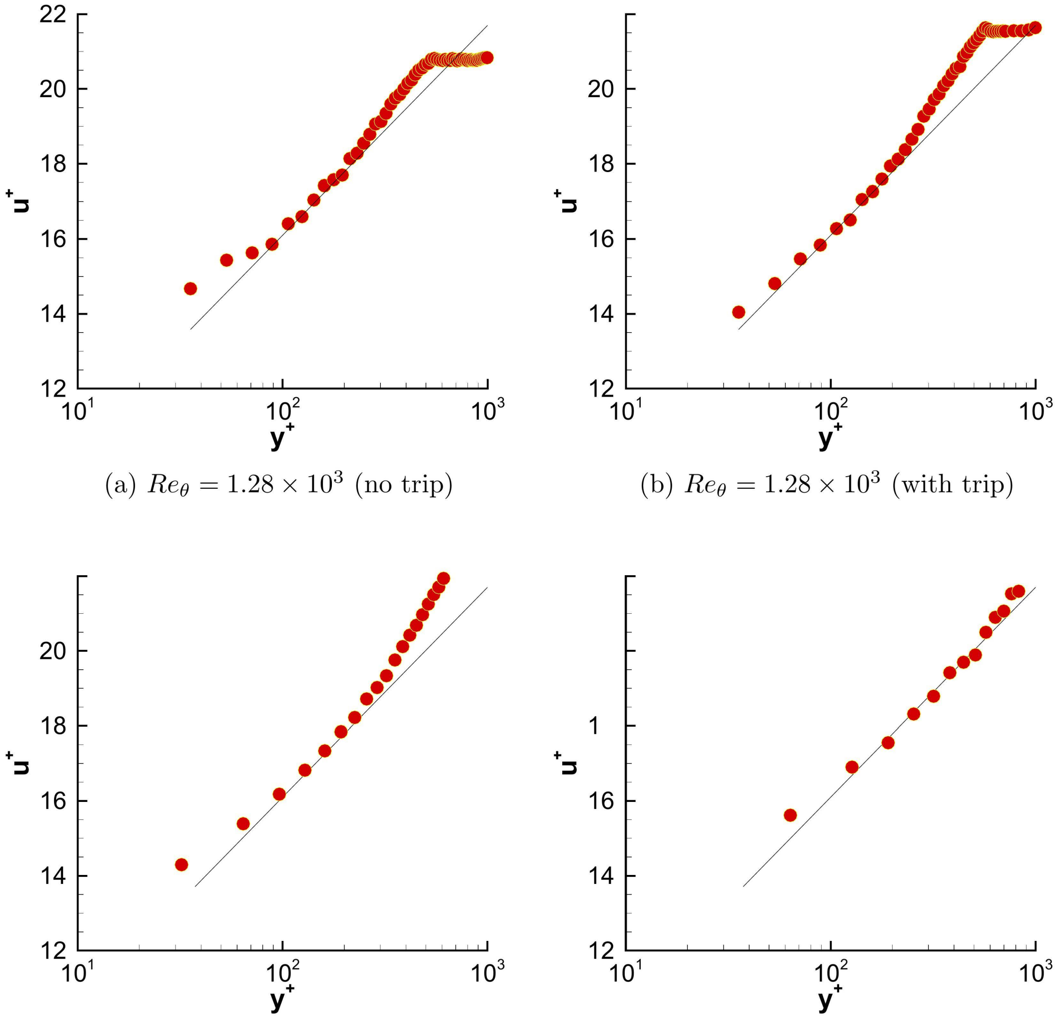

(a) $Re_\theta = 1.28 \times 10^3$ (no trip)

(b) $Re_\theta = 1.28 \times 10^3$ (with trip)

(c) $Re_\theta = 2.02 \times 10^3$ (with trip)

(d) $Re_\theta = 4.37 \times 10^3$ (with trip)

Figure 4.4: Dimensionless boundary layer velocity profiles at x/D = -0.33 for different Reynolds numbers. [circle: experimental data, solid line: $u^+ = 5.6\ log(y^+) + 4.9$].

$1.28 \times 10^3 \leq Re_\theta \leq 4.37 \times 10^3$, where Re_θ is the Reynolds numbers based on the momentum thickness of the boundary layer. The defination of the momentum thickness is provided in Appendix A. As suggested by Clauser (1956), the empirical constants A and C for the theoretical universal law (Equation A.7) are 5.6 and 4.9, respectively. To calculate the non-dimensional parameters $y^+ = y\ u_\tau/\upsilon$ and $u^+ = U/u_\tau$, the wall friction velocity u_τ is calculated using the Clauser chart method (Wei et al., 2005) rather than the direct method. This is because the direct method requires measurements of the velocity gradient very close to the wall, which are difficult to obtain. In the Clauser chart method, the wall friction velocity is calculated by fitting the experimental data with the universal law of the wall.

Using the Clauser chart method, the estimated wall friction velocities are 0.515 m/s, 1.23 m/s, and 1.75 m/s for $Re_\theta = 1.28 \times 10^3$, 2.02×10^3, and 4.37×10^3, respectively. Figures 4.4 (a) and 4.4 (b) compares the universal law of the wall at $Re_\theta = 1.28 \times 10^3$ for two cases: without a trip and with a trip upstream of the reference boundary layer. For both cases, the experimental data points coincide with the theoretical universal law of the wall within $100 \leq y^+ \leq 200$. This proves that the boundary layer for both cases is fully turbulent. However, it was decided to keep the trip on the model to ensure that the upstream boundary layer is always fully turbulent. At Re_θ of 2.02×10^3 and 4.37×10^3, the experimental data points coincide with the theoretical universal law of the wall within $100 \leq y^+ \leq 200$ and $200 \leq y^+ \leq 500$, respectively, as shown in Figures 4.4 (c) and 4.4 (d). This means that within the experimental range of the Reynolds numbers, the boundary layer remains fully turbulent. The reference boundary layer parameters for each free stream condition are provided in Table 4.2.

Table 4.2: Boundary layer parameters at $x/D = -0.33$ for each free stream condition.

U_f (m/s)	δ (mm)	δ^* (mm)	θ (mm)	Re_x (10^6)	Re_δ (10^3)	Re_{δ^*} (10^3)	Re_θ (10^3)
11.1	13.9	2.24	1.69	0.83	10.6	1.71	1.28
22.1	12.0	1.60	1.30	1.70	18.7	2.49	2.02
43.7	13.0	1.75	1.41	3.38	40.4	5.43	4.37

4 Streamwise and spanwise development of the boundary layer

The adhesive tape, which was used to mask the actuator, introduces a small step on the surface at $x/D \approx 1.9$. This step has a height of less than 1 mm. To check the impact of this step on the boundary layer, the boundary layer profile was investigated at three streamwise stations: x/D = -0.33, -2.33, and -4.33, as illustrated in Figure 4.5. The profiles are compared with the profile of zero-pressure gradient, turbulent boundary layer obtained from the experiments of Tomkins and Adrian (2003). The similarity between the present data and the data of Tomkins and Adrian (2003) indicates that the boundary layer at these streamwise locations is fully turbulent and hence the laminar to turbulent boundary layer transition takes place upstream of the small step.

To check the uniformity of the boundary layer along the span of the model, boundary layer measurements were taken at three spanwise stations: $z/D =$ -1, 0, and 1, as shown in Figure 4.6. As evident in the Figure 4.6 (a), the boundary layer

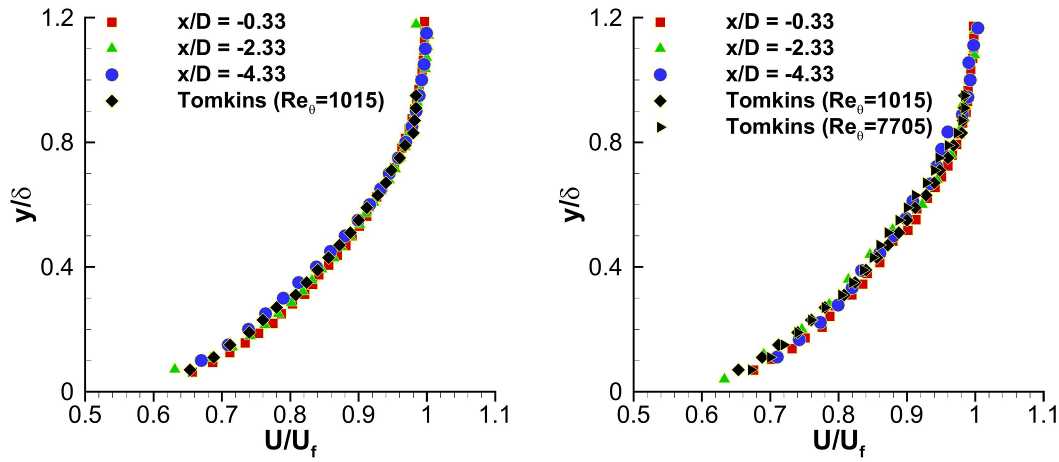

(a) $Re_\theta = 1.28 \times 10^3$ at $x/D =$ -0.33 (b) $Re_\theta = 4.37 \times 10^3$ at $x/D =$ -0.33

Figure 4.5: Dimensionless boundary layer velocity profiles at different streamwise stations.

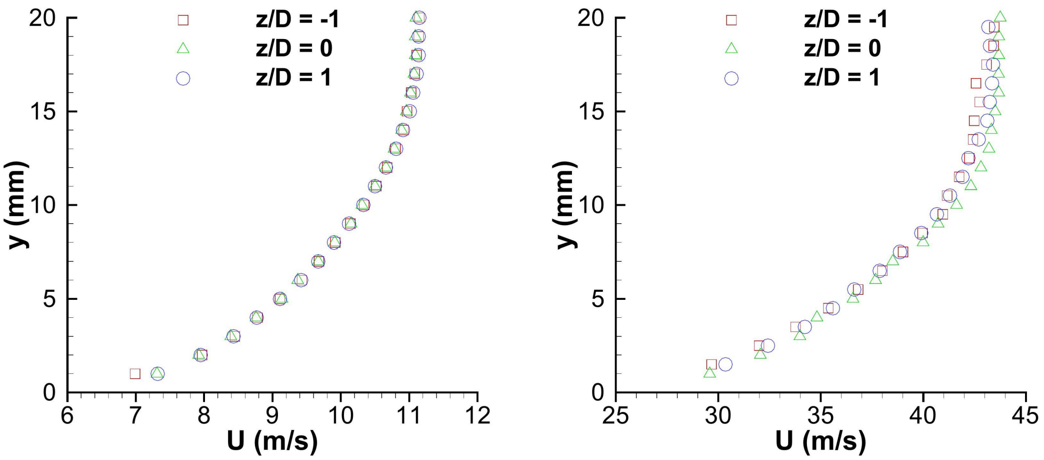

(a) $Re_\theta = 1.28 \times 10^3$ (b) $Re_\theta = 4.37 \times 10^3$

Figure 4.6: Boundary layer velocity profiles for different spanwise stations ($x/D =$ -0.33).

profiles are uniform at the lowest tested Reynolds number ($Re_\theta = 1.28 \times 10^3$). At the highest tested Reynolds number ($Re_\theta = 4.37 \times 10^3$) the profiles are slightly less uniform (Figure 4.6 (b)). Thus, the upstream boundary at the mid-span region is quite uniform along the z-axis, and hence it is assumed that the cavity separated shear layer at this region is uniform along this axis.

5 Characteristics of the blowing jets

The jet characteristics were examined in two stages: (i) HWA measurements for the jet outside the cavity model, and (ii) PIV measurements for the jet inside the cavity model. The first stage aims at achieving high spatial resolution measurements, while the second stage examines the global behaviour of the jets. HWA measurements were not carried out in the second stage due to the requirement of a complicated and flow-intrusive linking arm between the sensing element and the traverse system. The basics of the planar jets are provided in Appendix B.

5.1 Actuator outside the cavity model

The HWA experimental campaign started by optimising the spanwise uniformity of the jet using a mesh and a honeycomb. Figures 4.7(a), 4.7(b) and 4.7(c) show the jet time averaged streamwise velocity distribution along the z-axis at ($x/h = 10$, $y/h = 0$). The jet velocity is normalised by the mid-span velocity $U_{z=0}$. The velocity distribution of the initial set-up (without a mesh, nor a honeycomb) is not uniform, as evident from Figure 4.7(a). Adding a mesh and a honeycomb upstream of the nozzle (Figure 4.7(b)) yields a sharp velocity-gradient between the mid-span region of the jet and the sides of the jet. This is attributed to the impact of the honeycomb, which works as a flow straightener, and hence reduces the turbulence mixing in the air chamber. Removing the honeycomb and keeping the mesh (Figure 4.7(c)) greatly improves the velocity uniformity along the z-axis. This is because the mesh increases the back pressure inside the air chamber, and hence fluid mixing is enhanced there. Within the mid-span region ($-40 \geq z/h \geq 40$), the velocity variation is approximately 5%. The jet time-averaged streamwise velocity profiles at different stations along the z-axis for the case with mesh only is illustrated in Figure 4.7(d). The profiles confirm the uniformity of the jet. Therefore, the experimental campaign was continued with only the mesh upstream of the nozzle.

Averaging 600 PIV raw images yields regions of low-particle density, which represent the path of the unseeded jet. These images, as shown in Figure 4.8, highlight two important differences between the sharp edge and coanda jets. Firstly, at $J = 0.11\, kg/m.s^2$ (Figures 4.8 (a) and 4.8 (b)) the sharp edge jet exhibits a point of a sudden expansion at $x/h \approx 7$, while the coanda case does not show this transitional point. This point of sudden expansion was reported by Munro and Ahuja (2003) for a high aspect-ratio jet ($Re = 7000$). The author attributed this behaviour to the mixing transition from laminar to turbulent. The turbulent mixing generates a significantly higher jet growth rate than the laminar mixing,

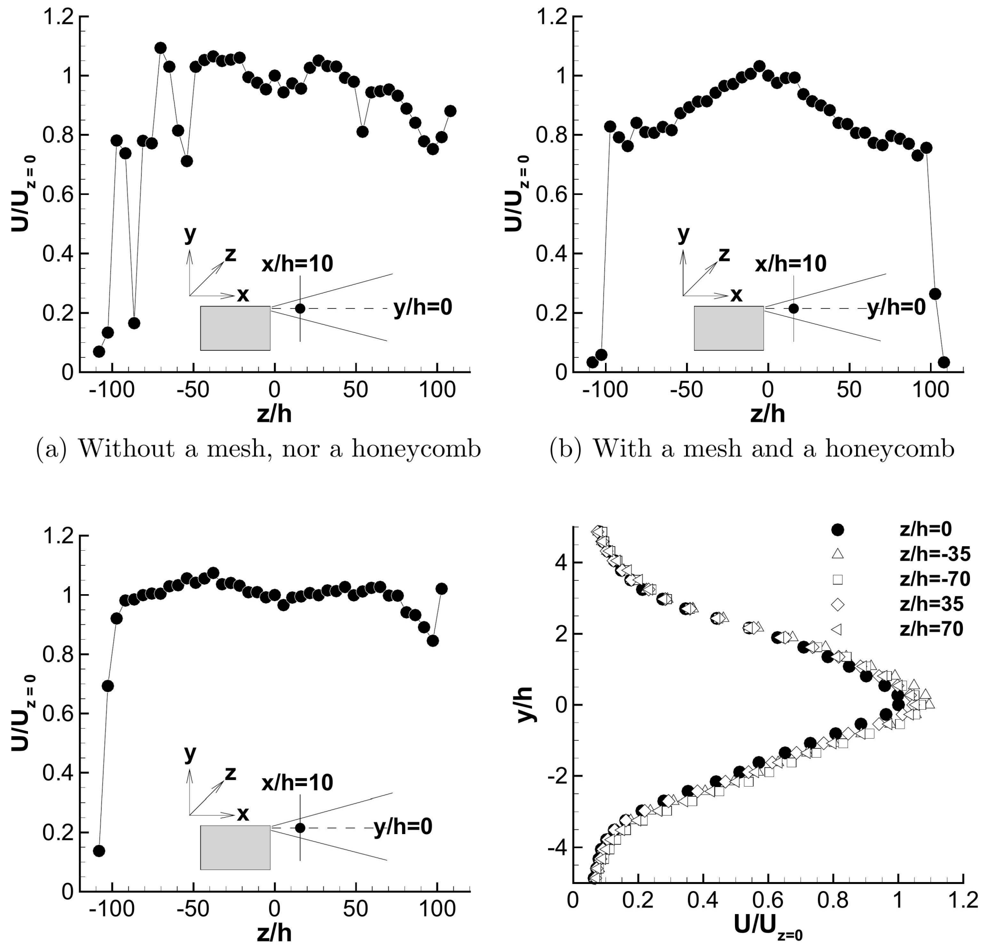

(a) Without a mesh, nor a honeycomb (b) With a mesh and a honeycomb

(c) with a mesh only (d) with a mesh only

Figure 4.7: Cases a, b, and c: distribution of the jet time-averaged streamwise velocity along z-axis at ($x/h = 10$, $y/h = 0$). Case d: jet profiles of the time-averaged streamwise velocity at $x/h = 10$ for different locations along the z-axis. Data is acquired for actuator outside the cavity model, Coanda slot, $J = 0.96\ kg/m.s^2$.

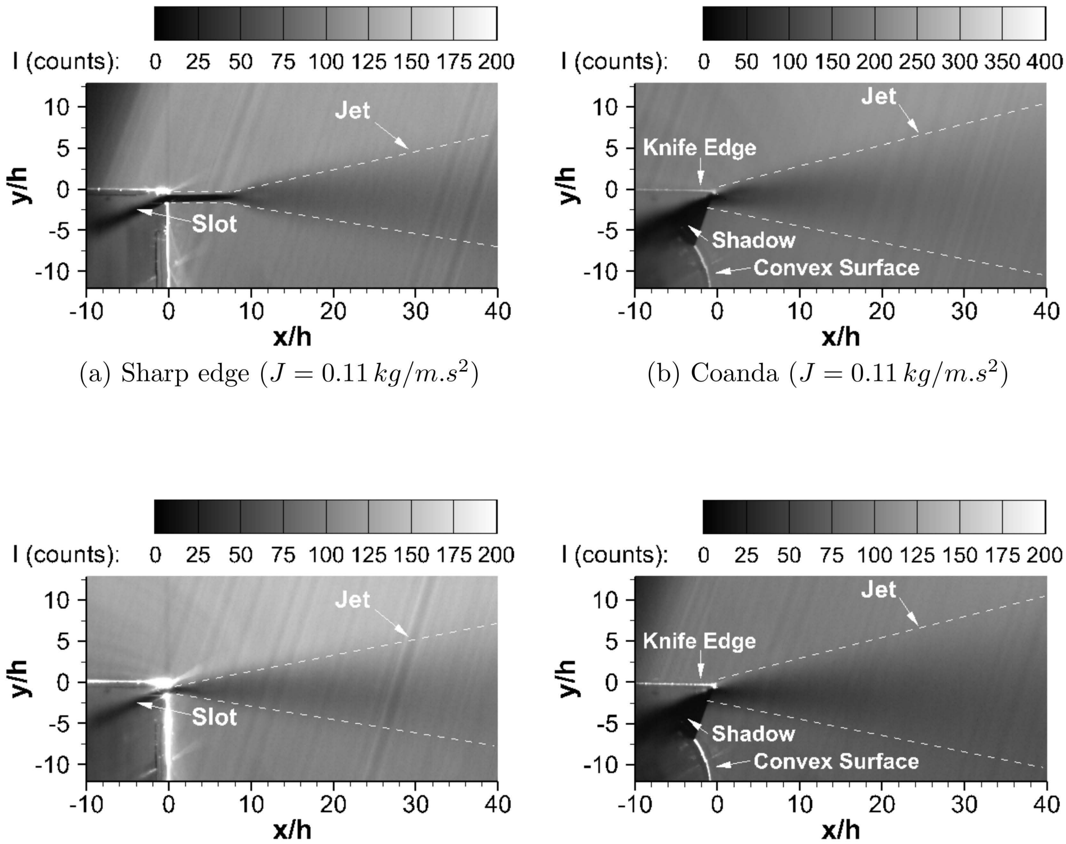

(a) Sharp edge ($J = 0.11\,kg/m.s^2$) (b) Coanda ($J = 0.11\,kg/m.s^2$)

(c) Sharp edge ($J = 0.44\,kg/m.s^2$) (d) Coanda ($J = 0.44\,kg/m.s^2$)

Figure 4.8: Time-averaged PIV raw images for actuator outside the cavity model, different slot configurations, different J.

as the former transfers momentum by eddies, while the later transfers momentum by the viscous effect. The transitional point does not appear in the coanda case, because the position of the virtual origin for this case is 20 mm upstream of the virtual origin of the sharp edge case, as illustrated in Figure 3.3 (d). For this reason, the jet in the coanda case is more developed than the jet in the sharp edge case. Secondly, for $J \geq 0.44\,kg/m.s^2$ (Figures 4.8 (c) and 4.8 (d)) the initial coanda jet thickness is noticeably larger than that of the sharp edge jet due to the difference in the position of the virtual origin between the two cases.

It is important to estimate the jet angle with respect to the x-axis. Figure 4.8 indicates that the jets' centrelines are parallel to the x-axis. The same thing was also observed at $J = 0.96\,kg/m.s^2$. To estimate the jet angle with respect to the x-axis, the vertical shift of the jet centre along the x-axis is shown in Figure

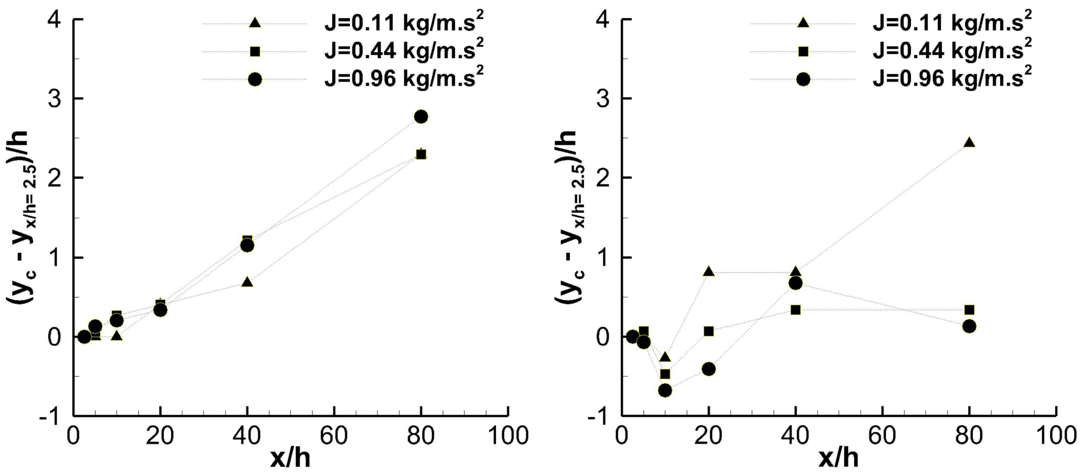

(a) Sharp edge

(b) Coanda

Figure 4.9: Shift of the jet centre along the x-axis for actuator outside the cavity model, different slot configurations, different J.

4.9. In this figure, y_c denotes the local y-position of the jet centre, while $y_{x/h=2.5}$ indicates the y-position of the jet centre at $x/h = 2.5$, which is the closest position to the slot that the HWA probe could reach without blocking the jet or damaging the HWA probe. Using the horizontal distance and the maximum vertical shift provided in the figure, the maximum estimated jet angles for the sharp edge and the coanda jets are 2.2° and 1.8°, respectively. These angles are negligibly small and likely due to the uncertainty of the HWA probe angle and the HWA velocity measurements (2.47%). Thus, it is concluded that outside the cavity model the centrelines of all jet cases are approximately parallel to the x-axis.

Unexpectedly, the jets in the coanda cases do not deflect towards the convex surface (coanda effect). The basics of the coanda effect are provided in Appendix B. Figures 4.8 (b) and 4.8 (d) demonstrate that the jet adheres to the surface of the knife edge, not to the convex surface. A similar observation is noted at $J = 0.96\,kg/m.s^2$. Figure 4.10 shows the time-averaged U and V velocity profiles at $x/h = 2.5$ for the sharp edge and the coanda cases. The U profiles have positive velocity values, while V profiles have negative velocity values. The figure illustrates the lack of symmetry around the jet centreline for the U profiles for the coanda cases compared to the sharp edge cases. The jet centre in the coanda cases tends towards the knife edge side, which means that the jet adheres to the surface of the knife edge and forms a wall jet. The jet adheres to the knife edge rather than the convex surface because the knife edge is closer to the jet. The jet would probably adhere to the convex surface if the knife edge was not extended above the coanda radius. However, it was decided not to shorten the knife edge. This decision was taken to avoid any gap at the cavity leading edge, that will perturb the cavity flow.

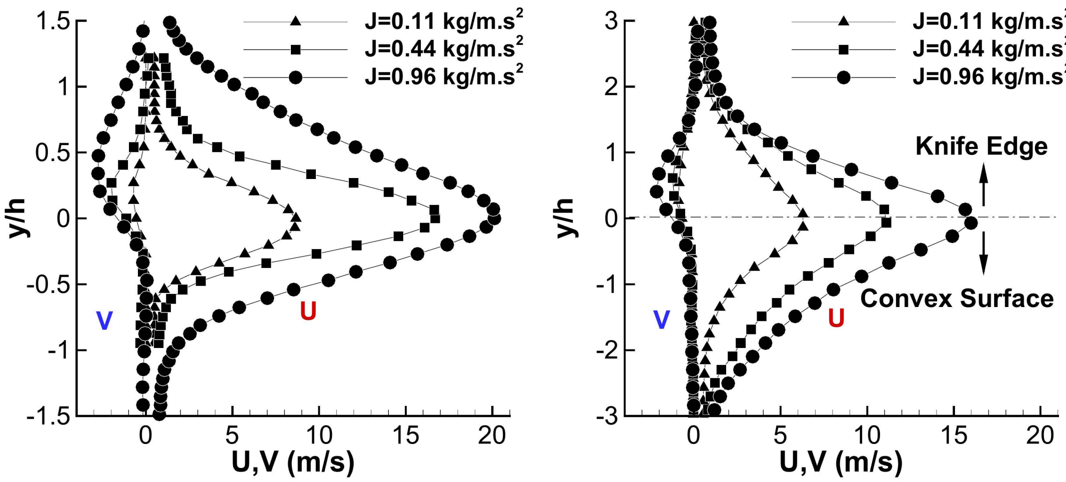

(a) Sharp edge (b) Coanda

Figure 4.10: The time-averaged U and V velocity profiles at $x/h = 2.5$ for actuator outside the cavity model, different slot configurations, different J.

The next step is to investigate the other characteristics of the jets and comparing them with the characteristics of turbulent planar jets. Figure 4.11 (a) shows the decay of the jet centre velocity along the x-axis. U_m denotes the local jet centre velocity, while U_0 denotes the jet centre velocity at $x/h = 2.5$. As illustrated in the figure, the decay rate $DR = d(U_0/U_m)^2/d(x/h)$ for all jet cases is constant and decreases with increasing J (or Re), which agrees with the experimental study of Namer and Ötügen (1988) on plane turbulent jets ($Re = 1000$ to 7000). The decay rate reported in this study is 0.239 at $Re = 1000$. This decay rate is lower than the decay rates of the sharp edge cases ($DR \approx 0.364$ to 0.212) and higher than the decay rates of the coanda cases ($DR \approx 0.252$ to 0.149). According to Namer and Ötügen (1988), there is no agreement on the value of the decay rate due to various reasons. One reason for this variation is the Reynolds number dependency.

The dimensionless jet half width b/h along the x-axis is shown in Figure 4.11 (b). The jet half width b is the distance between the centre of the jet to the y-position where $U = 0.5U_m$. As illustrated in the figure, the initial jet width for the coanda cases is noticeably larger than the initial width of the sharp edge cases, due to the difference in the position of the virtual origin between the two cases. On the other hand, the jet growth rates $GR = d(b/h)/d(x/h)$ for the sharp edge and the coanda cases are quite similar. The GR is between 0.136 and 0.114 for the sharp edge cases, and 0.139 to 0.117 for the coanda cases. These rates are relatively smaller to the growth rate reported by Namer and Ötügen (1988) at $Re = 1000$ ($GR \approx 0.179$).

The centreline turbulence intensity U_{rms}/U_m along the x-axis is shown in Figure 4.12 (a). U_{rms} denotes the root mean square of the U velocity fluctuations. As illustrated in the figure, the initial turbulence intensity at $x/h = 2.5$ for the coanda jets is substantially higher than the that for the sharp edge jets. This is probably because the virtual origin in the coanda cases is upstream of the knife edge, and hence the jets are more developed than the jets of the sharp edge cases. For both cases, the centreline turbulence intensity increases asymptotically with x-direction until it reach the asymptotic value between 0.25 and 0.2. This value is approximately similar to the asymptotic value reported by Namer and Ötügen (1988) for turbulent jets, which is 0.22. Figure 4.12 (b) shows the streamwise development of the dimensionless dominant frequency along the jet centreline. The dimensionless frequency $St = fb/U_m$ is calculated based on the local jet half

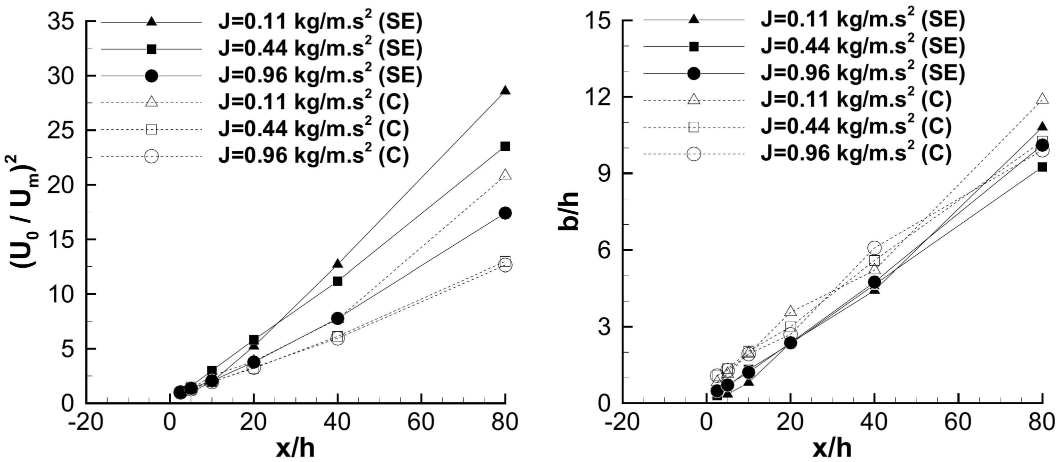

(a) $(U_0/U_m)^2$ (b) b/h

Figure 4.11: Comparison of the velocity decay $(U_0/U_m)^2$ and the dimensionless jet half width b/h for actuator outside the cavity model, different slot configurations, different J. SE: sharp edge slot, C: coanda slot.

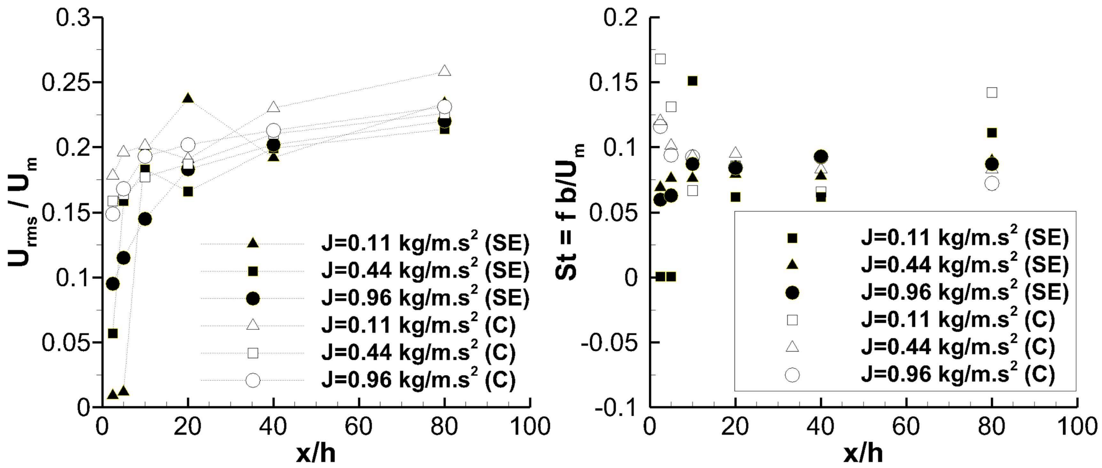

(a) U_{rms}/U_m (b) Dimensionless dominant frequency

Figure 4.12: The streamwise development of the U_{rms}/U_m and the dimensionless dominant frequency at $y/h = 0$ for actuator outside the cavity model, different slot configurations, different J. SE: sharp edge slot, C: coanda slot.

width b and the local jet centre velocity U_m. The figure shows the scattering of data points within the flow-development region ($x/h \leq 6$). However, as the jets become fully developed ($x/h \geq 6$), the data points collapse between $St = 0.05$ and 0.1. This agrees with the frequency range found by Deo et al. (2008) at $1500 < Re_h < 16500$ ($0.05 \leq St \leq 0.11$).

In conclusion, characterising the jet outside the cavity model showed that the coanda jets have higher turbulence intensity and larger initial width than the sharp edge jets. This is attributed to the positional difference of the virtual origin between the two cases. It was also shown that the jet characteristics for both cases are to some extent similar to the characteristics of the turbulent planar jets.

5.2 Actuator at the cavity model

Time-Averaged Characteristics

This subsection investigates the behaviour of the jets inside the open cavity at quiescent conditions. Figure 4.13 illustrates the time-averaged velocity streamlines and U/U_0 contours for all jet cases. As evident from the figure, the jet behaviour for the sharp edge and coanda cases is generally similar. For $J = 0.11\,kg/m.s^2$ and $0.44\,kg/m.s^2$, the jet deflects slightly towards the cavity floor, then it deflects upwards as it approaches the cavity trailing edge. For $J = 0.96\,kg/m.s^2$, the jet deflects significantly downwards until it reattaches at the cavity floor, then the jet impinges on the cavity trailing edge and deflects upwards. At the same time, portion of the jet is recirculated towards the cavity leading leading. The main

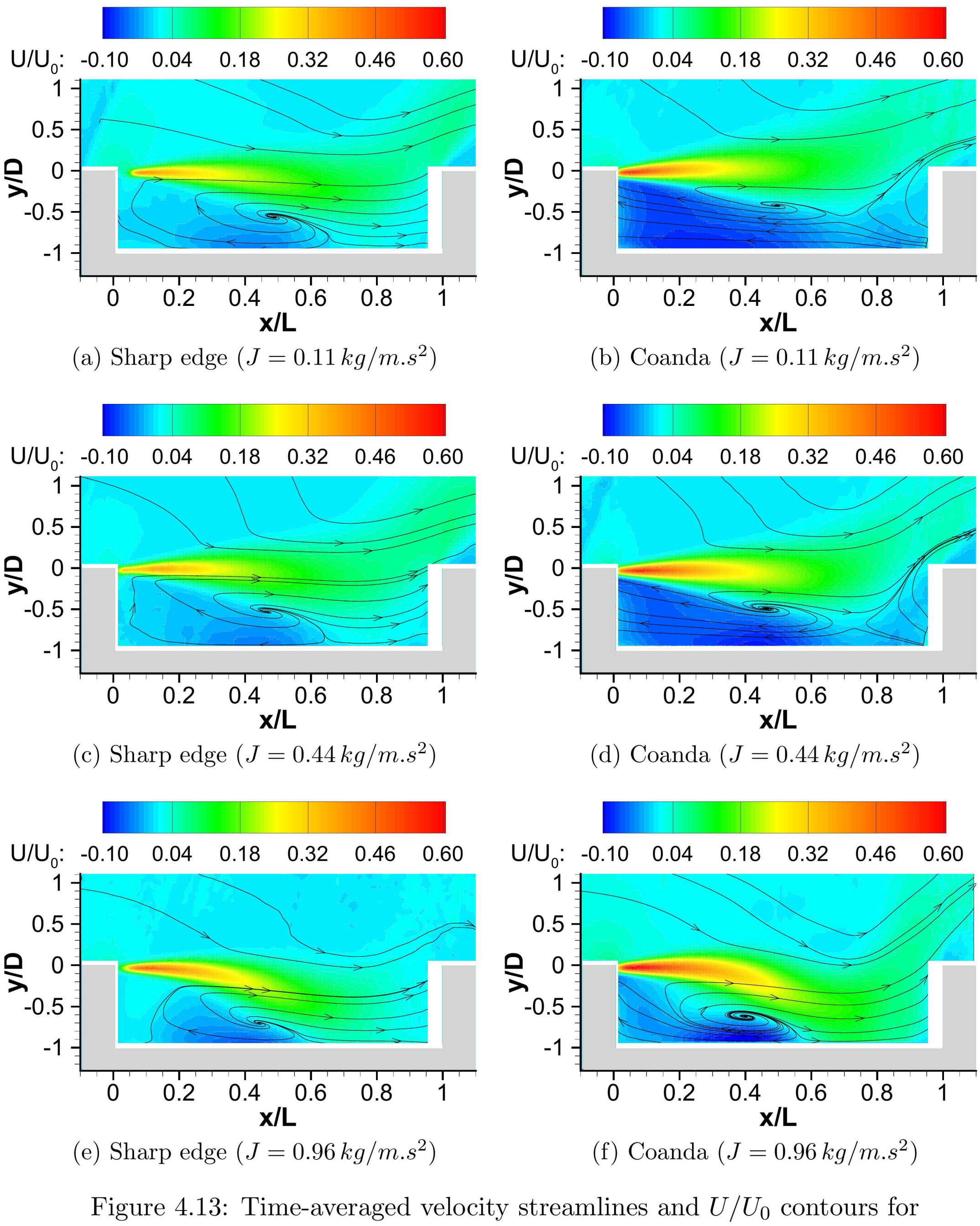

(a) Sharp edge ($J = 0.11\,kg/m.s^2$)

(b) Coanda ($J = 0.11\,kg/m.s^2$)

(c) Sharp edge ($J = 0.44\,kg/m.s^2$)

(d) Coanda ($J = 0.44\,kg/m.s^2$)

(e) Sharp edge ($J = 0.96\,kg/m.s^2$)

(f) Coanda ($J = 0.96\,kg/m.s^2$)

Figure 4.13: Time-averaged velocity streamlines and U/U_0 contours for actuator at the cavity model, different slot configurations, different J.

difference between the sharp edge and coanda cases seems to be how the jet interacts with the cavity trailing edge. In the sharp edge cases, the jets interact with the cavity trailing edge and then deflect upwards at a small angle. Similar behaviour is noted for the coanda cases, but with significantly larger deflection angle. This difference is probably attributed to the jet width difference between the two cases.

The jet deflection towards the cavity floor at $J = 0.96\,kg/m.s^2$ is attributed to the coanda effect. As the characteristic jet velocity (or J) increases, the jet entrains more fluid from the cavity (Morton et al., 1956). As a result, the static pressure at the cavity floor decreases, until it reaches a threshold point. Beyond this point, the pressure force causes the jet to deflect towards the cavity floor. Figure 4.14 shows the time-averaged V velocity distribution along the cavity floor ($y/D = -0.9$) for sharp edge and coanda cases. The positive V velocity indicates upward fluid movement or jet entrainment, while the negative V velocity indicates a downward fluid movement. For both slot configurations, the jet entrainment at $J = 0.11\,kg/m.s^2$ and $J = 0.44\,kg/m.s^2$ is quite small. Increasing J to $0.96\,kg/m.s^2$ yields a significant increase in the entrainment at the upstream half ($0 \leq x/L \leq 0.4$), which forces the jet to deflect downwards. As the jet deflects and reattaches onto the cavity floor, the sign of V shifts from positive to negative.

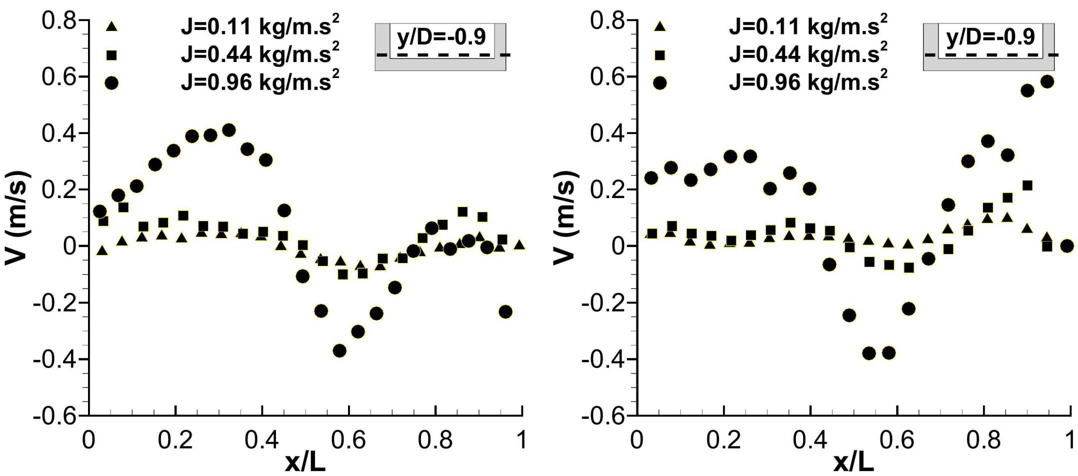

(a) Sharp edge (b) Coanda

Figure 4.14: The time-averaged V velocity distribution along $y/D = -0.9$ for actuator at the cavity model, different slot configurations, different J.

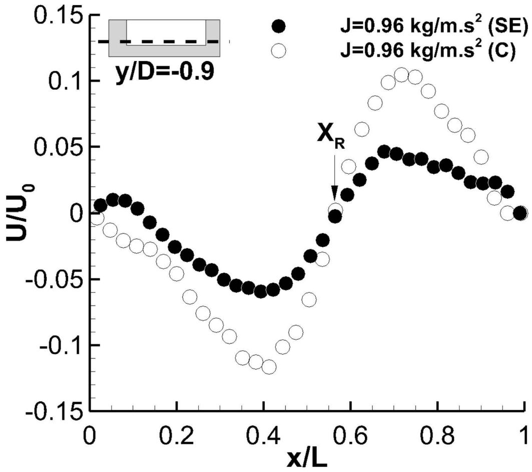

Figure 4.15: Distribution of the time-averaged U/U_0 at $y/D = 0.9$ for actuator at the cavity model, different slot configurations, $J = 0.96\,kg/m.s^2$ SE: sharp edge slot, C: coanda slot.

Figure 4.15 shows the distribution of the time-averaged U/U_0 along the cavity floor at $y/D = 0.9$ for $J = 0.96\,kg/m.s^2$. As illustrated in this figure, the reattachment point (X_R), which is identified based on the location of $U/U_f = 0$, is at $x/h \approx 0.58$. At this point, the sign of the streamwise velocity changes from negative to positive and hence this point indicates the location of jet reattachment on the cavity floor. The location of X_R for the sharp edge and coanda cases is almost identical, as illustrated in the figure.

Temporal Behaviour

The instantaneous flow fields show that the temporal behaviour of the sharp edge and slot cases is generally similar. Thus, only the temporal behaviour of the coanda cases will be investigated here. Figure 4.16 (a) shows a snapshot of the instantaneous R/U_0 field for the coanda case at $J = 0.11\,kg/m.s^2$, where $R = \sqrt{U^2 + V^2}$ is the velocity magnitude. As illustrated in the figure, the jet entrains fluid from above and below (regions "A" and "B"). Due to the turbulent mixing, the entrained fluid is mixed with the core of the jet (region "C"). As the jet travels downstream, it starts to flap at a larger amplitude (region "D"). Eventually, the jet breaks into coherent structures, such as region "E", which continue to travel downstream. At the cavity trailing edge, a portion of the jet deflects upwards, whilst the remainder is recirculated towards the cavity leading edge, region "F", where it is entrained by the jet. A similar behaviour was observed at $J = 0.44\, kg/m.s^2$ and $0.96\, kg/m.s^2$. However, at $J = 0.96\, kg/m.s^2$ the jet splits at the reattachment point into two streams: one deflects upwards and the other is recirculated towards the cavity leading edge, as illustrated in Figure 4.16 (b).

The instantaneous velocity fields show a complicated jet behaviour. Thus, to study the most dominant jet behaviours, the flow field is decomposed using the proper orthogonal decomposition (POD) into a large number of energy modes, then the instantaneous velocity fields were reconstructed using the most dominant modes. As a result, the low energy POD modes are filtered out, while the flow is only represented by the dominant modes. The POD was implemented using the snapshot method. The basics of POD and the procedure of the snapshot method is presented in Appendix H.

The instantaneous velocity fields were reconstructed using the first four POD modes, which represents 16.2% to 16.7% of the total energy for $J = 0.11\, kg/m.s^2$ and $J = 0.96\, kg/m.s^2$, respectively, as shown in Figures 4.17 and 4.18. Both figures show a significant jet flapping motion. Figure 4.17 shows the reconstructed instantaneous U/U_0 field for the coanda case at $J = 0.11\, kg/m.s^2$. As shown in Figure 4.17 (a), initially the jet impinges on the cavity trailing edge. Due to the increased pressure at the impingement region, the jet starts to deflect upwards, while the pressure inside the cavity drops due to the jet entrainment, as illustrated in Figure 4.17 (b). At a certain point, the jet stops deflecting upwards and starts deflecting downwards under the influence of the low-pressure inside the cavity.

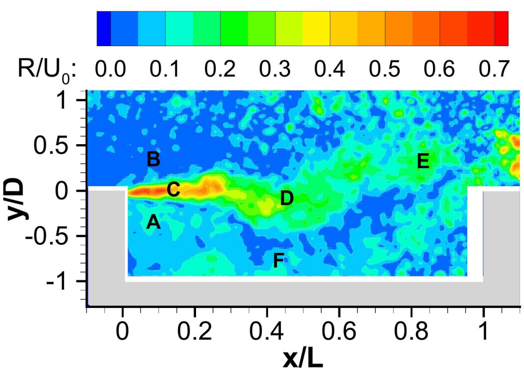

(a) $J = 0.11\, kg/m.s^2$

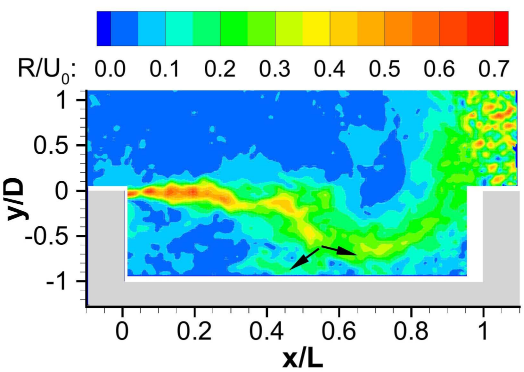

(b) $J = 0.96\, kg/m.s^2$

Figure 4.16: Snapshot of the instantaneous R/U_0 for actuator at the cavity model, coanda slot, different J.

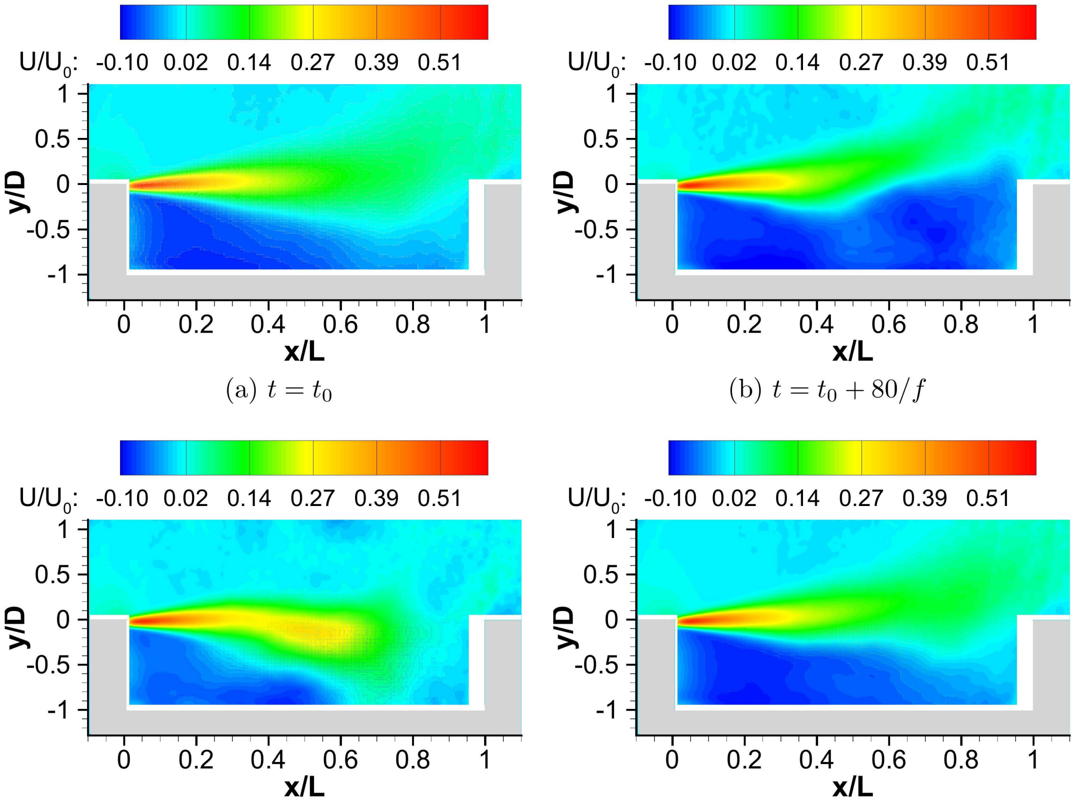

(a) $t = t_0$ (b) $t = t_0 + 80/f$

(c) $t = t_0 + 120/f$ (d) $t = t_0 + 160/f$

Figure 4.17: Snapshots of the instantaneous U/U_0 approximated by the first four POD modes (16.2% of the total energy) for actuator at the cavity model, coanda slot, $J = 0.11\, kg/m.s^2$.

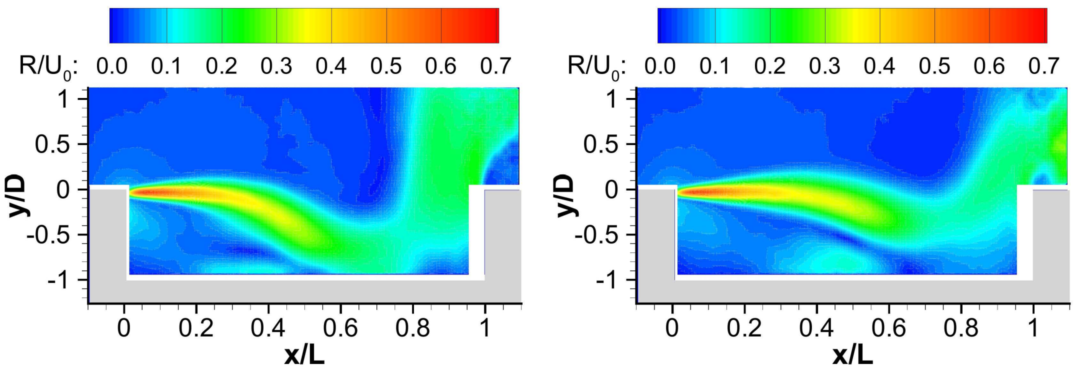

(a) $t = t_0$ (b) $t = t_0 + 30/f$

Figure 4.18: Snapshots of the instantaneous R/U_0 approximated by the first four POD modes (16.7% of the total energy) for actuator at the cavity model, coanda slot, $J = 0.96\, kg/m.s^2$.

As the jet deflects downward, more fluid is supplied to the recirculation region, and hence the pressure inside the cavity increases, as demonstrated in Figure 4.17 (c). Eventually, the gradual pressure increase forces the jet to deflect upwards, and the cycle repeats again. A similar temporal behaviour was observed for the coanda case at $J = 0.44\, kg/m.s^2$.

Figure 4.18 shows the reconstructed instantaneous R/U_0 field for the coanda edge case at $J = 0.96\, kg/m.s^2$. As the jet reattaches on the cavity floor, a portion of the jet is supplied to the recirculation region, as shown in Figure 4.18 (a). When the flow supplied to the recirculation region becomes more than the fluid entrained by the jet, the jet lifts up and interacts with the cavity trailing edge at a smaller angle, as demonstrated in Figure 4.18 (b). However, as the pressure inside the cavity drops due to the jet entrainment, the jet deflects back and reattaches again and the cycle repeats.

6 Concluding remarks

The characterisation of the free stream and the upstream boundary layer was performed at Re_θ of 1.28×10^3, 2.02×10^3, and 4.37×10^3, which corresponds to time-averaged free stream velocities of 11.1, 22.1, and 43.7 m/s and time-averaged free stream turbulence intensities of 1.82%, 1.95% and 2.29%, respectively. The characterisation outcomes are summarised as follows:

- The upstream boundary layer is fully turbulent for both tripped and not tripped cases. However, it was decided to keep the trip to ensure that the upstream boundary layer is always fully turbulent.
- The small step of the adhesive tape did not trip the boundary layer. The laminar to turbulent boundary layer transition takes place upstream of the small step.
- The upstream boundary layer at the mid-span region is acceptably uniform along the z-axis, and hence the cavity separated shear layer within this region is assumed to be uniform along this axis.

Next, the sharp edge and coanda blowing jets were characterised outside the cavity model at quiescent conditions for $0.11\, kg/m.s^2 \leq J0.96 \leq\, kg/m.s^2$. The characterisation outcomes are concluded as follows:

- Both jets' centrelines are almost parallel to the x-axis. The jet in the coanda case does not deflect towards the convex surface because it adheres to the knife edge rather than to the convex surface.
- The coanda jets have higher turbulence intensity and larger initial width compared to the sharp edge jets. This is because the virtual origin for the coanda case is upstream of the knife edge.
- The jet characteristics for the coanda and sharp edge jet cases, such as decay rates, growth rates, turbulence intensity, and dimensionless frequency are generally similar to the characteristics of the turbulent planar jets.

Eventually, the aforementioned jet cases were characterised inside the cavity model at quiescent conditions. The characterisation outcomes are as follows:

- For the coanda and sharp edge jet cases, no jet deflection was observed at $J = 0.11\,kg/m.s^2$ and $0.44\,kg/m.s^2$. However, at $0.96\,kg/m.s^2$ the coanda and sharp edge jets deflect downwards and reattach on the cavity floor due to the coanda effect.
- The instantaneous flow fields show a significant flapping motion for all jet cases.
- The time-averaged flow field and temporal behaviour for both jet cases are quite similar inside the cavity. However, the main difference between the sharp edge and coanda cases seems to be how the jet interacts with the cavity trailing edge at $J = 0.96\,kg/m.s^2$.

Chapter 5

Baseline Cavity Flow

This chapter examines the open cavity flow without a jet. The time-averaged flow field and the oscillations of the cavity separated shear layer at $Re_\theta = 1.28 \times 10^3$ (sharp edge at LE) are studied. This chapter also examines the influence of increasing the Reynolds number to $Re_\theta = 4.37 \times 10^3$ on the oscillations of the cavity separated shear layer.

1 Time-averaged flow field

The slot configurations used for flow control may affect the baseline flow. Figure 5.1 illustrates the impact of the slot configurations on the time-averaged U/U_f and V/U_f flow fields. Ensemble-averaging of 1800 instantaneous flow field was used to generate the time-averaged flow field. The definition of the ensemble-averaging is provided in Appendix C. Figure 5.1 shows a change in the centre of the main recirculation vortex between the three cases. The vortex centre is at $x/L \approx 0.65$, 0.7, and 0.8 for the sharp edge slot at the cavity leading edge, coanda slot at the cavity leading edge, and the sharp edge slot at the cavity trailing edge, respectively. This difference is attributed to the interaction between the slot and the cavity flow. Additionally, this difference maybe due to the uncertainty of the time-averaged PIV measurements, which is approximately 3.45%. Despite this difference, the time-averaged flow fields for the aforementioned cases are generally similar. Therefore, only a single slot configuration, which is the sharp-edge slot at the cavity leading edge, will be examined in this chapter.

To examine the three-dimensionality of the cavity flow, surface oil flow visualisation experiments were performed. Figure 5.2 illustrates the oil flow patterns

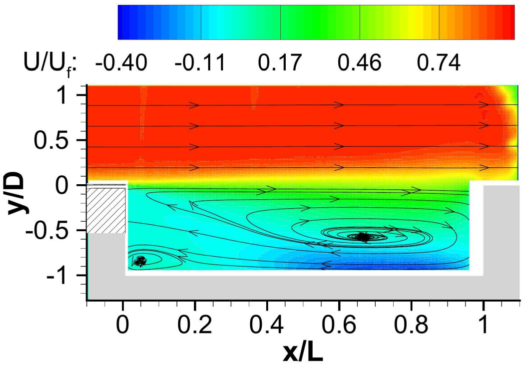

(a) Sharp-edge slot at cavity LE (U/U_f)

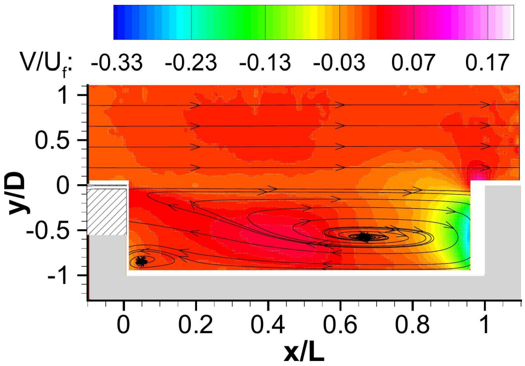

(b) Sharp-edge slot at cavity LE (V/U_f)

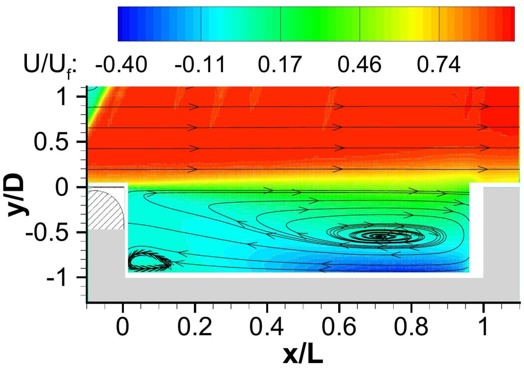

(c) Coanda slot at cavity LE (U/U_f)

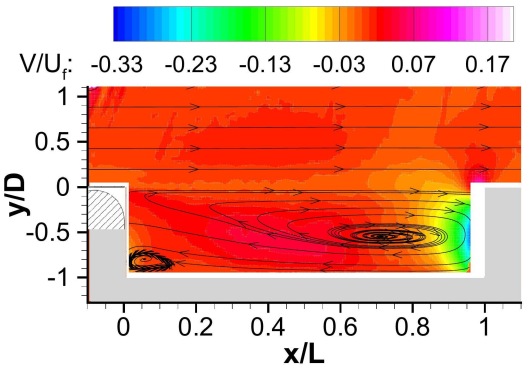

(d) Coanda slot at cavity LE (V/U_f)

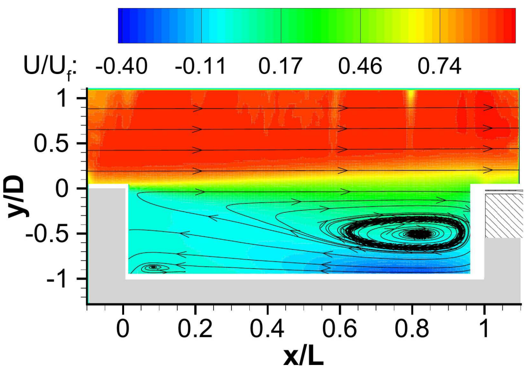

(e) Sharp-edge slot at cavity TE (U/U_f)

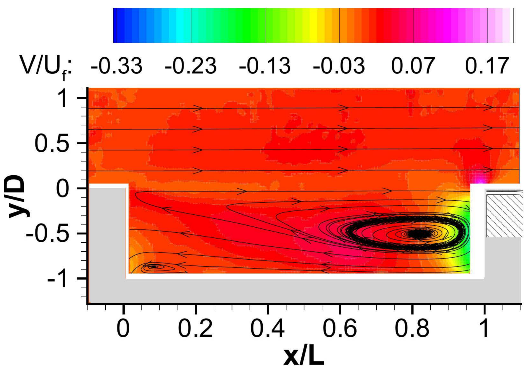

(f) Sharp-edge slot at cavity TE (V/U_f)

Figure 5.1: Time-averaged velocity fields for $Re_\theta = 1.28 \times 10^3$, different slots at LE, no jet.

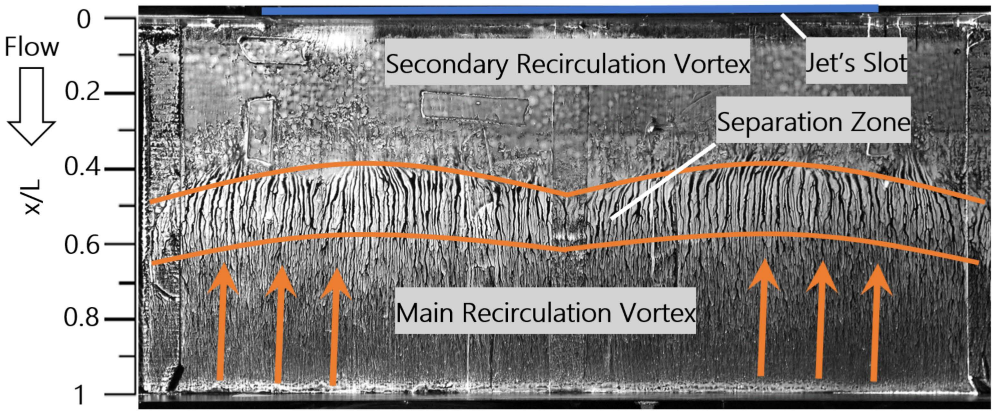

Figure 5.2: Surface oil flow visualisation for $Re_\theta = 1.28 \times 10^3$, sharp edge at LE, no-jet.

for the sharp edge slot with no jet at $Re_\theta = 1.28 \times 10^3$. To focus the images at the central portion of the cavity, the side regions of the cavity are cropped from the images. As illustrated in the figure, the reverse flow of the main recirculation vortex displaces the oil from the cavity trailing edge towards the cavity leading edge. As the reverse flow starts to separate, the oil accumulates at the middle of the cavity ($x/L \approx 0.55$). This accumulation of oil is believed to be the separation zone, where the reverse flow separates from the cavity floor. The oil patterns at the main recirculation and separation regions indicate that the flow is parallel to the x-axis, and hence the cavity flow is believed to be two-dimensional.

Velocity streamlines and contours of the time-averaged U/U_f are shown in Figure 5.3 (a). The figure demonstrates a typical shallow open cavity flow, that is similar to those described in the literature. As shown in the figure, the separated shear layer grows continuously until it impinges on the cavity trailing edge. As a result, a portion of the flow is recirculated towards the cavity leading edge. This reverse flow is eventually entrained by the cavity separated shear layer. Two recirculation vortices are formed inside the cavity: a large, relatively strong clockwise vortex (main recirculation vortex) at $x/L \approx 0.65$, $y/D \approx -0.5$, and a smaller, relatively weak anti-clockwise vortex (secondary recirculation vortex) at the lower corner of the cavity leading edge.

Figure 5.3 (b) shows the time-averaged U/U_f velocity profile along the cavity floor ($y/D \approx -0.9$). The maximum reverse flow velocity is approximately 30% of the free stream velocity, which is similar to the value reported by Ukeiley and Murray (2005) for shallow cavities at $Re_d \approx 70 \times 10^3$. The figure also shows that the reverse flow separates at $x/L \approx 0.2$. The separation location (X_R) is the

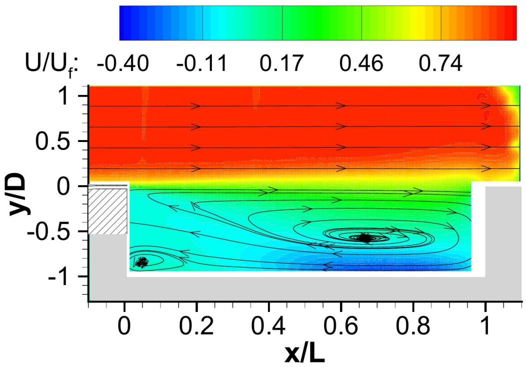

(a) U/U_f

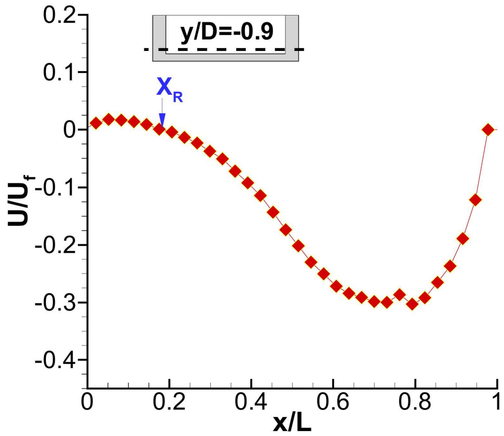

(b) Profiles of U/U_f at y/D = -0.9

Figure 5.3: Time-averaged U/U_f field and U/U_f profile at $y/D = -0.9$ for $Re_\theta = 1.28 \times 10^3$, sharp edge at LE, no-jet.

location where $U/U_f = 0$ at the cavity floor. This value differs significantly from the oil flow results, which is presented in Figure 5.2. The oil flow result indicates a much earlier separation ($x/L \approx 0.55$). The early oil flow separation is because the wall shear stress at $Re_\theta = 1.28 \times 10^3$ is too weak to push the accumulated oil to the actual separation location.

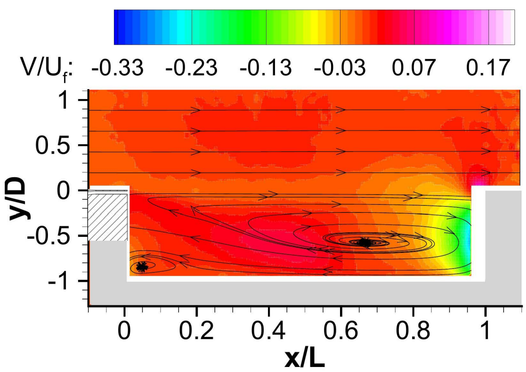

(a) V/U_f

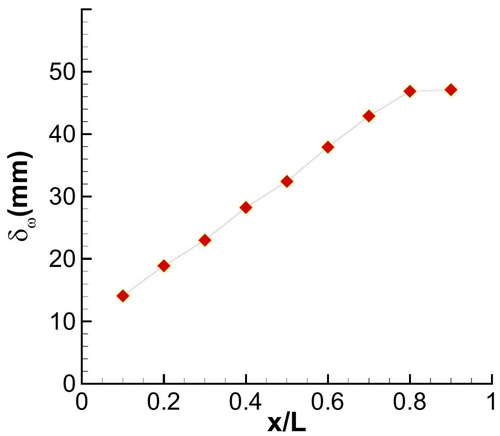

(b) Vorticity thickness

Figure 5.4: Time-averaged V/U_f field and vorticity thickness for $Re_\theta = 1.28 \times 10^3$, sharp edge at LE, no-jet.

The contours of the time-averaged V/U_f field are provided in Figure 5.4 (a).

The figure shows the momentum exchange between the cavity separated shear layer and the fluid inside the cavity. Within $0 \leq x/L \leq 0.85$, the cavity fluid is entrained by the cavity separated shear layer. Beyond $x/L \geq 0.85$, the cavity separated shear layer supplies fluid to the interior of the cavity. This momentum exchange affects the growth rate of the cavity separated shear layer. The growth rate of the cavity separated shear layer vorticity thickness is illustrated in Figure 5.4 (b). As shown in the figure, within $0.1 \leq x/L \leq 0.8$ the cavity separated shear layer grows steadily at a rate of $d\delta_\omega/dx \approx 0.18$ due to the entrainment of the cavity separated shear layer. This rate is noticeably higher than the growth rate reported by Ashcroft and Zhang (2005) at $M \approx 0.1$ and L/D between 2 and 4. A similar discrepancy has been observed by Rodi (1975) for mixing layer. Rodi (1975) attributed this discrepancy to: (i) the dependency on free stream turbulence, (ii) the dependency on initial conditions, and (iii) the sensitivity to the outer flow field. Beyond $x/L \geq 0.8$, the cavity separated shear layer stops growing as a portion of the cavity separated shear layer momentum is transferred to the cavity's interior.

The dimensionless Reynolds stress tensors, which represent the transfer of momentum due to turbulent fluctuations, are shown in Figures 5.5 (a), 5.5 (b), and 5.5 (c). The location and value of the peak stress is indicated in each figure. As evident from the figures, the velocity fluctuations of the cavity separated shear layer increase substantially along the streamwise direction until they reach the peak value upstream of the cavity trailing edge ($x/L \approx 0.7$ to 0.8). The peak location is similar to that reported by Al Haddabi et al. (2016) and Ukeiley and Murray (2005) for shallow open cavities. The peak location coincides with the end of the steady growth zone of the cavity separated shear layer. Downstream of this location, the velocity fluctuations decrease due to the splitting of the cavity separated shear layer, as evident from the time-averaged dimensionless vorticity field presented in Figure 5.5 (d). As demonstrated in the figure, beyond $x/L \approx 0.8$, the cavity separated shear layer splits into two parts: one part passes over the cavity trailing edge, while the other part deflects backwards at the cavity trailing edge (reverse flow).

In summary, the surface oil flow visualisations showed that the cavity flow is likely to be two-dimensional. The time-averaged flow fields demonstrate a typical shallow open cavity flow.

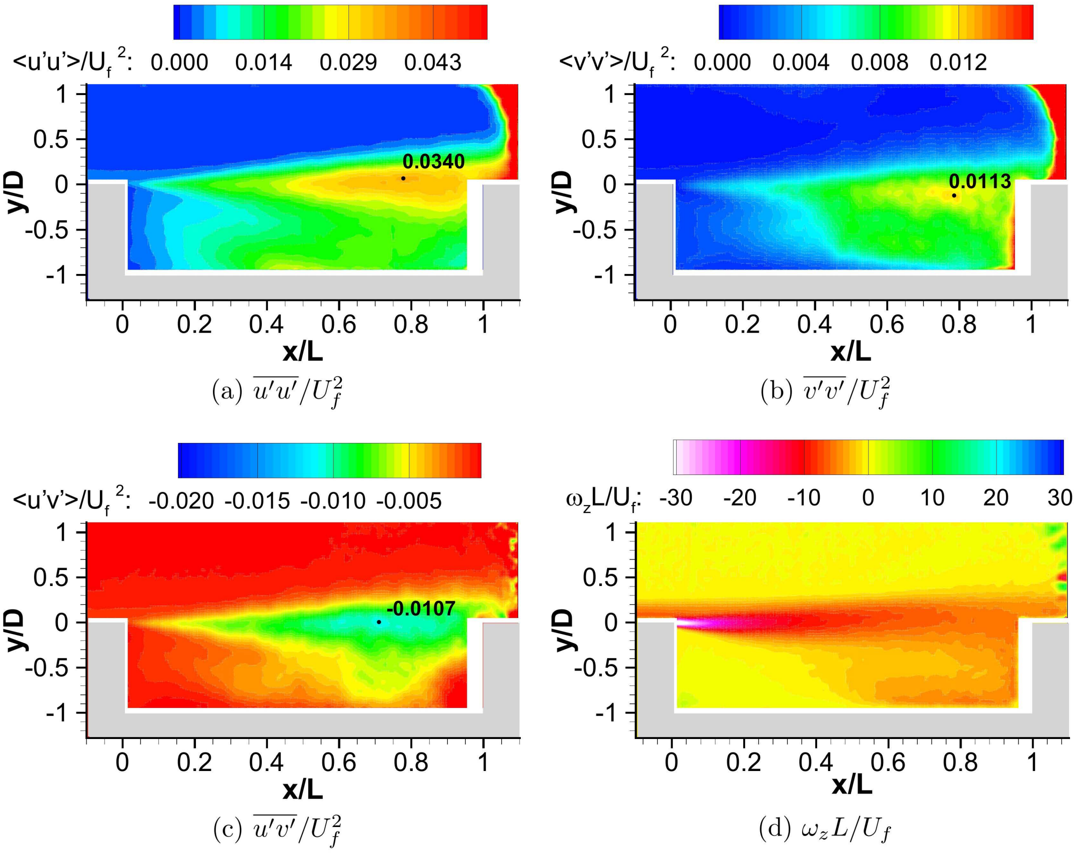

Figure 5.5: Dimensionless Reynolds stress components and z-vorticity for $Re_\theta = 1.28 \times 10^3$, sharp edge at LE, no-jet.

1.1 Comparing time-averged results with the literature

Figure 5.6 compares the time-averaged streamlines for the current experiment ($Re_d = 49.5 \times 10^3$) and Grace et al. (2004) experiment ($Re_d \approx 13 \times 10^3$). Both experiments were performed at L/D=4. The time-averaged flow behaviour for both cases is almost identical. However, the centre of the main recirculation vortex differers between the two experiments. In the current the vortex is centred at $x/L \approx 0.65$, while the vortex is centred at $x/L \approx 0.75$ in Grace et al. (2004) experiment. This difference is perhaps attributed to the presence of slot at the cavity leading edge, as it was observed previously in Figure 5.1.

Figure 5.7 compares the time-averaged dimensionless Reynolds shear stress $\overline{u'v'}/U_f^2$ profiles at x/L of 0.19 and 0.94 for the current experiments and Grace et al. (2004) experiments. In both cases, the dimensionless Reynolds shear stress in the Grace et al. (2004) experiments is significantly higher than the current

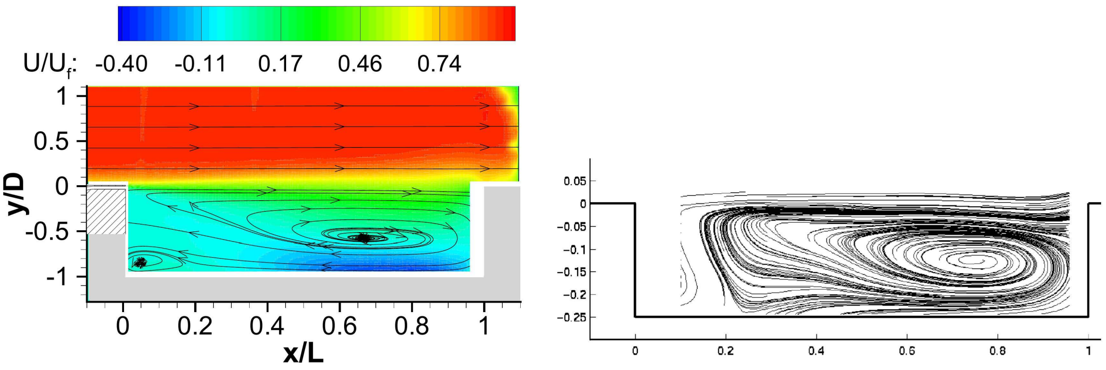

(a) current experiment (b) Grace et al. (2004) experiment

Figure 5.6: Time-averaged streamlines for: a) current experiment ($Re_d = 49.5 \times 10^3$), and b) Grace et al. (2004) experiment ($Re_d \approx 13 \times 10^3$).

experiment. This noticeable difference is probably attributed to flow conditions or to the accuracy of the flow diagnostic technique used (PIV for the current experiments, LDA for Grace et al. (2004) experiments).

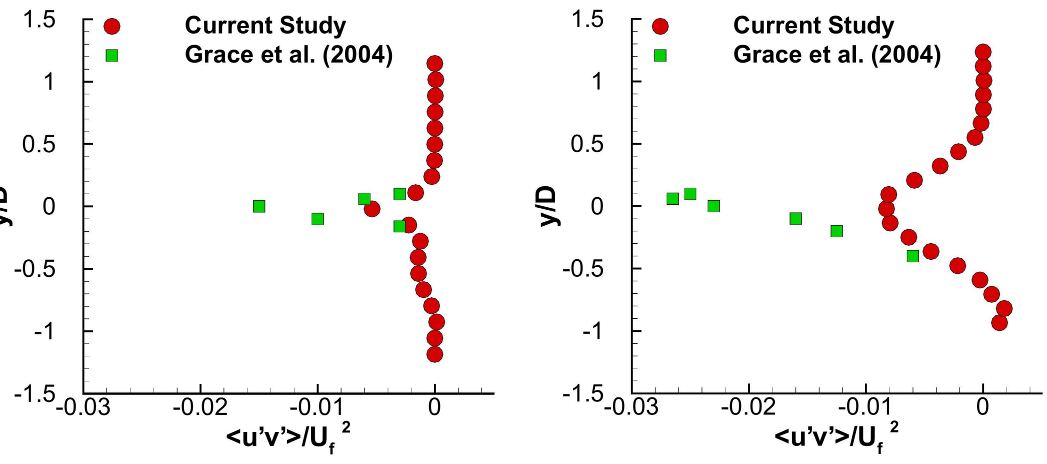

(a) x/L =0.19 (b) x/L =0.94

Figure 5.7: Time-averaged $\overline{u'v'}/U_f^2$ profiles at x/L of 0.19 and 0.94 for the current experiments and Grace et al. (2004) experiments

2 Oscillations of the cavity separated shear layer

2.1 Low-frequency instabilities

The reverse flow interaction with the cavity leading edge has a significant impact on the cavity oscillations. The temporal evolution of U/U_f at the cavity leading edge region $x/L = 0.2$ and cavity trailing edge region $x/L = 0.8$ is shown in Figure 5.8. As evident from Figure 5.8 (a), surges of reverse flow, which are indicated by arrows, arrive at the cavity leading edge region. The timing of these surges coincides with the timing of the oscillation peaks in the cavity separated shear layer, as demonstrated in Figure 5.8 (b). The reverse flow surge generates a large-amplitude flapping wave, as evident from the temporal evolution of U/U_f along the cavity separated shear layer (Figure 5.9). The dashed sloped line shown in the figure indicates that the wave propagates downstream.

Figure 5.10 presents snapshots of the instantaneous U/U_f field at the instance of peak oscillation. When the cavity separated shear layer deflects downwards (Figure 5.10 (a)), a reverse flow surge propagates upstream to impact the separation point of the cavity separated shear layer (Figure 5.10 (b)). As a result, an instability wave is generated at the separated shear layer (Figure 5.10 (c)). The instability wave amplifies as it propagates downstream until it impacts the

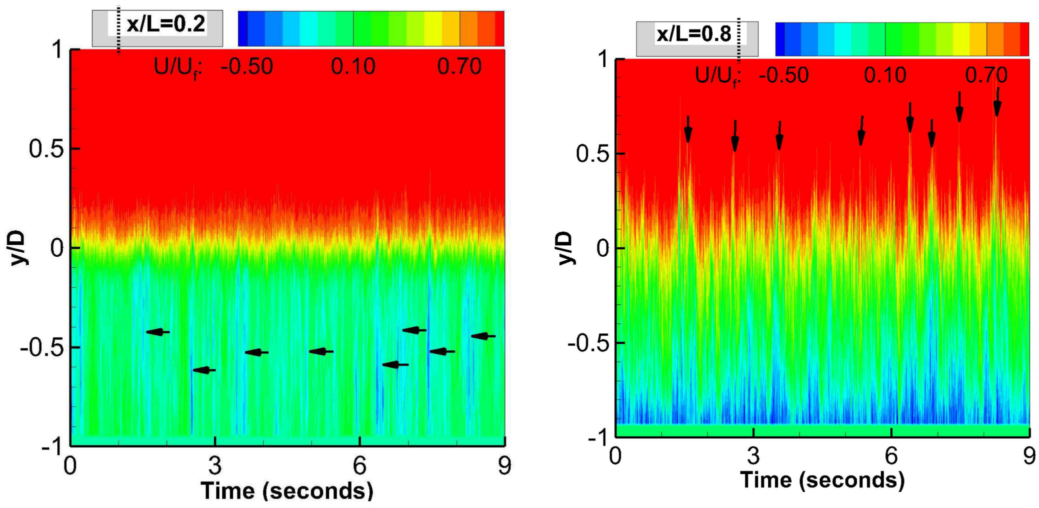

(a) x/L=0.2 (b) x/L=0.8

Figure 5.8: Temporal evolution of U/U_f at two streamwise stations for $Re_\theta = 1.28 \times 10^3$, sharp edge at LE, no-jet.

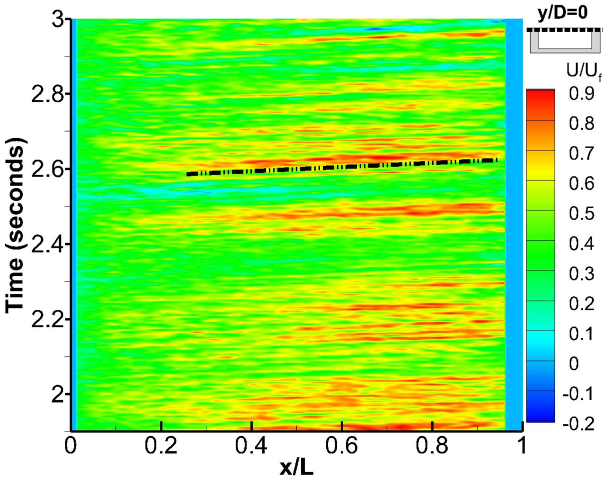

Figure 5.9: Temporal evolution of U/U_f at $y/D = 0$ for $Re_\theta = 1.28 \times 10^3$, sharp edge at LE, no-jet.

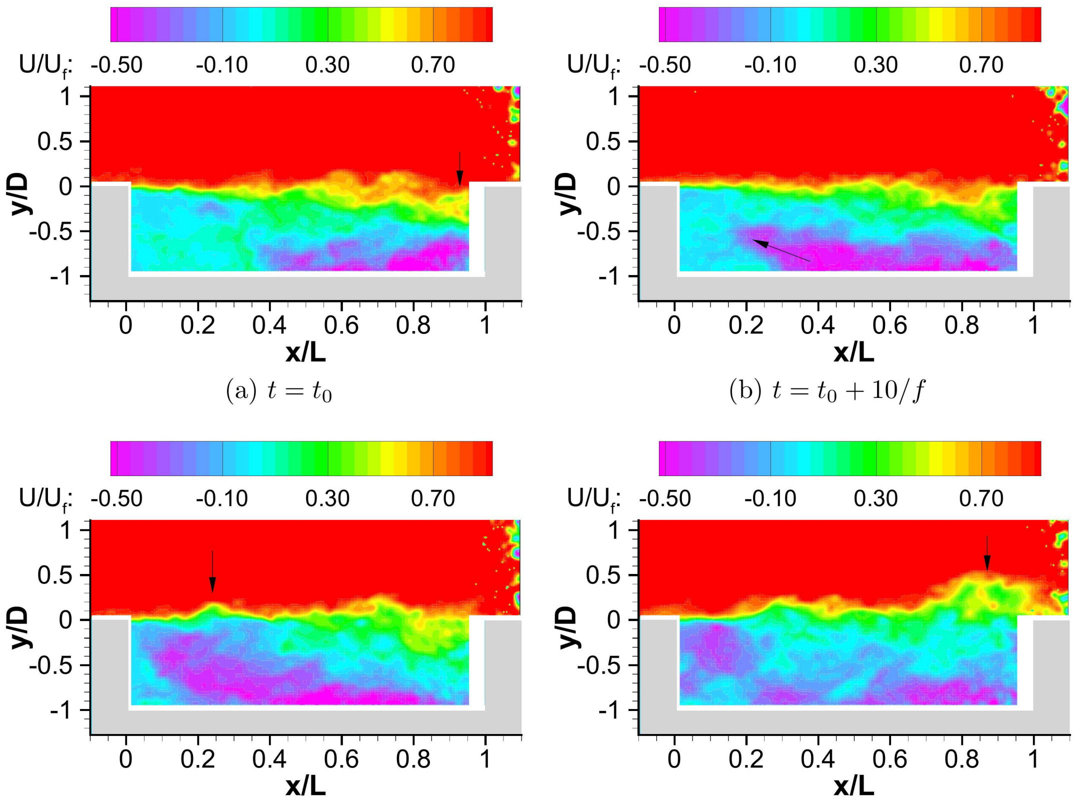

(a) $t = t_0$

(b) $t = t_0 + 10/f$

(c) $t = t_0 + 15/f$

(d) $t = t_0 + 20/f$

Figure 5.10: Snapshots of the instantaneous U/U_f for $Re_\theta = 1.28 \times 10^3$, sharp edge at LE, no-jet.

cavity trailing edge (Figure 5.10 (d)). Throughout this study, this interaction will be called "reverse flow interaction". This hydrodynamic interaction was also observed by Lin and Rockwell (2001) at $Re_{\theta_0} = 1.37 \times 10^3$ and $L/D = 4$. According to Lin and Rockwell (2001), the interaction is, at least, partially responsible for the amplitude and frequency modulations of the cavity separated shear layer oscillations.

To study the impact of this phenomenon on the velocity spectra of the cavity separated shear layer, spectral analysis of the streamwise velocity was performed at particular points along the cavity separated shear layer. The spectra were generated using 1800 processed PIV images acquired at a sampling rate of 200 Hz. 900 points FFT with Hanning window was used to compute the spectra. Although the sample size used to generate the velocity spectra is small, the existence of the spectral peaks is confirmed by repeating the spectral analysis at different locations along the cavity separated shear layer.

Figure 5.11 presents the development of the streamwise velocity spectra along the cavity separated shear layer. For clarity, the spectra were vertically separated by a margin of 20 dB. As evident from the figure, a low-frequency peak ($St \approx 0.05$) dominates the cavity separated shear layer. The existence of this spectral peak at different locations along the cavity separated shear layer confirms the actual existence of this peak in the flow.

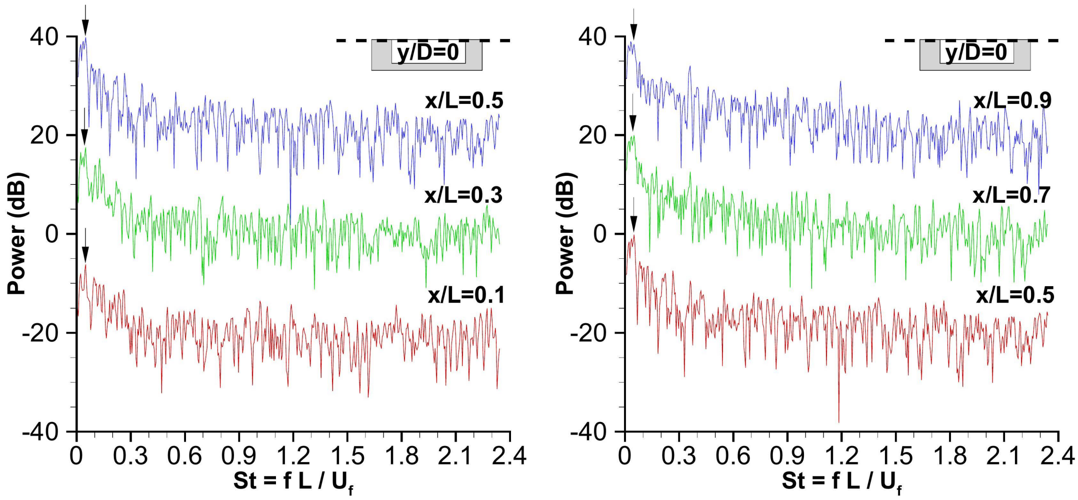

(a) upstream half (b) downstream half

Figure 5.11: Development of the streamwise velocity power spectra along the cavity separated shear layer ($y/D = 0$) for $Re_\theta = 1.28 \times 10^3$, no-jet.

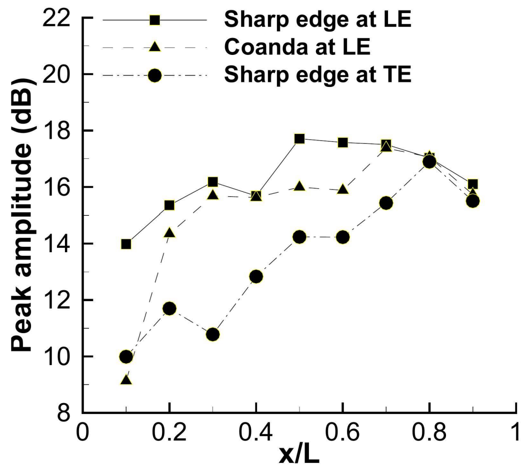

Figure 5.12: Peak amplitude of the dominant frequency along the cavity separated shear layer ($y/D = 0$) for $Re_\theta = 1.28 \times 10^3$, sharp edge at LE, no-jet.

The amplitude of the low-frequency peak was calculated along the cavity separated shear layer and is presented in Figure 5.12. The peak amplitude is calculated by subtracting the peak amplitude from the averaged broadband level of the spectrum. To check the repeatability of the results, the peak amplitudes of the other two baseline cases are included in the figure. The figure clearly indicates that the instability associated with this spectral peak is amplified along the upstream half of the cavity separated shear layer. However, at the downstream half, the amplitude of the instability peak starts to level out and eventually decreases upstream of the cavity trailing edge ($x/L = 0.8$) due to the interaction with the cavity trailing edge, which dissipates the energy of the instability.

To determine the source of this dominant spectral peak, the spectral analysis was performed along two flow paths, as demonstrated in Figure 5.13. Flow path 1 represents the cavity separated shear layer over the cavity trailing edge. Flow path 2 represents the cavity separated shear layer impinging at the cavity trailing edge and deflecting backwards. As evident from Figure 5.13 (a), the velocity spectrum of the upstream boundary layer (point "a") does not contain any low-frequency peaks. The peak appears at the cavity separated shear layer (point "b") and persists downstream of the cavity (point "c"). This indicates that the low-frequency peak is originated at the cavity separated shear layer and not upstream of the cavity. On the other hand, the spectral development along flow path 2 shows that the low-frequency peak disappears as the flow deflects backward at the cavity trailing edge, due to the broadband fluctuations of the recirculation zone.

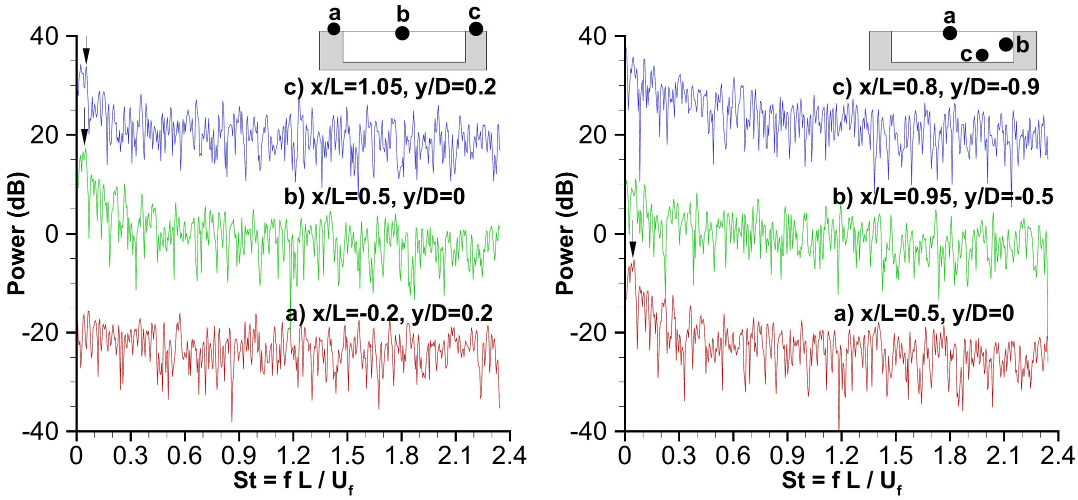

(a) Flow path 1 (b) Flow path 2

Figure 5.13: Development of the velocity power spectra along two flow paths for $Re_\theta = 1.28 \times 10^3$, sharp edge at LE, no-jet.

In conclusion, this figure indicates that the low-frequency peak is originated at the cavity separated shear layer, not upstream of the cavity nor the recirculation zone.

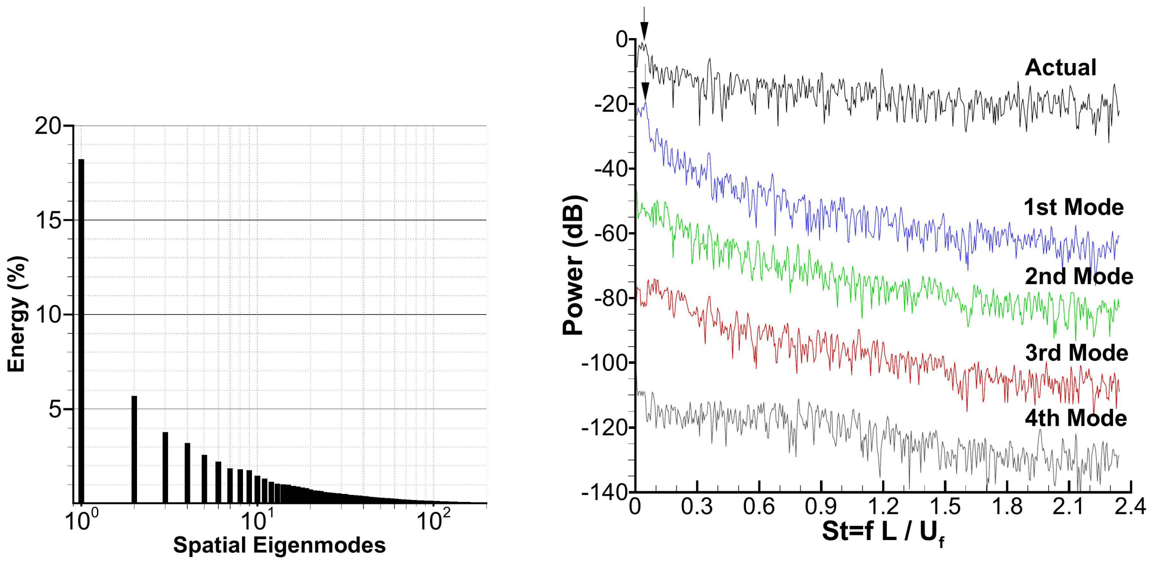

(a) Energy of spatial eigenmodes (b) Power spectra

Figure 5.14: Energy of the spatial eigenmodes and power spectra of the first four POD temporal coefficients for $Re_\theta = 1.28 \times 10^3$, sharp edge at LE, no-jet.

Figure 5.14 (a) shows the energy percentage of the spatial POD eigenmodes.

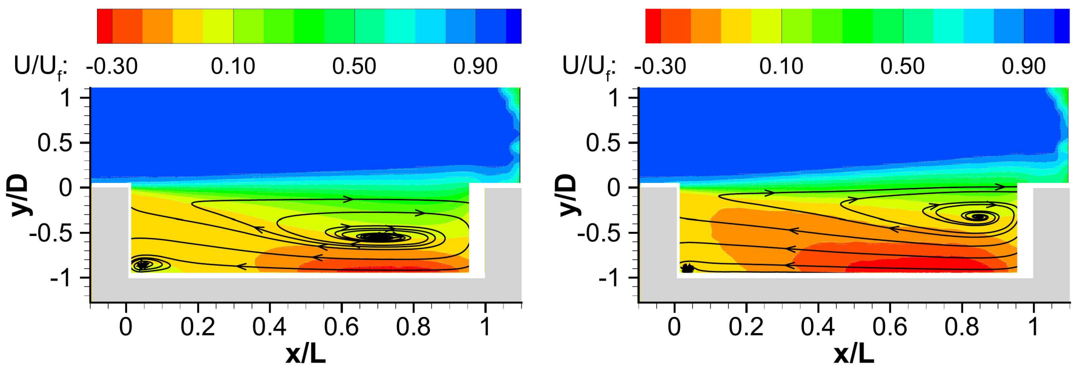

(a) No reverse flow interaction

(b) reverse flow interaction

Figure 5.15: U/U_f instantaneous fields approximated by the first POD mode for $Re_\theta = 1.28 \times 10^3$, sharp edge at LE, no-jet.

As illustrated in the figure, the first mode strongly dominates the flow (18% of the total energy). The spectra of this mode and the 2nd, 3rd, and 4th modes are presented in Figure 5.14 (b). The spectral analysis for these POD modes is generated using the time history of the POD temporal coefficients. As illustrated in the figure, the spectrum of the first mode is dominated by a spectral peak. This peak coincides with the low frequency peak of the actual flow field (without POD). Figure 5.15 demonstrates the U/U_f instantaneous images approximated by the first POD mode only. The figure relates the first POD mode with a large amplitude flapping of the cavity separated shear layer. From the above discussions, it can be concluded that the low frequency peak found in the velocity spectra of the cavity separated shear layer is associated with the large amplitude flapping motion, which is triggered by the reverse flow interaction.

In summary, the reverse flow interaction is a low frequency phenomenon. This interaction occurs occasionally and generates a large amplitude flapping wave in the cavity separated shear layer. As the wave propagates downstream, it amplifies until it reaches the cavity trailing edge where its energy is partially dissipated due to the interaction with the cavity trailing edge.

2.2 Higher-frequency instabilities

To reveal the large coherent vortical structures of the cavity separated shear layer, the fluctuating velocity flow fields were generated. The fluctuating velocity flow fields were produced by subtracting the instantaneous flow fields from the time-averaged field. Afterwards, a spatial filter with a Gaussian kernel was used

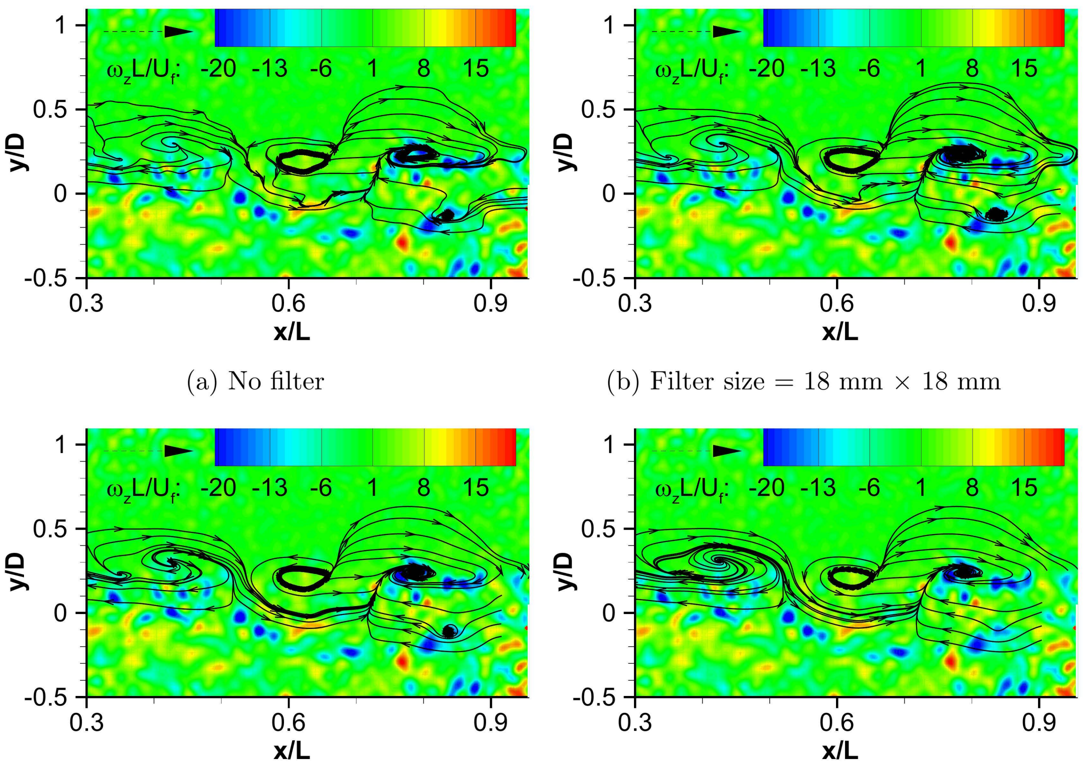

(a) No filter (b) Filter size = 18 mm × 18 mm

(c) Filter size = 27 mm × 27 mm (d) Filter size = 36 mm × 36 mm

Figure 5.16: Snapshot of the instantiation vorticity and the fluctuating velocity streamlines with different filter sizes. The dashed arrow indicates the free stream direction. $Re_\theta = 1.28 \times 10^3$, sharp edge at LE, no-jet

to filter out small structures, and hence it generates a clearer visualisation of the large coherent structures. Figure 5.16 (a) shows the unfiltered fluctuating velocity field. Two large vortical structures appear: one centred at ($x/L \approx 0.4$, $y/D \approx 0.3$) and the other centred at ($x/L \approx 0.8$, $y/D \approx 0.2$). Applying the spatial filter with a Gaussian kernel size of 18 mm × 18 mm (Figure 5.16 (b)) provides a clearer visualisation of vortical structures. Increasing the filter size to 27 mm × 27 mm (Figure 5.16 (c)) enhances the clarity of the large vortical structures further. Further increase in the kernel size (Figure 5.16 (d)) filters out some flow details without improving the clarity of the large vortical structures. Thus, it was decided to implement the spatial filter with a Gaussian kernel size of 27 mm × 27 mm. Using this method, sequential images were examined to count the coherent vortical structures passing over the cavity trailing edge. This method is time-consuming, and hence only 400 images were examined. For this reason, the vortex count provides a rough estimation of the shedding frequency.

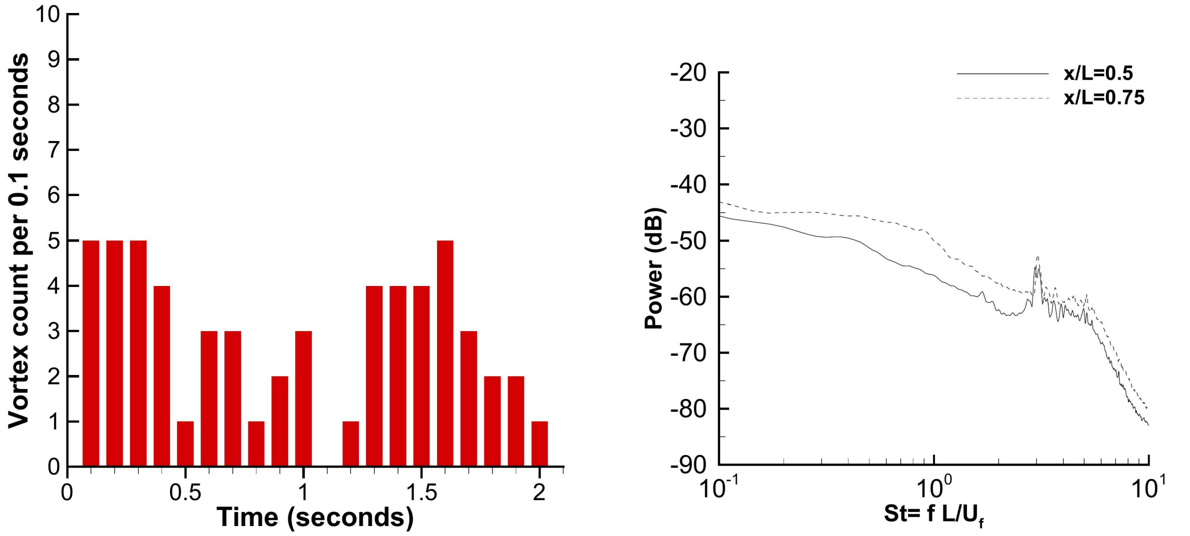

(a) Vortex count

(b) Development of the pressure power spectra

Figure 5.17: Vortex count of the coherent vortical structures and streamwise development of the unsteady pressure power spectra and for $Re_\theta = 1.28 \times 10^3$, sharp edge at LE, no-jet.

Figure 5.17 compares the vortex count results with the spectral development of the unsteady wall pressure at $x/L = 0.5$ and 0.75. Figure 5.17 (a) demonstrates that the shedding of the large vortical structures is highly intermittent and not regular with time. The average frequency estimated by the vortex count method is $St \approx 0.68$. This frequency is not visible in the unsteady wall pressure spectra presented in Figure 5.17 (b). This is due to the high intermittency of the vortical structures. For the same reason, Ashcroft and Zhang (2005) did not observe any sharp peak in the unsteady wall pressure spectra at $M \approx 0.1$ and L/D between 2 and 4. However, the figure shows a sharp spectral peak at $St \approx 3$. This frequency is four times higher than the frequency estimated by the vortex count and hence it cannot be related to the vortex shedding phenomenon. However, this frequency coincides with the first acoustic transversal mode estimated by Equation 2.6. The transversal acoustic mode has been observed by Ziada et al. (2003), Debiasi and Samimy (2004), Little et al. (2007), Chan et al. (2007) and Ashcroft and Zhang (2005). Therefore, it can be concluded that the narrow-band peak in the unsteady wall pressure spectra is attributed to the first acoustic transversal mode generated between the cavity and the wind tunnel.

2.3 Influence of the Reynolds number on the oscillations of the cavity separated shear layer

To examine the Reynolds number dependency of the aforementioned instabilities, the flow was tested at three Reynolds numbers, Re_θ, of: 1.28×10^3, 2.02×10^3, and 4.37×10^3. Figure 5.18 shows the influence of Re_θ on the temporal evolution of U/U_f near the cavity leading ($x/L = 0.2$) and trailing edges ($x/L = 0.8$) regions. The figures do not show any noticeable change in the surges of the reverse flow in Figures 5.18 (a), 5.18 (c), and 5.18 (e), nor in the oscillation peaks in Figures 5.18 (b), 5.18 (d), and 5.18 (f).

Figures 5.19 (a), 5.19 (c), and 5.19 (e) show the streamwise velocity spectra at ($x/L = 0.5$, $y/D = 0$) for different Re_θ. As illustrated in the figure, the low frequency peak is still dominating the cavity separated shear layer over the experimental range of Re_θ. The low frequency peaks are at $St \approx 0.05$, 0.018, and 0.008 for Re_θ: 1.28×10^3, 2.02×10^3, and 4.37×10^3, respectively. This indicates the dependency of the dimensionless frequency St on the Reynolds number Re_θ. The dimensionless frequency decreases with increasing Re_θ from 1.28×10^3 to 4.37×10^3. Figures 5.19 (b), 5.19 (d), and 5.19 (f) show the spectra of the unsteady wall pressure at $x/L = 0.5$ and $x/L = 0.75$. The figures show that the vortex shedding instability peak continues to disappear from the spectra due to the high intermittency. In contrast, the acoustic transversal mode continues to appear in the spectra. Increasing the Re_θ from 1.28×10^3 to 4.37×10^3 shifts the transversal mode from the first mode ($St \approx 3$) to the second mode ($St \approx 6$). On the other hand, no significant peak was found at $Re_\theta = 2.02 \times 10^3$.

Figure 5.20 shows the vortex count of the large coherent vortical structures at $Re_\theta = 1.28 \times 10^3$ and $Re_\theta = 2.02 \times 10^3$. No result was obtained for the $Re_\theta = 4.37 \times 10^3$ case. This is because at this Reynolds number, the propagation speed of the vortical structures is high, and hence the repetition rate of the PIV system is not sufficient to accurately count the vortical structures. The average frequency estimated by the vortex count method is $St \approx 0.68$ and 0.54 for $Re_\theta = 1.28 \times 10^3$ and 2.02×10^3, respectively. The variation of the dimensionless frequencies with the Re_θ is probably attributed to the uncertainty of the vortex count method. The figure also shows that the shedding phenomenon is still highly intermittent even at a higher Re_θ.

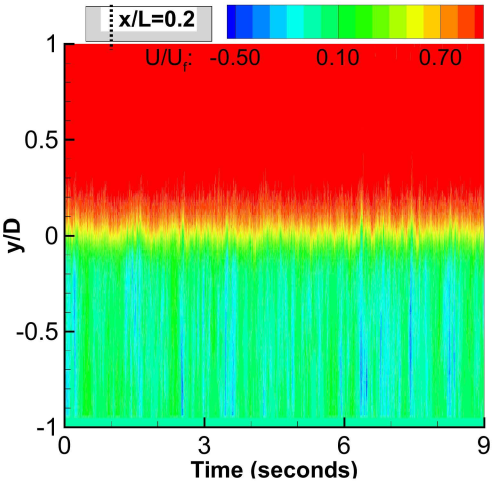

(a) $Re_\theta = 1.28 \times 10^3$ $(x/L = 0.2)$

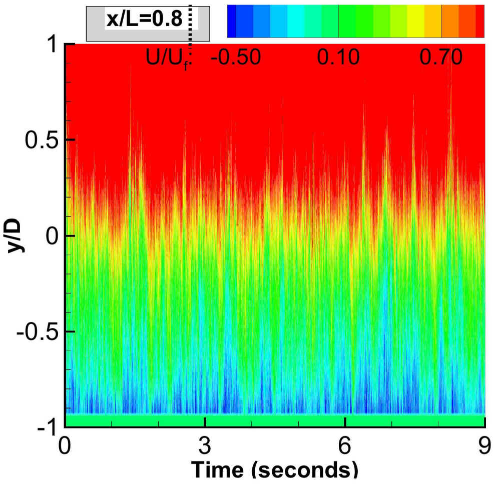

(b) $Re_\theta = 1.28 \times 10^3$ $(x/L = 0.8)$

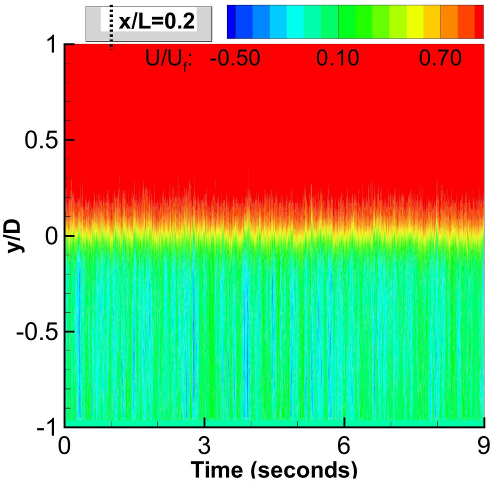

(c) $Re_\theta = 2.02 \times 10^3$ $(x/L = 0.2)$

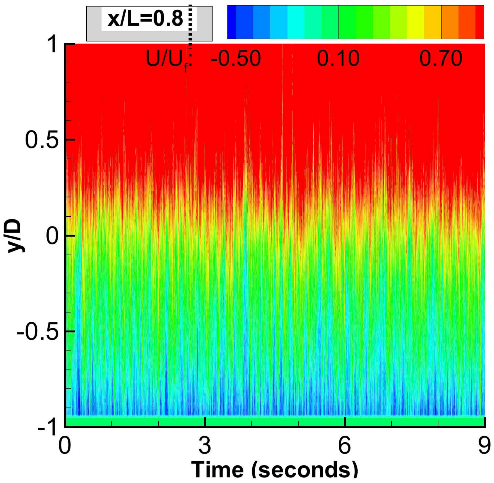

(d) $Re_\theta = 2.02 \times 10^3$ $(x/L = 0.8)$

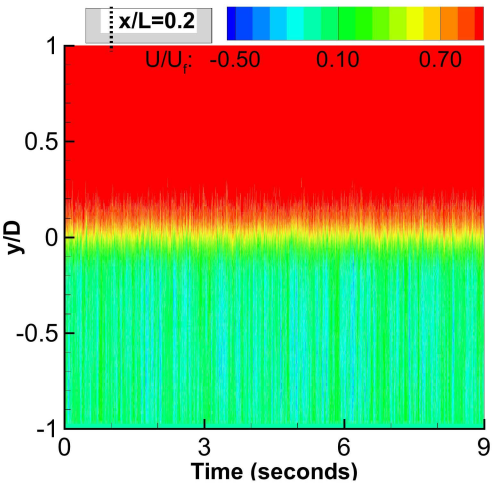

(e) $Re_\theta = 4.37 \times 10^3$ $(x/L = 0.2)$

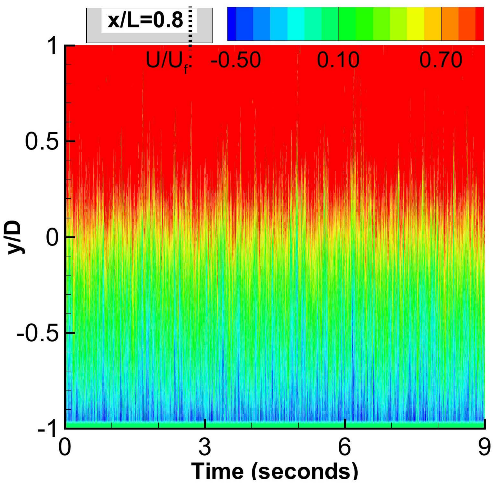

(f) $Re_\theta = 4.37 \times 10^3$ $(x/L = 0.8)$

Figure 5.18: Temporal evolution of U/U_f at two streamwise stations for different Re_θ, sharp edge at LE, no-jet.

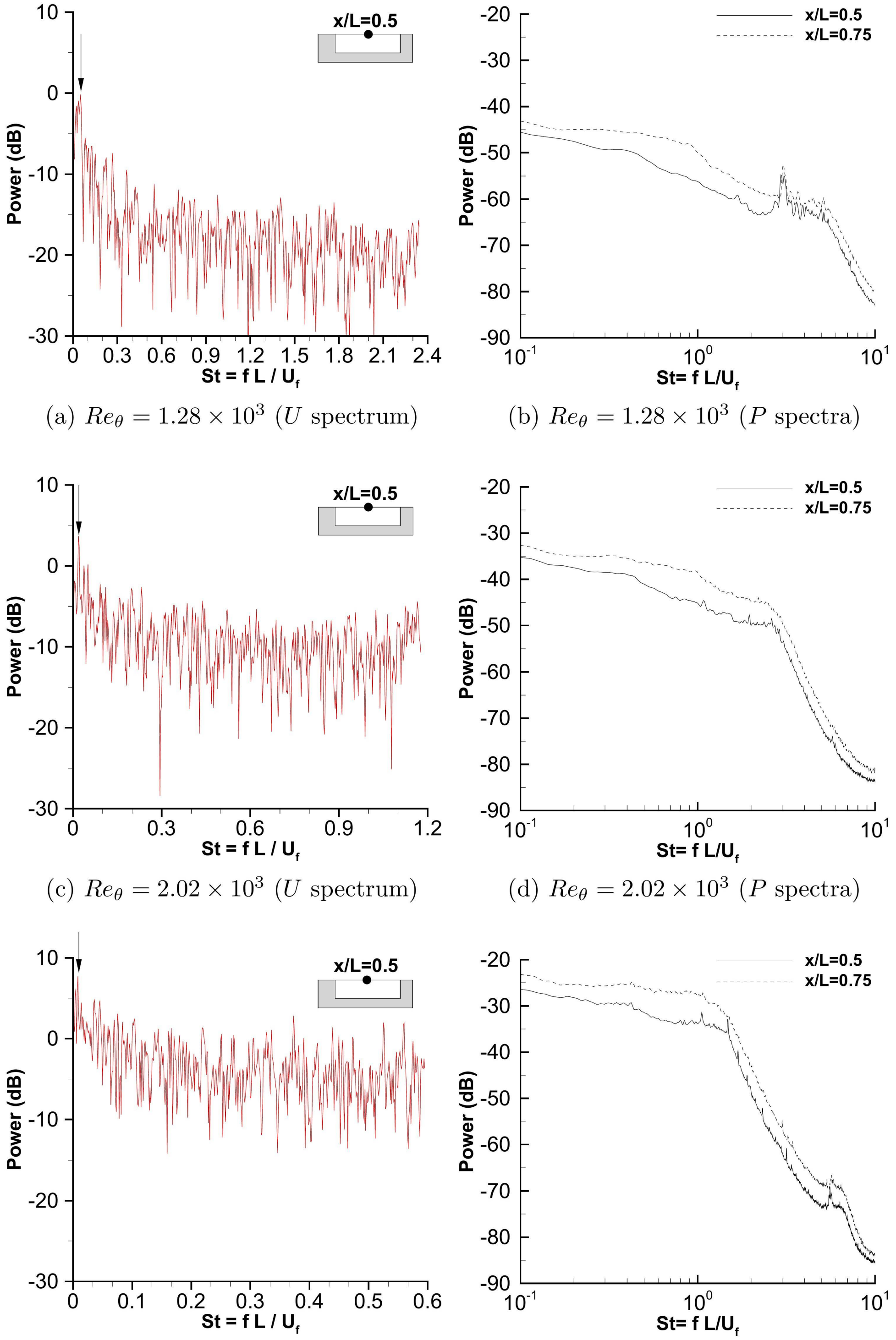

(a) $Re_\theta = 1.28 \times 10^3$ (U spectrum)

(b) $Re_\theta = 1.28 \times 10^3$ (P spectra)

(c) $Re_\theta = 2.02 \times 10^3$ (U spectrum)

(d) $Re_\theta = 2.02 \times 10^3$ (P spectra)

(e) $Re_\theta = 4.37 \times 10^3$ (U spectrum)

(f) $Re_\theta = 4.37 \times 10^3$ (P spectra)

Figure 5.19: Power spectra of the streamwise velocity at ($x/L = 0.5$,$y/D = 0$) and the unsteady pressure for different Re_θ, sharp edge at LE, no-jet.

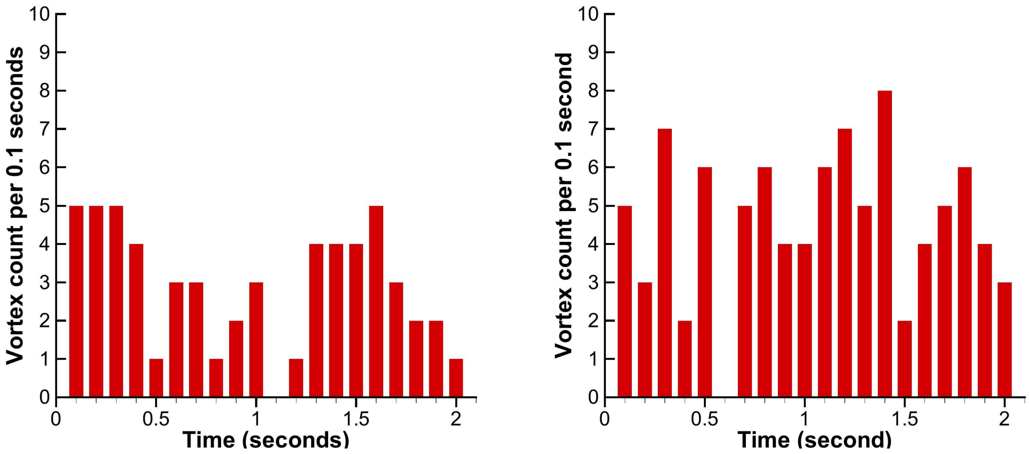

(a) $Re_\theta = 1.28 \times 10^3$ (b) $Re_\theta = 2.02 \times 10^3$

Figure 5.20: Vortex count of the coherent vortical structures for different Re_θ, sharp edge at LE, no jet.

3 Concluding remarks

Firstly, the time-averaged flow field and the instabilities of the cavity separated shear layer were investigated for the baseline cavity flow (without a jet) at $Re_\theta = 1.28 \times 10^3$. The first part of the investigation is concluded as follows:

- Changing the slot configuration influences the time-averaged flow field. Modifying the slot configuration causes a shift in the centre of the main recirculation vortex. However, the time-averaged flow fields for these cases are generally similar. Therefore, it was decided to focus this chapter on a single slot configuration, which is the cavity with the sharp edge slot at the cavity leading edge.

- The surface oil flow visualisations showed that the cavity flow is likely to be two-dimensional. The time-averaged flow fields demonstrate a typical shallow open cavity flow, that is similar to those described in the literature.

- The velocity spectra showed that a low frequency instability ($St \approx 0.05$) dominates the cavity separated shear layer. This instability is attributed to the reverse flow interaction. The interaction takes place when sudden reverse flow surges reach the sensitive separation point of the cavity separated shear layer. As a result, a large-amplitude flapping wave is produced. As the wave propagates downstream the cavity separated shear layer, it amplifies until it reaches the cavity trailing edge region, where the wave is partially dissipated due to the interaction with the cavity trailing edge.

- Higher frequency instabilities were identified in the flow: (i) the shedding of the large vortical structures ($St \approx 0.68$) which was estimated by the vortex count method, and (ii) the first transversal mode ($St \approx 3$) which was identified from the unsteady wall pressure spectra. The spectral peak related to the shedding of the large vortical structures was not found in the unsteady wall pressure spectra because the shedding phenomenon is highly intermittent and not well organised.

Secondly, the cavity flow was investigated at $1.28 \times 10^3 \leq Re_\theta \leq 4.37 \times 10^3$ to study the Reynolds number dependency of the cavity separated shear layer instabilities. The second part of the investigation is concluded as follows:

- The dimensionless frequencies of the reverse flow interaction and transversal mode showed a clear Reynolds number dependency. Increasing Re_θ from 1.28×10^3 to 4.37×10^3 causes a reduction in the dimensionless frequency of the reverse flow interaction from $St \approx 0.05$ to $St \approx 0.008$. Increasing Re_θ also causes the transversal mode to jump from the first to the second mode. In contrast, the variation of the dimensionless frequency for the shedding of the large vortical structures with Re_θ is probably attributed to the uncertainty of the vortex count method.

Chapter 6

Blowing from Cavity Leading Edge

This chapter investigates the impact of blowing from the cavity leading edge on the time-averaged cavity flow field and the oscillations of the cavity separated shear layer at $Re_\theta = 1.28 \times 10^3$. Two blowing jet cases will be examined: jets from the sharp edge slot and jets from the coanda slot. Both slots are a horizontal to the x-axis. The values of the jet momentum flux per unit width J are 0.11 $kg/m.s^2$, 0.44 $kg/m.s^2$, and 0.96 $kg/m.s^2$.

1 Surface oil flow visualisations

Figure 6.1 shows the images of the surface oil flow visualisations for no-jet and jet-on cases. At $J = 0.11$ $kg/m.s^2$, the reverse flow is parallel to the x-axis, as evident from Figure 6.1 (b). As J increases further, the reverse flow starts to diverge towards the side plates. This divergence increases with J, as illustrated in Figures 6.1 (c) and 6.1 (d). This divergence is attributed to the impingement of the jets at the cavity trailing edge. This impingement raises the stagnation pressure at the mid-span of the cavity compared to the side regions, where the jet is not applied. As a result, the reverse flow diverges towards the side regions of the cavity. Despite this flow divergence, the reverse flow at the mid-span region remains parallel to the x-axis, and hence the flow at this region, where the PIV and pressure measurements are acquired, is likely to be two-dimensional.

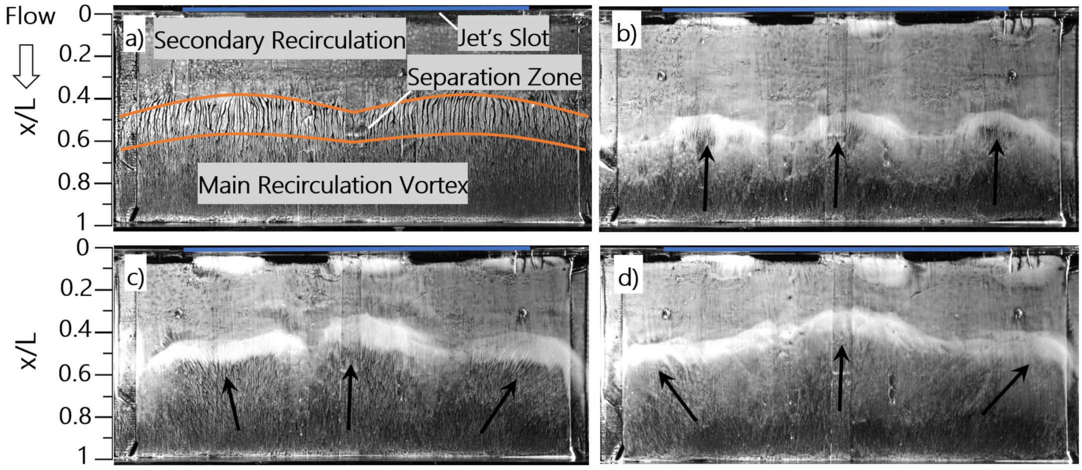

Figure 6.1: Surface oil flow visualisations for $Re_\theta = 1.28 \times 10^3$, sharp edge at LE, different J: a) no jet, b) $J = 0.11\ kg/m.s^2$, c) $J = 0.44\ kg/m.s^2$, and d) $J = 0.96\ kg/m.s^2$.

2 Time-averaged flow field

2.1 Jet penetration

Before examining the jet impact on the cavity flow, it is essential to study how the jet penetrates the cavity flow. Figure 6.2 shows the instantaneous PIV raw images and the time-averaged V/U_f fields for different values of J. As shown in Figures 6.2 (a) and 6.2 (c), the jet at $J = 0.11\ kg/m.s^2$ and $J = 0.44\ kg/m.s^2$ flows parallel to the cavity separated shear layer and then impinges at the upper part of the cavity trailing edge. On the other hand, the jet at $J = 0.96\ kg/m.s^2$ deflects downwards and impinges at the lower part of the cavity trailing edge, as illustrated in Figures 6.2 (e). This deflection is clearly indicated by a large downward V velocity in region "B", as demonstrated in Figure 6.2 (f). The jet impingement at the cavity trailing edge causes a significant increase in the upward V velocity at region "A", as illustrated in Figures 6.2 (b), 6.2 (d), and 6.2 (f). This increase in the upward V velocity, as it will be shown later, influences the boundaries of the cavity separated shear layer.

The jet deflection at $J = 0.96\ kg/m.s^2$ is attributed to two reasons: (i) the coanda effect, and (ii) the difference in the jet's growth rate between the upper and lower sides of the jet. The coanda effect causes the jet to deflect towards the cavity floor. This effect has been already observed in Chapter 4 for the jet at quiescent conditions (without free stream). Thus, the coanda effect is at least partially responsible for the jet deflection in the dynamic conditions (with free stream). On the other hand, the difference in the jet's growth rate between the two halves of the jet is because the upper side of the jet is in contact with the

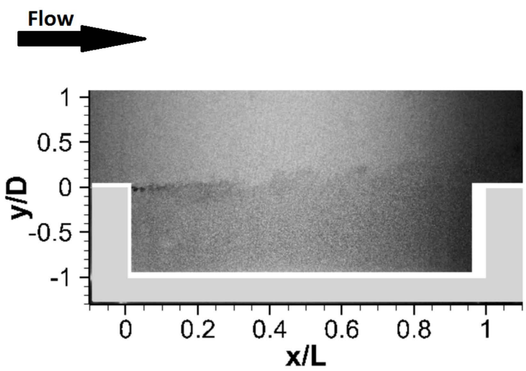

(a) Instantaneous raw image ($J = 0.11\ kg/m.s^2$)

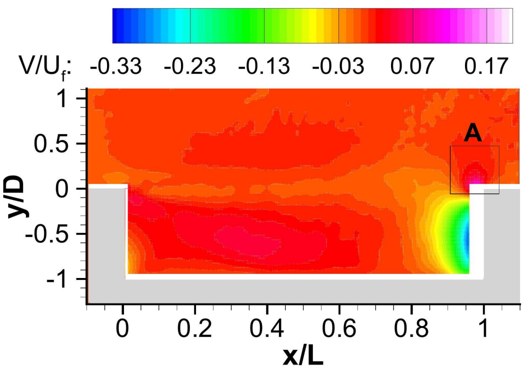

(b) V/U_f ($J = 0.11\ kg/m.s^2$)

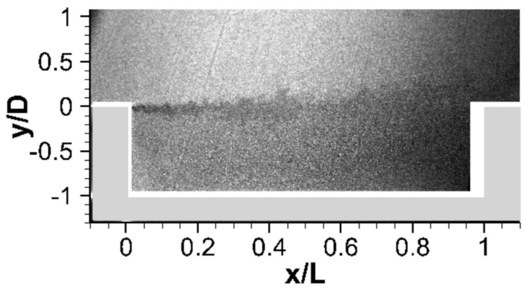

(c) Instantaneous raw image ($J = 0.44\ kg/m.s^2$)

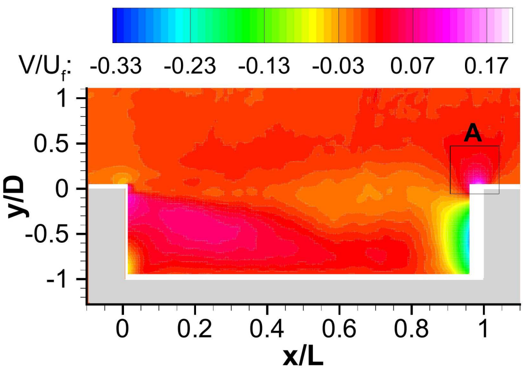

(d) V/U_f ($J = 0.44\ kg/m.s^2$)

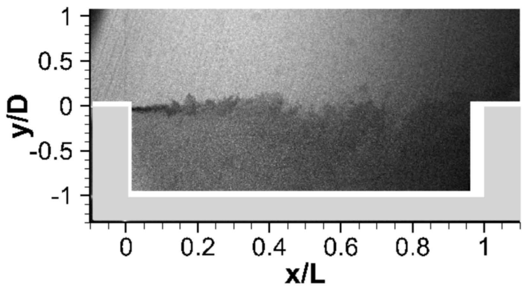

(e) Instantaneous raw image ($J = 0.96\ kg/m.s^2$)

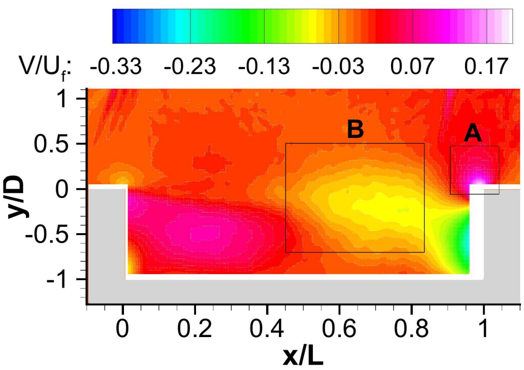

(f) V/U_f ($J = 0.96\ kg/m.s^2$)

Figure 6.2: The instantaneous PIV raw images and the time-averaged V/U_f for $Re_\theta = 1.28 \times 10^3$, sharp edge at LE, different J.

relatively fast-moving free stream, while the lower side of the jet is in contact with the relatively slow-moving cavity flow. As a result, the jet's growth rate of the lower side is much larger than that of the upper side. This is because the strongly advected side of the jet (the upper side) has difficulty in entraining the free stream fluid into the jet, as the jet momentum at this side of the jet is relatively small compared to the momentum of the free stream, and vice versa for the weakly advected side of the jet (the lower side) (Wang, 2000). This is consistent with many studies on jet interaction in a co-flowing free stream, such as the studies of Ben Haj Ayech et al. (2016) and Kalifa et al. (2016). These studies found that increasing the free stream velocity significantly reduces the jet's growth rate.

To examine the jet penetration further, the time-averaged U/U_f profiles for different axial stations are plotted in Figure 6.3 for various J values. To show the profiles clearly, they are separated by a margin of 0.25 along the U/U_f axis. At $J = 0.11\ kg/m.s^2$, the jet completely mixes with the cavity flow near the cavity leading edge, and hence it has almost no influence on the velocity profiles downstream, as illustrated in Figure 6.3 (a). However, at $J = 0.44\ kg/m.s^2$, the jet penetrates the cavity separated shear layer, as demonstrated in Figure 6.3 (b). As shown in the figure, the jet penetration is indicated by the excess streamwise velocity within the cavity separated shear layer (C.S.S.L). As the jet expands downstream, the excess velocity decreases until the two profiles collapse into one profile at $x/L \approx 0.6$. At $J = 0.96\ kg/m.s^2$, the penetration effect is stronger, as shown in Figure 6.3 (c). As evident from the figure, the lower side of the jet growths faster than the upper side. As the jet expands and deflects downwards, the excess velocity decreases until the two profiles collapse into one profile at $x/L \approx 0.9$. It is also important to notice that the jet causes a reduction in the streamwise velocity near the cavity trailing edge (region "C"), as demonstrated in Figures 6.3 (b) and 6.3 (c). This reduction is attributed to the increase of the upward V velocity at the cavity trailing edge, which impedes the flow of the cavity separated shear layer, as highlighted in region "A" in Figure 6.2.

2.2 Jet impact on the cavity flow topology

The next step is to investigate the jet impact on the cavity flow topology. The time-averaged U/U_f fields for the no-jet and jet-on cases are shown in Figure 6.4. Forcing the jet at $J = 0.11\ kg/m.s^2$ does not yield significant changes in the velocity field. As J increases to 0.44 $kg/m.s^2$, the jet penetration through the cavity separated shear layer appears clearly at the cavity leading edge region, as indicated by the arrow in Figure 6.4 (c). The centre of the main recirculation vortex shifts upstream, while the reverse flow rate increases significantly. Increasing J to 0.96 $kg/m.s^2$ causes a clearer jet penetration effect and shifts the main recirculation vortex further towards the cavity leading edge (centred at $x/L \approx 0.5$), due to the downward jet deflection, as illustrated in Figure 6.4 (d). On the other

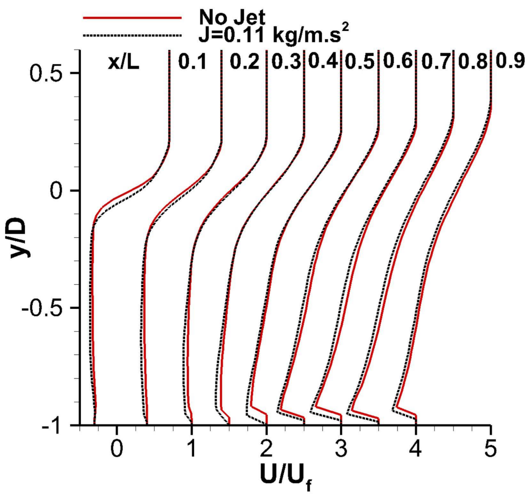

(a) $J = 0.11\ kg/m.s^2$

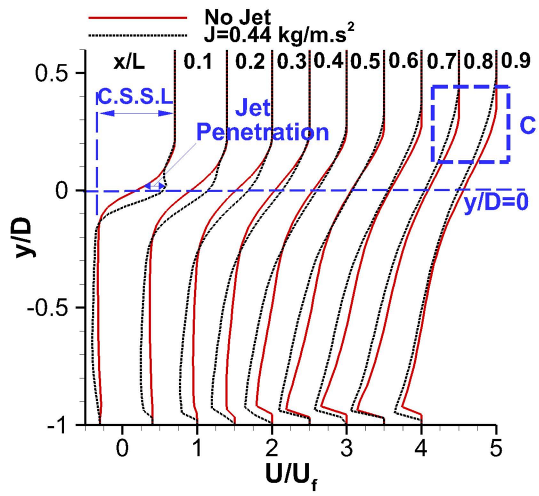

(b) $J = 0.44\ kg/m.s^2$

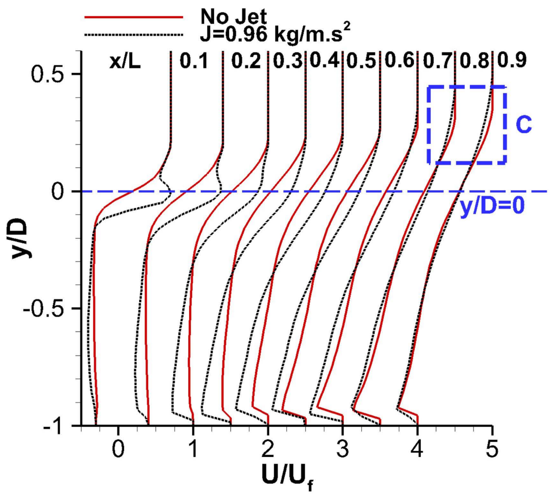

(c) $J = 0.96\ kg/m.s^2$

Figure 6.3: Time-averaged U/U_f profiles at different axial stations for $Re_\theta = 1.28 \times 10^3$, sharp edge at LE, different J. C.S.S.L: denotes the cavity separated shear layer.

hand, there is a small increase in the reverse flow rate for this case compared to the $J = 0.44\ kg/m.s^2$ case.

The increase in the reverse flow rate causes the separation zone to displace towards the cavity leading edge. Figure 6.5 shows the distribution of U/U_f along the cavity floor ($y/D = -0.9$). The streamwise locations X_{R1}, X_{R2}, and $X_{R3,4}$ denote the separation point for no-jet, $J = 0.11\ kg/m.s^2$, and $J = 0.44\ kg/m.s^2$ cases, respectively. The figure shows that for $J = 0.11\ kg/m.s^2$, the separation point is displaced upstream from $x/L \approx 0.2$ to $x/L \approx 0.1$. Increasing J to $0.44\ kg/m.s^2$ slightly shifts the separation point to $x/L \approx 0.07$. A similar position of the separation point is found at $0.96\ kg/m.s^2$.

Figure 6.6 compares the the time-averaged U/U_f for: a) blowing from the cavity leading edge in the current experiments, and b) blowing from the cavity leading edge in Suponitsky et al. (2005) simulation. The L/D and B_c for both

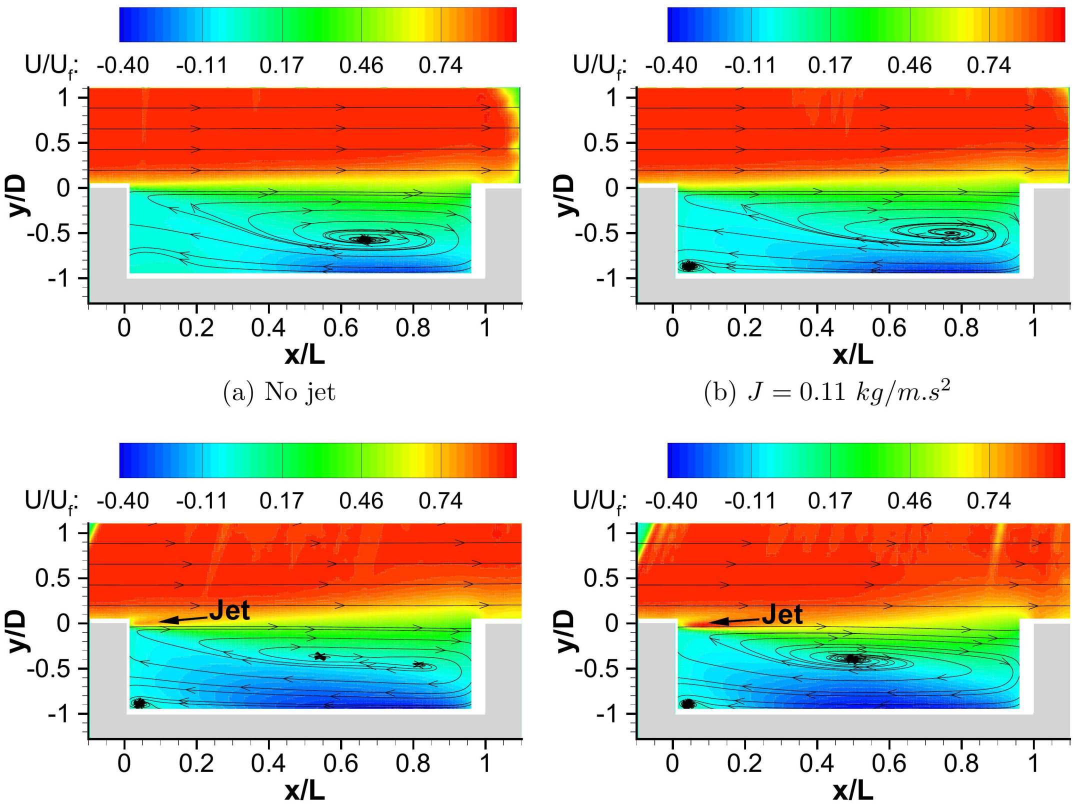

(a) No jet (b) $J = 0.11\ kg/m.s^2$

(c) $J = 0.44\ kg/m.s^2$ (d) $J = 0.96\ kg/m.s^2$

Figure 6.4: Contours of the time-averaged U/U_f for $Re_\theta = 1.28 \times 10^3$, sharp edge at LE, different J.

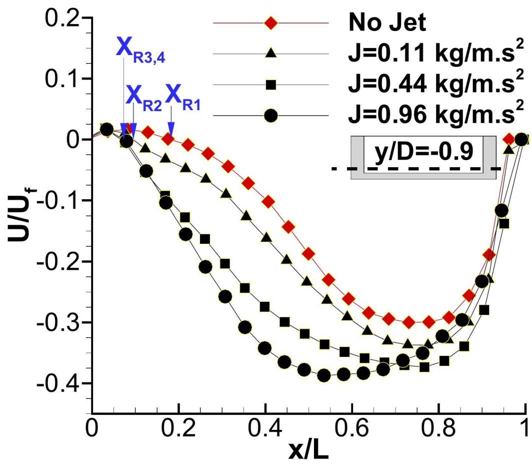

Figure 6.5: Distribution of U/U_f along the cavity floor ($y/D = -0.9$) for $Re_\theta = 1.28 \times 10^3$, sharp edge at LE, different J.

cases are 4 and 1%, respectively. $B_c =$ is blowing coefficient and is defined as

$$B_c = \frac{\rho_j U_j A_j}{\rho_f U_f A_{cavity}} \tag{6.1}$$

where ρ_j U_j A_j denote the jet density, jet velocity at the slot, and slot area, while ρ_f U_f A_{cavity} denote free stream density, free stream velocity, and cavity floor area. The Re_d are 49.5×10^3 and 5×10^3 for the current experiments and Suponitsky et al. (2005) simulation, respectively. According to Suponitsky et al. (2005), increasing B_c to 1% causes the cavity separated shear layer to be isolated from the recirculation zone. As a result, the main recirculation vortex becomes weaker and the maximum reverse flow velocity decreases from 37% to 10%. These findings contradict with the current study. According to the current study, increasing B_c to 1% causes a significant increase in the maximum reverse flow velocity from 30% to approximately 40%.

2.3 Jet impact on the cavity separated shear layer

The jet influences on the time-averaged cavity separated shear layer include: the Reynolds stresses, the boundaries of the cavity separated shear layer, and the growth rate. The Reynolds shear stresses indicate the momentum transfer by turbulent fluctuations. Figure 6.7 shows the time-averaged Reynolds shear stress for the no-jet and jet-on cases. As illustrated in the figure, increasing J yields

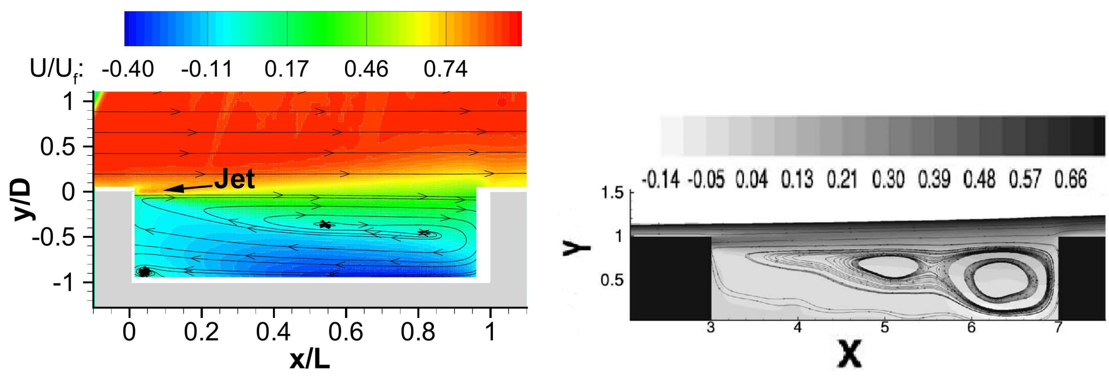

(a) $J = 0.44\ kg/m.s^2$ (B_c=1%) (b) Suponitsky et al. (2005) (B_c=1%)

Figure 6.6: Contours of the time-averaged U/U_f at B_c=1% for: a) current experiments, and b) Suponitsky et al. (2005)

a substantial increase in the Reynolds shear stress in the cavity separated shear layer. This increase is due to the jet disturbances. The jet disturbances consist of pairs of counter-rotating vortical structures generated due to the positive and negative vorticity regions downstream of the jet's slot, as illustrated in Figure 6.8 (b). These disturbances raise the turbulent fluctuation level in the cavity separated shear. Figure 6.7 also illustrates a noticeable downward shift in the peak location of the Reynolds shear stress from $y/D \approx 0$ for the no-jet case to $y/D \approx -0.36$ for the $J = 0.96\ kg/m.s^2$ case. This shift is attributed to the downward jet deflection.

Figure 6.9 (a) shows the time-averaged boundaries of the cavity separated layer. The upper and lower boundaries are based on the locations of $U/U_f = 0.9$ and $U/U_f = 0.1$, respectively. At the upstream half of the cavity separated shear layer ($x/L \leq 0.5$), increasing J yields a downward shift in the boundaries of the cavity separated shear layer. This shift is because the momentum is transferred from the jet to the surrounding fluid at both sides of the jet. On the other hand, at the downstream half of the cavity separated shear layer ($x/L \geq 0.5$), increasing J causes the $U/U_f = 0.9$ boundaries to lift up. This lift is caused by the upward V velocity observed in region "A", as shown previously in Figure 6.2. The upward V velocity impedes the flow of the cavity separated shear layer. As a result the streamwise velocity decreases and the thickness of the cavity separated shear layer increases.

Figure 6.9 (b) shows the vorticity thickness of the cavity separated shear layer along the x-axis. Based on this figure, the growth rates of the cavity separated shear layer for the no-jet and jet one cases are estimated in Table 6.1. As evident from the table, the growth rate increases with J. This increase is attributed to two reasons: (i) the transfer of jet momentum to the cavity flow at the upstream half of the cavity ($x/L \leq 0.5$), and (ii) the lifting of the $U/U_f = 0.9$ boundary for the cavity separated shear layer at the downstream half of the cavity ($x/L \leq 0.5$) due to the upward V velocity.

Table 6.1: Growth rate of the cavity separated shear layer for $Re_\theta = 1.28 \times 10^3$, sharp edge at LE, different J.

J $(kg/m.s^2)$	No Jet	0.11	0.44	0.96
$d\delta_\omega/dx$	0.180	0.183	0.229	0.256

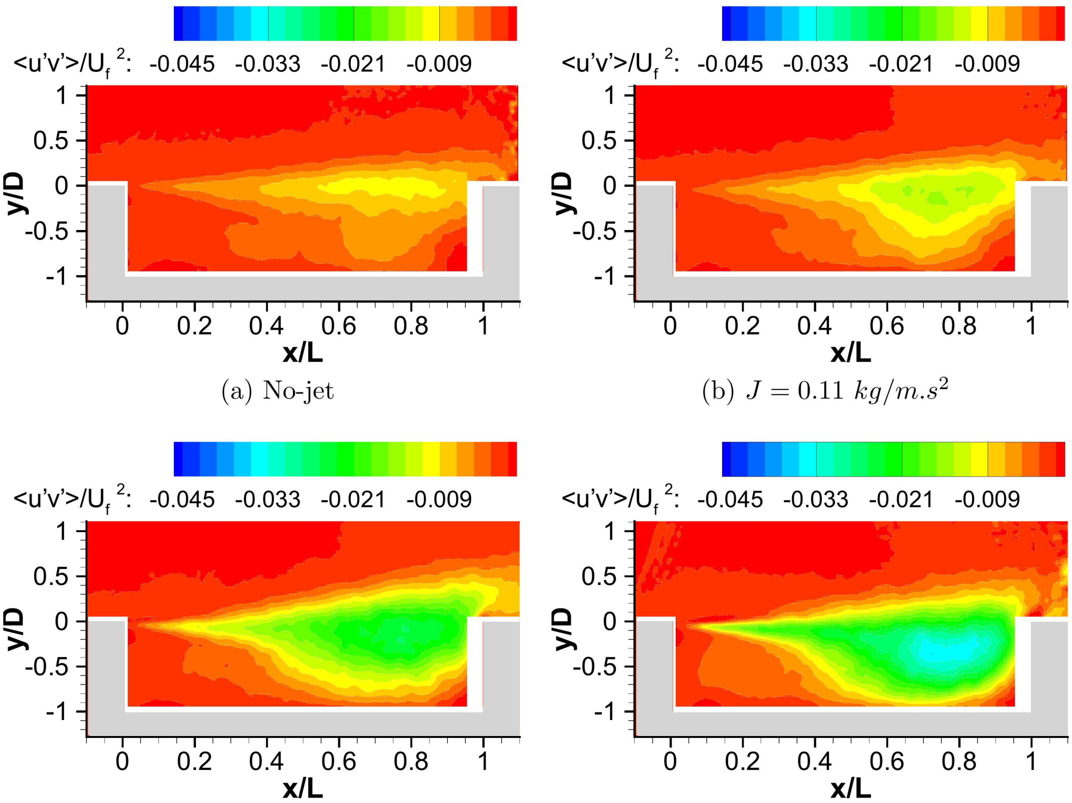

(a) No-jet

(b) $J = 0.11\ kg/m.s^2$

(c) $J = 0.44\ kg/m.s^2$

(d) $J = 0.96\ kg/m.s^2$

Figure 6.7: Contours of the time-averaged Reynolds shear stress for $Re_\theta = 1.28 \times 10^3$, sharp edge at LE, different J.

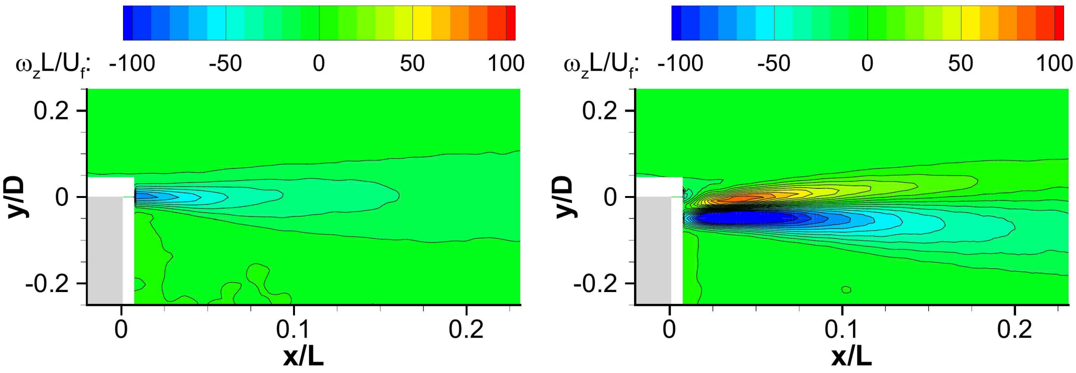

(a) No-jet (b) $J = 0.96\ kg/m.s^2$

Figure 6.8: Contours of the time-averaged $\omega_z L/U_f$ at the cavity leading edge region for
$Re_\theta = 1.28 \times 10^3$, sharp edge at LE, different J.

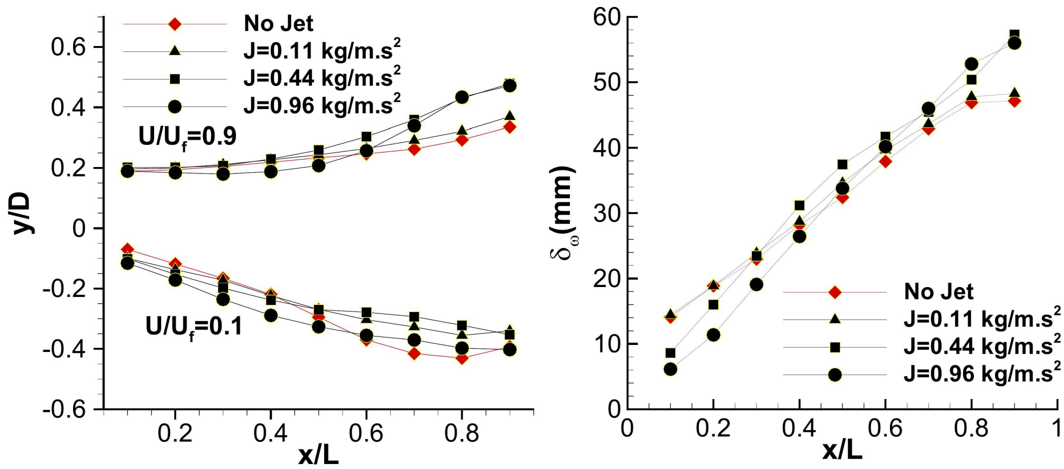

(a) Boundaries of the separated shear layer (b) Vorticity thickness

Figure 6.9: The time-averaged boundaries and vorticity thickness of the cavity separated shear layer along x-axis for
$Re_\theta = 1.28 \times 10^3$, sharp edge at LE, different J.

3 Oscillations of the cavity separated shear layer

The oscillations of the cavity separated shear layer are affected by the blowing from the cavity leading edge. Figure 6.10 illustrates the temporal evolution of U/U_f at $x/L = 0.2$ and 0.8 for the no-jet and jet-on cases. The figure does not show any noticeable change in the flow behaviour between the no-jet case and the $J = 0.11\ kg/m.s^2$ jet case. As J increases to $J = 0.44\ kg/m.s^2$, the number of the reverse flow surges arriving at $x/L = 0.2$ increases significantly, as evident from Figure 6.10 (e). Consequently, the number of the oscillation peaks in the cavity separated shear layer at $x/L = 0.8$ increases, as shown in Figure 6.10 (f). However, increasing J from 0.44 $kg/m.s^2$ to 0.96 $kg/m.s^2$ does not yield any noticeable increase in the number of the reverse flow surges, nor the oscillation peaks.

To quantify the frequency of the reverse flow interaction, the streamwise velocity power spectra at $x/L = 0.9$ and $y/D = 0$ is presented in Figure 6.11 (a). As shown in the figure, forcing the jet at $J = 0.11$ $kg/m.s^2$ does not produce any increase in the dominant frequency. However, as J increases to 0.44 $kg/m.s^2$, the dominant frequency increases from $St \approx 0.05$ to $St \approx 0.1$. Increasing J further to 0.96 $kg/m.s^2$ does not yield any further rise in the dominant frequency. The significant increase in the frequency of the reverse flow interaction at $J = 0.44$ $kg/m.s^2$ is attributed to the large increase in the reverse flow rate impacting the sensitive separation point at the cavity leading edge, as evident from the time-averaged V/U_f along the centre of the main recirculation vortex (Figure 6.11 (b)). As J increases, the jet impingement at the cavity trailing edge increases the reverse flow rate and pushes the main recirculation vortex upstream. As a result, more reverse flow impacts the cavity leading edge region, and hence the frequency of the reverse flow interaction increases. However, increasing J from 0.44 $kg/m.s^2$ to 0.96 $kg/m.s^2$ does not produce a significant increase in the amount of the reverse flow impacting the cavity leading edge, perhaps due to the increase in the divergence of reverse flow, as shown previously in Figure 6.1. Consequently, the frequency of the reverse flow interaction does not increase further.

The jets also supply the cavity with relatively small coherent structures. These structures are likely to impact the cavity flow and hence it is essential to study their temporal behaviour. Figure 6.12 shows snapshots of the instantaneous dimensionless z-vorticity for the no-jet and jet-on cases. As J increases, the jet populates the cavity separated shear layer with relatively smaller vortical structures, as indicated in Figures 6.12 (c) and 6.12 (d). The sequential snapshots of the fluctuating velocity field show that these structures develop at the proximity region of the slot. The fluctuating velocity field also shows that most of the jet vortical structures are rotating clockwise and few of them are rotating anti-clockwise. The lack of the anti-clockwise vortical structures is because the anti-clockwise vorticity region (positive vorticity) at the upper half of the jet is

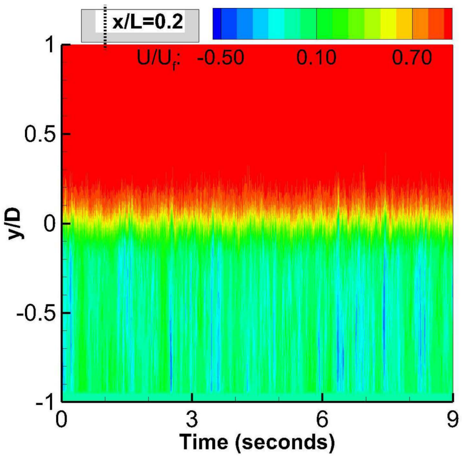

(a) No jet ($x/L = 0.2$)

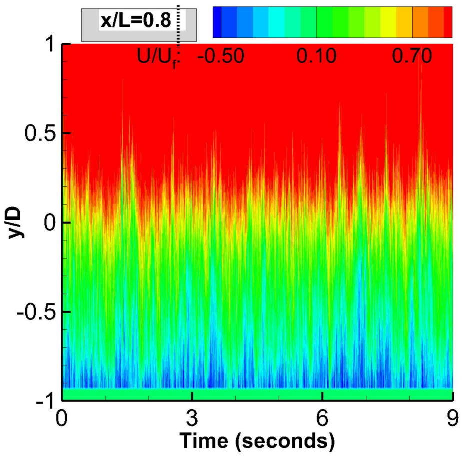

(b) No jet ($x/L = 0.8$)

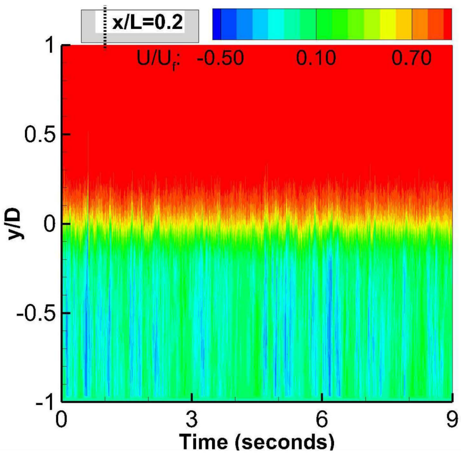

(c) $J = 0.11\ kg/m.s^2$ ($x/L = 0.2$)

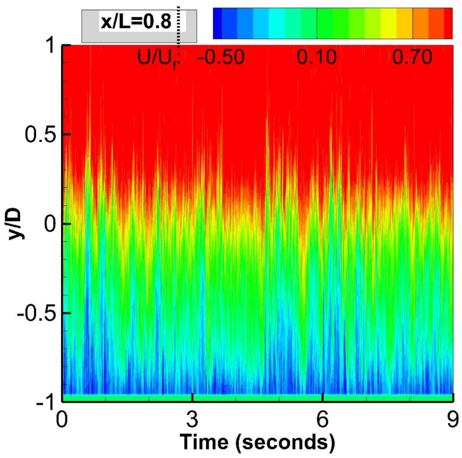

(d) $J = 0.11\ kg/m.s^2$ ($x/L = 0.8$)

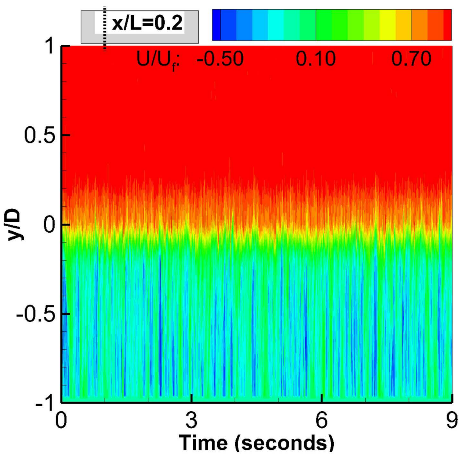

(e) $J = 0.44\ kg/m.s^2$ ($x/L = 0.2$)

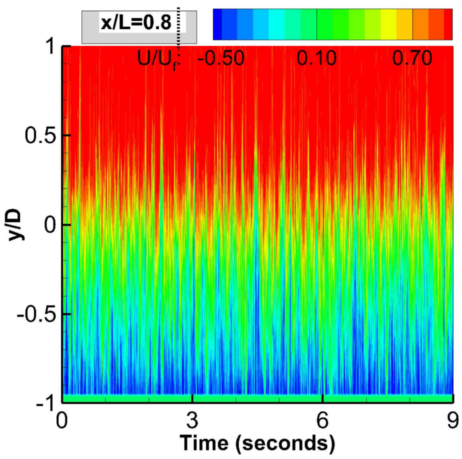

(f) $J = 0.44\ kg/m.s^2$ ($x/L = 0.8$)

Figure 6.10: Temporal evolution of U/U_f at x/L=0.2 and 0.8 for $Re_\theta = 1.28 \times 10^3$, sharp edge at LE, different J.

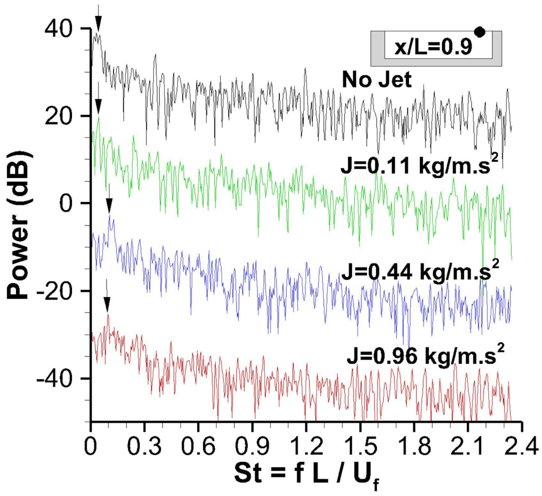

(a) U velocity spectra

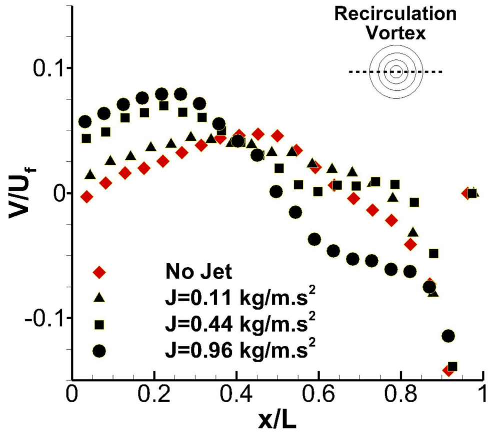

(b) V/U_f profiles along the recirculation vortex

Figure 6.11: U Velocity spectra at $x/L = 0.9$, $y/D = 0$ and profiles of the time-averaged V/U_f along the centre of the main recirculation vortex for $Re_\theta = 1.28 \times 10^3$, sharp edge at LE, different J.

highly suppressed by the clockwise vorticity of both the cavity separated shear layer and the lower half of the jet. At $J = 0.11\ kg/m.s^2$, the anti-clockwise vorticity region (positive vorticity) of the jet is completely suppressed, as illustrated in Figure 6.12 (b). The region of the anti-clockwise vorticity starts to appear at $J = 0.44\ kg/m.s^2$ and increases at $J = 0.96\ kg/m.s^2$, as indicated by the arrows in Figures 6.12 (c) and 6.12 (d). Consequently, the number of the anti-clockwise vortical structures observed in the flow increases.

The sequential snapshots of the fluctuating velocity field show that most of the jet vortical structures at $J = 0.44\ kg/m.s^2$ and $J = 0.96\ kg/m.s^2$ either dissipate, impinge at the cavity trailing edge, or deflect downwards. The fluctuating velocity field also shows that the large vortical structures are still present in the cavity separated shear layer along with the jet structures. It is difficult to quantify the impact of the jet structures on the shedding frequency for the coherent vortical structures of the cavity separated shear layer due to two reasons. First, the vortex count method provides a rough estimation of the shedding frequency. Second, it is sometimes difficult to distinguish between the jet structures and the structures of the cavity separated shear layer.

The jet structures are responsible for the rise in the turbulent fluctuation level and the turbulence broadband level of the unsteady wall pressure spectra

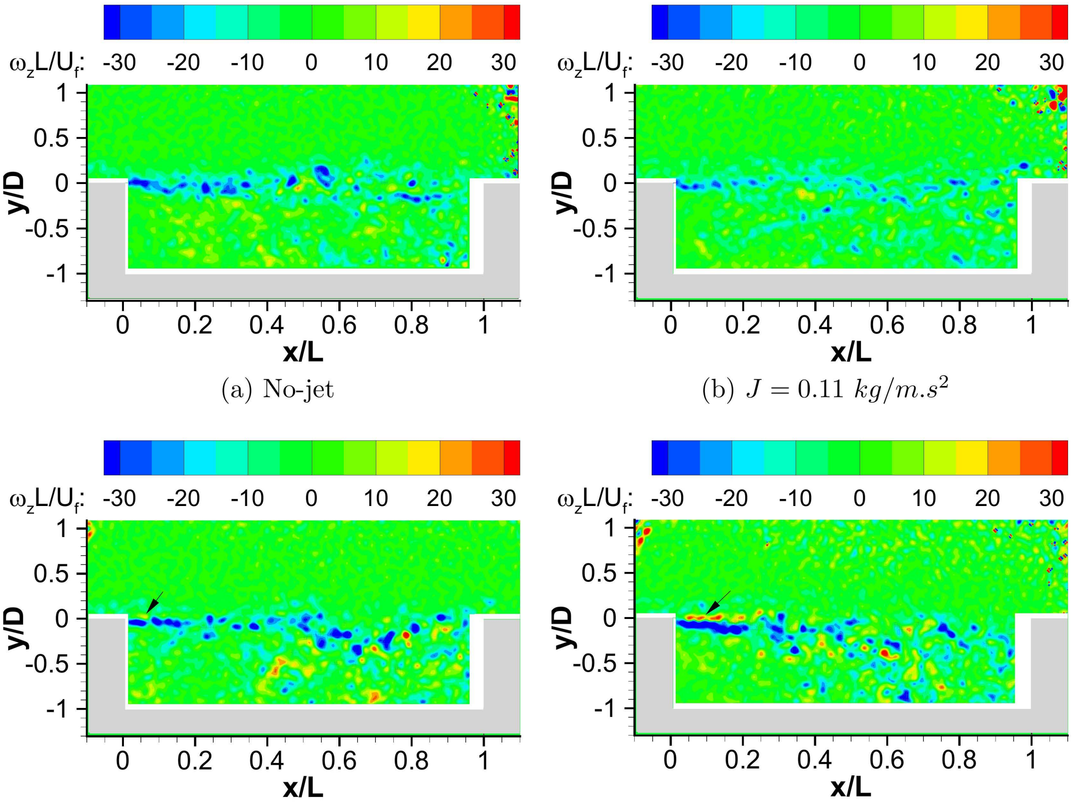

(a) No-jet (b) $J = 0.11\ kg/m.s^2$

(c) $J = 0.44\ kg/m.s^2$ (d) $J = 0.96\ kg/m.s^2$

Figure 6.12: Snapshots of the instantaneous dimensionless z-vorticity for $Re_\theta = 1.28 \times 10^3$, sharp edge at LE, different J.

at $x/L = 0.5$, as was illustrated in Figure 6.13. As evident from the figure, the turbulence broadband level increases with J. Although the jet supplies the cavity flow with additional disturbances, the spectral peak at $St \approx 3$ is not affected. This indicates again that this spectral peak is not related to the coherent structures of the cavity separated shear layer, but to the acoustic transversal mode.

4 Influence of the slot configuration

This section compares the impact of leading edge blowing at $Re_\theta = 1.28 \times 10^3$ and $J = 0.96\ kg/m.s^2$ for different slot configurations: the sharp edge and the coanda slots.

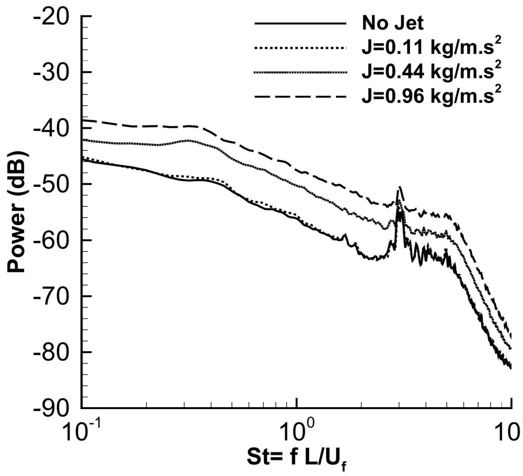

Figure 6.13: The unsteady wall pressure power spectra at $x/L = 0.5$ for $Re_\theta = 1.28 \times 10^3$, sharp edge at LE, different J.

4.1 Comparison of jet penetration

Figure 6.14 shows the instantaneous raw images and contours of the time-averaged V/U_f field for the sharp edge and coanda cases. Both the instantaneous raw images and the time-averaged V/U_f fields demonstrate a jet deflection for both cases. This deflection is evident by the strong downward V velocity in region "B" in Figures 6.14 (b) and 6.14 (d). The time-averaged V/U_f results also highlight a noticeable difference between the two cases in region "A". As evident from this region, the upward V velocity of the coanda case is significantly larger than the upward V velocity of the sharp edge case. This is probably attributed to the difference between the two cases in the jet-cavity trailing edge interaction, that was observed previously in the quiescent condition (Figures 4.13 (e) and 4.13 (f)).

Figure 6.15 illustrates the time-averaged U/U_f profiles at different axial stations for the no-jet, sharp edge, and coanda cases. As evident from the figure, the growth rate of the lower side for both jets is larger than the growth rate of the upper side of the jets. The reason behind this was previously discussed in Subsection 2.1. Region "A" in the figure indicates that the reduction of the streamwise velocity upstream of the cavity trailing edge in the coanda case is more than that of the sharp edge case. This is attributed to the relatively large upward V velocity at the cavity trailing edge for the coanda case, and hence the impedance against the flow for this case is relatively large.

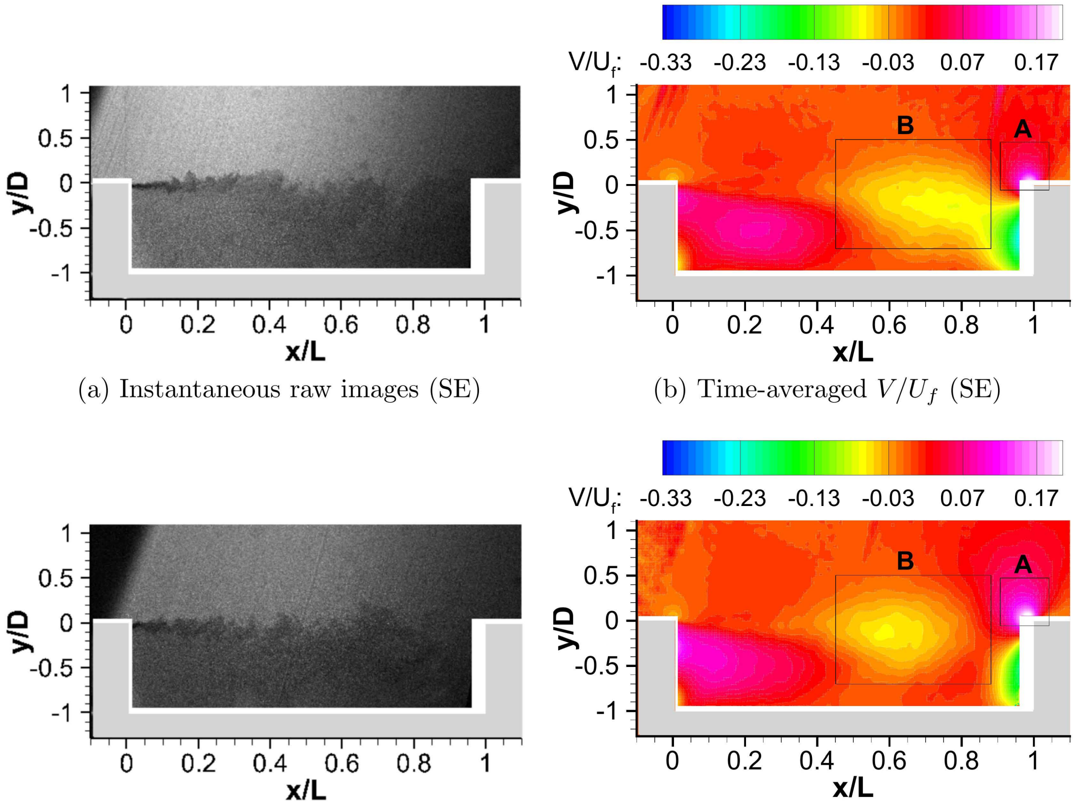

(a) Instantaneous raw images (SE)

(b) Time-averaged V/U_f (SE)

(c) Instantaneous raw images (C)

(d) Time-averaged V/U_f (C)

Figure 6.14: Instantaneous raw images and contours of the time-averaged V/U_f field for $Re_\theta = 1.28 \times 10^3$, different slots at LE, $J = 0.96\ kg/m.s^2$. C: Sharp edge slot, C: coanda slot.

4.2 Comparison of the time-averaged cavity flow

The time-averaged cavity flow shows some differences between the two jet cases. Figure 6.16 presents the time-averaged U/U_f fields of the two jet cases. As evident from the figure, the centre of the main recirculation vortex slightly shifts from $x/L \approx 0.5$ in the sharp edge case to $x/L \approx 0.45$ in the coanda case. This figure and Figure 6.15 also show that the reverse flow rate in the sharp edge case is more than the reverse flow rate in the coanda case.

Figure 6.17 provides the time-averaged dimensionless Reynolds shear stress for the sharp edge and coanda cases. The peak Reynolds shear stress in the coanda case is much larger than that of the sharp edge case. This is because the jet turbulence intensity of the coanda case is noticeably larger than that of the sharp edge case, as found previously in Figure 4.12 (a). The dashed line in the figure indicates the location of the upper boundary of the cavity separated

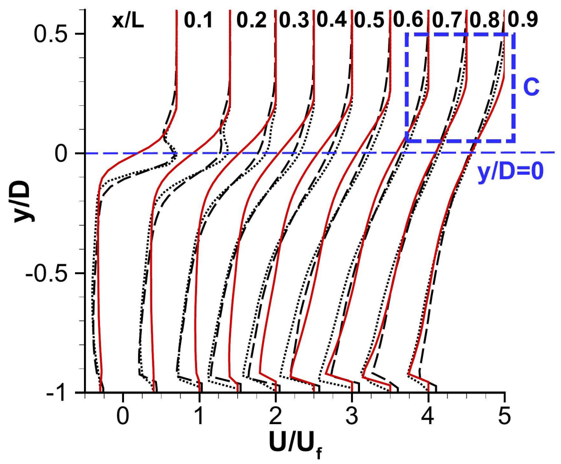

Figure 6.15: Time-averaged U/U_f profiles at different axial stations for $Re_\theta = 1.28 \times 10^3$, different slots at LE, $J = 0.96\ kg/m.s^2$. Solid line: no-jet, dotted line: blowing from the sharp edge slot, dashed line: blowing from the coanda slot.

shear layer, where the turbulent fluctuations of the cavity separated shear layer undergo a substantial drop. The dashed lines indicate a noticeable lift of the upper boundary of the cavity separated shear layer in the coanda case compared to the sharp edge case. This lift is attributed to the increase in the upward V velocity at the cavity trailing edge. This lift is also noted in the time-averaged boundaries for the sharp edge and coanda cases, as illustrated in Figures 6.18 (a) and 6.18 (b).

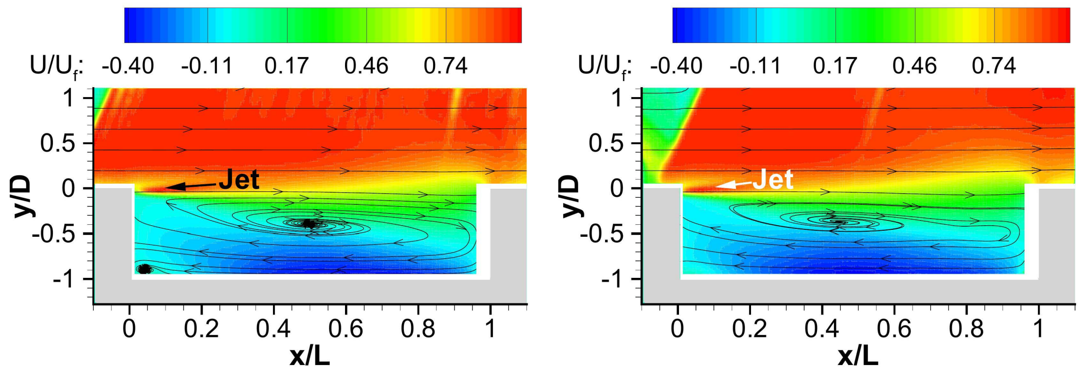

(a) Sharp edge slot (b) Coanda slot

Figure 6.16: Contours of the time-averaged U/U_f for $Re_\theta = 1.28 \times 10^3$, different slots at LE, $J = 0.96\ kg/m.s^2$.

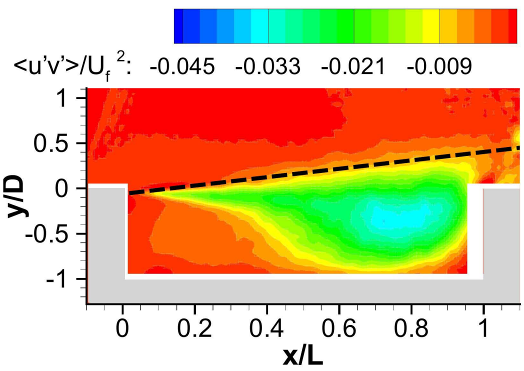

(a) Sharp edge slot

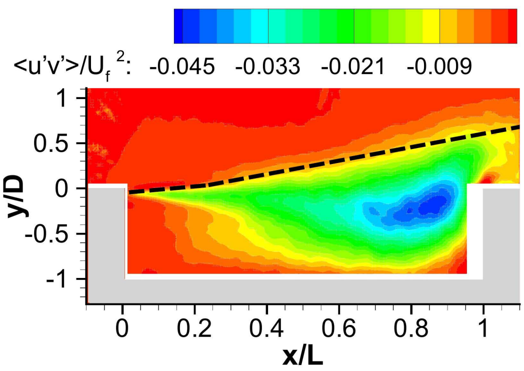

(b) Coanda slot

Figure 6.17: Contours of the time-averaged dimensionless Reynolds shear stress for $Re_\theta = 1.28 \times 10^3$, different slots at LE, $J = 0.96\ kg/m.s^2$.

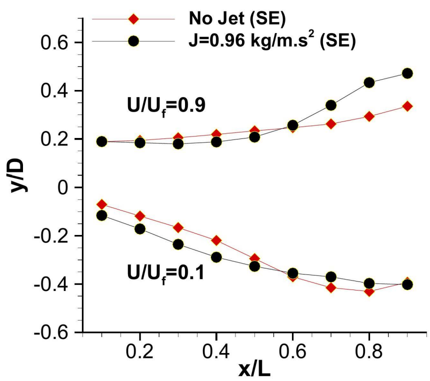

(a) Boundaries (sharp edge slot)

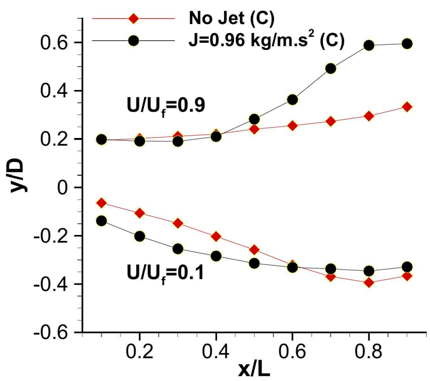

(b) Boundaries (coanda slot)

Figure 6.18: The time-averaged boundaries of the cavity separated shear layer for $Re_\theta = 1.28 \times 10^3$, different slots at LE, $J = 0.96\ kg/m.s^2$.

4.3 Comparison of the cavity separated shear layer oscillations

Unlike the time-averaged cavity flow field, the analysis of the cavity separated shear layer oscillations do not show any significant difference between the two cases. Figure 6.19 illustrates the power spectra of the streamwise velocity for the sharp edge and coanda cases. The spectra do not show any noticeable difference in the frequency of the dominant peak between the sharp edge and coanda cases. Also, no noticeable difference was noted in the unsteady wall pressure spectra, as shown in Figure 6.20. The sequential snapshots of the fluctuating field do not

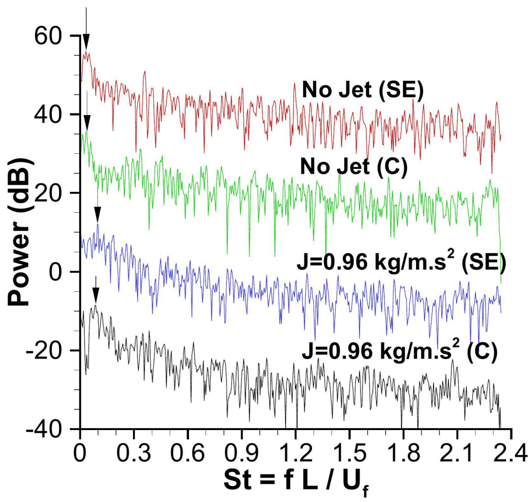

Figure 6.19: Spectra of the streamwise velocity at ($x/L = 0.9$, $y/D = 0$) for $Re_\theta = 1.28 \times 10^3$, different slots at LE, $J = 0.96\ kg/m.s^2$. SE: sharp edge slot, C: coanda slot.

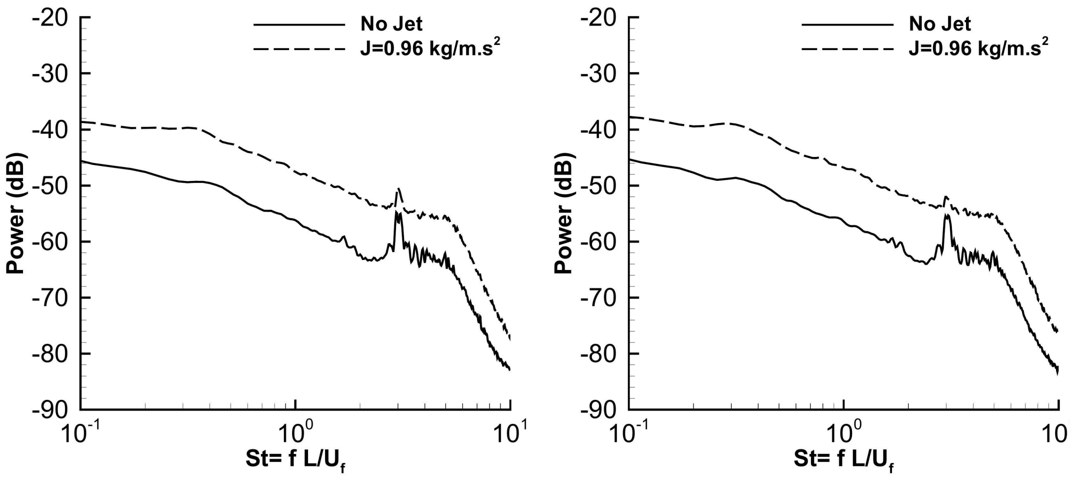

(a) Sharp edge slot

(b) Coanda slot

Figure 6.20: Spectra of the unsteady wall pressure at $x/L = 0.5$ for $Re_\theta = 1.28 \times 10^3$, different slots at LE, $J = 0.96\ kg/m.s^2$.

reveal any qualitative difference in the temporal behaviour of the cavity separated shear layer between the two cases. It is difficult to compare the shedding frequency of the large vortical structures between the two cases due to: (i) the rough estimation of the vortex count method, and (ii) the difficulty in distinguishing between the jet structures and the structures of the cavity separated shear layer.

5 Concluding remarks

Firstly, the impact of the cavity leading edge blowing with the sharp edge slot was investigated at $Re_\theta = 1.28 \times 10^3$ and $0.11\ kg/m.s^2 \leq J \leq 0.96\ kg/m.s^2$. This part of the investigation is concluded as follows:

- The surface oil flow visualisations showed that increasing J causes the reverse flow to diverge towards the side plates. This divergence is due to the increase in the stagnation pressure in the mid-span region compared to the side regions of the cavity, where the jet is not applied. However, the reverse flow in the mid-span region, where the pressure and PIV measurements are acquired, remains parallel to the x-axis and hence the flow there is likely to be two-dimensional.

- Increasing J to $0.96\ kg/m.s^2$ causes the jet to deflect downwards. This deflection is attributed to two reasons: (i) the coanda effect, and (ii) the difference in the jet's growth rate between the upper and lower sides of the jet.

- As J increases, the change in the time-averaged cavity flow field becomes more significant. The changes include: (i) upstream shift of the main recirculation vortex, (ii) increase in the reverse flow rate, (iii) lifting of the upper boundary of the cavity separated shear layer upstream of the cavity trailing edge, and (iv) increase in the turbulence fluctuation in the cavity separated shear layer due to the jet's disturbances.

- Increasing J to $J \geq 0.44\ kg/m.s^2$ causes the dimensionless frequency of the reverse flow interaction to increase from $St \approx 0.05$ to $St \approx 0.1$. This frequency rise is due to the increase in the amount of the reverse flow impacting the sensitive separation region of the cavity separated shear layer. Additionally, the jet's disturbances increase the turbulence broadband level of the unsteady wall pressure spectra.

Secondly, a comparison was made between the leading edge blowing with the sharp edge and the coanda slots at $Re_\theta = 1.28 \times 10^3$ and $J = 0.96\ kg/m.s^2$. The results of this comparison are summarised as follows:

- The time-averaged cavity flow fields show that both jets deflect downwards. However, the time-averaged results highlighted two main differences between the sharp edge case and coanda case. First, the upper boundary of the cavity separated shear layer in the coanda case is noticeably higher than the upper boundary in the sharp edge case. This difference is because the upward V velocity at the cavity trailing edge for the coanda case is relatively large, and hence this impedes the flow of the cavity separated shear layer and forces the upper boundary upwards. Second, the maximum Reynolds shear stress in the coanda case is significantly larger than that of the sharp edge case. This is because the turbulence intensity of the coanda jet is noticeably higher than that of the sharp edge jet.

- The velocity spectra, pressure spectra, and the snapshots of the fluctuating field did not reveal any noticeable differences in the oscillations of the cavity separated shear layer between the two cases.

Chapter 7

Blowing From Cavity Trailing Edge

This chapter examines the impact of blowing from the cavity trailing edge on the time-averaged cavity flow field and the oscillations of the cavity separated shear layer at $Re_\theta = 1.28 \times 10^3$ and $0.11\ kg/m.s^2 \leq J \leq 0.96\ kg/m.s^2$. Similar to leading edge blowing, the jet is forced through a horizontal slot, but opposite to the direction of the separated shear layer. This type of blowing aims to minimise the interaction between the separated shear layer and the cavity trailing edge and hence suppressing the oscillations of the separated shear layer. The chapter also compares these results with the results of blowing from the cavity leading edge presented in Chapter 6.

1 Surface oil flow visualisations

Figure 7.1 shows the images of the surface oil flow visualisations for no-jet and jet-on cases. Similar to the blowing from the cavity leading edge results, the reverse flow in the figure diverges with increasing J. The reason behind this divergence was explained in Chapter 6. Despite this divergence, the reverse flow at the mid-span region remains parallel to the x-axis, and hence the flow in this region, where the PIV and pressure measurements are acquired, is likely to be two-dimensional.

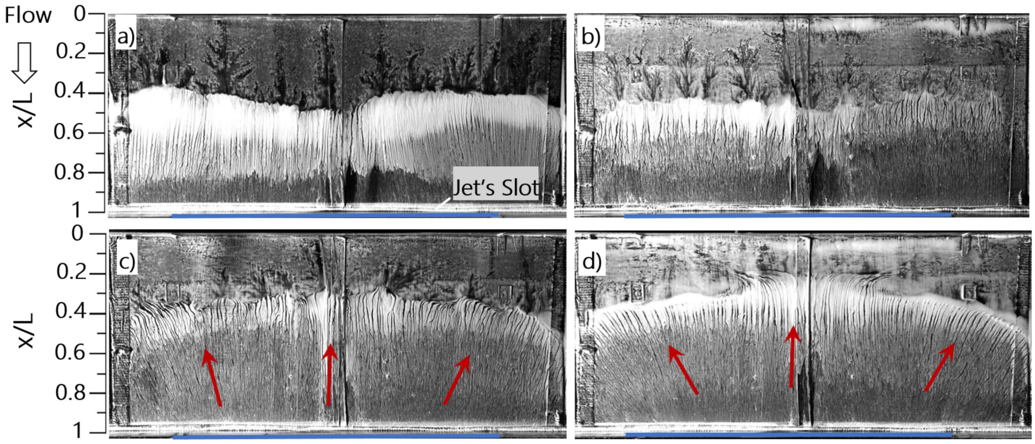

Figure 7.1: Surface oil flow visualisations for $Re_\theta = 1.28 \times 10^3$, sharp edge at TE, different J: a) no-jet, b) $J = 0.11\ kg/m.s^2$, c) $J = 0.44\ kg/m.s^2$, and d) $J = 0.96\ kg/m.s^2$.

2 Jet behaviour

Figure 7.2 shows the time-averaged dimensionless vorticity ($\omega_z L/U_f$) and the instantaneous raw images at $Re_\theta = 1.28 \times 10^3$ for different values of J. As illustrated in this figure, the cavity separated shear layer interacts strongly with the jet. The time-averaged vorticity field shows positive and negative vorticity regions at the cavity trailing edge, which represent the two shear layers of the jet. These regions indicate the time-averaged position of the jet, where the jet is flapping around. As demonstrated in the figure, the cavity separated shear layer forces the jet to deflect backward. At $J = 0.11\ kg/m.s^2$, the jet is blown away. However, as J increases, the jet deflects forward.

Snapshots of the instantaneous dimensionless velocity magnitude (R/U_f) for $J = 0.96\ kg/m.s^2$ are illustrated in Figure 7.3. The instantaneous velocity flow field shows that the jets flap around the time-averaged jet position. An imaginary line is drawn around the jet to highlight its instantaneous position. As the cavity separated shear layer (C.S.S.L) interacts with jet (Figure 7.3 (a)), the jet deflects backward. As a result, the cavity separated shear layer flows over the jet (Figure 7.3 (b)), while a portion of the cavity separated shear layer deflects downwards with the reverse flow. When the interaction between the cavity separated shear layer and the jet is reduced, the jet deflects forward and the cavity separated shear layer deflects down, as demonstrated in Figure 7.3 (c)). Occasionally, the jet is blocked due to the impingement of the cavity separated shear layer at the

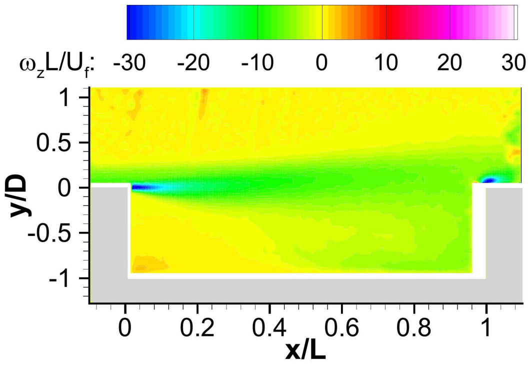

(a) $\omega_z L/U_f$ ($J = 0.11\ kg/m.s^2$)

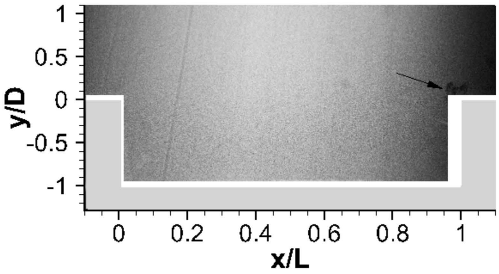

(b) Instantaneous image ($J = 0.11\ kg/m.s^2$)

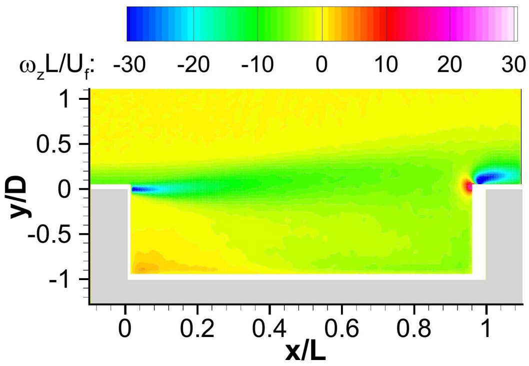

(c) $\omega_z L/U_f$ ($J = 0.44\ kg/m.s^2$)

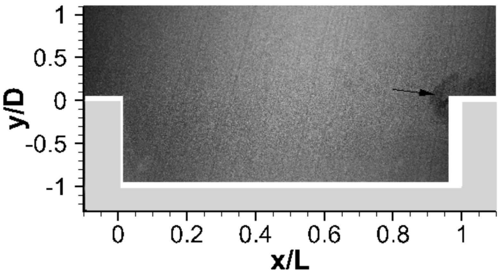

(d) Instantaneous image ($J = 0.44\ kg/m.s^2$)

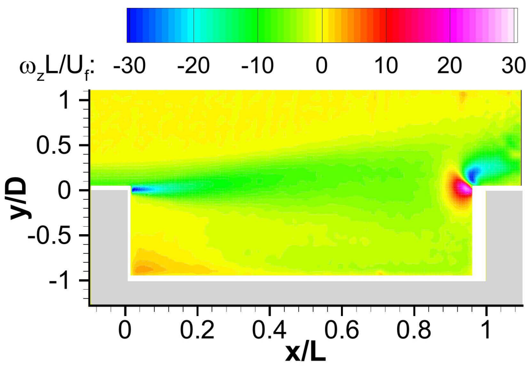

(e) $\omega_z L/U_f$ ($J = 0.96\ kg/m.s^2$)

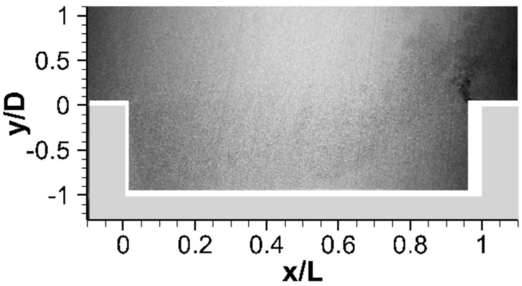

(f) Instantaneous image ($J = 0.96\ kg/m.s^2$)

Figure 7.2: The time-averaged $\omega_z L/U_f$ and the instantaneous raw images for $Re_\theta = 1.28 \times 10^3$, sharp edge at TE, different J.

jet's slot, as illustrated in Figure 7.3 (d). The flapping motion of the jet was also observed at lower J values, but with a smaller flapping magnitude.

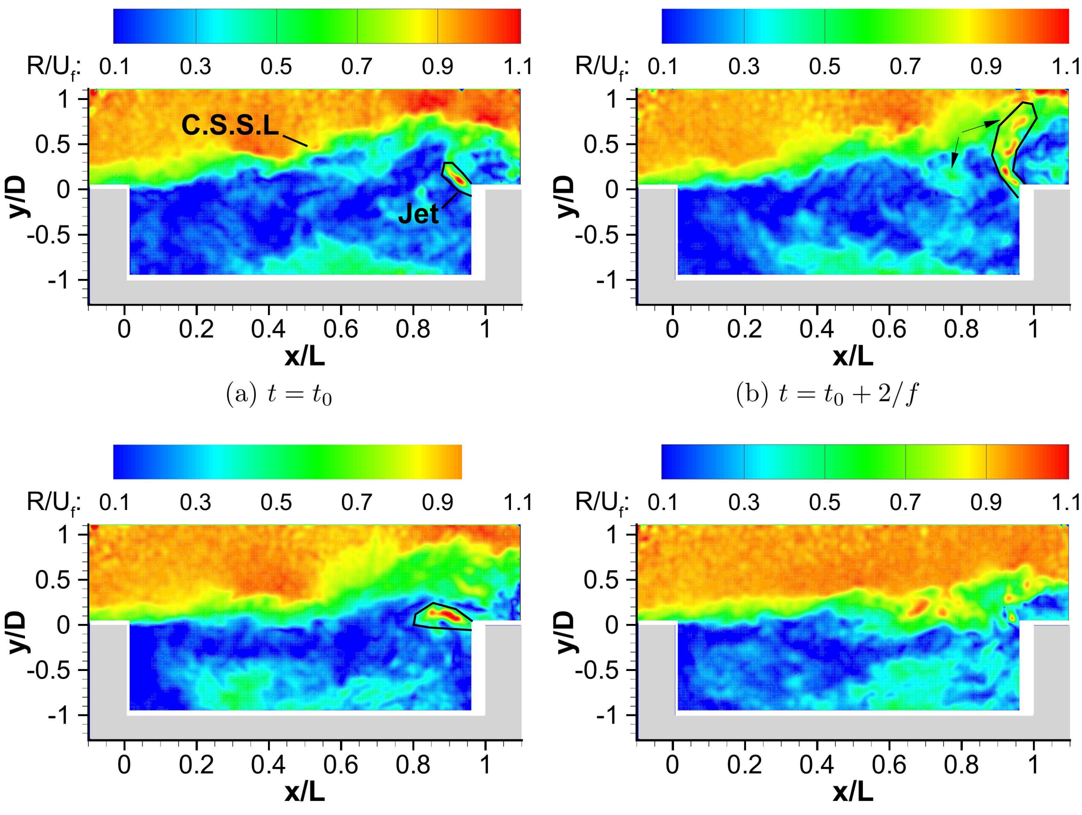

(a) $t = t_0$

(b) $t = t_0 + 2/f$

(c) $t = t_0 + 5/f$

(d) $t = t_0 + 9/f$

Figure 7.3: Snapshots of the instantaneous R/U_f for $Re_\theta = 1.28 \times 10^3$, sharp edge at TE, $J = 0.96\ kg/m.s^2$.

3 Jet impact on the cavity flow topology

To investigate the impact of the jets on the cavity flow topology, the time-averaged U/U_f fields for the no-jet and jet-on cases are shown in Figure 7.4. As J increases, the jet lifts up the cavity separated shear layer, causing a small recirculation bubble to form downstream of the cavity trailing edge. At the maximum value of J, the recirculation bubble becomes significantly large and the cavity separated shear layer splits into two parts: one part flows over the deflected jet, while the other part deflects down with the reverse flow, as visible in Figure 7.4 (d). The presence of this recirculation bubble causes more flow from the cavity separated shear layer to deflect downwards and hence the reverse flow rate increases, as evident from the figure.

The increase in the reverse flow rate influences the location of the separation zone. Figure 7.5 illustrates the distribution of U/U_f along the cavity floor ($y/D =$

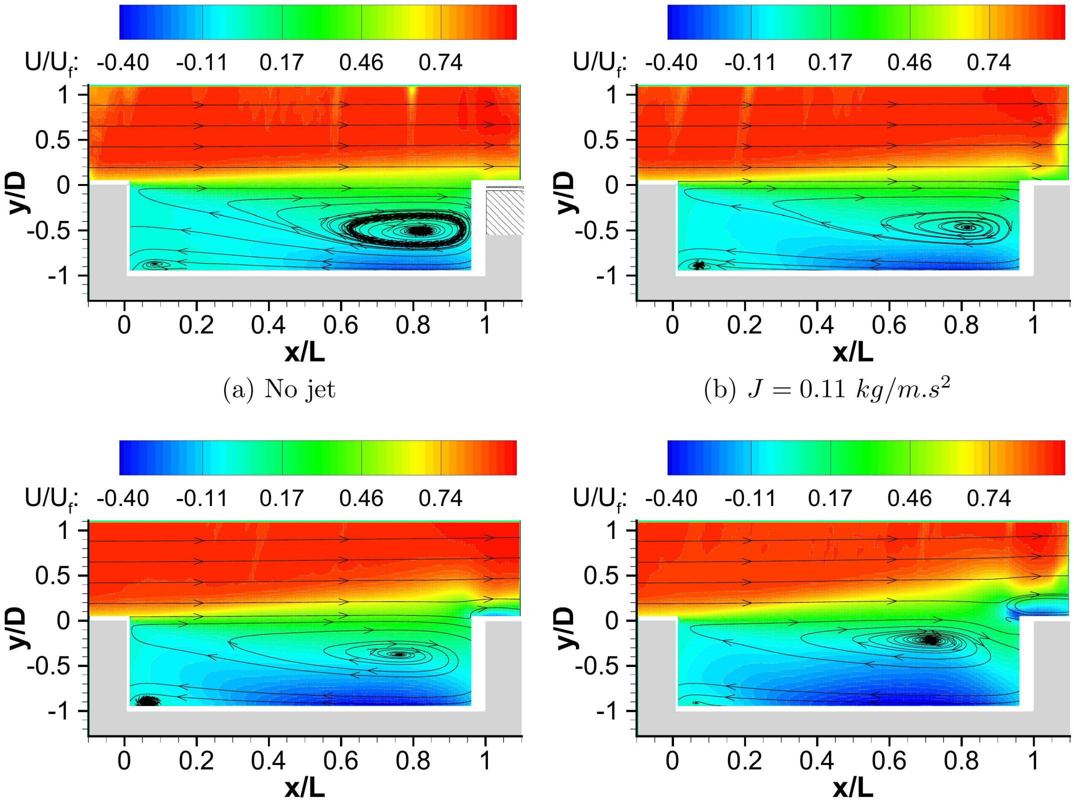

(a) No jet (b) $J = 0.11\ kg/m.s^2$

(c) $J = 0.44\ kg/m.s^2$ (d) $J = 0.96\ kg/m.s^2$

Figure 7.4: Contours of the time-averaged U/U_f for $Re_\theta = 1.28 \times 10^3$, sharp edge at TE, different J. C.S.S.L: denotes the cavity separated shear layer.

-0.9). The streamwise locations X_{R1}, $X_{R2,3}$, and X_{R4} denote the separation point for no-jet, $J = 0.11\ kg/m.s^2$, and $J = 0.96\ kg/m.s^2$ cases, respectively. The figure demonstrates that the separation point shifts upstream from $x/L \approx 0.2$ for the no-jet case to $x/L \approx 0.1$ for the $J = 0.96\ kg/m.s^2$ case.

4 Jet impact on the cavity separated shear layer

The fluctuations level, the boundaries, and the growth rate of the cavity separated shear layer are affected by the jet. Figure 7.6 illustrates the dimensionless Reynolds shear stress field for no-jet and jet-on cases. As J increases, two peak locations are observed. The first peak, which indicates the maximum Reynolds shear in the jet, is at the cavity trailing edge. The second peak location is found upstream of the former location and indicates the maximum Reynolds shear stress of the cavity separated shear layer. Increasing J causes the peak location of the

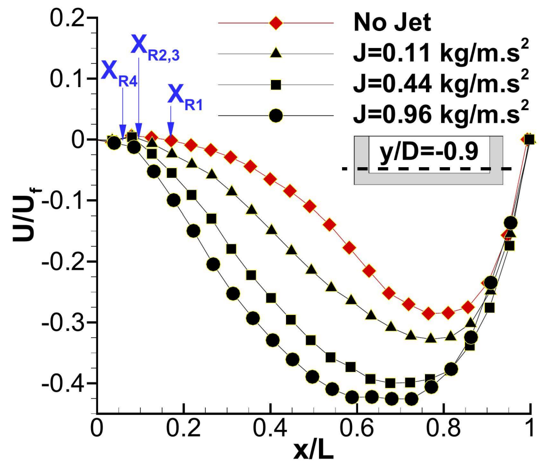

Figure 7.5: Distribution of the time-averaged U/U_f along $y/D = -0.9$ for $Re_\theta = 1.28 \times 10^3$, sharp edge at TE, different J.

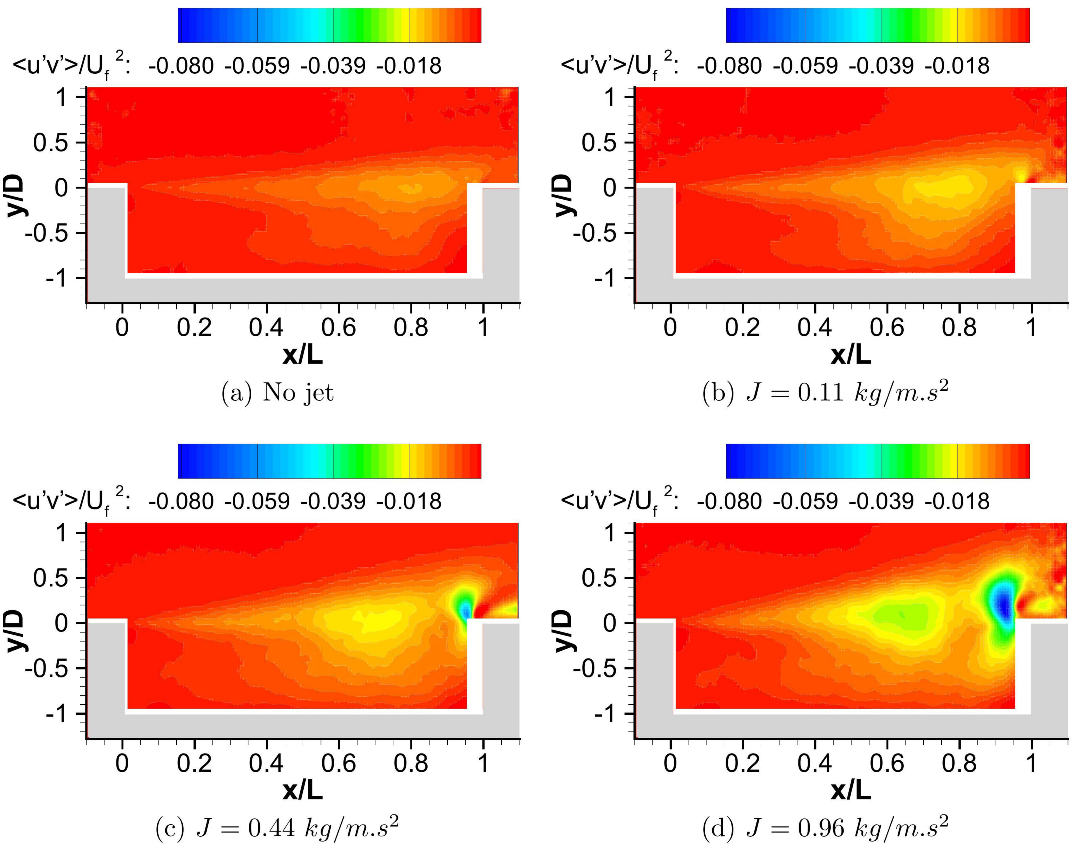

(a) No jet

(b) $J = 0.11\ kg/m.s^2$

(c) $J = 0.44\ kg/m.s^2$

(d) $J = 0.96\ kg/m.s^2$

Figure 7.6: Contours of the dimensionless Reynolds shear stress for $Re_\theta = 1.28 \times 10^3$, sharp edge at TE, different J.

cavity separated shear layer to increase in magnitude and shift upstream. This is because as J increases, the jet deflects forward and hence it interacts more intensively with the cavity separated shear layer.

Figure 7.7 (a) shows the time-averaged $U/U_f = 0.9$ and $U/U_f = 0.1$ boundaries of the cavity separated shear layer along the x-axis. This figure shows that as J increases, the entire cavity separated shear layer lifts up due to the presence of the recirculation bubble downstream. The time-averaged vorticity thickness of the cavity separated shear layer along the x-axis is demonstrated in Figure 7.7 (b). Based on this figure, the growth rate ($d\delta_\omega/dx$) of the cavity separated shear layer for the no-jet and jet-on cases are estimated in Table 7.1. As evident from the table, the growth rate increases with J. This increase is due to the flow impedance of the recirculation bubble, which reduces the streamwise velocity of the cavity separated shear layer, and hence thickening this layer.

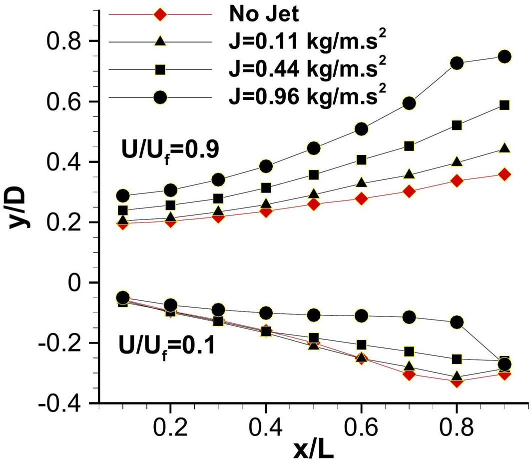

(a) Boundaries of the separated shear layer

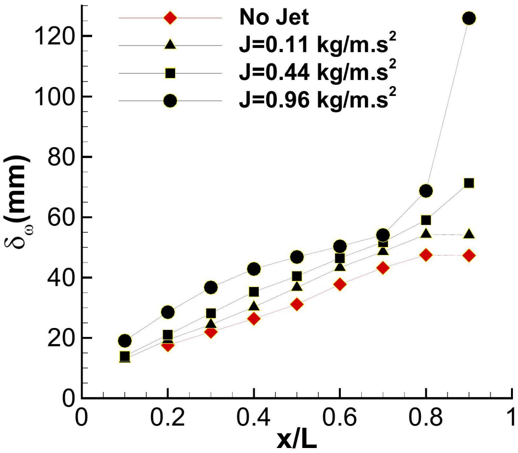

(b) Vorticity thickness

Figure 7.7: The time-averaged boundaries and vorticity thickness of the cavity separated shear layer along the x-axis for $Re_\theta = 1.28 \times 10^3$, sharp edge at TE, different J.

Table 7.1: Growth rate of the cavity separated shear layer for $Re_\theta = 1.28 \times 10^3$, sharp edge at TE, different J.

J $(kg/m.s^2)$	No Jet	0.11	0.44	0.96
$d\delta_\omega/dx$	0.193	0.227	0.247	0.273

5 Jet impact on the cavity separated shear layer oscillations

The jet affects the cavity separated shear layer oscillations. Figure 7.8 shows the temporal evolution of U/U_f at $x/L = 0.2$ and 0.8 for jet-on and no-jet cases. The figure shows that as J increases, the frequency of the reverse flow surges at $x/L = 0.2$ and the oscillation peaks of the cavity separated shear layer at $x/L = 0.8$ increases significantly. To quantify this frequency increase, velocity spectra are obtained at $x/L = 0.9$ and $y/D = 0$ for the no-jet and jet-on cases which are presented in Figure 7.9 (a). This figure shows that as J increases from 0 (no-jet case) to 0.96 $kg/m.s^2$, the non-dimensional frequency increases from approximately $St \approx 0.05$ to $St \approx 0.09$. Also, for $J = 0.96$ $kg/m.s^2$ an additional peak appears at $St \approx 0.03$. The spectral development of this peak along the x-axis is shown in Figure 7.9 (b). As evident from the figure, the peak appears at $x/L \approx 0.5$ and then increases in amplitude with the streamwise direction. This spectral peak is not present in the spectra of the no-jet case, nor the leading edge blowing cases. Thus, this peak is likely to be attributed to the interaction between the jet and the cavity separated shear layer.

The unsteady wall pressure power spectra at $x/L = 0.5$ are shown in Figure 7.10. Increasing J yields an increase in the broadband level of the fluctuations, due to the increase in the velocity fluctuation levels of the cavity separated shear layer. Again, the transversal mode at $St \approx 3$ is not affected because it is not related to the cavity separated shear layer. The sequential snapshots of the fluctuating field do not reveal any noticeable change in the temporal behaviour of the coherent vortical structures of the cavity separated shear layer.

6 Comparison between blowing from the cavity leading edge and blowing from the cavity trailing edge

This section compares the impact of leading edge and trailing edge blowing at $Re_\theta = 1.28 \times 10^3$ and $J = 0.96$ $kg/m.s^2$. Both blowing jet cases are performed with the sharp edge slot.

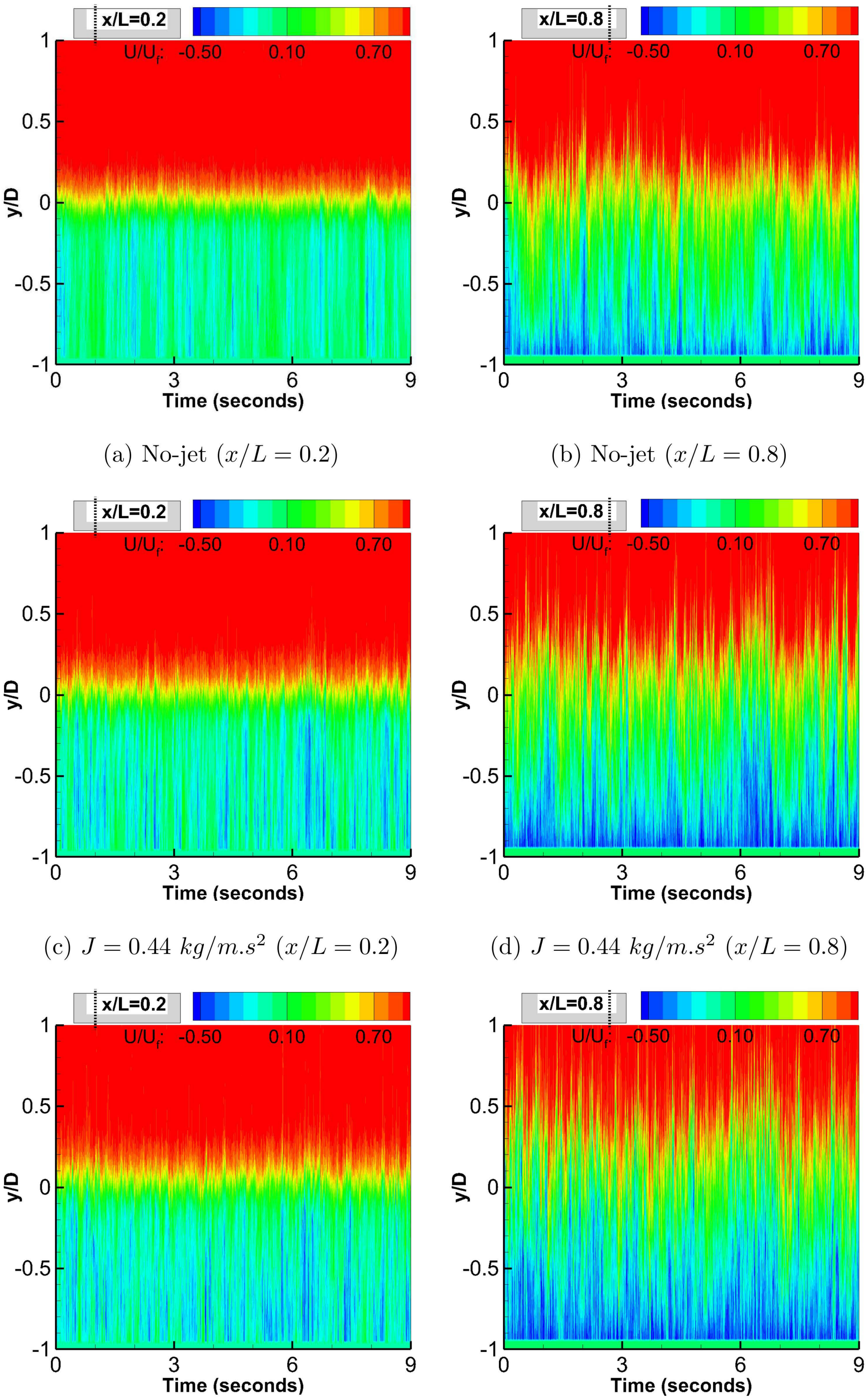

(a) No-jet ($x/L = 0.2$)

(b) No-jet ($x/L = 0.8$)

(c) $J = 0.44\ kg/m.s^2$ ($x/L = 0.2$)

(d) $J = 0.44\ kg/m.s^2$ ($x/L = 0.8$)

(e) $J = 0.96\ kg/m.s^2$ ($x/L = 0.2$)

(f) $J = 0.96\ kg/m.s^2$ ($x/L = 0.8$)

Figure 7.8: Temporal evolution of U/U_f at $x/L = 0.2$ and 0.8 for $Re_\theta = 1.28 \times 10^3$, sharp edge at TE, different J.

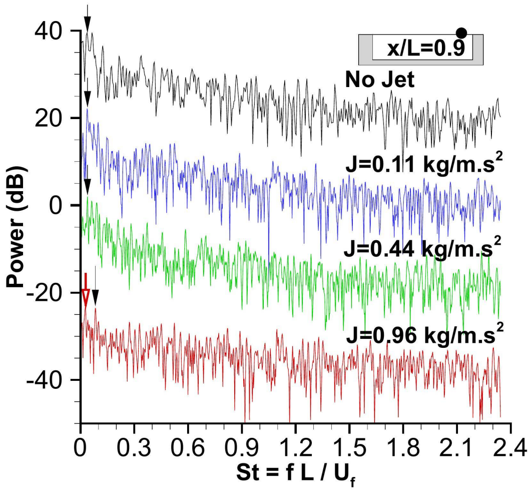

(a) Different J ($x/L = 0.9$, $y/D = 0$)

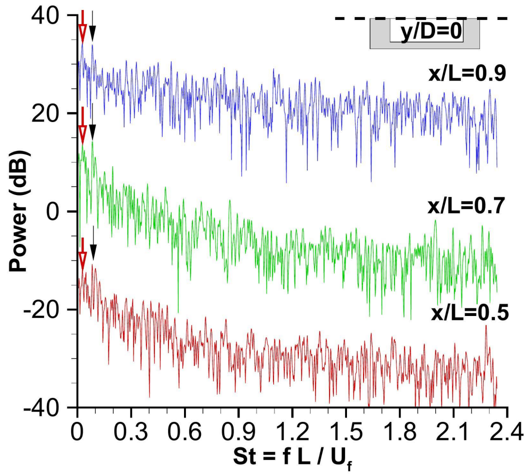

(b) $J = 0.96\ kg/m.s^2$ ($x/L = 0.5$ to 0.9)

Figure 7.9: Streamwise velocity power spectra at $y/D = 0$ for $Re_\theta = 1.28 \times 10^3$, sharp edge at TE, different J.

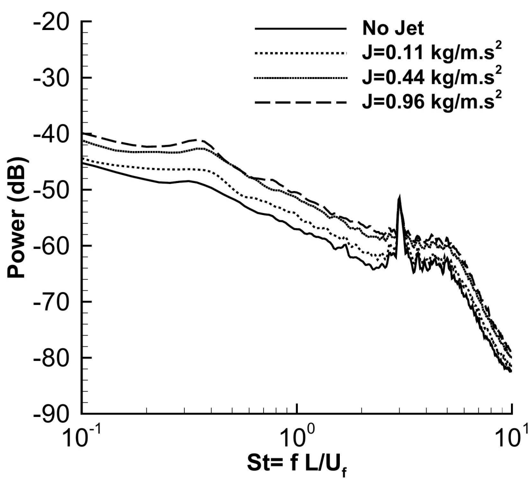

Figure 7.10: The unsteady wall pressure power spectra at $x/L = 0.5$ for $Re_\theta = 1.28 \times 10^3$, sharp edge at TE, different J.

6.1 Comparison of the time-averaged cavity flow

The leading and trailing edge blowing significantly affects the time-averaged cavity flow field. Figures 7.11 (a) and 7.11 (b) illustrate the time-averaged U/U_f for blowing from the cavity leading and trailing edges, respectively. As illustrated in the figures, the trailing edge blowing causes the entire cavity separated shear layer to lift upwards. On the other hand, the leading edge blowing shifts the main recirculation vortex downstream. The upstream shift of the main recirculation

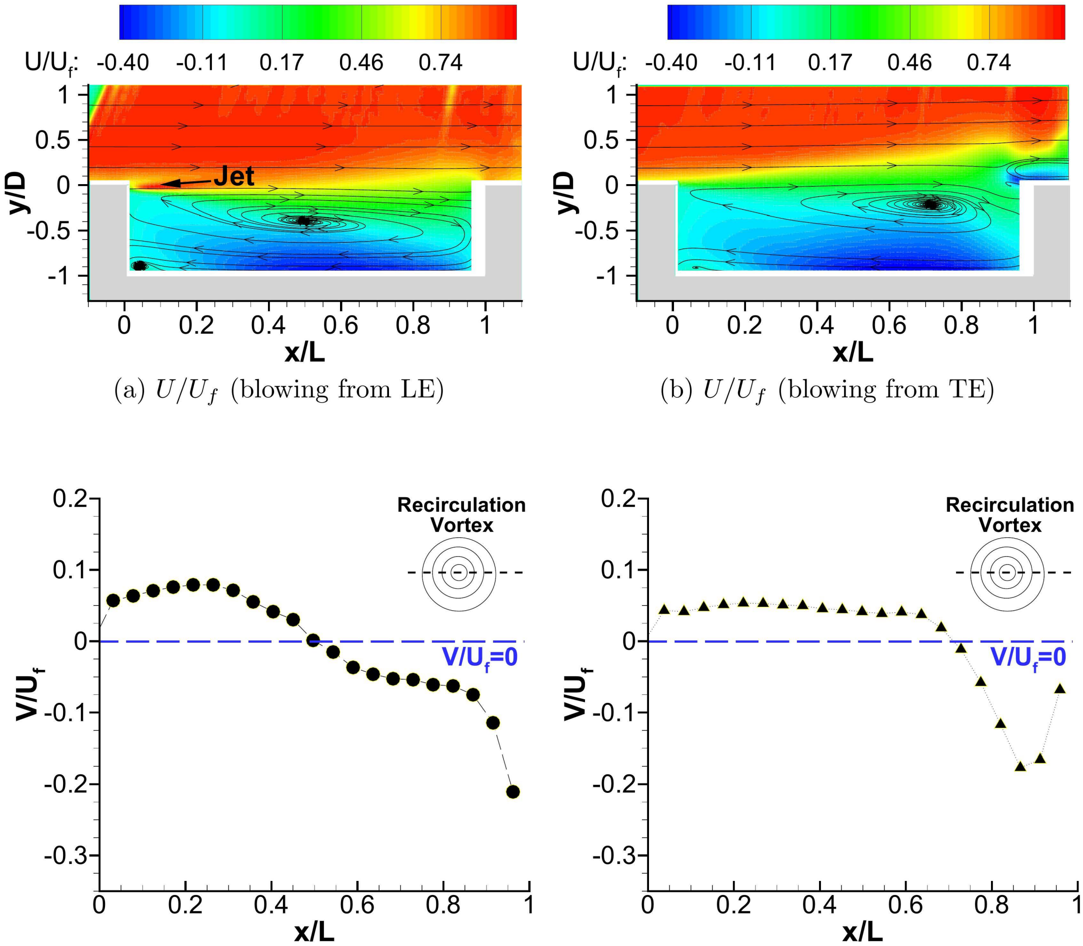

(a) U/U_f (blowing from LE) (b) U/U_f (blowing from TE)

(c) V/U_f (blowing from LE) (d) V/U_f (blowing from TE)

Figure 7.11: Contours of the time-averaged U/U_f and profiles of the time-averaged V/U_f along the centre of the main recirculation vortex for $Re_\theta = 1.28 \times 10^3$, sharp edge at LE or TE, $J = 0.96\ kg/m.s^2$.

vortex results in more reverse flow impacting the sensitive separation point of the cavity separated shear layer, as illustrated in Figure 7.11 (c) and 7.11 (d), which show the profiles of the time-averaged V/U_f along the centre of the main recirculation vortex for the leading and trailing edges blowing, respectively. Consequently, the leading edge blowing is likely to enhance the cavity separated shear layer oscillations more than the trailing edge blowing. Figure 7.12 highlights the differences in the cavity flow behaviour for leading and trailing edges blowing.

Figure 7.13 illustrates the time-averaged dimensionless Reynolds shear stress for blowing from leading and trailing edges. The magnitudes and locations of the peak values are indicated in the figure. This figure clearly shows that the

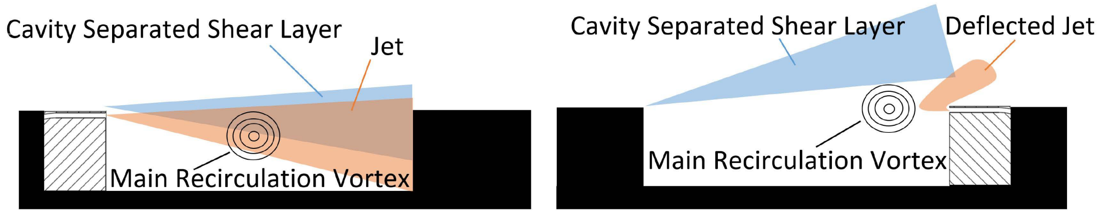

(a) Blowing from LE (b) Blowing from LE

Figure 7.12: Cavity flow behaviour for leading and trailing edges blowing for $Re_\theta = 1.28 \times 10^3$, sharp edge at LE or TE, $J = 0.96\ kg/m.s^2$.

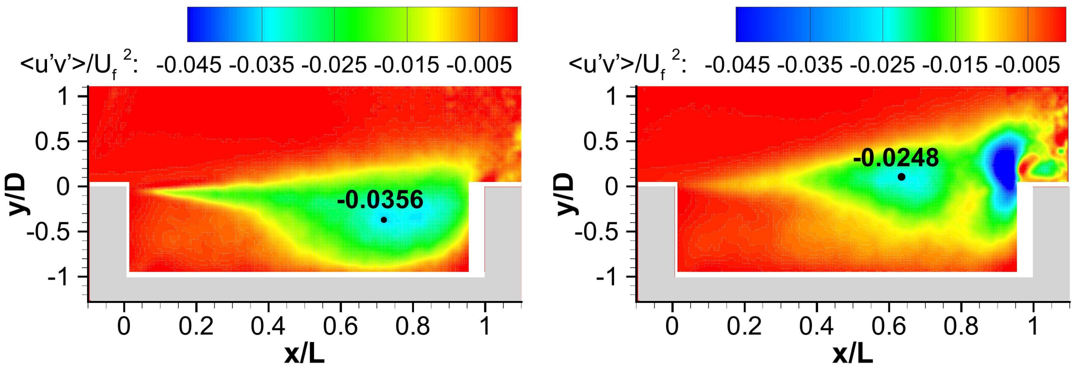

(a) Blowing from LE (b) Blowing from TE

Figure 7.13: Contours of the time-averaged dimensionless Reynolds shear stress for $Re_\theta = 1.28 \times 10^3$, sharp edge at LE or TE, $J = 0.96\ kg/m.s^2$.

Reynolds shear stress of the cavity separated layer in the leading edge blowing case is noticeably larger than that of the trailing edge blowing case. This is because most of the jet disturbances in the leading edge blowing are convected in the cavity separated shear layer, while the majority of the jet disturbances in the trailing edge blowing case are forced downstream of the cavity.

6.2 Comparison of the cavity separated shear layer oscillations

The blowing from the cavity leading and trailing edges impacts the frequency of the reverse flow interaction. Figure 7.14 illustrates the streamwise velocity power spectra at $x/L = 0.9$ and $y/D = 0$ for two blowing cases. The dominant frequency is indicated by a filled-head arrow. The reverse flow interaction frequency in the leading edge blowing case ($St \approx 0.1$) is higher than that of the trailing edge blowing case ($St \approx 0.09$). The frequency of the reverse flow interaction is

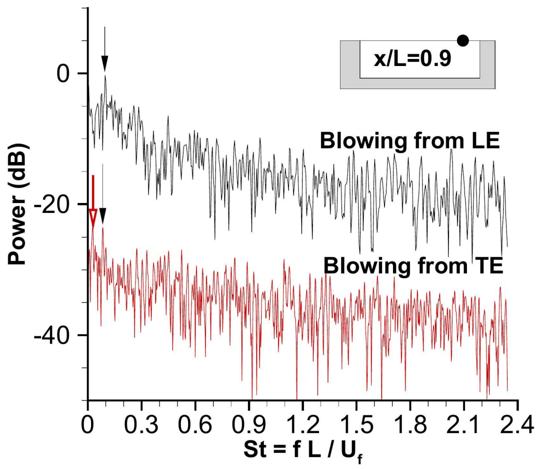

Figure 7.14: Streamwise velocity power spectra at ($x/L = 0.9$, $y/D = 0$) for $Re_\theta = 1.28 \times 10^3$, sharp edge at LE or TE, $J = 0.96$ $kg/m.s^2$.

higher in the leading edge blowing because more reverse flow impacts the sensitive separation point of the cavity separated shear layer compared to the coanda case, as previously shown in Figures 7.11 (c) and 7.11 (d). This frequency increase is also evident in Figure 7.15, which shows the temporal evolution of U/U_f at x/L = 0.2 and 0.8 for the two blowing cases.

Figure 7.16 shows the spectra of the unsteady wall pressure for the two blowing cases. This figure does not show any noticeable difference between the two cases apart from the broadband level. As evident from the figure, the leading edge blowing increases the turbulence broadband level more than the trailing edge blowing. This is because in the leading edge blowing case, the jet's disturbances are convected in the cavity separated shear layer, while the disturbances of the trailing edge blowing are forced downstream of the cavity.

From the above discussions, it is concluded that both blowing cases enhance the reverse flow interaction and rise the broadband level of the cavity separated shear layer oscillations. Therefore, these control approaches are not suitable for the control of the cavity separated shear layer oscillations. However, the trailing edge blowing showed a high capability in lifting the cavity separated shear layer and reducing the flow interaction with the cavity trailing edge. Thus, the trailing edge blowing is likely to be an effective method for controlling the cavity-induced drag.

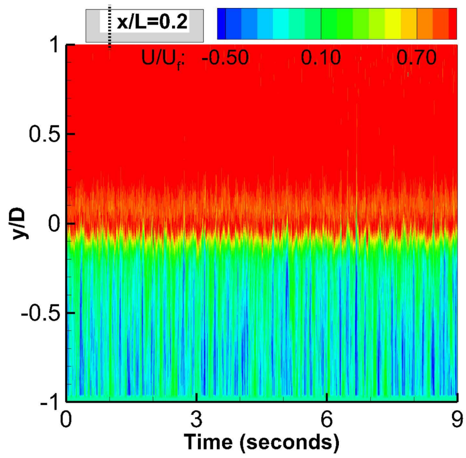

(a) $x/L = 0.2$ (blowing from LE)

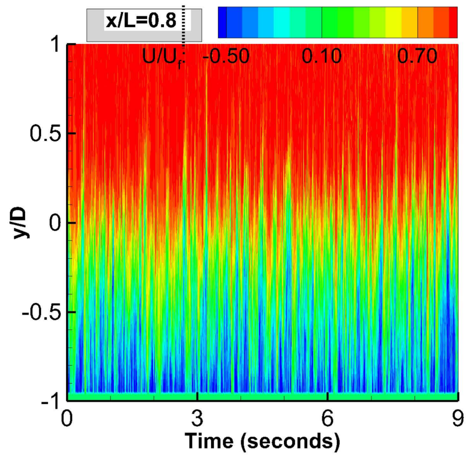

(b) $x/L = 0.8$ (blowing from LE)

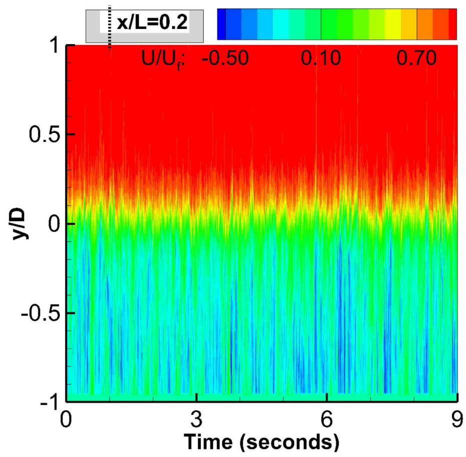

(c) $x/L = 0.2$ (blowing from TE)

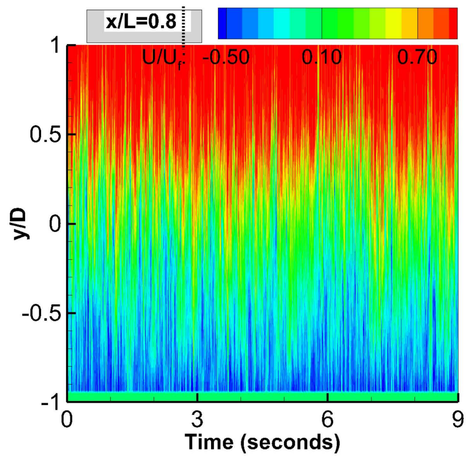

(d) $x/L = 0.8$ (blowing from TE)

Figure 7.15: Temporal evolution of U/U_f at $x/L = 0.2$ and 0.8 for $Re_\theta = 1.28 \times 10^3$, sharp edge at LE or TE, $J = 0.96\ kg/m.s^2$.

7 Concluding remarks

Firstly, the impact of the cavity trailing edge blowing with the sharp edge slot was examined at $Re_\theta = 1.28 \times 10^3$ and $J = 0.11\ kg/m.s^2$ to $0.96\ kg/m.s^2$. This part of the investigation is concluded as follows:

- Similar to the leading edge blowing, increasing J causes the reverse flow to diverge. However, the reverse flow at the mid-span region is still parallel to the x-axis, and hence the flow in this region is likely to be two-dimensional.

- The time-averaged flow field showed that the cavity separated shear layer

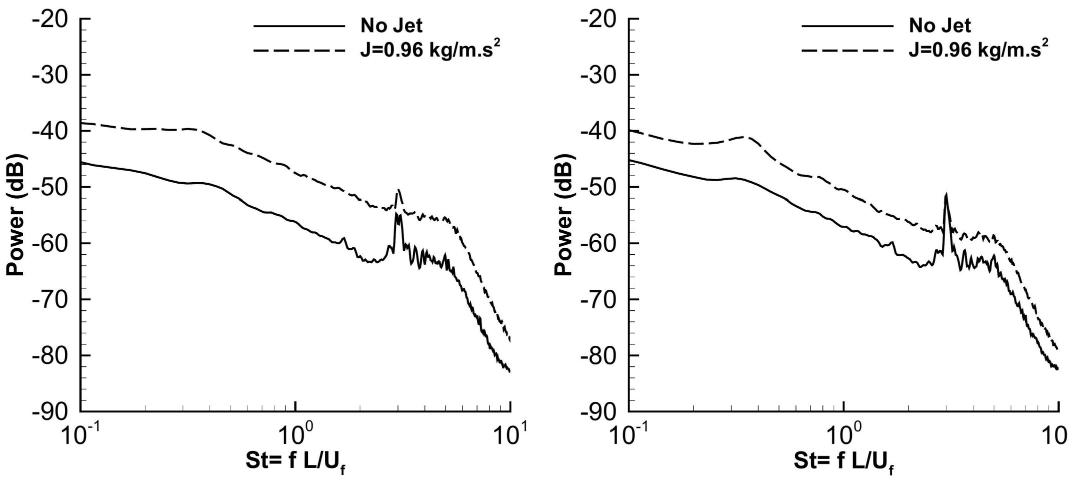

(a) Blowing from LE (b) Blowing from TE

Figure 7.16: Spectra of the unsteady wall pressure at $x/L = 0.5$ for $Re_\theta = 1.28 \times 10^3$, sharp edge at LE or TE, $J = 0.96$ $kg/m.s^2$.

forces the jet to deflect backward. However, as J increases, the jet deflects forward. The instantaneous flow field showed that the jets are flapping about the time-averaged position and the flapping amplitude increases with J. The interaction between the jet and the cavity separated shear layer raises the Reynolds shear stress in the cavity separated shear layer.

- The jet forces the he cavity separated shear layer to deflect upwards. As a result, a recirculation bubble is formed downstream of the cavity trailing edge. This recirculation bubble impedes the flow of the cavity separated shear layer and hence thickens it.

- The velocity spectra showed that as J increases from 0 to 0.96 $kg/m.s^2$ the dimensionless frequency of the reverse flow interaction increases from $St \approx 0.05$ to $St \approx 0.09$. This frequency rise is due to the increase in the reverse flow rate. An additional spectral peak is found at $St \approx 0.03$ and was attributed to the interaction between the jet and the cavity separated shear layer. The unsteady wall pressure spectra showed an increase in the broadband level of the cavity fluctuations.

Secondly, a comparison was made at $Re_\theta = 1.28 \times 10^3$ and $J = 0.96$ $kg/m.s^2$ between the impact of the leading edge and trailing edge blowing cases. In both cases the sharp edge slot is used. This comparison is summarised as follows:

- The location of the main recirculation vortex for the leading edge blowing is closer to the cavity leading edge compared to that of the trailing edge blowing. As a result, more reverse flow in the former case impacts the sensitive separation point of the cavity separated shear layer. Consequently, leading edge blowing enhances the reverse flow interaction more than trailing edge blowing. This enhancement is evident from the temporal evolution of U/U_f and the velocity spectra of the cavity separated shear layer.

- The time-averaged results showed that leading edge blowing increases the Reynolds shear stress of the cavity separated shear layer and the broadband level of the unsteady wall pressure spectra more than trailing edge blowing. This is because the jet's disturbances in the former case are convected in the cavity separated shear layer, while the jet's disturbances in the latter case are forced downstream of the cavity.

- The leading and trailing edge blowing cases enhance the reverse flow interaction and increase the broadband level of the oscillations. Thus these control methods are not suitable for controlling the oscillations of the cavity separated shear layer. However, the capability of the trailing edge blowing in lifting up the cavity separated shear layer makes it a candidate for controlling the cavity induced drag.

Chapter 8

Conclusions and Recommendations for Future Work

The current experimental study was performed for a two-dimensional open cavity flow with $L/D = 4$, fully turbulent boundary layer with $1.28 \times 10^3 \leq Re_\theta \leq 4.37 \times 10^3$. The process of this experimental study has three stages. In the first stage, the free stream, upstream boundary layer, and the steady jets were characterised using laser Doppler anemometry (LDA), hot-wire anemometry (HWA), and particle image velocimetry (PIV). In the second stage, the cavity flow with no-jet was investigated using PIV, surface oil flow visualisations, and unsteady wall pressure measurements. In the final stage, the impact of steady jets on the cavity flow was investigated at $Re_\theta = 1.28 \times 10^3$ using the three aforementioned flow diagnostic techniques. In this stage, the blowing jets were tested with different momentum fluxes ($J = 0.11\ kg/m.s^2, 0.44\ kg/m.s^2$, and $0.96\ kg/m.s^2$), slot configurations (sharp edge and coanda), and blowing locations (blowing from the cavity leading and trailing edges).

1 Conclusions

The main findings of the current study are as follows:

- **For the jets outside the cavity model and under quiescent conditions**, it was found that the sharp edge and coanda jets are parallel to the x-axis. The coanda jets did not deflect towards the convex surface because they adhere to the knife edge rather than to the convex surface. It was also revealed that the characteristics of the two jet cases are generally similar to that of the turbulent planar jets. However, the coanda jets have a higher turbulence intensity and a larger initial width compared to the sharp edge jets. This is because the virtual origin of the coanda jets is upstream of the knife edge.

- **For the jets inside the cavity model and under quiescent conditions**, the study discovered that increasing J from $0.44\,kg/m.s^2$ to $0.96\,kg/m.s^2$ caused the coanda and the sharp edge jets to deflect significantly downwards and reattach on the cavity floor, due to the coanda effect between the jet and the cavity floor. It was also found that the time-averaged flow field and the temporal behaviour of the coanda and the sharp edge cases are quite similar. However, the main difference between the two cases seems to be how the jet interacts with the cavity trailing edge at $J = 0.96\,kg/m.s^2$.

- **For the baseline cavity flow (without a jet) at $\boldsymbol{Re_\theta = 1.28 \times 10^3}$**, the velocity spectra showed that a low-frequency instability ($St \approx 0.05$) dominates the cavity separated shear layer. This instability is attributed to the reverse flow interaction. The interaction takes place when sudden reverse flow surges reach the sensitive separation point of the cavity separated shear layer. As a result, a large-amplitude flapping wave is produced. As the wave propagates downstream of the cavity separated shear layer, it is amplified until it reaches the cavity trailing edge region, where the wave is partially dissipated due to the interaction with the cavity trailing edge.

  Higher-frequency instabilities were identified in the flow: (i) the shedding of the large vortical structures ($St \approx 0.68$) which was estimated by the vortex count method, and (ii) the first transversal mode ($St \approx 3$) which was identified from the unsteady wall pressure spectra. The spectral peak related to the shedding of the large vortical structures was not found in the unsteady wall pressure spectra because the shedding phenomenon is highly intermittent and not well organised.

- **For the baseline cavity flow (no-jet) at $\boldsymbol{1.28 \times 10^3 \leq Re_\theta \leq 4.37 \times 10^3}$**, the study revealed that the dimensionless frequencies of the reverse flow interaction and transversal mode showed a clear Reynolds number dependency. Increasing Re_θ from 1.28×10^3 to 4.37×10^3 causes a reduction in the dimensionless frequency of the reverse flow interaction from $St \approx 0.05$ to $St \approx 0.008$. Increasing Re_θ also causes the transversal mode to jump from the first to the second mode. In contrast, the variation of the dimensionless frequency for the shedding of the large vortical structures with Re_θ is probably attributed to the uncertainty of the vortex count method.

- **For blowing from the cavity leading edge with the sharp edge slot at $\boldsymbol{Re_\theta = 1.28 \times 10^3}$ and $\boldsymbol{0.11\ kg/m.s^2 \leq J \leq 0.96\ kg/m.s^2}$**, it was discovered that increasing J to $0.96\ kg/m.s^2$ causes the jet to deflect downwards. This deflection is attributed to two reasons: (i) the coanda effect, and (ii) the difference in the jet's growth rate between the upper and lower sides of the jet.

  As J increases, the change in the time-averaged cavity flow field becomes more significant. The changes include: (i) upstream shift of the main recirculation vortex, (ii) increase in the reverse flow rate, (iii) lifting of the upper boundary of the cavity separated shear layer upstream of the cavity trailing edge, and (iv) increase in turbulence fluctuations of the cavity separated shear layer due to the jet's disturbances.

  Increasing to $J \geq 0.44\ kg/m.s^2$ causes the dimensionless frequency of the reverse flow interaction to increase from $St \approx 0.05$ to $St \approx 0.1$. This frequency rise is due to the increase in the amount of the reverse flow impacting the sensitive separation region of the cavity separated shear layer. Additionally, the jet's disturbances increase the broadband level of the unsteady wall pressure spectra.

- **From the comparison between the leading edge blowing with the sharp edge and the coanda slots at $\boldsymbol{Re_\theta = 1.28 \times 10^3}$ and $\boldsymbol{J = 0.96\ kg/m.s^2}$**, it was revealed that the sharp edge and coanda jets deflect downwards. However, two main differences were highlited between the sharp edge and coanda cases. First, the upper boundary of the cavity separated shear layer in the coanda case is noticeably higher than the upper boundary in the sharp edge case. This difference is because the upward V velocity at the cavity trailing edge for the coanda case is relatively large, and hence this impedes the flow of the cavity separated shear layer and forces the upper boundary upwards. Second, the maximum Reynolds shear stress in the coanda case is significantly larger than that of the sharp edge case. This is because the turbulence intensity of the coanda jet is noticeably higher than that of the sharp edge jet.

The velocity spectra, pressure spectra, and the snapshots of the fluctuating field did not reveal any noticeable difference in the oscillations of the cavity separated shear layer between the two cases.

- **For blowing from the cavity trailing edge using the sharp edge slot at $\boldsymbol{Re_\theta = 1.28 \times 10^3}$ and $\boldsymbol{0.11\ kg/m.s^2 \leq J \leq 0.96\ kg/m.s^2}$**, the study found that the cavity separated shear layer forces the jet to deflect backward. However, as J increases the jet deflects forward. The instantaneous flow field showed that the jets are flapping about the time-averaged position and that the flapping amplitude increases with J. The interaction between the jet and the cavity separated shear layer increases the Reynolds shear stress in the cavity separated shear layer.

  The jet forces the cavity separated shear layer to deflect upwards. As a result, a recirculation bubble is formed downstream of the cavity trailing edge. This recirculation bubble impedes the flow of the cavity separated shear layer, and hence thickens it.

  The velocity spectra showed that as J increases from 0 to 0.96 $kg/m.s^2$ the dimensionless frequency of the reverse flow interaction increases from $St \approx 0.05$ to $St \approx 0.09$. This frequency rise is due to the increase in the reverse flow rate. An additional spectral peak was found at $St \approx 0.03$ and was attributed to the interaction between the jet and the cavity separated shear layer. The unsteady wall pressure spectra showed an increase in the broadband level of the cavity fluctuations.

- **From the comparison between leading and trailing edge blowing at $\boldsymbol{Re_\theta = 1.28 \times 10^3}$ and $\boldsymbol{J = 0.96\ kg/m.s^2}$**, the study found that the location of the main recirculation vortex for the leading edge blowing is closer to the cavity leading edge than that of the trailing edge blowing. As a result, more reverse flow in the former case impacts the sensitive separation point of the cavity separated shear layer. Consequently, the leading edge blowing enhances the reverse flow interaction more than the trailing edge blowing. This enhancement is evident from the temporal evolution of U/U_f and the velocity spectra of the cavity separated shear layer.

The time-averaged results showed that leading edge blowing increases the Reynolds shear stress of the cavity separated shear layer and the broadband level of the unsteady wall pressure spectra more than the trailing edge blowing. This is because the jet's disturbances in the former case are convected in the cavity separated shear layer, while the disturbances in the latter case are forced downstream of the cavity.

The leading and trailing edge blowing cases enhance the reverse flow interaction and increase the broadband level of the oscillations. Thus, these control methods are not suitable for controlling the oscillations of the cavity separated shear layer. However, the high capability of the trailing edge blowing in lifting up the cavity separated shear layer makes it a candidate for controlling the cavity induced drag.

2 Recommendations for future work

With respect to the current study, the following ideas are recommended for future work.

- **The actuator's knife edge:** In the current study, the coanda jet did not deflect towards the convex surface, because it adheres to the knife edge instead of the convex surface. Eliminating the knife edge is not desirable, as it will create a gap at the cavity leading edge, which will perturb the incoming flow. Thus, it is recommended to curve down the knife edge. The curved knife edge will deflect the jet downwards without perturbing the incoming flow.

- **Tracking of the jet inside the cavity flow:** Examining how the jet penetrates the cavity flow and interacts with the cavity separated shear layer was a challenging task in the present study, specially for the leading edge blowing case. In the current study, the penetration and interaction of the jets were investigated using the instantaneous PIV raw images and time-averaged velocity profiles. However, as the jet mixes with the cavity flow, it becomes less observable. Thus, to overcome this issue, it is recommended to either apply a flow visualisation technique or develop a computational method, that allows a better tracking of the jet inside the cavity flow.

- **The sample size for velocity spectra:** The velocity spectra of the cavity separated shear layer in the current experimental study was generated using only 1800 PIV images, which is too small to perform a spectral analysis. On the other hand, increasing the number of the acquired PIV images would be extremely time consuming. Thus, it was decided to overcome this issue considering the spectral peaks which repeatedly appear along the cavity separated shear layer. However, this procedure might eliminate significant peaks in the spectra. Therefore, to produce a better velocity spectral analysis, it is recommended to acquire the data using a flow diagnostic technique with a high frequency response such as HWA, LDA, or high-speed PIV.

- **Blowing from the cavity trailing edge:** Trailing edge blowing showed a high capability in lifting up the cavity separated shear layer and reducing the interaction between the cavity separated shear layer and the cavity trailing edge. This makes trailing edge blowing a candidate for controlling the cavity induced drag. Therefore, it is recommended to perform drag measurements on a cavity model to test the effectiveness of this control method in reducing the cavity-induced drag.

Bibliography

Ahuja, K. K. and Mendoza, J. (1995). Effects of cavity dimensions, boundary layer, and temperature on cavity noise with emphasis on benchmark data to validate computational aeroacoustic codes, *Technical Report NASA, Contract Report number:4653*.

Al Haddabi, N. H., Wiinblad-Rasmussen, S., Kontis, K. and Zare-Behtash, H. (2016). Control of low-speed cavity flow using steady jets, *8th AIAA Flow Control Conference*, AIAA.
URL: *http://arc.aiaa.org/doi/10.2514/6.2016-3172*

Antonia, R. a. and Browne, L. W. B. (1983). On the organized motion of a turbulent plane jet, *J. Fluid Mech.* **134**: 49–66.

Ashcroft, G. and Zhang, X. (2005). Vortical structures over rectangular cavities at low speed, *Physics of Fluids* **17**(1).

Beavers, G. S. and Wilson, T. a. (2006). Vortex growth in jets, *Journal of Fluid Mechanics* **44**(1): 97–112.
URL: *http://www.journals.cambridge.org/abstract_S0022112070001714*

Ben Haj Ayech, S., Habli, S., Mahjoub Saïd, N., Bournot, P. and Le Palec, G. (2016). A numerical study of a plane turbulent wall jet in a coflow stream, *Journal of Hydro-Environment Research* **12**: 16–30.
URL: *http://dx.doi.org/10.1016/j.jher.2016.02.001*

Betts, P. L. and Umiastowski, J. (1976). On spatially growing disturbances in an inviscid shear layer between parallel streams., *Transactions of the Canadian Society for Mechanical Engineering* **4**(3): 521–544.

Bliss, D. B. and Hayden, R. E. (1976). Landing gear and cavity noise prediction,

Technical Report July, NASA, Contract Report number: 2714.
URL: *http://hdl.handle.net/2060/19760021873*

Browne, L. W. B., Antonia, R. A. and Chambers, a. J. (1984). The interaction region of a turbulent duct flow, *Journal of Fluid Mechanics* **149**: 355–373.

Cattafesta, L., Garg, S., Choudhari, M., Li, F., L. Cattafesta, I. I. I., Garg, S., Choudhari, M. and Li, F. (1997). Active control of flow-induced cavity resonance, *28th Fluid Dynamics Conference*, AIAA Paper 971804, Snowmass Village, CO.
URL: *http://dx.doi.org/10.2514/6.1997-1804*

Cattafesta, L. N. and Sheplak, M. (2011). Actuators for Active Flow Control, *Annual Review of Fluid Mechanics* **43**(1): 247–272.

Cattafesta, L. N., Williams, D. R., Rowley, C. W. and Alvi, F. S. (2003). Review of Active Control of Flow-Induced Cavity Resonance, *33rd AIAA Fluid Dynamics Conference*, AIAA 2003-3567, Orlando.

Cervantes de Gortari, J. G. (1978). *An Experimental Study of the Flapping Motion of a Turbulent Plane Jet (No. HL-78-40).*, PhD thesis, Purdue University.

Chan, S., Zhang, X. and Gabriel, S. (2007). Attenuation of low-speed flow-induced cavity tones using plasma actuators, *AIAA Journal* **45**(7): 1525–1538.

Chatellier, L., Laumonier, J. and Gervais, Y. (2004). Theoretical and experimental investigations of low Mach number turbulent cavity flows, *Experiments in Fluids* **36**(5): 728–740.

Clauser, F. H. (1956). The turbulent boundary layer, *Advances in applied mechanics* **4**: 1–51.

D. J. Tritton (1977). *Physical Fluid Dynamics*, Van Nostrand Reinhold Company, New York.

Dantec Dynamics (2013). Streamware Pro: Installation and user guide, *Technical report*, Dantec Dynamics, Skovlunde, Denmark.

Dantec Dynamics (2016). Laser doppler anemometry: Introduction to principles and applications.

URL: *http://www.dantecdynamics.com/docs/support-and-download/research-and-education/lda.zip*

Daoud, M., Naguib, A., Bassioni, I., Abdelkhalek, M. and Ghoneim, Z. (2006). Microphone-array measurements of the floor pressure in a low-speed cavity flow, *AIAA Journal* **44**(9): 2018–2023.

Debiasi, M. and Samimy, M. (2004). Logic-based active control of subsonic cavity flow resonance, *AIAA Journal* **42**(9): 1901–1909.

Denshchikov, V. A., Kondrat'ev, V. N. and Romashov, A. N. (1978). Interaction between two opposed jets, *Fluid Dynamics* **13**(6): 924–926.

Deo, R. C., Mi, J. and Nathan, G. J. (2008). The influence of Reynolds number on a plane jet, *Physics of Fluids* **20**(7).

Dewan, A. (2011). *Tackling turbulent flows in engineering*, Springer Science & Business Media.

Dimotakis, P. E. and Brown, G. L. (1976). The mixing layer at high Reynolds number: large-structure dynamics and entrainment, *Journal of Fluid Mechanics* **78**(3): 535–580.

D'Ovidio, A. (1998). *Coherent structures in turbulent mixing layers*, PhD thesis, University of Leicester.

D'Ovidio, A. and Coats, C. M. (2013). Organized large structure in the post-transition mixing layer. Part 1: experimental evidence, *Journal of Fluid Mechanics* **737**: 466–498.
URL: *http://dx.doi.org/10.1017/jfm.2013.553*

Driver, D. M., Seegmiller, H. L. and Marvin, J. G. (1987). Time-dependent behaviour of a reattaching shear layer, *AIAA Journal* **25**(7): 914–919.

East, L. F. (1963). Three-dimensional flow in cavities, *Journal of Fluid Mechanics* **16**(4): 620–632.

Englar, R. J. (1975). Subsonic two-dimensional wind tunnel investigations of the high lift capability of circulation control wing sections, *Technical report*, David Tylor Naval Ship Research and Development Centre-Aviation and Surface Effects Department, Maryland.

Ethembabaoglu, S. (1973). *On the fluctuating flow characteristics in the vicinity of gate slots*, Phd thesis, University of Trondheim, Norwegian Institute of Technology.

European Union (2011). Flightpath 2050: Europes Vision for Aviation.
URL: *ec.europa.eu/transport/modes/air/doc/flightpath2050.pdf*

Fekete, G. I. (1963). Coanda flow of a two-dimensional wall jet on the outside of a circular cylinder, *Technical report*, McGill University-Mechanical Engineering Research Laboratories, Report number: 63-11, Montreal.

Fiedler, H. E. (1987). *Coherent Structures*, Springer, Berlin, Heidelberg, pp. 320–336.
URL: *http://dx.doi.org/10.1007/978-3-642-83045-7_37*

Fox, J. A. (1977). *An introduction to engineering fluid mechanics*, Macmillan Education UK, London.
URL: *http://link.springer.com/chapter/10.1007/978-1-349-15835-5_5#page-1*

Franke, M. and Carr, D. (1975). Effect of geometry on open cavity flow-induced pressure oscillations, *2nd Aeroacoustics Conference*, AIAA.
URL: *http://dx.doi.org/10.2514/6.1975-492*

Fredsøe, J. (1990). *Hydrodynamik, Den private Ingeniørfond*, Danmarks tekniske Højskole, Stougaard Jensen, København.

Gad-el Hak, M., Pollard, A. and Bonnet, J.-P. (1998). *Flow control: fundamentals and practices*, Springer-Verlag Berlin Heidelberg.
URL: *http://link.springer.com/10.1007/3-540-69672-5*

Garrido, P. S. (2014). *Active control of a backward facing step flow with plasma actuators*, Phd thesis, Université de Poitiers.

German-pipe (2017). Parallel preinsulated pipes branch.
URL: *http://www.germanpipe.de/site/*

Gharib, M. (1987). Response of the cavity shear layer oscillations to external forcing, *AIAA Journal* **25**(1): 43–47.

Gharib, M. and Roshko, A. (1987). The effect of flow oscillations on cavity drag, *Journal of Fluid Mechanics* **177**: 501–530.

Giuni, M. (2013). *Formation and early development of wingtip vortices*, Phd thesis, University of Glasgow.

Goertler, H. (1942). Berechnung von Aufgaben der freien Turbulenz auf Grund eines neuen Niiherungsansatzes, *ZAMM-Journal of Applied Mathematics and Mechanics/Zeitschrift für Angewandte Mathematik und Mechanik* **22**(5): 244–254.

Grace, S. M., Dewar, W. G. and Wroblewski, D. E. (2004). Experimental investigation of the flow characteristics within a shallow wall cavity for both laminar and turbulent upstream boundary layers, *Experiments in Fluids* **36**(5): 791–804.

Grant, I. and Owens, E. (1990). Confidence interval estimates in PIV measurements of turbulent flows, *Applied Optics* **29**(10): 1400–1402.

Grundmann, S. and Tropea, C. (2009). Experimental damping of boundary-layer oscillations using DBD plasma actuators, *International Journal of Heat and Fluid Flow* **30**(3): 394–402.
URL: *http://dx.doi.org/10.1016/j.ijheatfluidflow.2009.03.004*

Guazzelli, E., Morris, J. F., Flanagan, R. C. and Seinfeld, J. H. (1988). Aerosols, *Fundamentals of air pollution engineering*, Prentice-Hall, Inc., Englewood Cliffs, New Jersey, pp. 290 – 357.
URL: *http://resolver.caltech.edu/caltechbook:1988.001*

He, B., Xiao, X.-b., Zhou, Q., Li, Z.-h. and Jin, X.-s. (2014). Investigation into external noise of a high- speed train at different speeds, *Journal of Zhejiang University - Science A: Applied Physics & Engineering* **15**(12): 1019–1033.

Heenan, a. F. and Morrison, J. F. (1998). Passive control of backstep flow, *Experimental Thermal and Fluid Science* **16**: 122–132.

Heller, H., Holmes, D. and Covert, E. (1971). Flow-induced pressure oscillations in shallow cavities, *Journal of Sound and Vibration* **18**(4): 545–553.

Jakobsen, H. A. (2008). Single phase flow, *Chemical reactor modeling: Multiphase reactive flows*, Springer-Verlag Berlin Heidelberg.

Jørgensen, F. (2002). How to measure turbulence with hot-wire anemometers. A practical guide, *Technical report*, Dantec Dynamics, Skovlunde, Denmark.

Kachanov, Y. (1994). Physical mechanisms of laminar-boundary-layer transition, *Annual Review of Fluid Mechanics* **26**: 411–482.

Kalifa, R. B., Habli, S., Saïd, N. M., Bournot, H. and Palec, G. L. (2016). The effect of coflows on a turbulent jet impacting on a plate, *Applied Mathematical Modelling* **40**(11-12): 5942–5963.

Keane, R. D. and Adrian, R. J. (1990). Optimization of particle image velocimeters. Part I: Double pulsed systems, *Meas. Sci. Technol.* **1**: 1202–1215.
URL: *http://iopscience.iop.org/0957-0233/1/11/013*

Knisely, C. and Rockwell, D. (1980). Observations of the three-dimensional nature of unstable flow past a cavity, *Physics of Fluids* **23**(3): 425–431.

Knisely, C. and Rockwell, D. (1982). Self-sustained low-frequency components in an impinging shear layer, *Journal of Fluid Mechanics* **116**: 157–186.

Konrad, J. H. (1977). *An experimental investigation of mixing in two-dimensional turbulent shear flows with applications to diffusion-limited chemical reactions*, Phd thesis, California Institute of Technology.

Kourta, A. and Leclerc, C. (2013). Characterization of synthetic jet actuation with application to Ahmed body wake, *Sensors and Actuators, A: Physical* **192**: 13–26.
URL: *http://dx.doi.org/10.1016/j.sna.2012.12.008*

Kourta, a. and Vitale, E. (2008). Analysis and control of cavity flow, *Physics of Fluids* **20**(7).

Kundu, P. and Cohen, I. (2010). Instability, *Fluid mechanics*, 4th edn, Academic Press, pp. 429–495.

Kuo, C. H. and Huang, S. H. (2001). Influence of flow path modification on oscillation of cavity shear layer, *Experiments in Fluids* **31**(2): 162–178.

Lavision (2017a). Flow Master: Advance PIV systems for quantitative flow field analysis.
URL: *www.piv.de/documents/BR_FlowMaster.pdf*

Lavision (2017b). Product manual: Flow master, *Technical report*, Göttingen.

Lazar, E., Deblauw, B., Glumac, N., Dutton, C., Elliott, G. and Head, A. (2010). A Practical approach to PIV uncertainty analysis, *27th AIAA Aerodynamic Measurement Technology and Ground Testing Conference*, AIAA Paper 2010-4355, Chicago, pp. 1–22.

Lee, I. and Sung, H. J. (2001). Characteristics of wall pressure fluctuations in separated flows over a backward-facing step. Part I: Time-mean statistics and cross-spectal analysis, *Experiments in Fluids* **30**(3): 273–282.

Li, W. F., Huang, G. F., Tu, G. Y., Liu, H. F. and Wang, F. C. (2013). Experimental study of planar opposed jets with acoustic excitation, *Physics of Fluids* **25**(1).

Lin, J.-C. and Rockwell, D. (2001). Organized oscillations of initially turbulent flow past a cavity, *AIAA Journal* **39**(6): 1139–1151.
URL: *http://dx.doi.org/10.2514/2.1427*

Little, J., Debiasi, M., Caraballo, E. and Samimy, M. (2007). Effects of open-loop and closed-loop control on subsonic cavity flows, *Physics of Fluids* **19**(6).

Little, J., Nishihara, M., Adamovich, I. and Samimy, M. (2010). High-lift airfoil trailing edge separation control using a single dielectric barrier discharge plasma actuator, *Experiments in Fluids* **48**(3): 521–537.

Mathis, R., Lebedev, a., Collin, E., Delville, J. and Bonnet, J. P. (2009). Experimental study of transient forced turbulent separation and reattachment on a bevelled trailing edge, *Experiments in Fluids* **46**(1): 131–146.

Merzkirch, W. (1987). *Flow visualization*, 2nd edn, Elsevier, Universitat Essen, Germany.

Micheau, P., Chatellier, L., Laumonier, J. and Gervais, Y. (2004). Active control of a self-sustained pressure fluctuation due to flow over a cavity, *10th AIAA/CEAS Aeroacoustics Conference*, AIAA, Manchester, United Kingdom.

Morton, B. R., Taylor, G. and Turner, J. S. (1956). Turbulent gravitational convection from maintained and instantaneous sources, *Proceedings of the Royal Society A: Mathematical, Physical and Engineering Sciences* **234**(1196): 1–23.

Munro, S. E. and Ahuja, K. K. (2003). Fluid dynamics of a high aspect-ratio jet, *9th AIAA/CEAS Aeroacoustics Conference and Exhibit*, Georgia Inst. of Tech, AIAA 2003-3129, South Carolina.
URL: *https://doi.org/10.2514/6.2003-3129*

Namer, I. and Ötügen, M. V. (1988). Velocity measurements in a plane turbulent air jet at moderate Reynolds numbers, *Experiments in Fluids* **6**(6): 387–399.

Neary, M. D. and Stephanoff, K. D. (1987). Shear-layer-driven transition in a rectangular cavity, *Physics of Fluids* **30**(10): 2936–2946.
URL: *http://link.aip.org/link/PFLDAS/v30/i10/p2936/s1&Agg=doi*

Ng, Y. T. (2012). transitional cavity flow, *The Aeronautical Journal* **116**: 1185–1199.

Nieuwstadt, F. T., Westerweel, J. and Boersma, B. J. (2016). *Turbulence: Introduction to theory and applications of turbulent flow*, Springer, Cham.

Nyquist, H. (2002). Certain topics in telegraph transmission theory, *Proceedings of the IEEE* **90**(2): 280–305.

Parkhi, D. (2009). *Aeroacoustics of cavity flow using time-resolved particle image velocimetry*, Master of science thesis, Delft University of Technology.

Patricia, J., Block, W. and Heller, H. (1975). Measurements of farfield sound generation from a flow-excited cavity, *Technical report*, NASA TM X-3292.

Raffel, M., Willert, C. E., Wereley, S. and Kompenhans, J. (2012). *Particle image velocity: a practical guide*, 2nd edn, Springer.

Rajaratnam, N. (1976). *Turbulent Jets*, Vol. 5 of *Developments in Water Science*, Elsevier.
URL: *http://www.sciencedirect.com/science/article/pii/S0167564808709158*

Rockwell, D. and Knisely, C. (1979). The organized nature of flow impingement upon a corner, *Journal of Fluid Mechanics* **93**(3): 413.

Rockwell, D. and Naudascher, E. (1978). Review - Self sustaining oscillations of flow past cavities, *Journal of Fluid Engineering* **100**: 152–165.

Rockwell, D. and Naudascher, E. (1979). Self-sustained oscillations of impinging free shear layers, *Annual Review of Fluid Mechanics* **11**(1): 67–94.

Rodi, W. (1975). A review of experimental data of uniform density free turbulent boundary Layers, *in* B. Launder (ed.), *Studies in Convection*, Vol. 1, Academic Press, London, pp. 79–165.

Roos, F. W. and Kegelman, J. T. (1986). Control of coherent structures in reattaching laminar and turbulent shear layers, *AIAA Journal* **24**(12): 1956–1963.
URL: *http://dx.doi.org/10.2514/3.9553*

Rossiter, J. E. (1964). Wind tunnel experiments on the flow over rectangular cavities at subsonic and transonic speeds, *Technical report*, Aeronautical Research Council Reports and Memoranda No. 3438 UK., Farnborough.

Rowley, C. W. and Williams, D. R. (2006). Dynamics and control of high-Reynolds-number flow over open cavities, *Annual Review of Fluid Mechanics* **38**(1): 251–276.

Samimy, M., Debiasi, M., Caraballo, E., Serrani, A., Yuan, X., Little, J. and Myatt, J. H. (2007). Feedback control of subsonic cavity flows using reduced-order models, *Journal of Fluid Mechanics* **579**: 315–346.

Sapienza, L. and Eudossiana, V. (1995). High amplitude vortex-induced pulsations in a gas transport system, *Journal of Sound and Vibration* **184**: 343–368.

Sarohia, V. and Massier, P. F. (1976). Control of cavity noise, *Journal of Aircraft* **14**(9): 833–837.
URL: *http://dx.doi.org/10.2514/3.58862*

Sato, H. (1960). The stability and transition of a two-dimensional jet, *Journal of Fluid Mechanics* **7**(01): 53.

Schetz, J. A. (1984). *Foundations of boundary layer theory for momentum, heat, and mass transfer*, Wiley Online Library.

Schlichting, H. and Klaus, G. (2001). Boundary layer theory: Revised and enlarged edition, *European Journal of Mechanics - B/Fluids* **20**(1): 155–157.
URL: *http://linkinghub.elsevier.com/retrieve/pii/S0997754600011018*

Schmid, H. (2012). How to use the FFT and matlabs pwelch function for signal and noise simulations and measurements, *Technical report*, Institute of Microelectronics, University of Applied Sciences NW Switzerland.

Schobeiri, M. T. (2010). *Free Turbulent Flow*, Springer, Berlin, Heidelberg, pp. 327–356.
URL: *http://dx.doi.org/10.1007/978-3-642-11594-3_10*

Schobeiri, M. T. (2012). Introduction into Boundary Layer Theory, *Turbomachinery Flow Physics and Dynamic Performance*, Springer, Berlin, Heidelberg, pp. 619–683.

Schwarz, W. H. and Cosart, W. P. (1961). The two-dimensional turbulent wall-jet, *Journal of Fluid Mechanics* **10**(4): 481–495.

Simpson, R. L. (1996). Aspects of turbulent boundary-layer separation, *Progress in Aerospace Sciences* **32**(5): 457–521.

Sirovich, L. (1987). Turbulence and the dynamics of coherent structures. II. Symmetries and transformations, *Quarterly of Applied Mathematics* **45**(3): 573–582.
URL: *http://www.ams.org/qam/1987-45-03/S0033-569X-1987-0910463-9/*

Skyscrapercity (2017). Ferrocarriles y transporte urbano.
URL: *http://www.skyscrapercity.com/showthread.php?t=1497374*

Stanek, M., Raman, G., Kibens, V., Ross, J., Odedra, J. and Peto, J. (2000). Control of cavity resonance through very high frequency forcing, *6th Aeroacoustics Conference and Exhibit*, Aeroacoustics Conferences, AIAA 2000-1905, Lahaina.
URL: *http://dx.doi.org/10.2514/6.2000-1905*

Suponitsky, V., Avital, E. and Gaster, M. (2005). On three-dimensionality and control of incompressible cavity flow, *Physics of Fluids* **17**(10).

Tam, C. K. W. and Block, P. W. (1978). On the tones and pressure oscillations induced by flow over rectangular cavities, *Journal of Fluid Mechanics* **89**(2): 373–399.

Tennekes, H. (1965). Similarity laws for turbulent boundary layers with suction or injection, *Technical report*, Delft University of Technology.
URL: *https://repository.tudelft.nl/islandora/object/uuid:1d32ed31-6f43-499d-9b05-02b1ca69ad58?collection=research*

Thomas, F. O. and Goldschmidt, V. W. (1986). Structural characteristics of a developing turbulent planar jet, *Journal of Fluid Mechanics* **163**: 227–256.
URL: *http://www.journals.cambridge.org/abstract_S0022112086002288*

Tollmien, W. (1926). Berechnung turbulenter ausbreitungsvorgänge, *ZAMMJournal of Applied Mathematics and Mechanics/Zeitschrift für Angewandte Mathematik und Mechanik* **6**(6): 468–478.

Tomkins, C. D. and Adrian, R. J. (2003). Spanwise structure and scale growth in turbulent boundary layers, *Journal of Fluid Mechanics* **490**: 37–74.
URL: *http://www.journals.cambridge.org/abstract_S0022112003005251*

Tracy, M. B., Plentovich, E. B. and Stallings, R. J. (1993). Experimental Cavity Pressure Measurements at Subsonic and Transonic Speeds, *Technical report*, NASA Technical Paper number: 3358.

Tropea, C., Yarin, A. L. and Foss, J. F. (2007). *Springer handbook of experimental fluid mechanics*, Springer-Verlag, Berlin, Heidelberg.

Tu, G., Li, W., Du, K., Huang, G. and Wang, F. (2014). Onset and influencing factors of deflecting oscillation in planar opposed jets, *Chemical Engineering Journal* **247**: 125–133.
URL: *http://dx.doi.org/10.1016/j.cej.2014.02.097*

Ukeiley, L. and Murray, N. (2005). Velocity and surface pressure measurements in an open cavity, *Experiments in Fluids* **38**(5): 656–671.

Virendra Sarohia (1975). *Experimental and analytical investigation of oscillatoins in flows over cavities*, Phd thesis, California Institute of Technology.

Wang, H. (2000). *Jet interaction in a still or co-flowing environment*, PhD thesis, Hong Kong University of Science and Technology.

Wei, T., Schmidt, R. and McMurtry, P. (2005). Comment on the Clauser chart method for determining the friction velocity, *Experiments in Fluids* **38**(5): 695–699.

White, F. M. (1991). *Viscous fluid flow*, 2nd edn, Mc Graw-Hill, New York.

Wille, R. and Fernholz, H. (1965). Report on the first European mechanics colloquium, on the coanda effect, *Journal of Fluid Mechanics* **23**(4): 801–819.

Williams, D., Fabris, D. and Morrow, J. (2000). Experiments on controlling multiple acoustic modes in cavities, *6th Aeroacoustics Conference and Exhibit*, Aeroacoustics Conferences, AIAA 2000-1903, Lahaina.
URL: *https://doi.org/10.2514/6.2000-1903*

Winant, C. D. and Browand, F. K. (1974). Vortex pairing: The mechanism of turbulent mixing-layer growth at moderate Reynolds number, *J. Fluid Mech.* **63**(2): 237–255.

Yamamoto, Y. (2004). Mathematical methods, *Fundamentals of noise processes*, Cambridge University Press.

Yan, P., Debiasi, M., Yuan, X., Little, J., Ozbay, H. and Samimy, M. (2006). Experimental study of linear closed-loop control of subsonic cavity flow, *AIAA Journal* **44**(5): 929–938.

Yoshida, T., Watanabe, T., Ikeda, T. and Iio, S. (2006). Numerical analysis of control of flow oscillations in open cavity using moving bottom wall, *JSME International Journal Series B* **49**(4): 1098–1104.

Young, A. (1989). *Boundary Layers (AIAA education series)*, AIAA.

Zhou, M. D., Heine, C. and Wygnanski, I. (1996). The effects of excitation on the coherent and random motion in a plane wall jet, *Journal of Fluid Mechanics* **310**: 1–37.

Ziada, S. and Lafon, P. (2014). Flow-excited acoustic resonance excitation mechanism, design guidelines, and counter measures, *Applied Mechanics Reviews* **66**.

Ziada, S., Ng, H. and Blake, C. E. (2003). Flow excited resonance of a confined shallow cavity in low Mach number flow and its control, *Journal of Fluids and Structures* **18**(1): 79–92.

Appendices

Appendix A

Turbulent Boundary Layers

This appendix gives a basic description of the development of a turbulent boundary layer along with the main characterising equations for a turbulent boundary layer.

1 Definition of the boundary layer

In the proximity of the solid boundaries, the flow is influenced by the frictional force. This influence forces the flow to slow down as it approaches the solid boundary until it reaches zero-velocity magnitude at the boundary (known as the no-slip condition). The flow region influenced by this fractional force is called boundary layer. Beyond this region, the flow is barely affected by the frictional force (known as the free stream condition)(Fox, 1977). The thickness of the boundary layer δ is arbitrarily defined as the distance between the solid boundary and the y location of $U = 0.99\ U_f$, where U_f is the free stream velocity. However, due to the scattering of the velocity data points, it is not easy to precisely define the location of $U = 0.99\ U_f$. In order to cancel the impact of data scattering, some integrals such as displacement thickness δ^* and momentum thickness θ, are used to define the boundary layer thickness (Schetz, 1984). These integrals are:

$$\delta^* = \int_0^\delta (1 - \frac{U}{U_f}) dy \tag{A.1}$$

$$\theta = \int_0^\delta (1 - \frac{U}{U_f}) \frac{U}{U_f} dy \tag{A.2}$$

2 Development of the turbulent boundary layer

Boundary layers develop in the streamwise direction. Figure A.1 illustrates the development of the boundary layer over a flat plate with a zero pressure gradient in the streamwise direction ($dP/dx = 0$). Initially, the boundary layer is laminar. The laminar boundary layer consists of parallel layers moving on top of each other. Thus, momentum is transferred from the free stream to the near-wall region via pure viscous shearing. As the flow passes along the plate, the boundary layer becomes thicker. As a result, the velocity gradient and the viscous shear force between the layers decreases, forcing the moving layers close to the plate to slow down. Beyond a certain point (i.e the transition point), the flow loss stability and starts to rotate between the slow and fast-moving layers, forming disturbances which lead eventually to a turbulent boundary layer (Fox, 1977).

There are two main regimes for laminar to turbulent boundary layer transition, which are: (i) the instability amplification regime, and (ii) the "bypass" regime. The former regime usually takes place when the environmental disturbances (i.e free stream disturbances and surface roughness) are quite small. In this regime, the transition occurs in three stages, as illustrated in Figure A.2. During the first stage, the instability waves (Tollmien-Schlichting waves) are generated. In the second stage, the instability waves are amplified until they reach a critical value. At this point, the process of non-linear breakdown, randomisation, and a final transition into the turbulent state takes place (the third stage). In the "bypass" regime, the environmental disturbances are significantly high, and hence the first and second stages are bypassed (Kachanov, 1994).

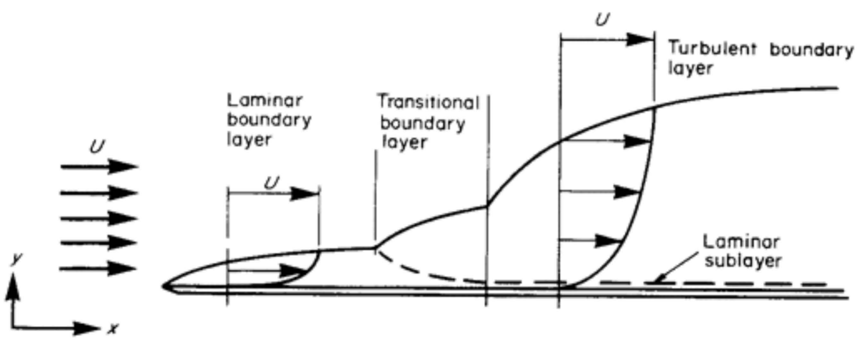

Figure A.1: Boundary layer development along a flat plate (Fox, 1977).

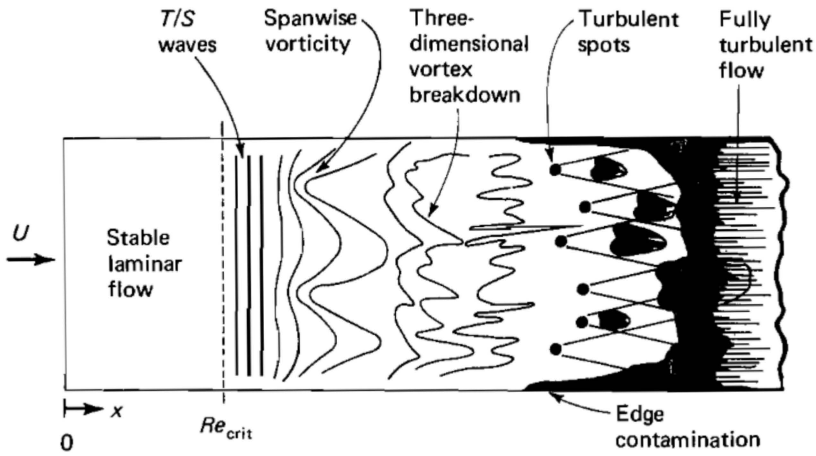

Figure A.2: Boundary layer transition process: instability amplification regime (White, 1991).

3 Characterising equations of the turbulent boundary layer

The Turbulent boundary layer (TBL) consists of four sublayers: (i) the viscous sublayer, (ii) the overlap sublayer, (iii) the logarithmic sublayer, and (vi) the outer sublayer, as shown in Figure A.3 (Schobeiri, 2012). To study these sublayers, the normal-to-wall distance is normalised with the wall friction velocity u_τ and kinematic viscosity υ, while the streamwise velocity is normalised with wall friction velocity as follows:

$$y^+ = \frac{y u_\tau}{\upsilon} \tag{A.3}$$

$$u^+ = \frac{U}{u_\tau} \tag{A.4}$$

where the the wall friction velocity is related to the wall shear stress τ_w by

$$u_\tau = \sqrt{\frac{\tau_w}{\rho}} \tag{A.5}$$

The viscous sublayer is a very thin laminar layer located in the proximity of the wall ($0 \lessapprox y^+ \lessapprox 5$). In this sublayer, all turbulent forces are damped out and momentum is transferred by viscous shearing (Fox, 1977). In the viscous sublayer, the following linear relationship applies:

$$u^+ = y^+ \tag{A.6}$$

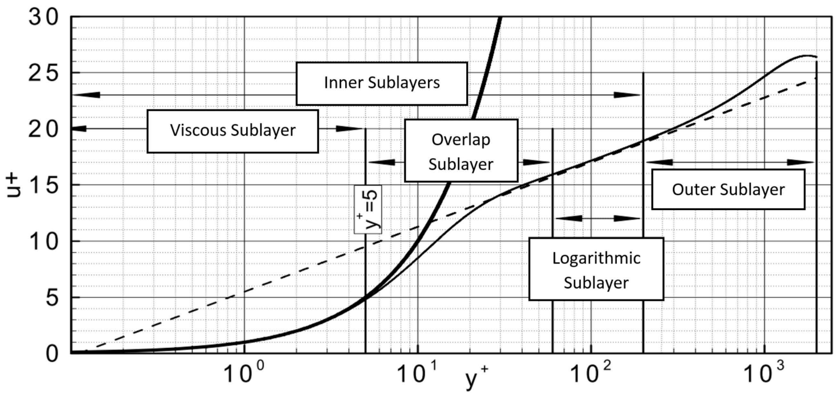

Figure A.3: The dimensionless profile and the sublayers of the turbulent boundary layer (Schobeiri, 2012).

The overlap sublayer ($5 \lessapprox y^+ \lessapprox 30$) links the viscous sublayer with the logarithmic sublayer. Both Viscous and turbulent effects are significant in the overlap sublayer. However, the turbulent effect becomes dominant at the logarithmic sublayer. The logarithmic sublayer extends from approximately $y^+ = 30$ to approximately $y^+ = 10^2$ or 10^3. The width of the logarithmic sublayer increases with increasing Reynolds number and decreases with increasing dP/dx (Young, 1989). The logarithmic sublayer is characterised by the universal law of the wall (Equation A.7), which is applicable for all streamwise pressure gradients except in the immediate vicinity of separation (Schetz, 1984).

$$u^+ = A\ log(y^+) + C \tag{A.7}$$

where A and C are empirical constants. Clauser (1956) suggested $A = 5.6$ and $C = 4.9$. However, these constants can change slightly with different experimental conditions. The wall friction velocity, which is required to calculate u^+ and y^+, is calculated by two methods: (i) Equation A.5, or (ii) the Clauser chart method (Wei et al., 2005). The former method requires measurements of the velocity gradient very close to the wall, which are difficult to obtain. On the other hand, the wall friction velocity in the Clauser chart method is calculated by fitting the experimental data with the universal law of the wall.

Moving towards the outer sublayer ($y^+ \gtrapprox 200$), the influence of the pressure gradient and free stream turbulence become significant, while the influence of the wall condition becomes less important. The governing law in this sublayer is called the velocity defect law. This law states that the dimensionless defect velocity is a function of the dimensionless normal-to-wall distance, wall shear stress, and the streamwise pressure gradient (Schobeiri, 2012). The law is written as,

$$\frac{U - U_e}{u_\tau} = f(\frac{y}{\delta}, \frac{\delta}{\tau_w}, \frac{dP}{dx}) \tag{A.8}$$

where U_e is the boundary layer edge velocity. According to Tennekes (1965), for zero pressure gradient $\frac{dP}{dx} = 0$ and a negligible dependency on the skin friction, which is a function of Reynolds number and surface roughness, the velocity defect law reduces to:

$$\frac{U - U_e}{u_\tau} = f(\frac{y}{\delta}) \tag{A.9}$$

For non-zero pressure gradient boundary layers $\frac{dP}{dx} \neq 0$, Clauser (1956) combined the second and third variables in right hand side of A.8 into one parameter (called Clauser equilibrium constant) as follows:

$$\beta = \frac{\delta^*}{\tau_w}\frac{dP}{dx} \tag{A.10}$$

According to Clauser (1956), for equilibrium boundary layer (i.e β is constant), the form of the velocity defect law does not change along the boundary layer. Each value of β corresponds to specific form of the defect law.

4 Summary

In summary, this appendix has reviewed the basics of boundary layers, particularly turbulent boundary layer. It has been seen that the thickness of the boundary layers is calculated by the $0.99U$ rule, displacement thickness, and momentum thickness. However, the displacement thickness and momentum thickness are more precise since they are integrals, which tend to cancel out the scattering nature of the acquired velocity. It was also found that transition from laminar to turbulent boundary layer occurs due to: (i) the instability amplification regime or (ii) the rapid regime. The former regime takes place when the environmental disturbances are low and vice versa for the latter regime. The appendix also reviewed the basics of turbulent boundary layer sublayers and their governing equations. It has been seen that the viscous sublayer is governed by a linear relationship (Equation A.6). The logarithmic sublayer is characterised by the universal law of the wall, which is applicable for all streamwise pressure gradients. On the other hand, the outer sublayer is governed by the velocity defect law, which is affected by a number of parameters such as the streamwise pressure gradient.

Appendix B

Other shear flows

This appendix provides the basics of some shear flows which are related to the current study, such as planar jets, opposing planar jets, coanda effect and flow over backward facing steps.

1 Planar jet

This section will review the time-averaged characteristics and the unsteady behaviour of the planar jets, particularly two-dimensional and turbulent planar jets.

1.1 Development regions of planar jets

As the planar jet expands, it develops two distinctive regions: (i) the flow-development region, and (ii) the fully-developed flow region, as illustrated in Figure B.1(a). The flow-development region starts from the virtual origin of the jet. The centre of the flow-development region consists of the potential core, where the jet velocity remains at its exit velocity U_0. As the jet moves in the streamwise direction, the potential core contracts due to the growth of two shear layers on both sides of the potential core. At the approximated streamwise station of $x = 12b_0$, where b_0 is the half width of the slot, the potential core disappears and the two shear layers merge. Beyond this point, the fully-developed flow region starts and the jet streamwise velocity profiles, which have a Gaussian distribution shape, become "self-similar" (Rajaratnam, 1976). When these profiles are non-dimensionalised by the jet centre velocity U_m and the jet half width b (see Figure B.1(c) for definitions), they collapse on a single profile. The self-similar profile was predicted satisfiedly by a number of numerical solutions such as Tollmien solution (Tollmien, 1926) and Goertle solution (Goertler, 1942).

1.2 Momentum flux of planar jets

Due to the substantial amount of fluid entrained by the jet, the volumetric flow rate per unit span of the jet increases in the streamwise direction. This entrainment has a rate proportional to the characteristic velocity (Morton et al., 1956). However, for infinitely small slot and negligible axial pressure gradient, the total jet momentum is assumed to be constant in the streamwise direction, as shown in Equation B.1 (Schlichting and Klaus, 2001).

$$\frac{d}{\mathrm{d}x}\int_{\infty}^{0} 2\rho U^2 \,\mathrm{d}y = 0 \tag{B.1}$$

where the integral part of Equation B.1 is the momentum flux per unit width J. Mometum flux is the momeutum rate per unit area. According to Rajaratnam (1976), the influence of the slot width and the jet velocity are combined in this quantity, and hence the behaviour of the planar jets can be determined from the momentum flux.

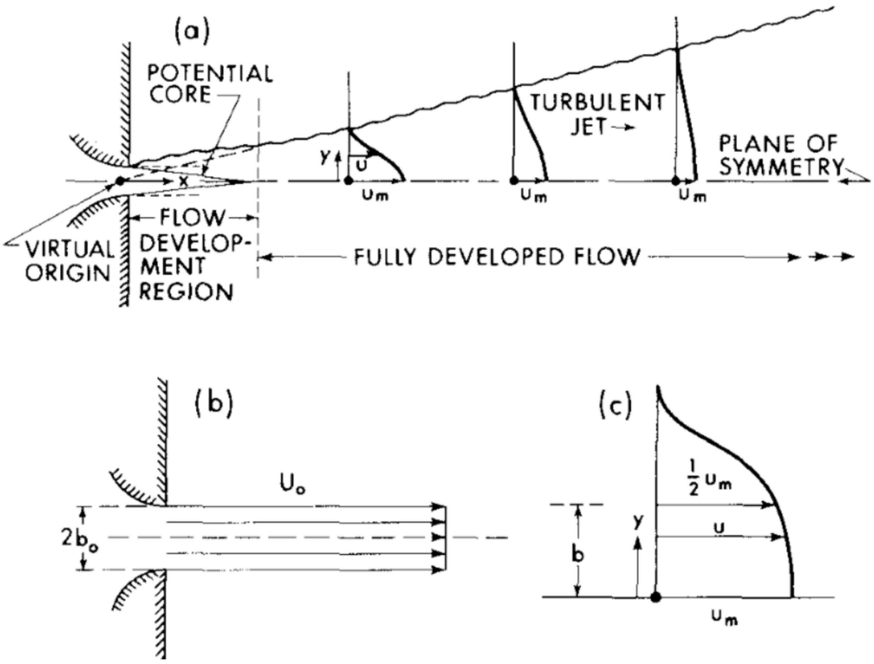

Figure B.1: Definition sketch for turbulent planar jet: a) jet development regions, b) potential core, and c) jet velocity profile (Rajaratnam, 1976).

1.3 Oscillations of planar jets

The unsteady behaviour of planar jets includes flapping motion and shedding of symmetrical/anti-symmetrical counter-rotating vortices pairs. The flapping motion is a lateral displacement of the jet boundaries. According to the observation of Cervantes de Gortari (1978) at Reynolds numbers Re_h based on slot width h and exit velocity between 7900 and 15100, this displacement travels in the streamwise direction at a speed slower than the convection speed of the jet vortical structures. The flapping motion is not caused by the bulk displacement of the jet mean velocity profile, but due to the quasi-periodic passage of the vortical structures (Antonia and Browne, 1983). The aforementioned study performed by Cervantes de Gortari (1978) found that the dimensionless flapping frequency in the farfield, $x/h > 30$, is approximately $St = fb/U_m = 0.11$, and is independent of Re_h.

Due to the higher velocity at the jet centre compared to the velocity at the jet boundaries, pairs of counter-rotating vortices are continuously shed in the streamwise direction, as illustrated in Figure B.2. The shedding of these structures is either symmetrical or asymmetrical with respect to jet centreline. The two modes differ in frequency and phase-relationship (Sato, 1960). The transition from the symmetrical to asymmetrical mode depends on a number of factors, such as nozzle shape, Re_h, and streamwise location. The impact of the first two factors on the jet symmetry were examined by Deo et al. (2008). The study revealed

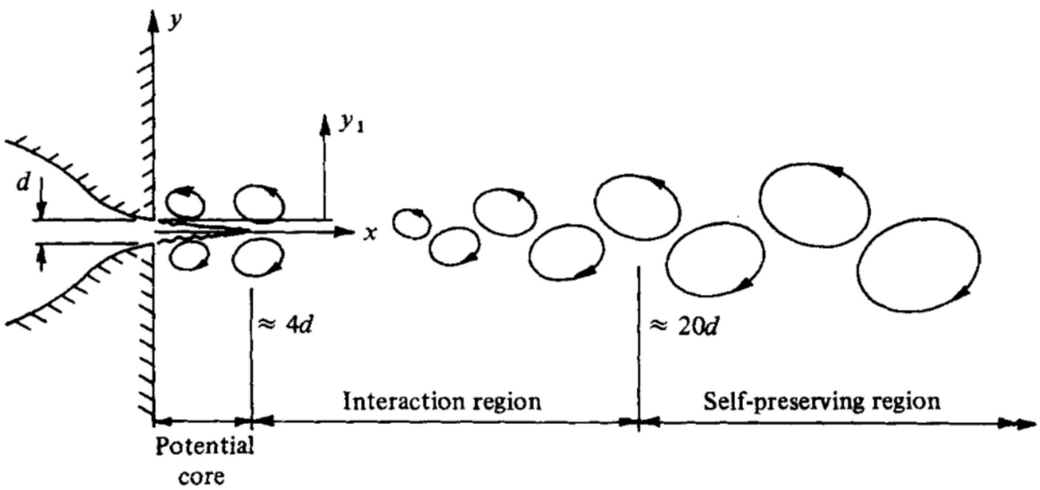

Figure B.2: Shedding of counter-rotating vortices pairs in a planar jet (Browne et al., 1984).

that smooth nozzles help to generate a symmetrical pattern, while the dominant pattern in the long/pipe nozzles is asymmetrical. The author also found that the dominance of the asymmetrical mode increases with increasing the Re_h from 1500 to 10000. Another study, performed by Thomas and Goldschmidt (1986), found a sudden jump from the symmetrical to asymmetrical pattern at the end of the potential core due to the merging of the two shear layers.

The periodicity of the vortex shedding in planar jets depends on the Reynolds number. At Re_h 400 to 500, Beavers and Wilson (2006) observed an intermittent shedding of vortices within a planar jet. However, when the Re_h increased from 500 to 3000, the shedding, according to the authors, becomes more periodic.

Different parameters have been used by the researchers to non-dimensionalise the shedding frequency of the planar jet. At Re_h between 500 and 3000, Beavers and Wilson (2006) found that the non-dimensional frequency based on slot height and exit velocity $St = fh/U_0$ for a symmetrical shedding is approximately 0.43. On the other hand, a study carried out by Sato (1960) found that $St = fh/U_0$ was approximately 0.23 for the symmetrical mode and 0.14 for the asymmetrical mode, and that these values were only constant at Re_h between 1500 and 8000. Thus, the author replaced h in the non-dimensional frequency with the momentum thickness θ. The non-dimensional frequency based on momentum thickness $St = f\theta/U_0$ remained constant at 0.015 over a wider range of conditions $100 < Re_\theta < 500$. Deo et al. (2008) used the local Strouhal number based on local $St = fb/U_m$ based on the local jet half width and local jet centre velocity. The study revealed that the local Strouhal number in the farfield $x/h = 20$ is between 0.05 and 0.11 within $1500 < Re_h < 16500$.

1.4 Section summary

This section summarises the time-averaged and the unsteady characteristics of planar jets. The section began with describing the characteristics of the streamwise development regions for planar jets. Then, the section introduces the definition of momentum flux for planar jets. Eventually, the section examines the oscillations of the planar jet, which include the flapping motion and the shedding of symmetrical/asymmetrical counter-rotating vortices pairs.

2 Opposing planar jets

The instability generated by two opposing planar jets has been investigated by a number of numerical and experimental studies. A numerical and experimental study, performed by Tu et al. (2014), on opposing planar jets at Re_h between 16 and 5000. The dimensionless distance between the two jet slots L/h was between 2 and 40. The study revealed that as the L/h ratio and/or Re_h increases, the flow displays a number of flow regimes and eventually reaches the stage of "deflecting oscillation" at $L/h > 10$ and $Re_h > 30$. As shown in Figure B.3, in the deflecting oscillation regime the two jets "*deflect off each other in the opposite directions and switch directions periodically*". As a result of the jet deflection, large vortices are formed periodically. According to the authors, as the Reynolds number increases, the amount of these vortices increases, while the size of them decreases.

The cycle of the deflecting oscillation starts with impingement between the two opposed jets. As a result, a region of positive pressure is developed in the impingement area. This region pushes the two opposed jet away from the symmetry plane causing both of them to deflect. After the deflection reaches a certain amount and the pressure in the impingement area is released, the two opposed jets deflect back towards the symmetry plane and collide again (Denshchikov et al., 1978). Under the impact of inertia, the two opposed jets continue their deflection in the opposite direction.

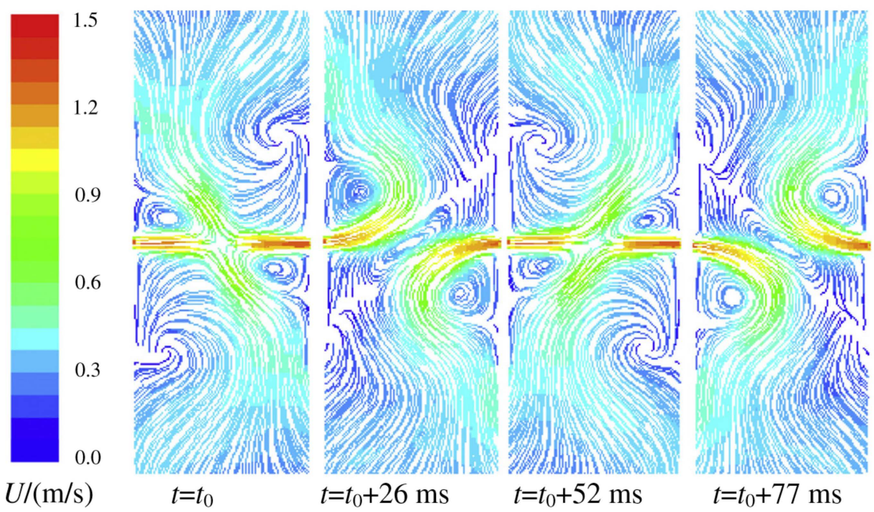

Figure B.3: Instantaneous time frames of the streamlines for deflecting oscillation regime of two opposing planar jets obtained by large eddy simulation at $Re_h = 250$ and $L/h = 10$ (Tu et al., 2014).

The oscillation period T of the deflecting oscillation has been found to be proportional to the ratio of L/U_0. The proportionality constant in the aforementioned study of Tu et al. (2014) is approximately 5.1. On other hand, Denshchikov et al. (1978) found that this constant is approximately 6 at Re_h between approximately 200 and 2000. Another experimental study, performed by Li et al. (2013) at Re_h between 242 and 2419, and L/h between 6 and 30, approximated the proportionality constant to 5.12.

3 Coanda effect

Jets can be deflected with the help of "coanda effect", which has many practical applications such as jet deflection devices and circulation control of aerofoils (Wille and Fernholz, 1965). Coanda effect is the tenancy of free jets to attach on nearby surfaces, as shown in Figure B.4 (a). Jets entrains fluid from the sides. Consequently, when a surface is in the proximity of a jet, a low-pressure region is generated between the jet and surface causing the jet to deflect towards the surface and attach to it (D. J. Tritton, 1977). The jet remainds attached to the surface due to a pressure force. This force, according to Wille and Fernholz (1965), is best explained by potential flow theory. According to the theory, if a jet is surrounded by a quiescent fluid from one side and a solid boundary from the other side, the pressure at the solid boundary will be lower than the pressure of the surrounding P_0. This pressure difference maintains the jet attachment.

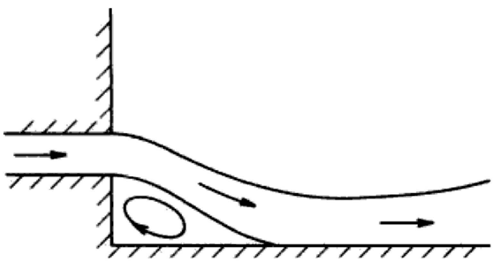

(a) Coanda effect

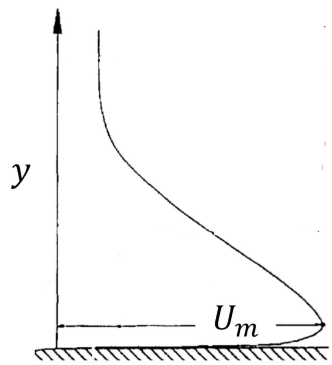

(b) Streamwise velocity profile of a wall jet

Figure B.4: Sketches for coanda effect (D. J. Tritton, 1977) and streamwise velocity profile of a wall jet (Zhou et al., 1996).

As the jet proceeds, the jet entrains more fluid and its velocity decreases. Consequently, the surface pressure increases to P_0 and the jet eventually separates (Fekete, 1963).

The attached jet is called a "wall jet". The wall jet has jet-like properties and is also influenced by the wall (Schwarz and Cosart, 1961). The wall jet velocity is zero at the surface and at the unbounded jet boundary, and somewhere between the surface and the jet boundary, the velocity reaches the maximum value, as illustrated in Figure B.4(b).

In order to generate a curved jet, the adjacent surface usually has a cylindrical shape, as illustrated in Figure B.5. The angular position at which the curved jet separates is called the separation angle ϕ_{sep}. Fekete (1963) performed an experimental study on coanda effect around a cylindrical surface. The jet was tangential to the cylinder surface, but not penetrating into it $t/h = 0$. The study examined the effect of Reynolds number based cylinder radius Re_R, slot width to cylinder radius ratio h/R, and surface roughens on the separation angle. The author found that the separation angle strongly increases with increasing Re_R. However, separation angle becomes independent of Reynolds number at $Re_R \gtrapprox 4 \times 10^4$. The study also showed some dependency of the separation angle on the h/R ratio, though reducing h/R ratio from 0.053 to 0.0074 did not produce a specific trend with the separation angle. On the other hand, increasing the surface roughness yields an earlier separation. However, this effect varies with Re_R and h/R ratio. On his experiment on airfoil circulation control, Englar (1975) reported that within $0.01 < h/R < 0.05$, the jet was strongly attached to

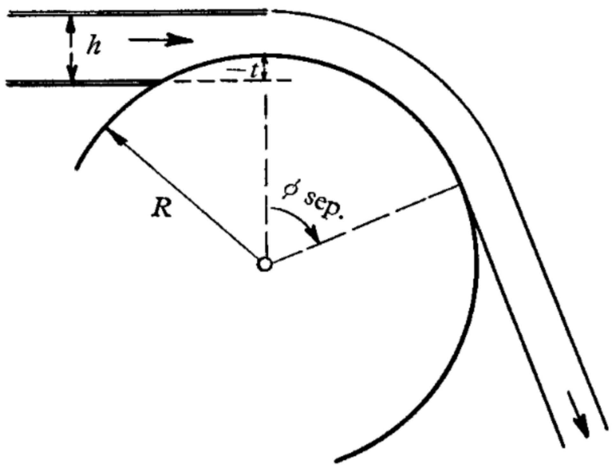

Figure B.5: Coanda effect over a convex surface (Wille and Fernholz, 1965).

the coanda surface. Another study performed by Wille and Fernholz (1965) with a jet penetrating into the cylinder $t/h \neq 0$ revealed that the maximum separation angle was achieved with t/h = -0.4.

4 Flow over backward facing step (BFS)

Flow over a BFS is considered as a benchmark for separating and reattachment flows. Figure B.6 shows the main features of a BFS flow. Due to a geometric discontinuity, the flow separates at the corner of the BFS forming a free shear layer. Due to momentum transfer, the free shear layer expands. At the same time, the free shear layer curves down and eventually impinges on the reattachment zone generating a strong adverse pressure gradient. A portion of the impinged fluid is recirculated towards the separation zone (Simpson, 1996).

The flow over BFS is highly unsteady. The wall pressure fluctuations in the reattachment zone are mainly due to the instabilities of the free shear layer (Lee and Sung, 2001). Two main instabilities are formed in the free shear layer: (i) the flapping motion of the free shear layer, and (ii) the shedding of coherent vortical structures. The flapping motion is a vertical displacement of the free shear layer, that causes the reattachment location to fluctuate in the streamwise direction as illustrated in Figure B.6. Driver et al. (1987) attributed the flapping behaviour in BFS flows to the inflation and collapse of the recirculation zone.

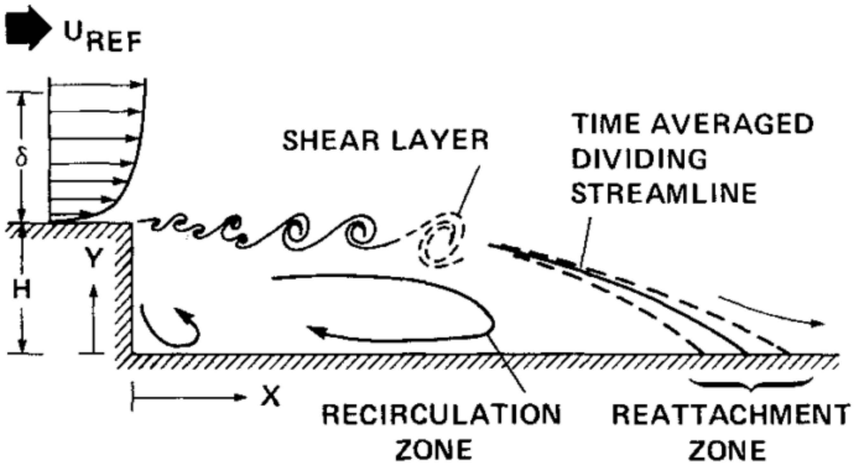

Figure B.6: Main features of BFS flow (Driver et al., 1987).

According to the authors, the recirculation zone collapses when vortical structures with high streamwise momentum escape the reattachment zone towards the farfield. As a result, less flow enters the recirculation zone, and hence the recirculation bubble collapses. This causes an increase in the curvature of the free shear layer, thus more flow starts to enter the recirculation zone and the bubble re-inflates. In contrast, Heenan and Morrison (1998) believed that the flapping of the free shear layer is due to the upstream convection of disturbances from the reattachment zone towards the free shear layer. The authors claimed that they completely eliminated the flapping motion by replacing the BFS floor with a permeable surface. When the free shear layer disturbances impinge at the permeable surface, they are damped inside plenum and then feedback to the recirculation zone as a relatively quiescent flow. At a free stream velocity (U_f) of 44.2 m/s and Reynolds number based on the momentum thickness (Re_θ) of 5000, Driver et al. (1987) found that the non-dimensional frequency $St = fb/U_{sl}$ for this motion is approximately 0.06, where b is the width of the free shear layer, U_{sl} is the average velocity of the free shear layer ($U_{sl} \approx 0.5U_f$). The study also found that this instability is random and has a lower energy than the shedding of the coherent vortical structures. The non-dimensional frequency for the shedding of the coherent vortical structures was approximately 0.2. The authors found that these structures dissipate or merge near the reattachment region to form a larger structure with a high convection speed.

Appendix C

Statistical Description of Turbulence

This appendix provides information about the statical quantities used to study turbulence, for example, spatial and temporal correlations, and Reynolds shear stresses.

1 Reynolds decomposition

In a turbulent flow, the instantaneous velocity $\tilde{U}_i$ can be split into two components: (i) the averaged velocity $\overline{U_i}$, and (ii) the fluctuating velocity $u_i^{'}$, as illustrated in Figure C.1 (Nieuwstadt et al., 2016). This decomposition is called Reynolds decomposition and is expressed as follows:

$$\tilde{U}_i = \overline{U_i} + u_i^{'} \tag{C.1}$$

For velocity averaging, different approaches are applied, such as time-averaging (Equation C.2) and ensemble-averaging (Equation C.3). Figure C.2 illustrates the difference between the two terms. In time-averaging, a quantity of a single system is averaged over a certain time interval. While in ensemble-averaging, a quantity of many identical systems is averaged at a certain time instance (Yamamoto, 2004). In the current study, ensemble-averaging with finite ensemble size N has been applied for velocity averaging.

$$\overline{U_i} = \frac{1}{T} \int_{+0.5T}^{-0.5T} \tilde{U}_i(t+\tau)d\tau \tag{C.2}$$

$$\overline{U_i} = \lim_{N \to \infty} \sum_{\alpha=1}^{N} \tilde{U}_i^{\alpha} \tag{C.3}$$

where T is the time interval, τ is the time step, N is the ensemble size, and index α indicates the time instance realised in the experiment.

The velocity fluctuations level is measured using the standard deviation (or the root mean square RMS), which is expressed mathematically as follows:

$$\sigma_u = U_{rms} = \sqrt{\overline{u'^2}} \tag{C.4}$$

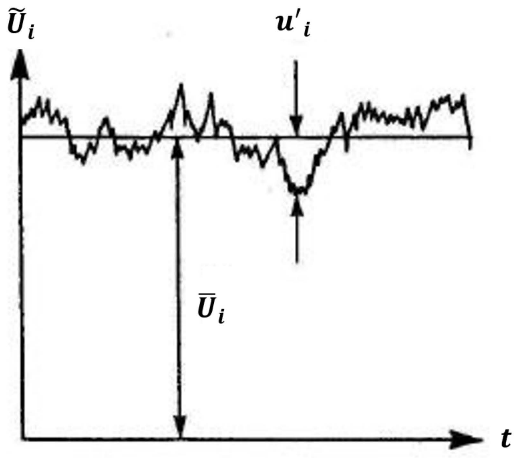

Figure C.1: Definition sketch for the instantaneous velocity, the averaged velocity, and the fluctuating velocity (Fredsøe, 1990).

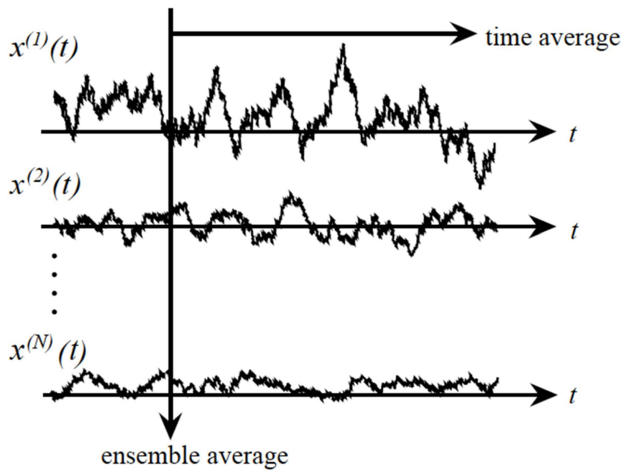

Figure C.2: Definition sketch for time and ensemble averaging of a quantity x (Yamamoto, 2004).

2 Temporal and spatial correlations

Turbulence statical quantities that are defined in a single point in space, such as standard deviation, are called single-point statistical moments. In order to examine the spatial and temporal structure of turbulence, multi-point statistical moments are acquired. The simplest form of multi-point moments is the correlation function, which correlates two variables at two different points (Nieuwstadt et al., 2016).

Correlating velocity fluctuations at a particular point in space at two time instances t_1 and t_2 is called auto-covariance, which can be expressed as follows:

$$R(\tau) = \overline{u_i'(t)u_i'(t+\tau)} \tag{C.5}$$

where $\tau = t_2 - t_1$. The normalised form of the above equation is called auto-correlation coefficient $\rho(\tau)$ (Jakobsen, 2008).

$$\rho(\tau) = \frac{\overline{u_i'(t)u_i'(t+\tau)}}{\overline{u_i'^2(t)}} \tag{C.6}$$

As the time difference increases $\tau \longrightarrow \infty$, the correlation diminishes $\rho(\tau) \longrightarrow 0$, as illustrated in Figure C.3. Integrating the auto-correlation coefficient between $\tau = 0$ and $\tau = \infty$ yields the integral time scale as shown in the following equation.

$$\mathcal{T} = \int_0^\infty \rho(\tau) d\tau \tag{C.7}$$

The integral time scale is "*a measure for the time difference over which the significant correlation persists*" (Nieuwstadt et al., 2016). Additionally, the auto-correlation coefficient reveals the temporal structure of turbulence, as shown in Figure C.3. When τ is approaching zero, the correlation describes the turbulent microstructures. On the other hand, when τ is approaching the integral time scale, the correlation describes the turbulent macrostructures. Therefore, the integral time scale is associated with the timescale of the turbulent macrostructures (Nieuwstadt et al., 2016).

Spatial correlation correlates velocity fluctuations at two points in space $\underline{x}_1$ and $\underline{x}_2$ at a particular point in time. It provides information about the spatial structure of the turbulence. The correlation tensor is expressed as follows:

$$R_{ij}(\underline{r}) = \overline{u_i'(\underline{x}_1)u_j'(\underline{x}_2)} \tag{C.8}$$

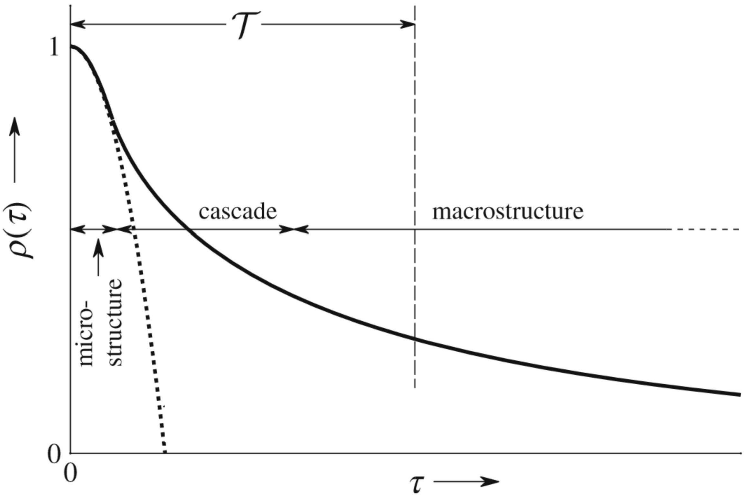

Figure C.3: The variation of the auto-correlation coefficient with time difference (Nieuwstadt et al., 2016).

where the separation vector $\underline{r}=\underline{x}_2 - \underline{x}_1$. The correlations tensor has 9 components. Depending on the orientation of the velocity fluctuation vectors u_i' and u_j' with respect to the separation vector, the tensor components are categorised into three main configurations: (i) longitudinal correlation, (ii) transversal correlation, and (iii) corss-correlation. The definition of these correlations is illustrated in Figure C.4 (Nieuwstadt et al., 2016). Examples for longitudinal correlation include $R_{uu}(\underline{r})$ and $R_{vv}(\underline{r})$ for $\underline{r} = (r, 0, 0)$ and $\underline{r} = (0, r, 0)$, respectively. Example for transversal correlation include $R_{vv}(\underline{r})$ for $\underline{r} = (r, 0, 0)$. Example for corss-correlation is $R_{uv}(\underline{r})$ for $\underline{r} = (r, 0, 0)$.

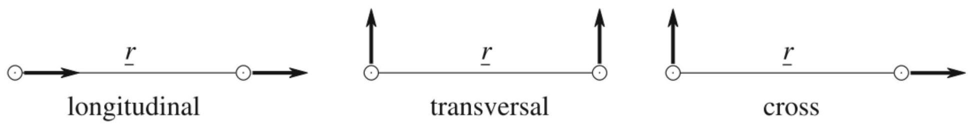

Figure C.4: The orientation of the velocity fluctuations vectors (bold arrows) in spatial correlation with respect to the separation vector (Nieuwstadt et al., 2016).

3 Reynolds stresses

The Reynolds-averaged NavierStokes equation for incompressible flow, which describes the transport of mean momentum in the x_i direction, states that:

$$\frac{\partial \overline{U_i}}{\partial t} + \overline{U_j}\frac{\partial \overline{U_i}}{\partial x_j} + \frac{\partial \overline{u_i' u_j'}}{\partial x_j} = \frac{1}{\rho}\frac{\partial \overline{P}}{\partial x_i} + \nu \frac{\partial^2 \overline{U_i}}{\partial x_j \partial x_i} \tag{C.9}$$

The physical interpretation of the above equation is that the change in the average velocity of a fluid element equals the sum of the time-averaged pressure and viscous forces plus a contribution of the $\overline{u_i' u_j'}$ term. This term represents the transfer of momentum due to the turbulent fluctuation and is called the Reynolds stress tensor. The Reynolds stress tensor correlates two components of velocity fluctuations at one spatial point. The tensor is physically interpreted as the flux of the ith momentum in the jth direction due to turbulent fluctuations (Jakobsen, 2008).

Appendix D

Calculation of Stroke Number

The Stokes number (STK) is the ratio between the relaxation time of the seeding particle and the characteristic time of the moving fluid. The Stokes number indicates the inertia of the seeding particle, which shows how fast the particle adopts the flow velocity (Guazzelli et al., 1988). According to Tropea et al. (2007), $STK < 0.1$ yields an acceptable flow tracking accuracy with errors less than 1%. In the current experiments, the Aerosol Generator PivPart160 atomiser generated olive oil particles with a mean diameter of 1 μm. The particle relaxation time is:

$$\tau_p = \frac{\rho_p d_p^2}{18\mu_g} = \frac{800 \times (1 \times 10^{-6})^2}{18 \times 1.7 \times 10^{-5}} = 2.5 \times 10^{-5} seconds \tag{D.1}$$

where p denotes the seeding particles, while g denotes the moving fluid. The characteristic time of the moving fluid is:

$$\tau_g = 10\frac{\delta_{ref}}{\Delta V} = 10\frac{13 \times 10^{-3}}{43.7} = 2.97 \times 10^{-3} seconds \tag{D.2}$$

where δ_{ref} and ΔV are the reference boundary layer thickness and the maximum particle slip velocity, respectively. The Stokes number is:

$$STK = \frac{\tau_p}{\tau_g} = \frac{2.5 \times 10^{-5}}{2.97 \times 10^{-3}} = 8.43 \times 10^{-4} \tag{D.3}$$

Since $STK \lll 0.1$, it can be concluded that the seeding particles track the flow.

Appendix E

Convergence Study for PIV

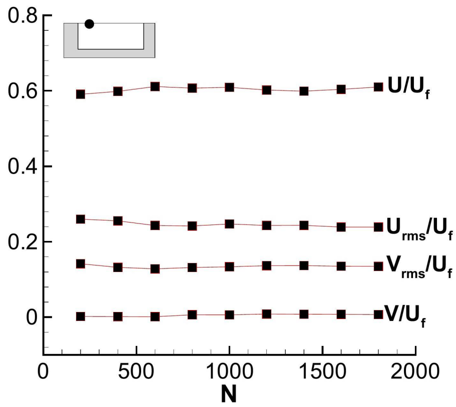

(a) x/L = 0.16, y/D = 0

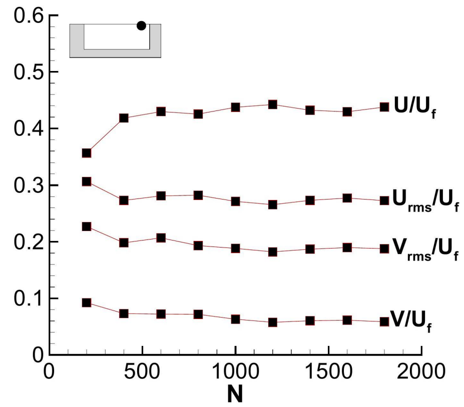

(b) x/L = 0.90, y/D = 0

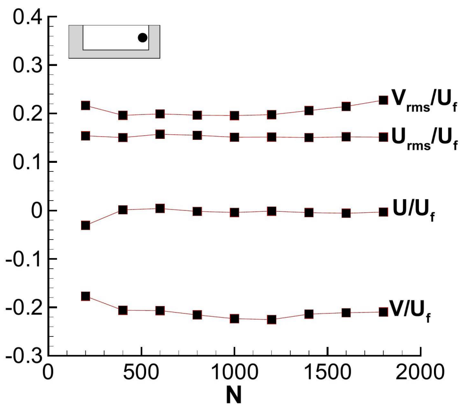

(c) x/L = 0.94, y/D = -0.46

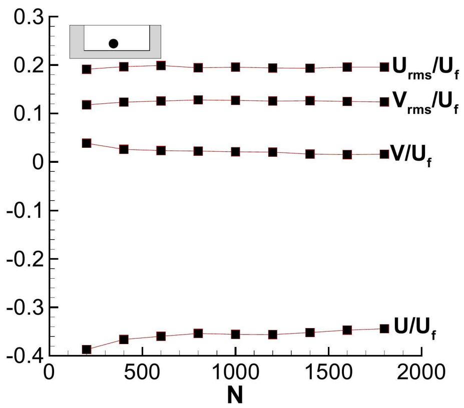

(d) x/L = 0.43, y/D = -0.79

Figure E.1: Convergence study at different locations in the cavity for baseline case (no-jet) at U_f of 11.1 m/s.

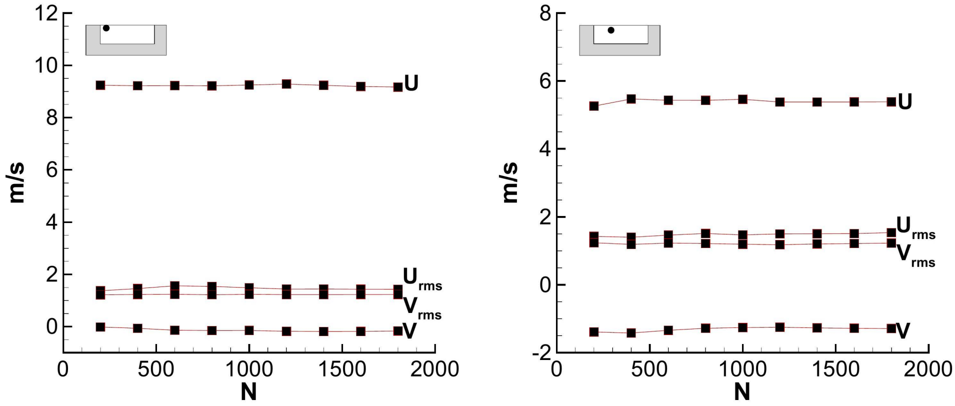

(a) x/L = 0.10, y/D = -0.05

(b) x/L = 0.37, y/D = -0.18

Figure E.2: Convergence study at different locations in the cavity for blowing from the cavity leading edge (wind tunnel off). The jet case is coanda ($J = 0.96$ $kg/m.s^2$).

Appendix F

Uncertainty Calculations for the PIV Measurements

Lazar et al. (2010) identified four sources of uncertainty for time-averaged two-dimensional PIV measurements: the PIV equipments σ_E, the seeding particle lag σ_L, the sampling size σ_S, and the processing algorithm σ_P.

The equipment uncertainty, which is mainly due to the calibration factor and the timing accuracy of the time step dt, is assumed to be negligible. The seeding Particle lag uncertainty is due to the tracking error between the seeding particles and the flow. Since $STK \lll 0.1$, the seeding particle lag uncertainty is assumed to be zero. The sampling size uncertainty is related to the number of processed images used to compute the time-averaged velocity field and the turbulence quantities (Lazar et al., 2010). Grant and Owens (1990) estimated the sampling uncertainty by

$$\sigma_S = \frac{Z_c}{\sqrt{2N}\sqrt{1+2T_i^2}} \tag{F.1}$$

where Z_c, N, and T_i are the confidence coefficient, the total number of the processed images, and local turbulence intensity, respectively. The maximum turbulence intensity is 0.2. The confidence coefficient is 1.96 for a confidence level of 95%. The total number of the processed images is 1800. Thus the sampling size uncertainty is:

$$\sigma_S = \frac{1.96}{\sqrt{2\times 1800}\sqrt{1+2\times 0.2^2}} = 3.39 \tag{F.2}$$

The processing uncertainty is mainly due to the assumption that the computed velocity vector represents the centre velocity of the interrogation window. This uncertainty can reach 5 to 10% at regions of high velocity gradient, but generally it is less than 1% over the majority of the flow field (Lazar et al., 2010). The combined uncertainty is:

$$\sigma_T = \sqrt{\sigma_E^2 + \sigma_L^2 + \sigma_S^2 + \sigma_P^2} = \sqrt{0 + 0 + 3.39^2 + 1^2} = 3.45\% \tag{F.3}$$

Appendix G

Relative Expanded Uncertainty for HWA Measurements

The calculations of the relative expanded uncertainty for HWA velocity sample follow the instructions from the manufacturer of the HWA system (Jørgensen, 2002). The relative standard calibrator uncertainty is:

$$U(U_{cal}) = \frac{1}{100} \times STDV(U_{calibrator}) = \frac{1}{100} \times 0.01 = 0.01 \tag{G.1}$$

where $STDV(U_{calibrator})$ for a good dedicated calibrator, such as the one used in the current study, is typically 1%. The relative standard linearisation uncertainty is:

$$U(U_{lin}) = \frac{1}{100} \times STDV(\triangle U_{lin}) = \frac{1}{100} \times 0.005 = 0.005 \tag{G.2}$$

where the standard deviation of the curve fitting errors in the calibration points $STDV(\triangle U_{lin})$ is approximately 0.5%. The relative standard resolution uncertainty of the A/D converter is:

$$U(U_{res}) = \frac{E_{AD}}{\sqrt{3} \times U \times 2^n} \times \frac{\partial U}{\partial E} = \frac{5}{\sqrt{3} \times 10 \times 2^{16}} \times 43.3 = 0.00019 \tag{G.3}$$

where E_{AD} is the A/D board input range, n is its resolution in bits, U the velocity, and $\partial U/\partial E$ is the slope of the inverse calibration curve. The relative standard uncertainty for probe positioning is:

$$U(U_{pos})) = \frac{1 - cos\theta}{\sqrt{3}} = \frac{1 - cos0.017}{\sqrt{3}} \approx 0 \qquad \text{(G.4)}$$

where the typical angle alignment uncertainty θ is 1° (0.017 rad). The relative standard uncertainty for the ambient temperature variation is ignored, since the temperature variation effect was greatly minimised during the experiments. The relative standard uncertainty of the ambient pressure variation is:

$$U(U_P)) = \frac{1}{\sqrt{3}} \times \frac{P_0}{P_0 + \triangle P} = \frac{1}{\sqrt{3}} \times \frac{101.32}{101.32 + 10} = 0.005 \qquad \text{(G.5)}$$

where P_0 is the standard atmospheric pressure in kPa, while the typical ambient pressure variation $\triangle P$ is 10 kPa. The relative standard uncertainty of the ambient humidity variation is:

$$U(U_{hum}) = \frac{1}{\sqrt{3}} \times \frac{1}{U} \times \frac{\partial U}{\partial P_{wv}} \times \triangle P_{wv} = \frac{1}{\sqrt{3}} \times \frac{1}{10} \times 0.01 \times 1 = 0.00057 \qquad \text{(G.6)}$$

The relative expanded uncertainty for the HWA velocity sample is:

$$U(U_{sample}) = 2 \times \sqrt{\sum U(U_i)^2} = 0.0247 = 2.47\% \qquad \text{(G.7)}$$

where $U(U_i)$ is the relative standard uncertainties.

Appendix H

The proper orthogonal decomposition (POD)

The proper orthogonal decomposition (POD) is “a method used to decompose a set of vector fields (2D or 3D) into a set of empirical eigenfields, which describes the dominant behavior or dynamics of a given problem” (Lavision, 2017b). Each eigenfield is associated with an energy value, that is a fraction of the overall energy of the vector fields. According to these energy values, the eigenfields are numbered from the most dominant behaviour to the least dominant. It is also possible to reconstruct the vector field by super-positioning the most important eigenfields (Lavision, 2017b).

The POD in the current study was performed using the Davis 8 software. First, the ensemble average was subtracted from each single vector field. Then, the POD algorithm was implemented using the method of snapshots (Lavision, 2017b). This method is suitable for highly resolved flows, since ”the number of sampled points do not enter in the calculation in an essential way” (Sirovich, 1987). In this method, the instantaneous flow fields (snapshots) are expressed as follows:

$$v^{(n)} = v(x, n\tau) \tag{H.1}$$

where τ is a time scale. The instantaneous flow fields are uncorrelated for different values of n. The kernel (K) is formed as follows:

$$K(x, x') = \lim_{M\to\infty} \frac{1}{M} \sum_{n=1}^{M} v^{(n)}(x) v^{(n)}(x') \tag{H.2}$$

The kernel (K) is approximately:

$$K(x, x') = \frac{1}{M} \sum_{n=1}^{M} v^{(n)}(x) v^{(n)}(x') \tag{H.3}$$

where the number of snapshots (M) is sufficiently large. The kernel (K) in Equation H.3 has eigenfunctions of the form:

$$\psi = \sum_{k=1}^{M} v^{(n)} A_k v^{(k)} \tag{H.4}$$

where A_k is a constant, that has to be found (Sirovich, 1987). Introducing Equations H.3 and H.4 in the following equation:

$$\int K(x, x') v(x') dx' = \lambda v(x) \tag{H.5}$$

yields

$$CA = \lambda A \tag{H.6}$$

where λ are the eigenvalues, while A is

$$A = (A_1, ..., A_M) \tag{H.7}$$

and

$$C_{mn} = \frac{1}{M} (v^{(M)}, v^{(n)}) \tag{H.8}$$

A more detailed procedure for the snapshots method is found in the study of Sirovich (1987).